# Experimental Characterisation of Bubbly Flow using MRI

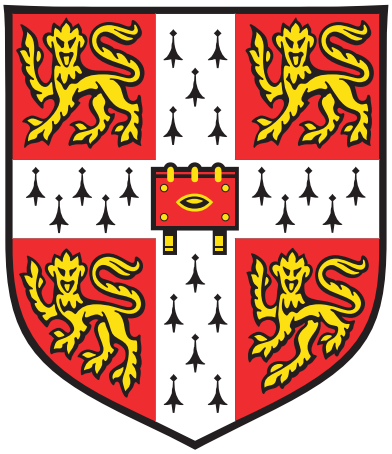

Alexander B. Tayler
Trinity College

A Thesis submitted for the degree of Doctor of Philosophy
May 2011

Department of Chemical Engineering and Biotechnology
University of Cambridge

# Acknowledgements

I would like to thank my supervisor, Professor Lynn Gladden, firstly for her encouragement and guidence over the course of this project, and secondly for allowing me a great amount of freedom to develop my own research interests. I am also indebted to Dr Andy Sederman and Dr Daniel Holland, who have provided me with day-to-day support over the last three years. I would also like to thank Dr Mick Mantle, for his expertise in magnetic resonance, and Thusara Chandrasekera for many helpful discussions. Dr Paul Stevenson is thanked for several valuable insights. I would like to acknowledge the contribution of Dr Michael O'Sullivan, in performing surface tension measurements, and Surinder Sall, who constructed various pieces of electrical apparatus. The EPSRC equipment pool is thanked for the loan of a high-speed camera. For financial support, I gratefully acknowledge the Cambridge Australia Trust, Trinity College, Cambridge, and the Cambridge Philosophical Society.

ABT

*This thesis is the original work of the author, it contains nothing which is the outcome of work done in collaboration with others, except as specified in the text and Acknowledgements. Neither this work, nor any part thereof, has ever been submitted for any other degree. The research described herein was performed at the Magnetic Resonance Research Centre, in the Department of Chemical Engineering and Biotechnology, University of Cambridge, between October 2007 and May 2011. This thesis contains not more than 65,000 words.*

**Abstract**

This thesis describes the first application of ultra-fast magnetic resonance imaging (MRI) towards the characterisation of bubbly flow systems. The principle goal of this study is to provide a hydrodynamic characterisation of a model bubble column using drift-flux analysis by supplying experimental closure for those parameters which are considered difficult to measure by conventional means. The system studied consisted of a 31 mm diameter semi-batch bubble column, with 16.68 mM dysprosium chloride solution as the continuous phase. This dopant served the dual purpose of stabilising the system at higher voidages, and enabling the use of ultra-fast MRI by rendering the magnetic susceptibilities of the two phases equivalent.

Spiral imaging was selected as the optimal MRI scan protocol for application to bubbly flow on the basis of its high temporal resolution, and robustness to fluid flow and shear. A velocimetric variant of this technique was developed, and demonstrated in application to unsteady, single-phase pipe flow up to a Reynolds number of 12,000. By employing a compressed sensing reconstruction, images were acquired at a rate of 188 fps. Images were then acquired of bubbly flow for the entire range of voidages for which bubbly flow was possible (up to 40.8%). Measurements of bubble size distribution and interfacial area were extracted from these data. Single component velocity fields were also acquired for the entire range of voidages examined.

The terminal velocity of single bubbles in the present system was explored in detail with the goal of validating a bubble rise model for use in drift-flux analysis. In order to provide closure to the most sophisticated bubble rise models, a new experimental methodology for quantifying the 3D shape of rising single bubbles was described. When closed using shape information produced using this technique, the theory predicted bubble terminal velocities within 9% error for all bubble sizes examined. Drift-flux analysis was then used to provide a hydrodynamic model for the present system. Good predictions were produced for the voidage at all examined superficial gas velocities (within 5% error), however the transition of the system to slug flow was dramatically overpredicted. This is due to the stabilising influence of the paramagnetic dopant, and reflects that while drift-flux analysis is suitable for predicting liquid holdup in electrolyte stabilised systems, it does not provide an accurate representation of hydrodynamic stability.

Finally, velocity encoded spiral imaging was applied to study the dynamics of single bubble wakes. Both freely rising bubbles and bubbles held static in a contraction were examined. Unstable transverse plane vortices were evident in the wake of the static bubble, which were seen to be coupled with both the path deviations and wake shedding of the bubble. These measurements demonstrate the great usefulness for spiral imaging in the study of transient multiphase flow phenomena.

# Contents

# Chapter 1

# Introduction

Systems in which a gaseous phase is dispersed throughout a liquid are commonly encountered in both nature and industry. Known as gas-liquid flows, these systems occur in situations as diverse as the bow wave of a ship to the cooling system in a nuclear power plant. The structure of a gas-liquid flow depends upon the relative flow-rates of the two phases, and, for flow in a vertical pipe, can be categorised into four regimes [1]. As illustrated in Figure 1.1, these flow regimes are:

(i) Bubbly flow. At low gas-fractions, the liquid is continuous and the gas exists as individual bubbles. Some authors make the distinction between homogeneous (or dispersed) and heterogeneous (or discrete) bubbly flow. Homogeneous flow occurs at low voidages, where the bubble size distribution (BSD) is narrow and there exists little interaction between bubbles, while with increasing gas-fraction the distribution broadens and bubble coalescence and break-up begin to occur. The boundary between homogeneous and heterogeneous bubbly flow is not well defined, however, and in the present work bubbly flow shall be treated as a single regime.

(ii) Slug flow. As the gas-fraction increases, bubble coalescence becomes more prolific and the mean bubble size increases until slugs form which approach the diameter of the column. These slugs are periodic, and may exist with discrete bubbles still present in the intermediary.

(iii) Churn flow. In this regime neither phase is continuous; large irregular plugs of gas flow exist interspersed with slugs of liquid.

(iv) Annular flow. At high enough gas-flow rates only a film of liquid exists at the walls of the tube, with liquid droplets also entrained in the flow. Some authors describe other regimes at higher gas flow rates, including whispy annular flow [2].

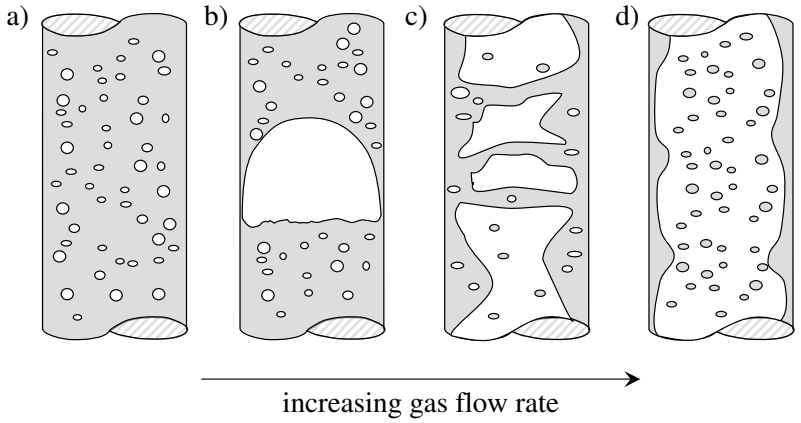


Figure 1.1: Flow regimes for vertical gas-liquid flow.

In the present work, we are only concerned with gas-liquid flows in the bubbly flow regime. Bubbly flows are a very common subset of gas-liquid flows; a list of industrial processes which employ bubbly flow is given in Table 1. One of the most fundamental forms of a bubbly flow system is the bubble column reactor. The operation of this device is quite simple: a vertical column is filled with liquid, which can be either flowing or stationary, and gas is introduced to the system through a distributor at the base of the column. Several variants of bubble column reactor have been produced, as described in detail by Deckwer [3], however in the present work we will only consider the most simple, semi-batch (i.e. no net liquid flow) vertical bubble column.

## 1.1 Design of bubble columns

The principle goal in bubble column design is to produce bubbles of an appropriate size, and the desirable hydrodynamic flow conditions. A system that is mass transfer limited (i.e. the rate of chemical reaction is high), for example, requires a large amount of interfacial area, and hence the generation of smaller bubbles with a correspondingly higher voidage. These conditions lead to decreased circulation in the column, however, which reduces the liquid phase heat and mass transfer coefficients [13]. The design of bubble column reactors is plagued by conflicts such as this [3]. Further compounding the

Table 1.1: Industrial applications of bubbly flow

| Unit operation | Applications | References |
|---|---|---|
| Bubble column reactors | Oxidation of ethylene, cumene, butane, toluene and xylene; chlorination of aliphatic and aromatic hydrocarbons; isobutene hydration; carbonylation of methanol | [3, 4] |
| Bubble slurry reactors | Liquefaction of solid fuels | [5] |
| | Fischer-Tropsch synthesis | [6] |
| Froth flotation cells | Mineral separation | [7, 8] |
| Foam fractionation | Water purification | [9] |
| Two-phase pipe flow | Oil transportation | [10] |
| Heat exchangers | Nuclear cooling systems | [11] |
| Mass transfer units | Fluid aeration; bioreactors | [12] |

problem, both bubble size and the hydrodynamics of bubbly flow are difficult to predict and measure (as reviewed in Section 1.3). The subject of the present thesis is the measurement of these parameters using magnetic resonance imaging (MRI).

The bubble column examined in the present thesis is of internal diameter 31 mm. While this is a small diameter column, even by laboratory standards, this limitation is imposed by the physical dimensions of the bore of the MRI magnet used in this study. The MRI methodologies developed in this thesis, however, could be equally well employed, hardware permitting, on a larger diameter system in future studies. It is generally acknowledged that the influence of the column walls only becomes significant for columns which are less than an order of magnitude greater than bubble diameter [3]. Thus, the present study shall be restrained to the consideration of bubbles of equivalent diameter $d_e < 3$ mm. Much choice exists in the selection of a gas sparger. Industrially, several types of jet and Venturi distributors are used [3]. In laboratory scale experimentation, however, porous frits are more commonly employed. Alternatively, it has been noted by several authors that flexible spargers (such as a porous rubber hose) are useful for the generation of uniform bubble size distributions [13, 14]. It was recently demonstrated by Harteveld [13] that a highly uniform size distribution (in this case generated by a computer controlled sparger) can enable bubbly flow to be obtained for extremely high voidages (up to a voidage of 55% has been demonstrated [15]). In order to test the developed experimental methodologies across a broad range of voidages, a flexible sparger will be used in the present study.

The contemporary design of bubble columns commonly involves the use of multiphase

computational fluid dynamics codes. Several approaches have been developed for the numerical modelling of bubbly flow; these may be broadly grouped into three categories [16]:

(i) Eulerian/Eulerian models. Both phases are treated as continuum (i.e. no spatial separation of the phases is enforced). A population balance model may be coupled with the two-fluid model for tracking the evolution of the bubble size [17].

(ii) Eulerian/Lagrangian models. This approach solves the continuous phase as a continuum, however bubbles are individually tracked. This approach is computationally limited to systems of no more than $10^6$ bubbles at present [16].

(iii) Interface tracking models, such as the volume of fluid approach [18]. This technique provides an accurate description of the interface between two fluids, however becomes too computationally intensive for systems of more than 100 bubbles [16].

The validation of numerical modelling schemes, such as those described above, is the ultimate goal of experimental measurements of bubbly flow. However, as the focus of the present work lies on the experimental characterisation of bubbly flow, only a lumped parameter model is considered in detail in the present thesis. As mentioned above, the primary goal of this thesis is the measurement of bubble size, interfacial area and liquid phase hydrodynamics. To demonstrate the usefulness of these measurements in bubble column design, it is sought to characterise the overall hydrodynamics of a model bubble column using drift-flux analysis [19, 20]. In this model, a slip velocity, defined as the difference between phase-fraction normalised gas and liquid superficial velocities, is expressed as:

$$U_{\mathrm{R}} = \frac{U_{\mathrm{g}}}{\varepsilon} - \frac{U_{\mathrm{l}}}{1-\varepsilon} \tag{1.1}$$

where $U_{\mathrm{g}}$ and $U_{\mathrm{l}}$ are the gas and liquid superficial velocities, and $\varepsilon$ is the voidage. It is common to predict the slip velocity using a Richardson-Zaki correlation of the form:

$$U_{\mathrm{R}} = U_{\mathrm{T}\infty}(1-\varepsilon)^{N-1} \tag{1.2}$$

where $U_{\mathrm{T}\infty}$ is the rise velocity of a single bubble in an infinite medium and $N$ is a function of the bubble Reynolds number. Substituting equation (1.2) into equation (1.1):

$$(1-\varepsilon)U_{\mathrm{g}} - \varepsilon U_{\mathrm{l}} = U_{\mathrm{T}\infty}\varepsilon(1-\varepsilon)^{N}. \tag{1.3}$$

Equation (1.3) may be solved to determine the liquid hold-up for a range of operating conditions. For the successful application of drift-flux analysis, both the mean bubble

size and liquid hold-up must be accurately measured, and an accurate model for the single bubble rise velocity must be used. The measurement of these parameters and the validation of a single bubble rise model are the subject of individual chapters of this thesis, with the produced measurements then combined to provide a hydrodynamic characterisation of the model bubble column using drift-flux analysis.

## 1.2 Influence of dopants on bubbly flow

In a pure solution the gas-liquid interface cannot support any stress and is completely mobile. This permits interphase momentum transfer, which generates recirculating vortices within rising bubbles: decreasing drag and increasing the bubble terminal velocity. Further, liquid films between approaching bubbles are able to rapidly drain, which allows bubble coalescence to readily occur. These behaviours are dramatically altered in aqueous systems, however, by the presence of surface active molecules [21]. Surfactants (i.e. organic molecules composed of both a hydrophobic non-polar segment, typically an aliphatic chain, and a hydrophilic polar functional group, such as a hydroxyl) tend to adsorb at the interface, where the hydrophobic tail extends into the gas phase, while the hydrophilic head resides in the water. These surfactants lower the surface tension, which decreases bubble sizes and thus increases liquid hold-up. By accumulating at the interface the surfactant molecules alter the interfacial shear condition, which can range from the formation of a 'rigid cap', as the surfactants are swept to the rear of the bubble as it rises, to a no-slip boundary condition covering the entire surface of bubble for heavily contaminated systems [21]. This loss of interfacial mobility leads to increased skin friction, which slows the bubble rise velocity. Further, the adsorbed surfactants introduce Marangoni forces that slow the film drainage process, and hence hinder bubble coalescence and stabilise bubbly flow at higher voidages [22].

While the influence of organic surfactants on gas-liquid flows is well known, the impact of inorganic molecules is less well understood. It is well established that the presence of inorganic ions at moderate concentrations can either increase or decrease the surface tension of water [23], which can have a stabilising influence on bubbles. At concentrations lower than that required to significantly alter the surface tension, however, some (but not all [24, 25]) inorganic salts still exert a strong influence on the behaviour of bubbly flow. It has been observed by many authors that a small concentration of salt greatly decreases bubble coalescence [26, 27, 28, 29, 30, 31, 32, 33, 34], with this phenomenon attributed to a slowing of the film drainage process [35, 36]. These effects are noted to only occur

above a certain transitional concentration, at which point a step-change in the stability of bubbly flow occurs [37, 33]. While it is known that the influence of electrolytes is ion specific [24, 25], it remains contested in the literature whether low concentrations of electrolyte have an influence on the dynamics of single bubbles, with Henry *et al.* [38] and Sato *et al.* [39] claiming no effect, while Jamialahmadi and Müller-Steinhagen [30] stating that salt slows bubble rise. The mechanisms of bubble stabilisation by inorganic dopants are not well understood; Zieminski and Whittemore [28] discuss the possibility of ion-water interactions, which render the film between bubbles more cohesive, while, Craig *et al.* [40] discuss suggest some form of hydrophobic interaction.

The specific composition of the continuous phase examined is largely unimportant to the goal of the present work (the application of MRI to high voidage bubbly flow), and surface active materials or inorganic dopants may be included or excluded as convenient to provide a model system for the application of MRI.

## 1.3 Experimental studies of bubbly flow

Motivated by the many applications of bubble columns, a vast amount of work has been devoted to the experimental characterisation of bubbly flow. Much difficulty has been encountered, however, in obtaining accurate experimental data on high voidage systems. The challenges associated with experiments on high voidage systems essentially stem from three aspects of the nature of bubbly flow: it is opaque, which restricts optical measurements to boundary flows; the gas-liquid interface cannot support significant stress, which fundamentally undermines the accuracy of intrusive measurements; and the system structure is highly dynamic, which imposes a challengingly short time scale to obtain measurements by tomographic means. Accurate experimental measurements on bubbly flow systems are needed to contribute to a fundamental understanding of these systems, for the validation of increasingly prevalent multiphase computational fluid dynamics codes, and to provide the basis of tools for process measurement and control. Experimental investigations into bubbly flow tend to focus upon either the characterisation of the bubbles themselves, or of the liquid phase hydrodynamics. These two areas of research are reviewed in the present section.

### 1.3.1 Measurement of bubble size and interfacial area

The measurement of bubble size distributions is highly desirable, as it is this property which governs the bubble rise velocity and hence the residence time in a given unit oper-

ation. The measurement of interfacial area is also important, as it is this property which (when multiplied by some driving force) governs rates of interphase mass, momentum and energy transfer. Experimental techniques for the measurement of these two parameters are reviewed in this section.

Many techniques have been developed for the measurement of bubble size. Most prominent are photographic techniques, which are reviewed by Tayali and Bates [41]. This approach involves obtaining photographs of bubbly flow through a transparent section of the column. Several improvements to the basic technique have been suggested, such as shadowgraphy, which removes the influence of the position of bubbles within the column by projecting bubble shapes onto an opaque medium, such that the focal length of the camera is the same for all bubbles. Bubble sizes were measured in this way by van den Hengel [42] and Majumder *et al.* [43]. Due to the occlusion of the dispersed phase in the bulk flow, however, these optical techniques are typically limited to relatively low gas-fractions. Also commonly used are acoustic techniques, wherein the frequency of pressure variations in the column (caused by either passive or driven bubble shape oscillations) are measured and used to infer bubble size. The acoustic measurement of bubble size is reviewed in full by Leighton [44]. Like optical techniques, however, acoustic measurements fail at higher voidages, where the pressure fluctuations in the column are increasingly dominated by bubble-bubble interactions [45]. For low voidage systems the acoustic technique was found to be more accurate than optical measurements (by comparison with volumetric measurements on bubbles captured in a funnel) [46]. This reflects the problem of obtaining a true measurement of bubble volume from 2D projections of a bubble, as discussed by Lunde and Perkins [47].

To permit bubble size measurements in high voidage systems, many invasive probes have been developed. These typically consist of single or multi-point electrical conductivity or fibre optic local phase probes, as reviewed by Saxena *et al.* [5]. These probes have been employed in many previous studies [48, 49, 50]. The systematic error generated by the intrusive nature of these problems has been the subject of much work; a comprehensive review of which is provided by Julia *et al.* [51]. More recently, wire-mesh sensors have become popular for their two dimensional visualisation capability [52, 53]. While these sensors possess excellent time resolution (on the order of thousands of frames per second), they are currently limited to a spatial resolution on the order of 1 mm, which is insufficient for the accurate determination of bubble size distributions. Additionally, the errors associated with the distortion of bubble shape due to the wire mesh have not yet

been explored in full, and as the mesh is completely destructive to the structure of the two phase flow, wire mesh sensors cannot be used for measurements which explore the evolution of the dispersed phase.

Several tomographic techniques have been explored for the characterisation of gas-liquid flows, however finding a workable balance between temporal and spatial resolution has proved difficult. Electrical tomographies (including electrical resistance tomography, electrical capacitance tomography and electrical impedance tomography) have been investigated, however, despite having extremely short acquisition times, are of far too low spatial resolution for the identification of individual bubbles [54]. A range of radiographic tomographies, reviewed by Chaouki *et al.* [55], have also been explored. In particular, computer aided x-ray tomography has been widely tested, however the need to mechanically rotate the emission source around the sample decreases the time resolution below that required. To overcome this problem, ultra-fast x-ray scanners, which use a number of fixed emission sources, have been developed, however the limited number of emitters and detectors employed to date has reduced the spatial resolution below that required for the accurate measurement of bubble size [56]. Most recently, Bieberle *et al.* [57] have demonstrated the use of an auspicious alternative method of x-ray tomography. In their technique, Bieberle *et al.* scan an electron beam back and forth across a block of tungsten, which emits x-rays through a bubble column to a ring of detectors on its opposite side. This permits temporal resolutions on the order of milliseconds to be achieved, while imaging at a spatial resolution of approximately 1 mm. Thus this technique demonstrates spatial and temporal resolutions on the same order of magnitude as wire mesh sensors, with the additional advantage of being non-invasive. With further refinement to yield higher resolution images, this technique may be very useful for the measurement of bubble size and shape in high voidage systems, particularly if the high temporal resolution of the technique can be exploited for the rapid production of 3D images.

The measurement of interfacial area is closely related to that of bubble size, with an estimate of surface area able to be calculated from measured bubble sizes by assuming some bubble shape. To improve the accuracy of the measurement of interfacial area, therefore, it is desirable to also measure some information about bubble shape. Beyond optical techniques at low void fractions, the measurement of bubble shape is very difficult. Some previous work has focused upon the determination of bubble shape from chord lengths which may be measured using local phase probes [58]. Alternatively, spatially averaged interfacial area may be determined for a system undergoing chemisorption by

measuring the concentration of the reactants at various points in the column. Common chemisorption systems used for this purpose are discussed by Deckwer [3].

### 1.3.2 Measurement of liquid-phase hydrodynamics

Bubbly flow is a hydrodynamically complex system. The entrainment of fluid with the rising bubbles leads to the formation of large scale recirculation vortices [1], which govern liquid-side mass and heat transfer. Much work has focused on the quantification of liquid phase velocities in bubbly flow, with a broad range of experimental techniques being developed. Hot film anemometry, wherein the local fluid velocity is determined around a heating element by measurement of the heat flux [59], was the first technique to be explored. Like local phase probes, however, hot film anemometry is highly intrusive; the errors associated with the invasive nature of the probe are discussed by Rensen *et al.* [60]. As an alternative, laser Doppler anemometry (LDA) has found considerable use [61, 62, 63]. This technique measures the light scattered by small seed particles as they flow through an interference pattern generated by two intersecting laser beams or laser sheets. LDA may also be used to infer a measurement of bubble size [58]. Particle imaging velocimetry (PIV), which uses high-speed cameras to track the motion of seed particles, has also recently increased in popularity, and has been applied to the study of bubble flow [64]. Both LDA and PIV are, however, optically based, which limits the applicability of the techniques to low voidage systems. The highest gas-fraction bubbly flow system to which optical velocimetry has been applied was of voidage 25%, however those authors reported an exponential decrease in sampling rate as they sampled further from the column wall [65]. To overcome the optical limitation, a variant of PIV has been proposed that uses x-rays and x-ray absorbing seed particles [66], while phase contrast x-ray velocimetry techniques have also been demonstrated [67]. Lastly a computer aided radioactive particle tracking technique (CARPT) has been applied to bubbly flow by Devanathan *et al.* [68]. In this technique, a single radioactive particle is allowed to circulate in a bubble column, and by tracking the particle's position over several hours the time averaged flow field inside of the column can be determined.

## 1.4 Application of MRI to bubbly flow

An emergent theme from Section 1.3 is that sensitivity of the gas-liquid interface to invasive probes, and the optical opacity of the system at high voidages, are responsible for the majority of difficulties encountered in the experimental characterisation of bubbly flow. Magnetic Resonance Imaging (MRI) is therefore a very a promising technique for

application to bubbly flow systems, as it avoids these two problems entirely. Further, MRI can be used to produce both structural images and quantitative velocity maps of a system [69]. There exist fairly limited applications of magnetic resonance to bubbly flow in the literature, and most studies produce only temporally or spatially averaged measurements. Bubbly flows were first examined using magnetic resonance by Lynch and Segel [70], who used spatially averaged measurements to quantify the void fraction present in their system. They demonstrated a linear dependence between NMR signal and volume-averaged gas fraction. Abouelwafa and Kendall [71] subsequently used a similar technique to estimate the voidage and flow rate of each phase. Leblond *et al.* [72] used pulsed field gradient (PFG) NMR (a technique for the measurement of molecular displacement) to quantify liquid velocity distributions for gas-liquid flows and obtained some measurement of the flow instability. Barberon and Leblond [73] applied the same technique to the quantification of flow around singular Taylor bubbles and were able to demonstrate the existence of recirculation vortices in the bubble's wake. Le Gall *et al.* [74] also used PFG NMR to study liquid velocity fluctuations associated with bubbly flow in different geometries. Daidzic *et al.* [75] obtained 1D projections of bubbly flow with a time resolution of approximately 10 ms, however, due to hardware limitations, were only able to produce time averaged 2D images. Similarly, temporally averaged 2D measurements were acquired by Reyes [76], who examined gas-liquid slug flow, and by Sankey *et al.* [77], who investigated bubbly flow in a horizontal pipe. Most recently, Stevenson *et al.* [78] used gas-phase PFG NMR to size bubbles in a butane foam, and Holland *et al.* [79] produced a Bayesian technique for determining bubble sizes from MRI signals. The only study in the literature which demonstrates MRI measurements with both temporal and spatial resolution on a gas-liquid system is that of Gladden *et al.* [80], who presented velocity fields in the vicinity of a Taylor bubble. The present study is the first to apply ultra-fast MRI imaging towards the characterisation of dispersed bubbly flow.

## 1.5 Scope of thesis

The subject of the present thesis is the use of magnetic resonance imaging (MRI) to fully characterise a bubbly flow system for the entire range of voidages for which dispersed bubbly flow is possible. In doing so, the instantaneous position, size, and shape of the bubbles (which will in turn yield a measure of the bubble size distribution and interfacial area) are measured, together with the liquid phase hydrodynamics. The primary goals of this thesis are to develop MRI techniques for the measurement of these data, and

to apply the developed methodologies towards the hydrodynamic characterisation of a model bubbly flow system.

The specific goals of the present thesis are as follows:

(i) Attempt the first application of ultra-fast MRI to bubbly flow systems.

(ii) Develop experimental MRI methodologies for the measurement of bubble size, interfacial area and quantitative velocity fields in high voidage systems.

(iii) Use drift-flux analysis in combination with the above measurements to hydrodynamically characterise the examined bubble column.

(iv) Apply the newly developed MRI techniques to the study of single bubble dynamics.

This body of work is structured as follows:

**Chapter two** gives the background and theory of MRI, with particular focus paid to ultrafast imaging sequences, and quantitative flow measurement using MRI. The techniques discussed in this section represent the *status quo* of MRI, and provide the basis for the development of measurements specifically for application to bubbly flow.

**Chapter three** describes the first application of ultrafast MRI to bubbly flow. The challenges associated with imaging this system are established, and a velocity measurement technique which addresses some of these problems is proposed.

**Chapter four** selects an optimal MRI protocol for the visualisation of high shear systems, such as bubbly flow. The implementation of this technique is described, and a velocity measurement variant is proposed. The effect of fluid flow and shear on the chosen technique are quantified, and the technique is then demonstrated on an example high-shear system. Finally, high-temporal resolution velocity imaging using a compressed sensing reconstruction is demonstrated.

**Chapter five** shows the application of the selected MRI protocol to bubbly flow for the quantification of bubble size, interfacial area and liquid phase velocity fields. Particular focus is given to procedures for the automation of data analysis, and the limitations of the MRI measurements.

**Chapter six** examines single bubble dynamics, with the goal of validating a model for single bubble terminal velocity for use with drift-flux analysis. In doing this, a new experimental procedure for determining the 3D shape of rising single bubbles is described, and employed close to a singe bubble rise model. Additionally classical models for bubble shape oscillation are compared to the reconstructed bubble shapes.

**Chapter seven** characterises the hydrodynamics of the model bubble column using drift-flux analysis. In doing this, the MRI measurements of bubble size and shape are employed, as is the single bubble rise model previously validated. The accuracy and limitations of drift-flux analysis in application to the present system are assessed.

**Chapter eight** examines the dynamics of single bubble wakes using the previously developed velocity measurement technique. Both freely rising bubbles, and bubbles held static in a contraction against a downward flow are examined, and the influence of the bubble wake upon single bubble behaviours is discussed.

**Chapter nine** gives conclusions and recommendations for future work.

# Bibliography


[1] Mudde, R.F., 2005. Gravity-driven bubbly flows. *Annu. Rev. Fluid Mech.*, 37, pp. 393–423.

[2] Hetsroni, G., 1982. *Handbook of multiphase systems.* Hemisphere publishing, New York.

[3] Deckwer, W.D., 1985. *Bubble column reactors.* Wiley, Chichester.

[4] Jacobsen, H.A., 2008. *Chemical reactor modeling.* Springer-Verlag, Berlin.

[5] Saxena, S.C., Patel, D., Smith, D.N. and Ruether, J.A., 1988. An assessment of experimental techniques for the measurement of bubble size in a bubble slurry reactor as applied to indirect coal liquefaction. *Chem. Eng. Comm.*, 63, pp. 87–127.

[6] Krishna, R. and Sie, S.T., 2000. Design and scale-up of the Fischer-Tropsch bubble column slurry reactor. *Fuel Proc. Tech.*, 64, pp. 73–105.

[7] Finch, J.A. and Dobby, G.S., 1991. Column flotation: A selected review. Part I. *Int. J. Min. Proc.*, 33, pp. 343 – 354.

[8] Pal, R. and Masliyah, J., 1989. Flow characterization of a flotation column. *Can. J. Chem. Eng.*, 67, pp. 916–923.

[9] Stevenson, P., Fennell, P.S. and Galvin, K.P., 2008. On the drift-flux analysis of flotation and foam fractionation processes. *Can. J. Chem. Eng.*, 86, pp. 635–642.

[10] Szilas, A.P., 1975. *Production and transport of oil and gas.* Akademiai Kiado, Budapest.

[11] Poullikkas, A., 2003. Effects of two-phase liquid-gas flow on the performance of nuclear reactor cooling pumps. *Prog. Nucl. Energ.*, 42, pp. 3 – 10.

[12] Enes, K., 2010. *Survey of gas-liquid mass transfer in biorectors.* Ph.D. thesis, Iowa State University.

[13] Harteveld, W., 2005. *Bubble columns: structures or stability?* Ph.D. thesis, Delft University of Technology.

[14] Rice, R.G., Tupperainen, J.M.I. and Hedge, R.M., 1981. Dispersion and hold-up in bubble columns - comparison of rigid and flexible spargers. *Can. J. Chem. Eng.*, 59, pp. 677–687.

[15] Mudde, R.F., Harteveld, W.K. and van der Akker, H.E.A., 2009. Uniform flow in bubble columns. *Ind. Eng. Chem. Res.*, 48, pp. 148–158.

[16] Bove, S., 2005. *Computational fluid dynamics of gas-liquid flows including bubble population balances*. Ph.D. thesis, Esbjerg Institute of Engineering.

[17] Wang, T. and Wang, J., 2007. Numerical simulation of gas-liquid mass transfer in bubble column with a CFD-PBM coupled model. *Chem. Eng. Sci.*, 62, pp. 7107–7118.

[18] Krishna, R. and van Baten, J.M., 1998. Simulating the motion of gas bubbles in a liquid. *Nature*, 398, p. 208.

[19] Wallis, G.B., 1969. *One-dimensional two-phase flow*. McGraw-Hill, New York.

[20] Zuber, N. and Findlay, J., 1965. Average volumetric concentration in 2-phase flow systems. *ASME J.*, 87, p. 453.

[21] Takagi, S. and Matsumoto, Y., 2011. Surfactant effects on bubble motion and bubbly flows. *Annu. Rev. Fluid. Mech.*, 43, pp. 615–636.

[22] Růžička, M.C., Vecer, M.M. and Drahoš, O.J., 2008. Effect of surfactant on homogeneous regime stability in bubble column. *Chem. Eng. Sci.*, 63, pp. 951–967.

[23] Weissenborn, P.K. and Pugh, R.J., 1996. Surface tension of aqueous solutions of electrolytes: relationship with ion hydration, oxygen solubility, and bubble coalescence. *J. Colloid Interf. Sci.*, 184, pp. 550–563.

[24] Craig, V.S.J., 2004. Bubble coalescence and specific-ion effects. *Curr. Opin. Colloid In.*, 9, pp. 178–184.

[25] Henry, C.L., Dalton, C.N., Scruton, L. and Craig, W.S.J., 2007. Ion-specific coalescence of bubbles in mixed electrolyte solutions. *J. Phys. Chem. C*, 111, pp. 1015–1023.

[26] Marrucci, G. and Nicodemo, L., 1967. Coalescence of gas bubbles in aqueous solutions of inorganic electrolytes. *Chem. Eng. Sci.*, 22, pp. 1257–1265.

[27] Lessard, R.R. and Zieminski, S.A., 1971. Bubble coalescence and gas transfer in aqueous electrolytic solutions. *Ind. Eng. Chem. Fundamen.*, 10, pp. 260–269.

[28] Zieminski, S.A. and Whittemore, R.C., 1971. Behavior of gas bubbles in aqueous electrolyte solutions. *Chem. Eng. Sci.*, 26, pp. 509–520.

[29] Kelkar, B.G., Phulgaonkar, S.R. and Shah, Y.T., 1983. The effect of electrolyte solutions on hydrodynamic and backmixing characteristics in bubble columns. *Chem. Eng. J.*, 27, pp. 125–133.

[30] Jamialahmadi, M. and Müller-Steinhagen, 1992. Effect of alcohol, organic acid and potassium chloride concentration on bubble size, buble rise velocity and gas hold-up in bubble columns. *Chem. Eng. J.*, 50, pp. 47–56.

[31] Deschenes, L.A., Barrett, J., Muller, L.J., Fourkas, J.T. and Mohanty, U., 1998. Inhibition of bubble coalescence in aqueous solutions. 1. electrolytes. *J. Phys. Chem. B*, 1998, pp. 5115–51,193.

[32] Ruthiya, K.C., van der Schaaf, J., Kuster, B.F.M. and Schouten, J.C., 2006. Influence of particles and electrolyte on gas hold-up and mass transfer in a slurry bubble column. *Int. J. Chem. React. Eng.*, 4, p. A13.

[33] Ribeiro, C.P. and Mewes, D., 2007. The influence of electrolytes on gas hold-up and regime transition in bubble columns. *Chem. Eng. Sci.*, 62, pp. 4501–4509.

[34] Orvalho, S., Růžička, M. and Drahoš, J., 2009. Bubble columns with electrolytes: gas holdup and flow regimes. *Ind. Eng. Chem. Res.*, 48, pp. 8237–8243.

[35] Marrucci, G., 1969. A theory of coalescence. *Chem. Eng. Sci.*, 24, pp. 975–985.

[36] Henry, C.L., Karakashev, S.I., Nguyen, P.T. and Craig, V.S.J., 2009. Ion specific electrolyte effects on thin film drainage in nonaqueous solvents propylene carbonate and formamide. *Langmuir*, 25, pp. 9931–9937.

[37] Zahradník, J., Fialová, M., Růžička, M., Drahoš, J., Kaštánek, F. and Thomas, N.H., 1997. Duality of the gas-liquid flow regimes in bubble column reactors. *Chem. Eng. Sci.*, 1997, pp. 3811–3826.

[38] Henry, C.L., Parkinson, L., Ralston, J.R. and Craig, V.S.J., 2008. A mobile gas-water interface in electrolyte solutions. *J. Phys. Chem. C*, 39, pp. 15,094–15,097.

[39] Sato, A., Aoki, M. and Wananabe, M., 2010. Single bubble rising motion in aqueous solution of electrolyte. *J. Fluid Sci. Tech.*, 5, pp. 14–25.

[40] Craig, V.S.J., Ninham, B.W. and Pashley, R.M., 1993. The effect of electrolytes on bubble coalescence in water. *J. Phys. Chem.*, 97, pp. 10,192–10,197.

[41] Tayali, N.E. and Bates, C.J., 1990. Particle sizing techniques in multiphase flows: a review. *Flow. Meas. Instrum.*, 1, pp. 77–103.

[42] van den Hengel, E., 2004. *Multi-level modeling of gas-liquid two-phase flow in a bubble column.* Ph.D. thesis, University of Twente.

[43] Majumder, S.K., Kundu, G. and Mukherjee, D., 2006. Bubble size distribution and gas-liquid interfacial area in a modified downflow bubble column. *Chem. Eng. J.*, 112, pp. 1–10.

[44] Leighton, T.G., 1997. *The acoustic bubble.* Academic Press, San Diego.

[45] Manasseh, R., LaFontaine, R.F., Davy, J., Shepherd, I. and Zhu, Y.G., 2001. Passive acoustic bubble sizing in sparged systems. *Exp. Fluids*, 30, pp. 672–682.

[46] Vazquez, A., Sanchez, R.M., Salinas-Rodrigguez, E., A., S. and Manasseh, R., 2005. A look at three measurement techniques for bubble size determination. *Exp. Therm. Fluid Sci.*, 30, pp. 49–57.

[47] Lunde, K. and Perkins, R.J., 1998. Shape oscillations of rising bubbles. *Appl. Sci. Res.*, 58, pp. 387–408.

[48] Magaud, F., Souhar, M., Wild, G. and Boisson, N., 2001. Experimental study of bubble column hydrodynamics. *Chem. Eng. Sci.*, 56, pp. 4597–4607.

[49] Hibiki, T., Goda, H., Kim, S., Ishii, M. and Uhle, J., 2003. Experimental study on interfacial area transport of a vertical downward bubbly flow. *Exp. Fluids*, 35, pp. 100–111.

[50] Kalkach-Navarro, S., Lahey, R.T., Drew, D.A. and Meyer, R., 1993. Interfacial area density, mean radius and number density measurements in bubbly two-phase flow. *Nuc. Eng. Des.*, 142, pp. 341–351.

[51] Juliá, J.E., Harteveld, W.K., Mudde, R.F. and Van den Akker, H.E.A., 2005. On the accuracy of the void fraction measurements using optical probes in bubbly flows. *Rev. Sci. Instrum.*, 76, p. 035,103.

[52] Prasser, H.M., Scholz, D. and Zippe, C., 2001. Bubble size measurement using wire-mesh sensors. *Flow Meas. Instr.*, 12(4), pp. 299–312.

[53] Prasser, H.M., Beyer, M., Carl, H., Gregor, S., Lucas, D., Pietruske, H., Schutz, P. and Weiss, F.P., 2007. Evolution of the structure of a gas-liquid two-phase flow in a large vertical pipe. *Nucl. Eng. Des.*, 237(15-17), pp. 1848–186.

[54] Wang, F., Marashdeh, Q., Fan, L.S. and Warsito, W., 2010. Electrical capacitance volume tomography: design and applications. *Sensors*, 10, pp. 1890–1917.

[55] Chaouki, J., Larachi, F. and Dudukovic, M.P., 1997. Noninvasive tomographic and velocimetric monitoring of multiphase flows. *Ind. Eng. Chem. Res.*, 36, pp. 4476–4503.

[56] Prasser, H.M., Misawa, M. and Tiseanu, I., 2005. Comparison between wire-mesh sensor and ultra-fast x-ray tomograph for an air-water flow in a vertical pipe. *Flow Meas. Instr.*, 16(2-3), pp. 73–83.

[57] Bieberle, M., Fischer, F., Schleicher, D., Koch, D., Menz, H.J., Mayer, H.G. and Hampel, U., 2009. Experimental two-phase flow measurement using ultra fast limited-angle-type electron beam x-ray computed tomography. *Exp. Fluids*, 47, pp. 369–378.

[58] Kulkarni, A.A., Joshi, J.B. and Ramkrishna, D., 2004. Determination of bubble size distributions in bubble columns using LDA. *AIChE J.*, 50, pp. 3068–3084.

[59] Bruun, H.H., 1996. Hot-film anemometry in liquid flows. *Meas. Sci. Technol.*, 7, pp. 1301–1312.

[60] Rensen, J., Stefan, L., de Vries, J. and Lhose, D., 2005. Hot-film anemometry in bubbly flow I: bubble-probe interaction. *Int. J. Multiphase Flow*, 31, pp. 285–301.

[61] Becker, S., Sokolichin, A. and Eigenberger, G., 1994. Gas-liquid flow in bubble columns and loop reactors: Part II: Comparison of detailed experiments and flow simulations. *Chem. Eng. Sci.*, 49, pp. 5747–5762.

[62] Becker, S., De Bie, H. and Sweeney, J., 1999. Dynamic flow behaviour in bubble columns. *Chem. Eng. Sci.*, 54, pp. 4929–4935.

[63] Borchers, O., Busch, C. Sokolichin, A. and Eigenberger, G., 1999. Applicability of the standard k-$\varepsilon$ turbulence model to the dynamic simulation of bubble columns. Part II: Comparison of detailed experiments and flow simulations. *Chem. Eng. Sci.*, 54, pp. 5927–5935.

[64] Delnoij, E., Kuipers, J.A.M.and van Swaaij, W. and Westerweel, J., 2000. Measurement of gas-liquid two-phase flow in bubble columns using ensemble correction PIV. *Chem. Eng. Sci.*, 55, pp. 3385–3395.

[65] Mudde, R.F., Groen, J.S. and van Den Akker, H.E.A., 1997. Liquid velocity field in a bubble column: LDA experiments. *Chem. Eng. Sci.*, 52, pp. 4217–4224.

[66] Seeger, A., Affeld, K., Goubergrits, K., Kertzscher, U. and Wellnhofer, E., 2001. X-ray based assessment of the three-dimensional velocity of the liquid phase in a bubble column. *Exp. Fluids*, 31, pp. 193–201.

[67] Kim, G.B. and Lee, S.J., 41. X-ray PIV measurements of blood flows without tracer particles. *Exp. Fluids*, 2006, pp. 195–200.

[68] Devanathan, N., Moslemian, D. and Dudukovic, M.P., 1990. Flow mapping in bubble columns using CARPT. *Chem. Eng. Sci.*, 45, pp. 2285–2291.

[69] Fukushima, E., 1999. Nuclear magnetic resonance as a tool to study flow. *Annu. Rev. Fluid Mech.*, 31, pp. 95–123.

[70] Lynch, G.F. and Segel, S.L., 1977. Direct measurement of void fraction of a 2-phase fluid by nuclear magnetic resonance. *Int. J. Heat Mass Transfer*, 20, pp. 7–14.

[71] Abouelwafa, M.S.A. and Kendall, E.J.M., 1979. Optimization of continuous wave nuclear magneticresonance to determine in situ volume fractions and individual flowrates in 2 component mixtures. *Rev. Sci. Instrum.*, 55, pp. 1545–1549.

[72] Leblond, J., Javelot, S., Lebrun, D. and Lebon, L., 1998. Two-phase flow characterization by nuclear magnetic resonance. *Nucl. Eng. Design*, 184, pp. 229–237.

[73] Barberon, F. and Leblond, J., 2001. Intermittent two-phase flow study by NMR. *C. R. Acad. Sci. Paris, Chimie*, 4, pp. 853–856.

[74] Le Gall, F., Pascal-Ribot, S. and Leblond, J., 2001. Nuclear magnetic resonance measurements of fluctuations in air-water two-phase flow: pipe flow with and without 'disturbing' section. *Phys. Fluids*, 13, pp. 1118–1129.

[75] Daidzic, N.E., Schmidt, E., Hasan, M.M. and Altobelli, S., 2005. Gas-liquid phase distribution and void fraction measurements using MRI. *Nucl. Eng. Design*, 235, pp. 1163–1178.

[76] Reyes, J.N., 1998. The use of MRI to quantify multi-phase flow patterns and transitions: an application to horizontal slug flow. *Nucl. Eng. Des.*, 184, pp. 213–228.

[77] Sankey, M., Yang, Z., Gladden, L.F., Johns, M.L., Lister, D. and Newling, B., 2009. SPRITE MRI of bubbly flow in a horizontal pipe. *J. Magn. Reson.*, 199, pp. 126–136.

[78] Stevenson, P., Sederman, A.J., Mantle, M.D., Li, X. and Gladden, L.F., 2010. Measurement of bubble size distribution in a gas-liquid foam using pulsed-field gradient nuclear magnetic resonance. *J. Colloid Interface Sci.*, 352, pp. 114–120.

[79] Holland, D.J., Blake, A., Tayler, A.B., Sederman, A.J. and Gladden, L.F., 2011. A Bayesian approach to characterising multi-phase flows using magnetic resonance: Application to bubble flows. *J. Magn. Reson.*, 209, pp. 83–87.

[80] Gladden, L.F., Akpa, B.S., Anadon, L.D., Heras, J.J., Holland, D.J., Mantle, M.D., Matthews, S., Mueller, C., Sains, M.C. and Sederman, A.J., 2006. Dynamic MR imaging of single- and two-phase flows. *Chem. Eng. Res. Des.*, 84(A4), pp. 272–281.

# Chapter 2

# MRI Theory

In late 1945, a group of researchers at Harvard University, lead by Purcell [1], almost simultaneously with Bloch [2] and contemporaries working independently at Stanford University, showed that certain nuclei could absorb and subsequently emit radiofrequency (r.f.) energy when placed in a magnetic field at a certain nuclei-specific strength. These were the first observations of the phenomenon known as nuclear magnetic resonance (NMR). Purcell and Bloch were awarded the Nobel prize for their discovery in 1952, which has since developed into a routine technique for chemical analysis. In 1973, Lauterbur [3] and Mansfield and Grannell [4] showed that by application of a spatially variable magnetic field, the position of the emitting nuclei could be determined. This was the foundation of magnetic resonance imaging (MRI). Mansfield subsequently developed MRI for applications in medicine [5], and MRI has since become one of the most potent medical diagnostic tools available today. Most recently, MRI has emerged as a useful tool for research in the natural sciences and engineering, where it is enabling measurements unavailable to previous generations of researchers.

In this chapter the basic principles of MRI are introduced. In doing this, the underlying science of NMR is firstly discussed. Initially quantum mechanics are used to describe the physical basis of these measurements, however the more intuitive vector model is then adopted as a full quantum mechanical description of MRI is beyond the scope of this thesis. Particular emphasis is given to fast imaging protocols, as the imaging of highly

dynamic bubbly flow is the object of the present work. Only a basic introduction is given to each technique in this section, with further analysis of the employed techniques given, as relevant, in subsequent chapters. A full treatment of the theory described in this chapter is given by standard texts such as those of Callaghan [6], Levitt [7] and Haacke [8].

## 2.1 Basic principles of NMR

### 2.1.1 Zeeman splitting

Nuclear spin is an intrinsic property of sub-atomic particles. While spin is not produced by the physical rotation of a particle, it does possess a form of angular momentum. Spin angular momentum is described by the spin quantum number, $I$, and is quantised in increments of $\frac{1}{2}$. A particle can adopt one of the $2I + 1$ energy levels between $-I$ and $I$, which are, in the absence of an external field, degenerate (that is, all energy levels are of equal energy and thus have the same likelihood of occurring). If a magnetic field is applied, however, this degeneracy is broken, and each of the $2I + 1$ states have a slightly different energy. This phenomenon is known as Zeeman splitting. Transition between two non-degenerate states is possible by absorption or emission of a photon of energy:

$$\Delta E = \frac{1}{2\pi} h\gamma B_0 \tag{2.1}$$

where $h$ is Planck's constant ($6.63 \times 10^{-34}$ J s$^{-1}$), $\gamma$ is a nuclei-specific constant of proportionality known as the gyromagnetic ratio (4257 Hz G$^{-1}$ for $^1$H), and $B_0$ is magnetic field strength. A hydrogen nucleus, for example, has $I = \frac{1}{2}$ and can take one of two energy levels ($\pm\frac{1}{2}$). A Zeeman diagram for this nucleus is shown in Figure 2.1.

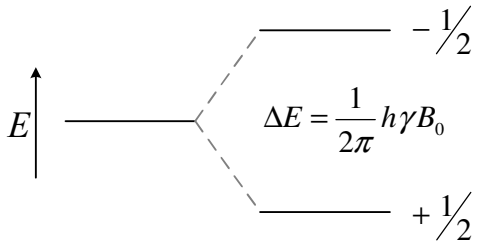


Figure 2.1: Zeeman diagram for a spin-$\frac{1}{2}$ nuclei. The lower energy state is slightly more populous than the higher energy state. Absorption or emission of a photon of the appropriate energy is required for transition between the two states.

Zeeman splitting is responsible for the manifestation of NMR on a macroscopic level, as it is the difference in energy level populations that is detectable. Thus NMR signal can only be received for nuclei with $I \neq 0$. While several common nuclei such as $^{12}$C, $^{14}$N and $^{16}$O cannot be studied using NMR for this reason, most such nuclei do have an isotope which is NMR active. These isotopes tend to have low natural abundances (for example only 1.07% of carbon naturally exists as $^{13}$C), which renders the signal-to-noise ratio of the experiments problematic. In the present thesis, only $^{1}$H and $^{19}$F will be considered, both of which exhibit natural abundances of 100%.

For a system with $I = \frac{1}{2}$, the population of spins in either state at thermal equilibrium is given by a Boltzmann distribution:

$$\frac{N_{-1/2}}{N_{1/2}} = \mathrm{e}^{-\Delta E/kT} \tag{2.2}$$

where $k$ is Boltzmann's constant ($1.38 \times 10^{-23}$ J K$^{-1}$), and T is absolute temperature. The majority of experiments in the present thesis are performed at 9.4 T (equivalent to a proton resonance frequency of 400 MHz) and 20 °C. Under these conditions equation (2.2) predicts a relative difference in high and low energy populations of approximately $1 \times 10^{-5}$. While this population divide is very small, and imposes an inherent limit to the sensitivity of NMR experiments, the large number of molecules in a sample (one teaspoon of water contains on the order of $3 \times 10^{23}$ protons) renders a net signal detectable.

### 2.1.2 Bloch vector model

As we are considering a signal averaged over a large ensemble of spins, the net magnetic moment may be considered to be a vector, and described in classical terms. Analogous to classical angular momenta, the bulk magnetisation vector may be described as:

$$\frac{d\mathbf{M}}{dt} = \mathbf{M} \times \gamma\mathbf{B} \tag{2.3}$$

where $\mathbf{B}$ is a magnetic field vector and $t$ is time. This description of spin precession is known as the Bloch vector model. For a static field, $B_0$, equation (2.3) may be rewritten as:

$$\omega_0 = \gamma B_0 \tag{2.4}$$

where $\omega_0$ is known as the Larmor frequency. This is the basic equation of NMR, and reflects that spin precession frequency about a magnetic field is directly proportional to field strength.

In NMR, a strong, static magnetic field, which in the present study is always aligned with the vertical $z$-axis, is used for spin polarisation as described above. The NMR signal is detected by electromagnetic induction in a coil surrounding the precessing spins (as described in more detail in Section 2.1.3). For signal detection, therefore, it is necessary that the spin precession contains some transverse plane component such that there is motion of the net magnetisation vector with respect to the receiver coil. In order to generate this transverse plane magnetisation, the spins must be disturbed from thermal equilibrium with the polarisation field. This is achieved by application of a second magnetic field (in practice a pulse of radiofrequency radiation), which will be referred to as $B_1$. It is important that $B_1$ oscillates in resonance with the precession of the spins about $B_0$, such that the simultaneous precession about $B_1$ tips the magnetisation vector into the transverse plane. These short bursts of $B_1$ are hereafter be referred to as 'r.f. pulses'. It is convenient to consider the effect of r.f. pulses in a frame of reference where the observer is rotated about the axis of the polarisation field at the Larmor frequency. In this so-called 'rotating frame', an r.f. pulse is seen to induce a circular precession about the axis along which the pulse was applied. The concept of the rotating frame is demonstrated in Figure 2.2.

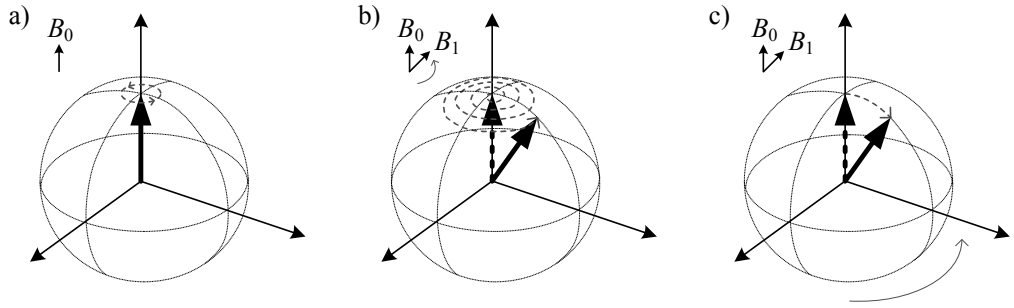


Figure 2.2: The behaviour of the net magnetisation vector, **M**, in different reference frames. a) In the laboratory frame **M** precesses about $B_0$ at the Larmor frequency. b) Upon application of an r.f. pulse, $B_1$, **M** precesses simultaneously about both $B_1$ and $B_0$ in the laboratory reference frame. c) In the rotating frame the precession about $B_1$ can be viewed in isolation of that about $B_0$.

By carefully controlling the duration of an r.f. pulse the extent of the precession about $B_1$ can be limited, and it is possible to control the final position of the magnetisation vector such that the angle of rotation from the polarisation axis is given by $\theta = \gamma B_1 t_{\text{pulse}}$. A

pulse which tips the vector through some angle $0 < \theta < 180°$, such that some component of the magnetisation is contained in the transverse plane, as shown in Figure 2.3 a), is known as an excitation pulse. In quantum mechanical terms, this pulse provides the energy $\Delta E$ necessary to induce a transition between spin states for some spins in the system, with the subsequent release of energy corresponding to the return to thermal equilibrium (known as relaxation, which is discussed with regard to the vector model in Section 2.1.4). Subsequent to an excitation pulse, a pulse which tips the vector through 180°, as shown in Figure 2.3 b), is known as a refocusing pulse, which is useful for the formation of 'echoes', as discussed in detail in Section 2.1.5.

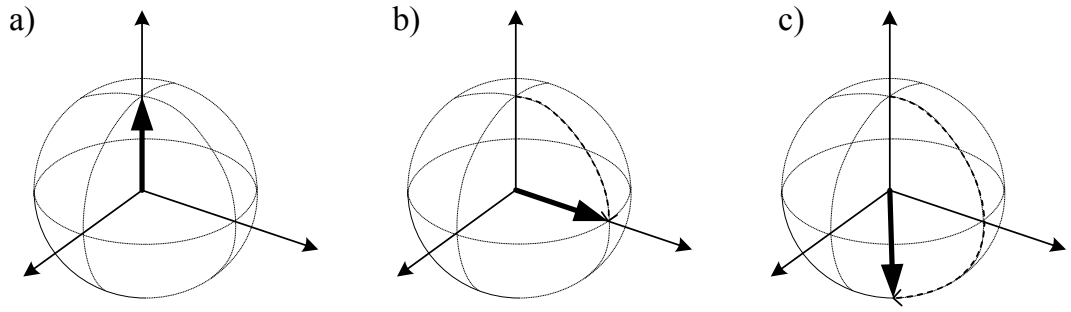


Figure 2.3: Demonstration of a) a 90° 'excitation' pulse and b) 180° 'refocusing' pulse.

### 2.1.3 Signal detection

Following an excitation pulse, **M** precesses freely at the Larmor frequency in the transverse plane. In the laboratory frame, and in the absence of relaxation effects (described in Section 2.1.4), this precession may be described for a 90° pulse as:

$$M_{\mathrm{x,y}}(t) = M_0 \cos \omega_0 t + \mathrm{i} M_0 \sin \omega_0 t \tag{2.5}$$

where $M_0$ is the bulk magnetisation at thermodynamic equilibrium. Note that complex notation has been used as it is a convenient method of describing motion in a 2D plane. Equation (2.5) may be rewritten as:

$$M_{\mathrm{x,y}}(t) = M_0 \mathrm{e}^{\mathrm{i}\omega_0 t} \tag{2.6}$$

This precession induces a voltage (directly proportional in magnitude to $M_{\mathrm{x,y}}$) in a coil surrounding the sample. This signal is heterodyned with two reference signals 90° out of phase with each other such that both 'real' and 'imaginary' components of $M_{\mathrm{x,y}}$ are sampled (known as quadrature detection), and only an offset frequency $\Delta\omega = \omega_0 - \omega_{\mathrm{r}}$

need be considered (effectively transforming the acquired signal into the rotating frame). The NMR signal is therefore given by:

$$S(t) \propto M_0 \mathrm{e}^{\mathrm{i}\phi_\mathrm{r}} \mathrm{e}^{\mathrm{i}\Delta\omega t} \tag{2.7}$$

where $\phi_\mathrm{r}$ is the (arbitrary) receiver phase. For the identification of resonant frequencies present in a sample it is convenient to transform the time-domain signal to the frequency domain via a Fourier transform:

$$S(\omega) = \int_{-\infty}^{\infty} S(t) \mathrm{e}^{\mathrm{i}2\pi\omega t} dt. \tag{2.8}$$

For a simple experiment consisting of a single excitation pulse, the magnetisation decays exponentially, as discussed in Section 2.1.4. The induced signal in this case is known as a free induction decay (FID). A so-called 'pulse-sequence' diagram for the acquisition of an FID, and the corresponding spectrum are shown in Figure 2.4.

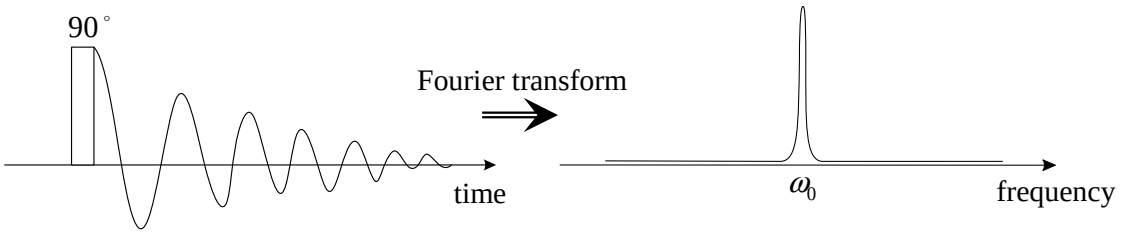


Figure 2.4: A pulse sequence diagram for a simple pulse-acquire experiment, which leads to the generation of an FID. This signal may be Fourier transformed to yield a frequency distribution.

In practice the NMR signal must be digitally sampled at a given rate. The time between sampling each complex data point is known as the dwell time ($t_d$), which corresponds to frequencies sampled over a window (known as the 'spectral width') of $1/t_d$. In accordance with the Nyquist-Shannon sampling theorem, the spectral width must be at least twice the maximum frequency present in the signal under detection. It is common to repeat the acquisition of a signal multiple times in order to improve the signal-to-noise ratio (the signal scales with the number of experiments, $n$, while the noise scales with $\sqrt{n}$). In performing this signal averaging it is possible to vary the phase of the r.f. pulses and receiver for the removal of some NMR artefacts. This process is known as phase cycling, and is discussed in Section 2.1.7.

### 2.1.4 Relaxation

In quantum mechanical terms, an excitation pulse provides the energy $\Delta E$ necessary to induce a transition between spin states, with the subsequent release of this energy corresponding to the return to thermal equilibrium. The mechanisms of the release of this energy are known as relaxation.

#### Spin-lattice relaxation

Excited spins return to alignment with the polarisation field via a process known as $T_1$ or 'spin-lattice' relaxation, which describes the exchange of energy between the spins and surrounding molecules. This mode of relaxation is described by:

$$\frac{dM_z}{dt} = \frac{-(M_z - M_0)}{T_1} \tag{2.9}$$

where $M_z$ is the $z$ component of the magnetisation and $T_1$ is a time constant describing the rate at which $M_z$ relaxes. The solution of equation (2.9) is:

$$M_z(t) = M_z(0)e^{-t/T_1} + M_0\left(1 - e^{-t/T_1}\right). \tag{2.10}$$

Following a 90° excitation pulse ($M_z(0) = 0$), the time-constant $T_1$ represents the time for 63% of the magnetisation to return to equilibrium with $B_0$. Spin-lattice relaxation is related to the rate of molecular tumbling within the sample, with the motion of each individual spin generating a local magnetic field that interacts with the surrounding spins. Those molecules tumbling close to the Larmor frequency, therefore, interact more strongly with spin precession. For this reason, $T_1$ is seen to decrease with an increasing rate of molecular tumbling, and therefore decreases with increasing temperature, and is smaller for liquids than solids. Additionally, the introduction of paramagnetic ions to a system (that is, ions with a valance band structure that generates a permanent magnetic dipole) also decrease $T_1$ as these ions generate strong localised magnetic fields during molecular tumbling. Further discussion of the physics underlying $T_1$ relaxation is given by Levitt [7].

The $T_1$ relaxation constant may be quantified using a variety of methods, which are well reviewed by Fukushima and Roeder [9]. The most common approach is known as inversion-recovery. This technique employs an initial 180° pulse to invert the magnetisation, followed by a 90° pulse to return the magnetisation to the $x - y$ plane after some time $\tau$. Upon application of the initial condition equation $M_z(0) = -M_0$ and evaluated

at $t = \tau$, equation (2.10) reduces to:

$$M_z(\tau) = M_0 \left(1 - 2\mathrm{e}^{-\tau/T_1}\right). \tag{2.11}$$

Thus, for a series of FIDs acquired at different values of $\tau$, equation (2.11) may be fitted to provide a value of $T_1$. A pulse-sequence for the inversion-recovery technique is given in Figure 2.5. Prior to each measurement, it is important that all longitudinal magnetisation is allowed to recover to equilibrium. According to equation (2.11) a time of $5T_1$ is sufficient for this, which provides a recovery of 98.7% of $M_\mathrm{z}$. An interesting feature of this technique is that $T_1$ may be obtained from a single point measurement from the time at which the signal changes from negative to positive (i.e. $M_\mathrm{z}(\tau) = 0$) [6]. At this point, equation (2.11) gives that $T_1 = 1.443\tau$. Known as inversion-nulling, this method provides a reasonable estimate of $T_1$, however it relies upon the accurate generation of a 180° pulse and becomes convoluted for multicomponent spectra. It is important to note that inversion-null also forms the basis of a signal suppression technique, wherein magnetisation of a certain nuclei can be saturated by application of a 180° pulse at a time $0.6931T_1$ prior to the imaging sequence.

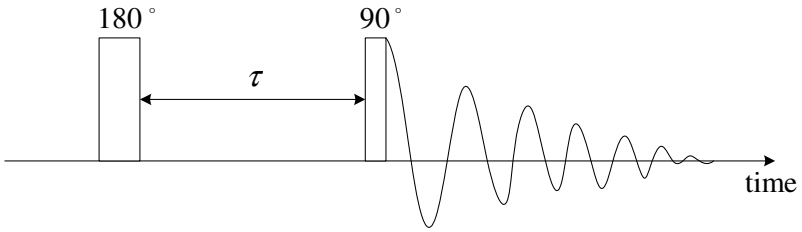


Figure 2.5: The inversion-recovery pulse sequence used for the measurement of $T_1$. FIDs are measured for several values of $\tau$ such that equation (2.11) may be fitted to determine $T_1$.

Alternatively, $T_1$ may be measured by the saturation recovery sequence, which employs a train of 90° pulses such that no net magnetisation exists at $t = 0$. The evolution of $M_\mathrm{z}$ may then be observed by application of an additional 90° pulse at a time $\tau$. The principle advantage of the saturation recovery is that it removes the necessary waiting period between each measurement as all longitudinal magnetisation is destroyed at the beginning of the sequence. Applying the initial condition $M_z(0) = 0$ to equation (2.10) provides:

$$M_\mathrm{z}(t) = M_0 \left(1 - \mathrm{e}^{-t/T_1}\right). \tag{2.12}$$

### Spin-spin relaxation

While $T_1$ relaxation governs the return of $M_z$ to thermal equilibrium, the transverse plane components of the magnetisation, $M_x$ and $M_y$ also undergo relaxation. Known as $T_2$ or 'spin-spin' relaxation, this phenomenon is caused by the slightly different Larmor frequency exhibited by each individual spin, as each nuclei is exposed to a local magnetic field influenced by the tumbling of surrounding molecules. This has the influence of dephasing spin precession for the ensemble of spins, and leads to a decay of the net transverse plane magnetisation:

$$\frac{dM_{x,y}}{dt} = -\frac{M_{x,y}}{T_2} \tag{2.13}$$

where $T_2$ is a time constant describing the rate of coherent magnetisation decay due to spin-spin relaxation. The solution to equation (2.13) is:

$$M_{x,y}(t) = M_{x,y}(0)e^{-t/T_2}. \tag{2.14}$$

Note that $T_2$ relaxation is irreversible, and always occurs at a rate faster than $T_1$ as only the $z$-component of the magnetic fields generated by molecular tumbling influence $T_1$, whereas $T_2$ is affected by both transverse plane components. An additional source of $T_2$ style dephasing exists in that, in practice, it is difficult or impossible to render $B_0$ perfectly homogeneous, and thus spins in different spatial locations will be subject to different Larmor frequencies. A time constant $T_2'$ can be identified with the rate of dephasing due to $B_0$ inhomogeneity, which allows the total apparent dephasing to be defined as:

$$\frac{1}{T_2^*} = \frac{1}{T_2'} + \frac{1}{T_2}. \tag{2.15}$$

For a homogeneous field, $T_2^*$ approaches $T_2$. The rate of $T_2^*$ decay can be estimated for a single peak from the frequency-domain line width for a pulse-acquire experiment, as it is predominately this factor which generates a distribution of frequencies around the resonance frequency. Assuming the peak to approximate a Lorentzian distribution (i.e. that it is the Fourier transform of only an exponential decay), $T_2^*$ can be calculated using:

$$T_2^* = \frac{1}{\pi \Delta v} \tag{2.16}$$

where $\Delta v$ is the width of the peak at half of its height. A technique for measuring $T_2$ in isolation of $T_2^*$ is described in Section 2.1.5. Including the effects of signal attenuation

due to $T_2^*$, the NMR signal given in equation (2.7) becomes:

$$S(t) \propto M_0 \mathrm{e}^{\mathrm{i}\phi} \mathrm{e}^{\mathrm{i}\Delta\omega t} e^{-t/T_2^*}. \tag{2.17}$$

### 2.1.5 Echoes

#### Spin echoes

Relaxation times are important parameters for consideration in planning any NMR experiment as they dictate the total time available for signal encoding and acquisition. In particular, $T_2^*$ can impose challenging short timescales. In practical NMR experiments it is common to manually manipulate $B_0$ using a secondary 'shim' magnetic field to minimise the degree of magnetic field heterogeneity, however, it is often difficult or impossible to render $B_0$ homogeneous for samples which contain many phase interfaces between materials of different magnetic susceptibility (which therefore generate significant $B_0$ heterogeneity). This is a potential problem for application of NMR and MRI to bubbly flow, as there exists a strong magnetic susceptibility difference between water and air [10].

An important tool in NMR, which somewhat overcomes this problem, is the spin-echo. Spin-echoes were discovered accidentally in 1950 by Hahn [11], who was experimenting with the effects of multiple sequential pulses in NMR. A spin-echo is achieved by application of a 180° refocusing pulse at a time $\tau$ subsequent to the initial 90° excitation. This second pulse rotates the magnetisation about the axis along which it was applied into the opposite half of the transverse plane; inverting the in-phase components of the magnetisation vector while maintaining the position of the dephased magnetisation vectors relative to each other. Whilst the magnetisation is now a mirror image of what it was prior to the refocusing pulse, the magnetic field inhomogeneities responsible for the dephasing effect are not altered. Thus, the inhomogeneity now acts to rephase the magnetisation, and after an additional period $\tau$, the magnetisation regains coherence and an echo is produced. The period of $2\tau$ between initial excitation and echo formation is know as the echo time. This procedure is illustrated in Figure 2.6 together with a pulse sequence for the generation of a spin-echo.

Using spin-echoes it is possible to measure the rate of $T_2$ decay in isolation of $T_2^*$. This is achieved by measuring the signal attenuation associated with echoes of varying echo time. This approach, however, assumes that the $B_0$ inhomogeneity experienced by any

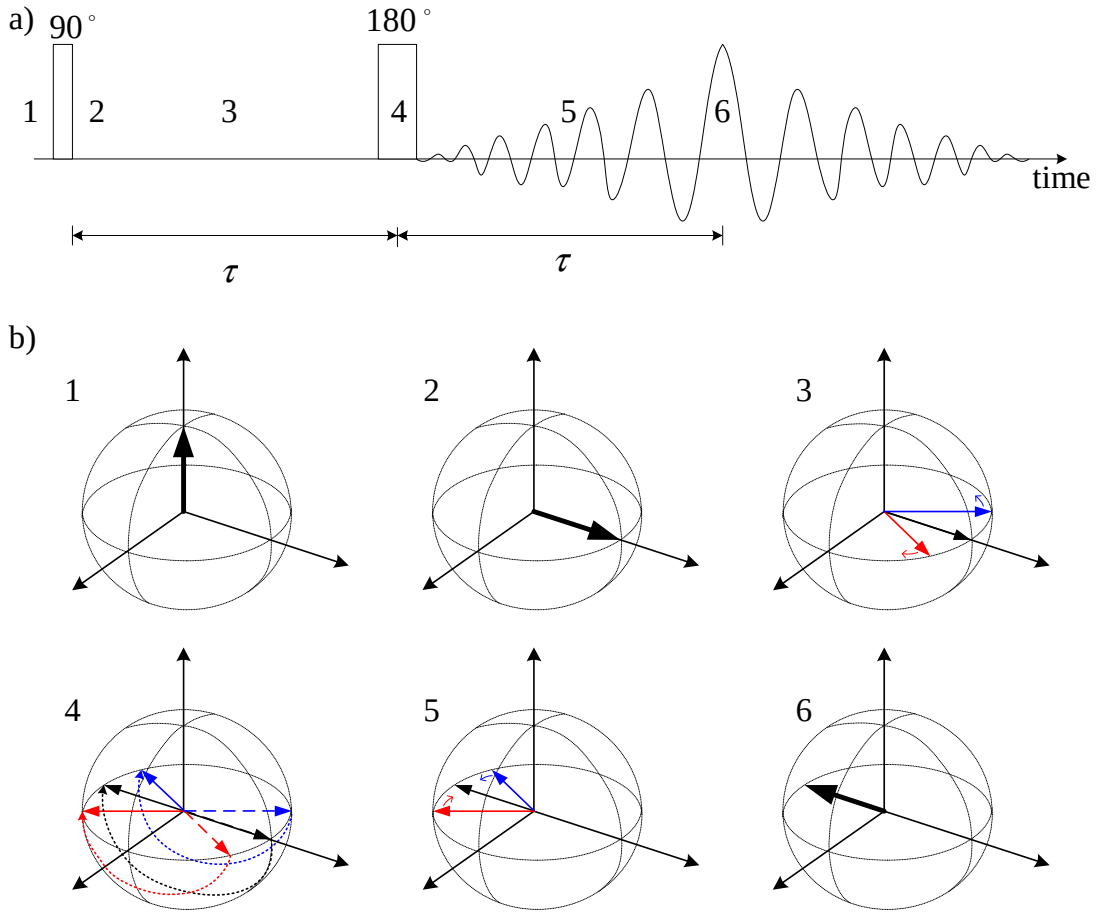


Figure 2.6: a) Pulse sequence for the formation of a spin-echo and b) demonstration of the behaviour of the magnetisation vector during this pulse sequence. The magnetisation is disturbed from thermal equilibrium (1) by an excitation pulse, which tips it into the transverse plane (2) where it precesses at the Larmor frequency. Due to off-resonance effects ($B_0$ inhomogeneity and chemical shift) the magnetisation dephases over time, which can be thought of as a broadening of the magnetisation vector (3). At some time $\tau$ after the excitation pulse, a refocusing pulse is applied, which imparts a 180° phase shift to the spins (4). The off-resonance effects act on the dephased magnetisation in the same manner as they did before the refocusing pulse, which now rephases the magnetisation (5). At a time $2\tau$ after the excitation pulse, the magnetisation regains phase coherence (6), before beginning to dephase again. The signal that is formed during this magnetisation refocusing is known as a spin-echo.

given spin does not change during the echo time. If the molecules move within $B_0$ (due to either convection or diffusion), the rephasing following the refocusing pulse will not exactly cancel the dephasing prior to the pulse, resulting in a net signal loss. This problem is overcome using the CPMG sequence [12, 13], which uses a train of 180° pulses with a very short echo-time such that the magnetisation is continuously being refocused. A pulse sequence for a standard CPMG experiment is shown in Figure 2.7. While the echo-time is held constant for this experiment, the total time for dephasing is varied by changing the number of echoes, $N$. Thus, following a 90° pulse ($M_{\mathrm{x,y}}(0) = M_0$), $T_2$ may be quantified by application of equation (2.14):

$$M_{\mathrm{x,y}}(2N\tau) = M_0 \mathrm{e}^{-2N\tau/T_2}. \tag{2.18}$$

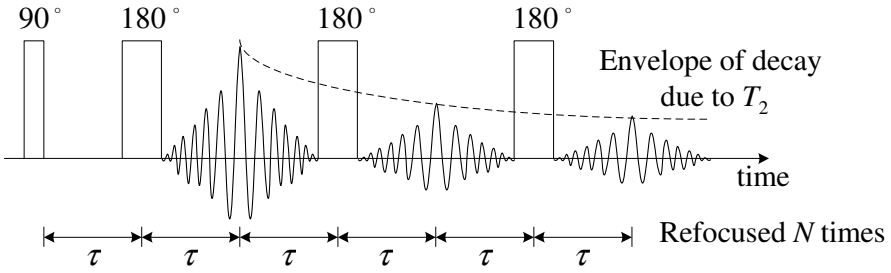


Figure 2.7: The CPMG pulse sequence. A train of refocusing pulses is used to continually refocus off-resonance effects, while maintaining a short echo time such that signal attenuation due to diffusion or flow is minimised. The total time for $T_2$ dephasing can be varied by the number of refocusing pulses, $N$.

It is important to note that echo formation is not limited to 180° refocusing pulses, but may be instigated by a pulse of almost any size. This occurs as a distribution of tip angles are imparted to a spin ensemble following any pulse, and some of these will lead to magnetisation refocusing. While the Bloch vector model begins to break-down in situations such as this, where the net magnetisation vector is no longer representative of individual spins, an interpretation of the behaviour of the vector is provided by Hennig [14]. The formation of echoes from any combination of pulses is an important factor for consideration in the design of pulse sequences which make use of multiple sequential pulses, as any combination of these pulses can give rise to the formation of echoes. These echoes are often undesirable, and must be actively suppressed by either phase cycling (see Section 2.1.7) or spoiling (see Section 2.2.3) to prevent them from interfering with the desired signal. The formation of these echoes can be tracked by construction of a phase coherence diagram, as discussed by Keeler [15].

### Stimulated echoes

A stimulated echo is a special case of multiple-pulse phase coherence. It is formed following the application of three sequential 90° pulses. As shown in Figure 2.8, a 90° excitation pulse is followed by a 90° refocusing pulse and some time $\tau$. This has the effect of storing the $z$ component of the dephased magnetisation along the longitudinal axis. This process does not lend itself to depiction with the vector model depiction, as the phase of the spins is preserved despite the net magnetisation vector being aligned with the longitudinal axis. While stored in this state, the magnetisation will not dephase any further due to off-resonance effects. This magnetisation can be held like this for some period of time $T_{\text{store}}$, during which it only undergoes relaxation only due to $T_1$. This is useful for situations in which $T_1 \gg T_2$. This stored magnetisation can be returned to the transverse plane by application of an additional 90° refocusing pulse. Note that as the magnetisation is stored in its dephased state, following the final refocusing pulse it will rephase over a period of $\tau$ for the formation of a 'stimulated echo'. A complication exists in that spin-echoes can also form from any combination of the three pulses used for the stimulated echo. For this reason it is common to dephase all transverse plane magnetisation following the first refocusing pulse using a spoiler gradient (described in Section 2.2.3), as shown in Figure 2.8.

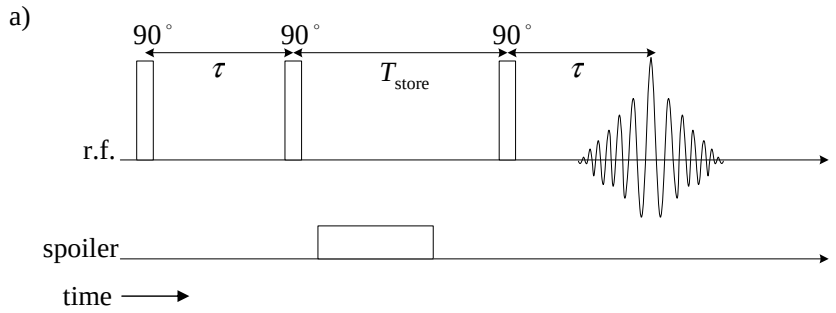


Figure 2.8: The formation of firstly a stimulated echo from three 90° pulses. The magnetisation is disturbed from equilibrium with an excitation pulse, after which it dephases in the transverse plane under the influence of off-resonance effects. By application of an additional 90° pulse some component of the magnetisation is returned to the longitudinal direction in a dephased state. Note that the retention of phase information for spins aligned with the longitudinal axis is difficult to represent with the vector model. After some storage time, $T_{\text{store}}$, during which the system only undergoes $T_1$ relaxation, the magnetisation can be returned to the transverse plane by application of a final 90° pulse. This dephased magnetisation then rephases to form a stimulated echo. It is common to suppress spin-echo formation in this process using a spoiler gradient prior to the third pulse.

### 2.1.6 Chemical shift

Atoms in different parts of a molecule may be subject to different chemical environments. These effects are extremely subtle, with slight changes in the number and position of orbiting electrons having an influence. The effect of this slightly different chemical environment is to slightly alter the Larmor frequency of not only elements but specific functional groups. This effect renders NMR a very useful tool for chemical analysis, as each functional group and molecular arrangement holds a unique chemical finger-print. As the present study focuses only on systems containing a single resonant frequency, the effect of chemical shift will not be dwelt upon. The interested reader is directed to standard texts on NMR spectroscopy, such as that of Keeler [15].

### 2.1.7 Phase cycling

Phase cycling is an NMR technique by which the pulse and receiver phases are varied over several repeat experiments (in which the signal is averaged) to allow some sources of NMR artefacts to cancel themselves out. While phase cycling has not been extensively employed in the present thesis (signal averaging was not possible due to the highly transient nature of the systems being examined), it remains an important consideration in the application of many NMR and MRI measurements. The principle of phase cycling is best demonstrated by description of a basic phase cycle. Consider, therefore, a simple two-step phase cycle used for correction of a direct current (D.C.) offset artefact. This artefact is generated by the real and imaginary components of the signal being acquired with different, non-zero baselines. These baselines have the effect after Fourier transformation of generating a high intensity pixel at the zero-frequency point at the centre of the spectra. The two-step phase cycle simply acquires two signal averages with a 180° offset in both receiver and pulse phases, as shown in Table 2.1. The signal between these two scans therefore adds constructively, while the baseline (which is generated by the electronics, and therefore independent of pulse phase) is cancelled out between the two scans.

Table 2.1: Phase cycle for the removal of a D.C. artefact.

| Scan | Pulse phase | Receiver phase |
|---|---|---|
| 1 | 0° | 0° |
| 2 | 180° | 180° |

Another common phase cycle is known as cyclically ordered phase sequence (CYCLOPS) [16], which removes the quadrature artefact caused by imbalances between real and imaginary channels. It achieves this by acquiring four scans with an increment of 90° in both pulse

and receiver phase, such that both real and imaginary components of the magnetisation are sampled equally by both receiver channels. This phase cycle is summarised in Table 2.2.

Table 2.2: Pulse and receiver phases for the CYCLOPS phase cycle.

| Scan | Pulse phase | Receiver phase |
|---|---|---|
| 1 | 0° | 0° |
| 2 | 90° | 90° |
| 3 | 180° | 180° |
| 4 | 270° | 270° |

The final phase cycle which is commonly used in imaging is known as exorcycle [17]. This phase cycle is used with spin-echo based measurements, and greatly minimises the effect of imperfect excitation or refocusing pulses caused by $B_1$ heterogeneity, which can lead to the formation of an FID from the refocusing pulse. Over four signal averages, exorcycle increments the refocusing pulse phase by 90°, while inverting the receiver phase, as shown in Table 2.3. This has the effect of preserving only magnetisation excited by the original 90° pulse.

Table 2.3: Pulse and receiver phases for the exorcycle phase cycle.

| Scan | 90° pulse phase | 180° pulse phase | Receiver phase |
|---|---|---|---|
| 1 | 0° | 0° | 0° |
| 2 | 0° | 90° | 180° |
| 3 | 0° | 180° | 0° |
| 4 | 0° | 270° | 180° |

Note that different phase cycles can be 'nested' within each other to combine effects. Phase cycling is a powerful tool, and can be used to great effect in both imaging and spectroscopy. The interested reader is directed to the review of Kingsley [18]

## 2.2 Principles of MRI

The present study is primarily concerned with the production of images by NMR, which is a field known as magnetic resonance imaging (MRI). MRI is enabled by applying a magnetic field gradient such that the precession frequency of spins in the sample is spatially dependent, and thus the frequency distribution of the received signal (obtained by Fourier transform) reveals the position of the spins. In the presence of a constant

gradient, equation (2.4) may be written as:

$$\omega(\mathbf{r}) = \gamma(B_0 + (\mathbf{G} \cdot \mathbf{r})) \tag{2.19}$$

where $\mathbf{G} = \nabla\mathbf{B}$ and $\mathbf{r}$ is the position vector $[x\ y\ z]$. A demonstration of this principle is shown in Figure 2.9.

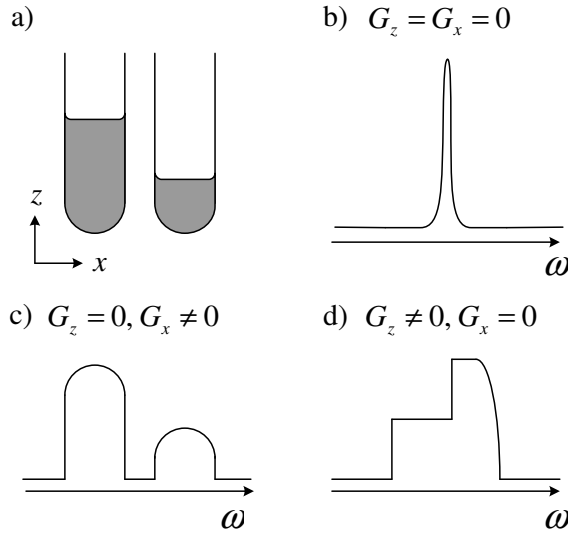


Figure 2.9: The basic principle of MRI. Consider: a) a phantom of two half-filled test tubes. b) In the absence of magnetic field gradients only the distribution of frequencies (generated by $T_2^*$ relaxation) about Larmor frequency is present in the measured frequency distribution. If, however, $\mathbf{B}$ is rendered variable in c) $x$ or d) $z$ directions, the frequency distribution reveals a one dimensional projection of the sample. Note that the same line broadening effect seen in b) is present in the spatially encoded images. In this way, an unencoded spectra can yield a point spread function for an image.

After equation (2.7), the signal detected from an element of volume $dV$ at position $\mathbf{r}$ is:

$$dS(\mathbf{G}, t) \propto \rho(\mathbf{r}) dV \mathrm{e}^{\mathrm{i}\omega(\mathbf{r})t} \tag{2.20}$$

where $\rho(\mathbf{r})$ is defined as the spin-density distribution. For the signal intensity to be quantitatively representative of the number of spins it is necessary to determine the constant of proportionality, which may be achieved using reference scans of a sample of known volume. For convenience, we shall presently neglect this constant. Additionally, we will assume the signal to be heterodyned at a reference frequency of $\gamma B_0$. Equation (2.20) may then be integrated over the entire sample volume to yield:

$$S(\mathbf{G}, t) = \iiint \rho(\mathbf{r}) \mathrm{e}^{\mathrm{i}\gamma \mathbf{G} \cdot \mathbf{r} t} d\mathbf{r}. \tag{2.21}$$

Mansfield and Grannell [4] recognised that this equation is of the form of a Fourier transform. They thus introduced the concept of **k**-space, which has developed into a useful and powerful tool for the design of imaging protocols. The reciprocal space vector, **k**, is defined as:

$$\mathbf{k} = \frac{\gamma \mathbf{G} t}{2\pi} \tag{2.22}$$

or in the presence of a time-varying gradient:

$$\mathbf{k} = \frac{\gamma}{2\pi} \int \mathbf{G}(t) dt. \tag{2.23}$$

Substituting equation (2.22) into equation (2.21) gives:

$$S(\mathbf{k}) = \iiint \rho(\mathbf{r}) \mathrm{e}^{\mathrm{i}2\pi \mathbf{k}\cdot\mathbf{r}} d\mathbf{r} \tag{2.24}$$

with the equivalent Fourier pair:

$$\rho(\mathbf{r}) = \iiint S(\mathbf{k}) \mathrm{e}^{-\mathrm{i}2\pi \mathbf{k}\cdot\mathbf{r}} d\mathbf{k}. \tag{2.25}$$

Hence by sampling **k**-space, a map of spin density (i.e. an image) may be produced by inverse Fourier transform. Equations (2.24) and (2.25) do not account for relaxation, which can have a strong influence and introduce (either desirable or otherwise) contrast to an image. Note that this image is complex: the magnitude of the signal present in each pixel is given by the image modulus, while the argument contains any phase information (other than that used for image encoding) accrued by the spins. The image argument, or 'phase image', therefore provides a very useful basis for encoding additional information into an MRI image. In particular, it can be used for velocity encoding for the quantitative imaging of flow, which is discussed in Section 2.3.

### 2.2.1 Image encoding and k-space

At first glance, **k**-space seems an abstract concept. In this section, the subtleties of **k**-space, and its usefulness in planning an MRI experiment are explored. **k**-space represents the mathematical domain in which MRI signals are acquired; images are reconstructed from **k**-space by Fourier transformation. The same number of Fourier coefficients must be sampled in **k**-space as will be present in the final image, and it is common practice to sample images to an $2^N \times 2^M$ grid, such that images may be reconstructed in a compu-

tationally inexpensive manner using a fast-Fourier transform (FFT) [19]. Figure 2.10 a) shows an example of a **k**-space raster, with the corresponding b) modulus and c) phase images. The slight variation across the phase image is due to the presence of $B_0$ heterogeneity. As **k**-space is the reciprocal of true space, the field-of-view (FOV) of an image is determined by the spacing between adjacent points in **k**-space while the image resolution is determined by the breadth of **k**-space that sampled. If the sampling increment in **k**-space is too large, and hence the image FOV too small for the sample under examination (i.e. the Nyquist-Shannon sampling theorem is being violated), aliasing will occur, with the signal outside of the FOV being misregistered to the opposite side of the image, as shown in Figure 2.10 d). This is known as the 'fold-over' artefact, which imposes a limit to the minimum FOV of MRI images. The centre of **k**-space contains all low resolution information (i.e. the bulk of the image intensity) while the edges of **k**-space contain high spatial frequency data (i.e. image edges). This is demonstrated in Figure 2.10 e) and f), where images reconstructed from only the low and high spatial-frequency coefficients are reconstructed.

For the sampling of all Fourier coefficients in a **k**-space raster, **k**-space must be traversed to the location of each coefficient and the NMR signal acquired. In accordance with equation (2.23) the two parameters which may be varied for the navigation of **k**-space are $t$ and $\mathbf{G}(t)$. Applying a known gradient for a fixed period of time has the effect of imparting a spatially-dependent phase shift to the spins (i.e. dephasing the net spin ensemble, which is only totally in-phase at the centre of **k**-space). This is known as 'phase encoding'. Sampling the NMR signal following a phase encode allows a single Fourier coefficient to be measured. To sample the entire **k**-space raster in this way is time-consuming, and it is possible to acquire continuously during the application of an image encoding gradient; sampling Fourier coefficients at the spectral frequency of the image. This is known as 'frequency encoding'. A mixture of phase and frequency encoding are often employed, with each technique used to encode separate, perpendicular directions. By convention, the phase encoding is used in the 'phase direction', and frequency encoding is used in the 'read direction'.

A 'gradient echo' is a **k**-space sampling strategy wherein an entire line of **k**-space is sampled using frequency encoding. For the formation of a gradient echo the magnetisation is initially dephased (**k**-space is traversed to its outer edge) and subsequently rephased and dephased again while complex Fourier coefficients are sampled at $t_d$ intervals. This concept is demonstrated with the corresponding pulse sequence in Figure 2.11 a). The

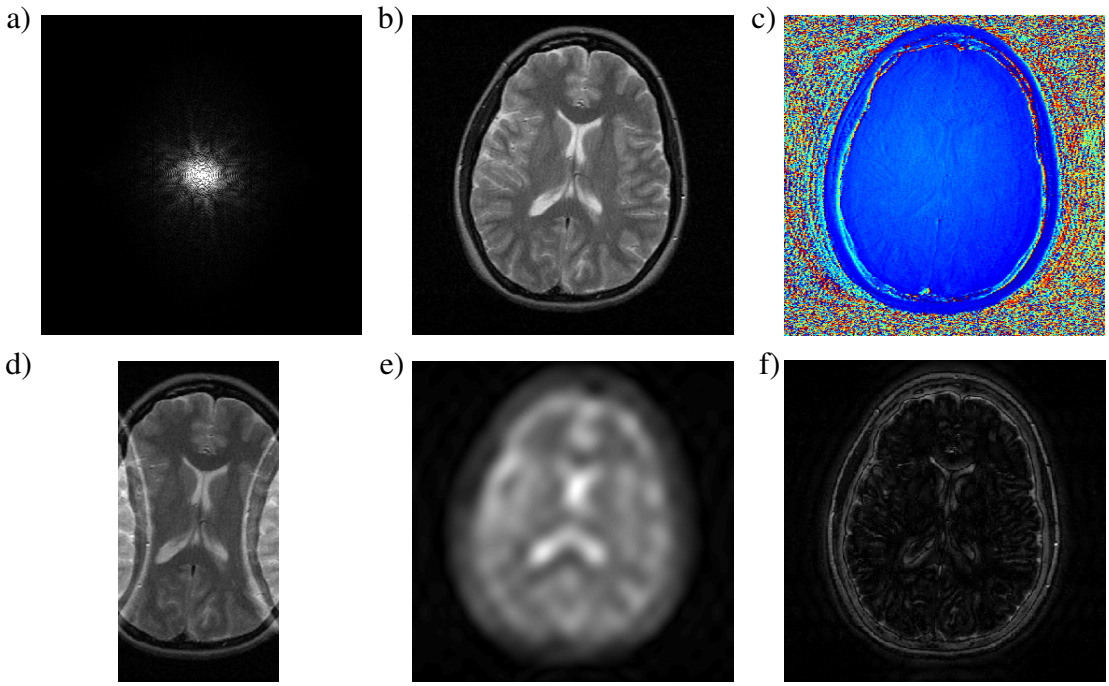


Figure 2.10: a) An example **k**-space raster with the b) modulus and c) phase of a two-dimensional Fourier transform of these data. d) The same image reconstructed using only every other Fourier coefficient in one direction. This has the effect of halving the field-of-view, which leads to aliasing of the spatial frequencies. e) the modulus image reconstructed using only the 100 central **k**-space points, and f) all but the 100 central points. This reflects that the majority of image intensity is contained in the centre of **k**-space, while progressively further in **k**-space must be sampled to enable higher spatial resolutions. These data are from M. Lustig's open source sparse MRI reconstruction package [20].

final tool used for motion in **k**-space is the spin-echo. As discussed in Section 2.1.5, the refocusing pulse associated with a spin-echo applies a 180° phase shift to all spins in the sample. This has the effect of flipping spatial encoding to the opposite quadrant of **k**-space, as shown in Figure 2.11 b). Note that while the refocusing of off-resonant effects associated with a spin-echo occurs independent of position in **k**-space, it is common to time pulse sequences such that the spin-echo refocusing coincides with a gradient echo refocusing, such that the highest power signal contains minimal phase artefacts, and to apply a convenient apodisation function to the edges of **k**-space.

Many MRI techniques, or 'pulse-sequences', exist which make use of varying combinations of the above tools. For example, the spin-warp sequence [21], which is routinely used in medical applications, samples **k**-space using spin-echoes, as shown in Figure 2.11 b), with slice selection performed on the refocusing pulse (described in detail in Section 2.2.2).

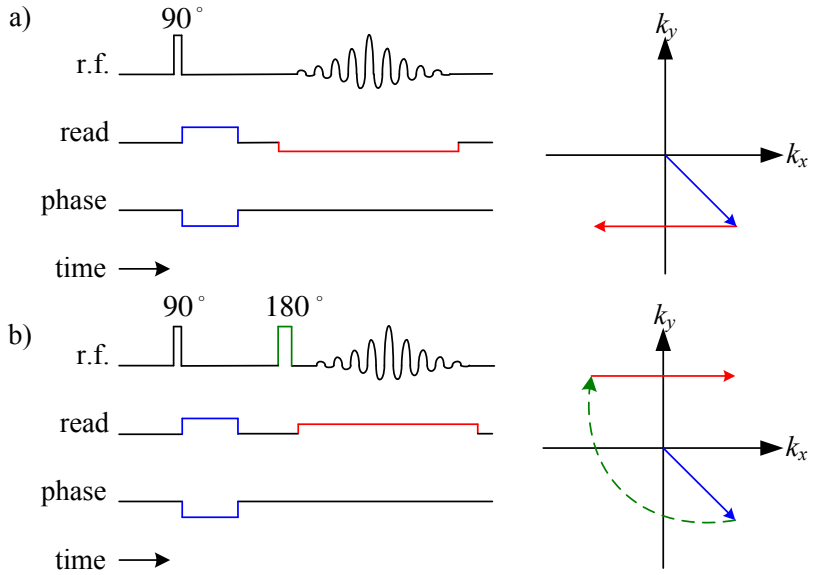


Figure 2.11: a) Pulse sequence and **k**-space raster for acquiring a line of **k**-space using a gradient echo. The magnetisation is initially dephased, prior to being re- and dephased again during signal acquisition. b) Pulse sequence and **k**-space raster for acquiring a line of **k**-space using a spin echo. The magnetisation is dephased, prior to a 180° phase shift being imparted by the refocusing pulse. The line of **k**-space is then read-out using a gradient echo. The refocusing of the spin-echo is timed to coincide with sampling the lowest spatial frequency Fourier coefficients.

Alternatively, the sequence 'fast low angle shot' (FLASH ) [22], uses only gradient echoes, as shown in Figure 2.11 a), with slice selection performed on low tip angle excitation pulses (FLASH is discussed in detail in Section 2.4.1). The field of view of images acquired in a rectilinear fashion such as this is given by the reciprocal of the sampling increment in **k**, and is therefore equivalent to:

$$FOV_{\text{read}} = \frac{2\pi}{\gamma G_{\text{read}} t_{\text{d}}} \tag{2.26}$$

in the read direction, and:

$$FOV_{\text{phase}} = \frac{2\pi}{\gamma G_{\text{inc}} t_{\text{p}}} \tag{2.27}$$

in the phase direction, where $G_{\text{read}}$ is the gradient strength used in the read direction, $G_{\text{inc}}$ is the increment in gradient strength used in the phase direction, and $t_{\text{p}}$ is phase encoding time. There exist many other pulse sequences, each with their own benefits and disadvantages. A discussion on the most appropriate pulse sequence for application to bubbly flow is presented in Section 2.4.

### 2.2.2 Slice selection

In all earlier discussion of excitation and refocusing r.f. pulses, it has been assumed that the pulse affects all spins in the sample identically. This is achieved in practice by application of a short duration (and hence wide bandwidth), high-power 'hard' pulse. It is, however, desirable to also be able to selectively excite a small frequency range of spins. This is useful for exciting spins with a certain chemical shift (for chemically selective NMR), or, if a magnetic field gradient is used simultaneously to the r.f. pulse to render precession frequencies spatially dependent, for excitation of a specific slice of the sample. A so-called 'soft' pulse is of relatively low power and long duration, such that only a narrow band of frequencies, $\Delta\omega_{\mathrm{s}}$, are excited. The thickness of the excited slice is then given by:

$$\Delta z = \frac{\Delta\omega_{\mathrm{s}}}{\gamma \mathbf{G}_{\mathrm{s}}} \tag{2.28}$$

where $\mathbf{G}_{\mathrm{s}}$ is the gradient strength used for slice selection.

The gradient used for slice selection will also act like an image encoding gradient, and begin to dephase any magnetisation that exists in the transverse plane. For slice selective excitation pulses, it is therefore necessary that this magnetisation be rephased before continuing with the pulse sequence. In doing this, it can be assumed that the magnetisation reaches the transverse plane half-way through the soft excitation pulse. The change in $\mathbf{k}$ due to the slice gradient from this point must therefore be balanced by a slice refocusing gradient. In practice, it is common to simply include a gradient of half the duration and equal magnitude, but opposite direction, to the slice encoding gradient. An example refocused slice gradient for a soft excitation pulse is shown in Figure 2.12 a). An additional slice refocusing gradient is commonly not necessary for a refocusing pulse, as the dephasing that occurs during the first half of a refocusing slice gradient is balanced by the refocusing that occurs when the magnetisation undergoes a 180° phase inversion. For this reason, some 180° pulses are said to be 'self-refocusing'. An example waveform for a slice selective refocusing pulse is shown in Figure 2.12 b).

The shape of the excited slice can be controlled by applying a pulse with the form of the appropriate Fourier pair. It is commonly desirable to obtain a rectangular slice excitation profile, the Fourier transform of which is a sinc function. It is, in practice, impossible to apply a perfect sinc pulse, however, as the sinc function never completely decays to zero, and it is necessary to truncate it at some point. The effect of this truncation is to

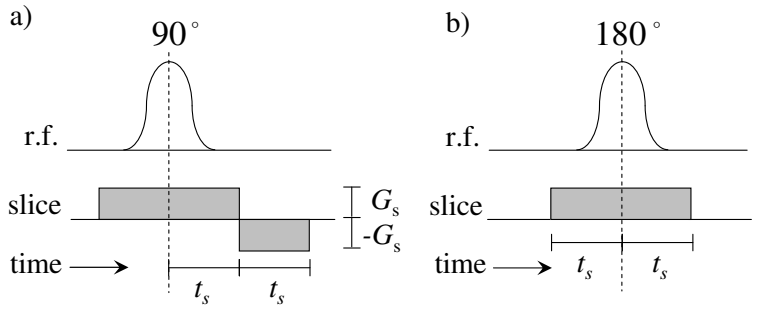


Figure 2.12: Slice gradients with refocusing for a) an excitation pulse and b) a refocusing pulse.

introduce side lobes to the slice excitation profile. Several other mathematical functions have been suggested to provide rectangular excitation profiles: in particular the pulses generated from Hermite functions may be used for excitation, and the Mao [23] function is suitable for refocusing pulses. If the slice excitation profile is not important, it is common to simply use a Gaussian pulse, for which the Fourier pair is also Gaussian.

### 2.2.3 Spoiler gradients

In some situations it is desirable to destroy the coherent transverse magnetisation present in a sample. This particularly occurs during the use of spin echoes, where imperfect refocusing pulses can generate an undesirable FID, and stimulated echoes. It is possible to dephase magnetisation, and hence prevent it from contributing to the signal emitted by the sample, simply by applying a gradient in order to encode all present transverse plane magnetisation outside of the examined region of **k**-space. This is known as a spoiler, or crusher gradient. The necessary gradient strength and duration to fully dephase the magnetisation can be calculated using equation (2.22). For destroying the transverse plane magnetisation prior to the final pulse of a stimulated echo (where all desirable magnetisation is stored in the longitudinal direction, and will not be dephased), a gradient can be simply applied as shown in Figure 2.8. For spoiling the FID associated with a spin-echo, however, it is necessary to prepare the desirable magnetisation such that it is unaffected by the spoiler gradient. This is achieved automatically for some slice-selective 180° pulses (which are self refocusing: see Section 2.2.2), where a spoiler can be applied simply by symmetrically lengthening the slice selection gradient, as shown in Figure 2.13 a). For non-slice selective 180° pulses, however, it is necessary to apply a separate dephasing gradient prior to the r.f. pulse, such that the desirable magnetisation is rephased simultaneously to the undesirable being dephased. This combination of gradients is shown in Figure 2.13 b).

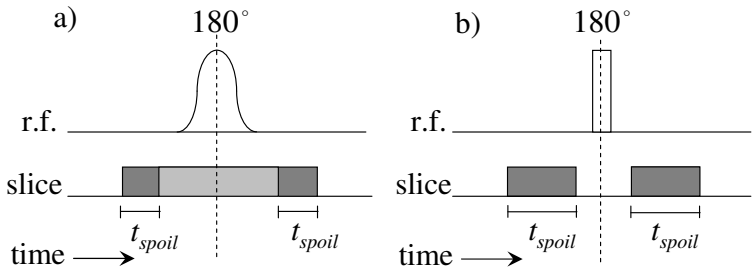


Figure 2.13: Gradient waveforms for a) slice selective refocusing pulses and b) broadband refocusing pulses.

## 2.3 Flow measurement using MRI

One of the great advantages of MRI is the broad spectrum of information it can reveal. In addition to the spatial position of the spins, contrast can be introduced on the basis of chemical selectivity and relaxation rates. Further, MRI can produce quantitative measurements of flow. To understand the basis of these measurements, consider two subsequent spatial encoding gradients, of equal strength and duration but applied in opposite directions, separated by some small time, $\Delta$, as shown in Figure 2.14 a). In the absence of flow, the first gradient will dephase the spins in the direction of its application, which will then be perfectly rephased by the second gradient. If, however, some coherent motion of the spins exists in the direction of the gradient, the dephasing due to the first gradient will not be perfectly undone by the rephasing of the second, as the (dephased) spins have now shifted with respect to the (second) applied gradient. This phase shift due to molecular displacement is preserved through the Fourier transform (together with phase accrued due to off-resonance effects), and is present in the argument of the frequency domain data, hence allowing a measurement of displacement (or velocity as the time $\Delta$ is known) to be obtained.

More formally, the MRI signal, given in equation (2.21), can be rewritten as:

$$S(\phi, t) = \iiint \rho(\mathbf{r}) \mathrm{e}^{-\mathrm{i}\phi} d\mathbf{r} \tag{2.29}$$

where the phase of the signal is given by:

$$\phi = \gamma \mathbf{r} \int \mathbf{G}(t) dt + \gamma \frac{d\mathbf{r}}{dt} \int t \mathbf{G}(t) dt + \ldots \tag{2.30}$$

The first term in equation (2.30) represents the position dependent (or zeroth moment) phase used for spatial encoding. The second term in this equation (first moment phase)

is proportionate to velocity, and is the source of flow artefacts in MRI images when accrued incidentally during image encoding or may be purposely applied for velocity measurements. Higher order motions (e.g. acceleration) will also contribute a phase shift, however these will be assumed to be negligibly small in comparison to the first moment phase shift. The deliberate impartation of first moment phase is known as flow encoding. For simplicity it is common to keep flow and image encoding separate, thus it is desirable to identify gradient waveforms which can impart a first moment phase shift to the spins in a system, without changing the zeroth moment phase. The simplest way of achieving this is using a bipolar gradient pair, two variations of which are shown in Figure 2.14. These combinations of gradients are commonly known as pulsed field gradients (PFG). Note that the flow encoding gradients surrounding a refocusing pulse, shown in Figure 2.14 b), are applied in the same direction due to the 180° phase shift imparted by the pulse. These gradients are also of the same form as those used for the spoiler shown in Figure 2.13, reflecting that this gradient waveform may serve the dual purpose of flow encoding and spoiling the FID generated by a refocusing pulse.

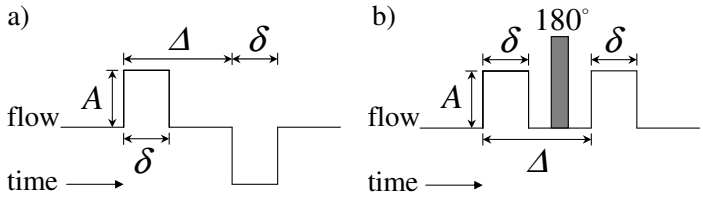


Figure 2.14: Gradient waveforms for flow encoding: a) bipolar gradient pair and b) using a refocusing pulse.

For the bipolar gradient pair given in Figure 2.14 a), equation (2.30) may be expressed as:

$$\phi = \gamma \mathbf{r} \int_0^{\delta} (-A)dt + \gamma \frac{d\mathbf{r}}{dt} \int_0^{\delta} t(-A)dt + \gamma \mathbf{r} \int_{\Delta}^{\Delta+\delta} (A)dt + \gamma \frac{d\mathbf{r}}{dt} \int_{\Delta}^{\Delta+\delta} t(A)dt \quad (2.31)$$

where $A$ is the flow encoding gradient strength per unit length, $\delta$ is the flow encoding time and $\Delta$ is the flow contrast time. Equation (2.31) evaluates to:

$$\phi = \gamma \frac{d\mathbf{r}}{dt} A\delta\Delta. \quad (2.32)$$

For a bipolar gradient waveform the accrued phase is thus proportional to the fluid velocity. For quantitative velocity measurements it is generally necessary to consider the difference between two measurements with an increment in the amount of velocity encoding present. In this way, sources of first moment and off-resonance phase accrual other

than the flow encoding are removed, as are phase effects generated by eddy currents in the system. The bipolar gradient pair is the fundamental building block of flow encoding with NMR: it preconditions the spins to have a velocity sensitive component. It is possible to apply spatial encoding subsequent to flow encoding, such that spatially resolved velocity measurements are contained in the argument of the Frequency domain image. The combination of flow encoding and ultrafast MRI imaging is discussed in Section 2.4.4.

### 2.3.1 Propagator measurements

In NMR spectroscopy a phase distribution generated by the differing Larmor frequencies of dissimilar nuclei is Fourier transformed to yield a frequency distribution that reflects the chemical identity of those nuclei. In MRI, the phase distribution is rendered spatially dependent, such that the frequency distribution reveals the position of the nuclei. If therefore, a phase distribution can be rendered velocity proportionate, it may be Fourier transformed to produce a velocity distribution of the system. Such a measurement is known as a propagator. For the measurement of a propagator it is common to acquire phase distributions with several increments in the velocity encoding gradient, $\mathbf{G}_{\mathrm{v}}$. By analogy with **k**-space, Karger and Heink [24] defined a reciprocal space vector which depends only on displacement:

$$\mathbf{q} = \frac{\gamma \mathbf{G}_{\mathrm{v}} \delta}{2\pi}. \tag{2.33}$$

The behaviour of **q**-space is identical to that of **k**-space, with the field of flow ($FOF$: the range of velocities observable without incurring fold-over) set by the increment in flow encoding. Thus, if the encoding time is held constant:

$$FOF = \frac{1}{\mathbf{q}\Delta} = \frac{2\pi}{\gamma G_{\mathrm{v,inc}} \delta \Delta}. \tag{2.34}$$

Propagators are useful because, unlike measurements based upon a single increment in velocity encoding (which reveal only the velocity averaged over the flow contrast time for that measurement), the full range of velocities present in a system are represented, which can be insightful for the characterisation of complex flow systems. A slight variation to the propagator technique enables the measurement of molecular self diffusion. These measurements are performed based on PFG with the phase distribution generated only by molecular self-motion. For a spatially averaged measurement, this phase distribution will lead to net signal attenuation. The theory of Stejskal and Tanner [25] is then employed for the quantification of a diffusion coefficient. This technique is sensitive enough to

distinguish hindered from free diffusion, and has found applications in bubble and droplet sizing in foams and emulsion [26, 27], and in the characterisation of molecular transport in catalyst particles [28]. Diffusion measurements are, however, not the focus of this work, and will not be further considered. The interested reader is directed to several comprehensive reviews in the literature [29, 30, 31].

### 2.3.2 Flow compensation

Just as a pair of flow encoding gradients can impart a first moment phase shift to a spin ensemble, so can any other gradients present in the pulse sequence. As mentioned above, it is common to acquire two measurements with an increment in flow encoding, such that, by considering the difference between the two, the phase shift due to flow encoding can be viewed in isolation of other sources of phase accrual in the system. For temporally resolved measurement of non-steady state flows, however, this practice cannot remove first moment phase, as any two scans will be exposed to differing velocity fields. To this end, it is necessary to prevent the accrual of undesired first moment phase in the first place. This may be achieved by designing gradient waveforms such that their first moment is zero while still performing their desired task. Velocity compensated waveforms for several common pulse-sequence objects are given by Pope and Yao [32]; those for slice selection gradients (both excitation and refocusing) and a spoiler are given in Figure 2.15.

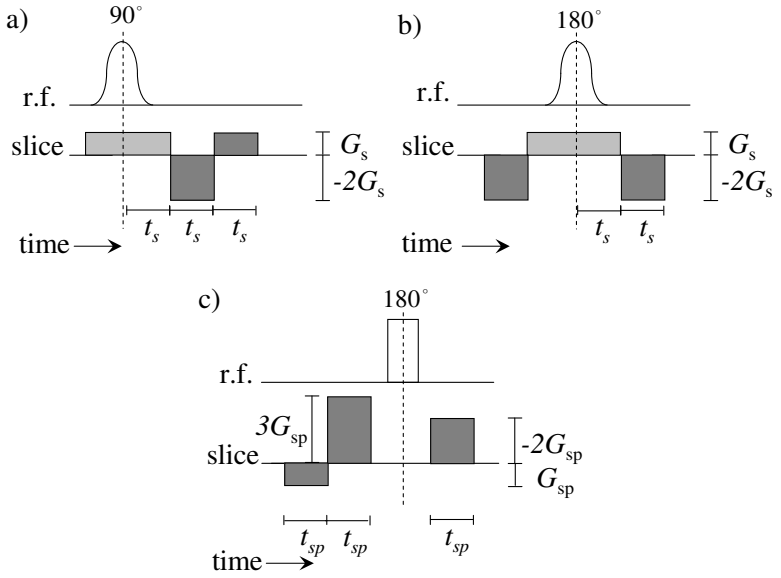


Figure 2.15: Gradient waveforms for flow compensated a) slice selective excitation pulse, b) slice selective refocusing pulse and c) spoiler for a broadband refocusing pulse.

## 2.4 Ultrafast MRI protocols

In this section we examine in detail those pulse sequences by which bubbly flow might successfully be imaged. Conventional MRI sequences, (such as spin-warp; discussed in Section 2.2.1) typically require several minutes for image encoding, and are clearly incapable of producing temporally resolved images of a highly dynamic, non-periodic systems. To minimise temporal blurring, image encoding must be applied as quickly as possible. In this respect, we are limited to the so-called 'ultrafast' imaging techniques, which are capable of sub-second image acquisitions. The three most common ultra-fast techniques are presently considered: 'Fast, Low tip Angle SHot' (FLASH) [22], 'Rapid Acquisition with Relaxation Enhancement' (RARE) [33], and 'Echo-Planar Imaging' (EPI) [5].

### 2.4.1 FLASH

FLASH is a technique which samples **k**-space using only gradient echoes, with each line of **k**-space being acquired from a fresh slice-selective excitation, as shown in Figure 2.16. Each line of **k**-space can generally be acquired within 1 ms, giving the technique a temporal resolution (in milliseconds) approximately equivalent to the number of phase encode steps. As FLASH uses no spin-echoes, off-resonance effects are not refocused and the signal is therefore weighted by $T_2^*$ rather than $T_2$. Despite this, the technique remains highly robust to $B_0$ homogeneity due to the high bandwidth with which each line of **k**-space is sampled.

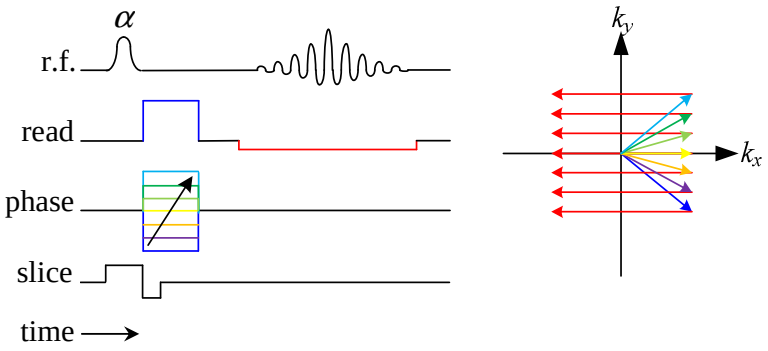


Figure 2.16: Pulse sequence and **k**-space raster for FLASH. Note that the slice gradient can be replaced with a velocity compensated waveform, as shown in Figure 2.15.

The high temporal resolution of FLASH is enabled by the use of low tip angles (typically $\alpha < 10°$), which allows rapid repeat excitations without relaxation weighting. A significant decrease in the signal-to-noise ratio is unavoidable in the use of low tip angle excitations, and particularly in situations were the repetition time, $T_\mathrm{r}$, is significantly

less than the time required for full $T_1$ relaxation. In these cases, the magnetisation reaches some equilibrium saturation value, the optimum of which can be determined by calculation of the Ernst angle [6]:

$$\cos \alpha_{\mathrm{E}} = \mathrm{e}^{-T_{\mathrm{r}}/T_1}. \tag{2.35}$$

It is important to note that when not allowing full transverse plane relaxation that spin and stimulated echoes can form from the combination of repeat excitation pulses. In order to avoid these undesirable coherences it is common in FLASH to use an extended read gradient, which acts to spoil all transverse plane magnetisation remaining after signal acquisition is complete.

### 2.4.2 RARE

RARE is an extension of spin-warp imaging (described in Section 2.22), wherein a train of 180° pulses are used to repeatedly refocus the magnetisation for each line of **k**-space sampled. A pulse sequence and **k**-space raster for single-shot RARE are shown in Figure 2.17. In RARE, the spins are dephased in the read direction and a 180° pulse is applied prior to dephasing the spins in the phase direction. A line of **k**-space is then read-out, and the phase direction is rephased. Following this, another 180° pulse can be applied for the refocusing of off-resonance effects during the acquisition of the next line of **k**-space. The repeated use of 180° pulses ensures that phase shifts due to $B_0$ heterogeneity and chemical shift are refocused for every line of **k**-space. In the general application of RARE, the number of times the magnetisation is refocused per excitation pulse can be varied (the 'RARE factor'), however in the present thesis we will consider only single-shot RARE.

While it is impossible, in practice, to apply perfect 180° pulses (principally due to $B_1$ heterogeneity), RARE is designed to utilise the magnetisation from refocusing pulses with any distribution of tip angles. The repeated use of imperfect refocusing pulses creates many coherence pathways, as the distribution of tip-angles gives rise to a broad array of spin and stimulated echoes. The interaction of these echoes is complicated, however it can be considered as follows. The first line of **k**-space acquired using RARE contains only signal generated by a spin echo, with some magnetisation stored in the longitudinal direction. Some amount of this stored magnetisation will be returned to the transverse plane by the next imperfect 180° pulse, and will refocus to form a stimulated echo. This stimulated echo forms concurrently with the spin echo during the acquisition of the sec-

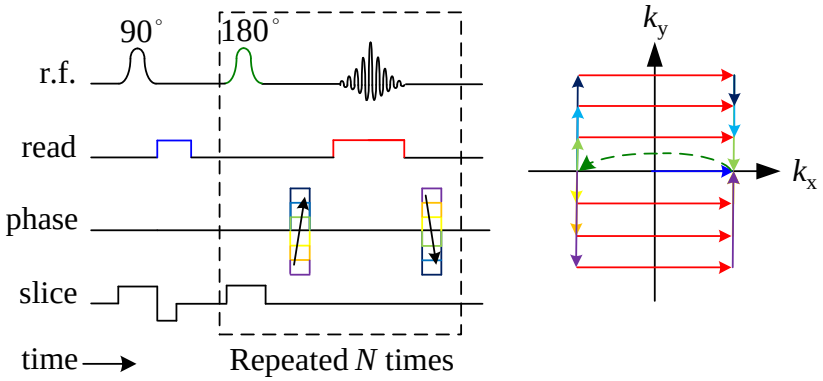


Figure 2.17: Pulse sequence and **k**-space raster for RARE. The number of repeats of the highlighted section of the sections depends on the RARE factor, which for single-shot imaging is set to the image dimension, $N$.

ond line of **k**-space. While every subsequent line of **k**-space contains a progressively more complex mixture of spin and stimulated echoes, those echoes which have undergone an odd number of refocusing pulses add coherently to form a single 'parity echo', as do those which have undergone an even number of refocusing pulses [34]. For a single line of **k**-space both odd and even parity echoes occur simultaneously. It is important to return to the same point in **k**-space prior to the application of each refocusing pulse, such that signal from both spin and stimulated echoes contain identical spatial encoding. Because the parity echoes with which RARE samples **k**-space are a mixture of spin and stimulated echos, RARE images experience a mix of $T_1$ and $T_2$ relaxation weighting. This can be advantageous for systems where $T_1 \gg T_2$, and it is common to encourage the formation of stimulated echoes (and hence increase the amount of $T_1$ weighting) by using soft refocusing pulses.

As each line of **k**-space sampled with RARE contains a mixture of odd and even parity echoes, any phase preconditioning (i.e. flow encoding) applied before the imaging sequence is lost. This can render phase-contrast velocity measurements based on RARE difficult. The problem can be overcome by acquisition of multiple images using phase cycling, such that the real and imaginary components of the magnetisation are preserved in separate images (thus allowing the reconstruction of a phase angle) [34, 35, 36]. This approach comes at the expense of halving the temporal resolution of the technique. Two techniques have recently been proposed for single-shot RARE velocity measurements. Firstly, the sequence 'FLow Imaging Employing Single-Shot ENcoding' (FLIESSEN) [37] imparts flow encoding immediately prior the dephasing of each line of **k**-space. The flow encoding is then undone by the opposite bipolar gradient pair immediately after read-out

and **k**-space rephasing. By applying and undoing flow encoding for every line of **k**-space individually in this way (which can be thought of as the dephasing and rephasing **q**-space; analogous to the rephasing of **k**-space prior to every refocusing pulse) the flow encoded phase is prevented from being lost to the odd/even echo effect. Additionally, FLIESSEN introduces velocity compensation to the phase gradients. The strength of FLIESSEN lies in its careful control of the signal phase. This control comes at significant cost to acquisition time, however, and favourable relaxation times ($T_2 > 1$ s) are necessary for single-shot acquisitions. An alternative single-shot imaging technique which largely preserves the temporal resolution of RARE was recently implemented by Sederman *et al.* [38]. This technique shifts the time domain sampling window for every other line of **k**-space, such that odd and even components of the magnetisation form gradient echoes at separate points in time. In this way, the odd and even echoes can be separated, and phase information retained.

### 2.4.3 EPI

EPI was among the earliest demonstrations of MRI, and remains the fastest imaging technique available today. In general, EPI refers to the acquisition of all of **k**-space using only read gradients following a single excitation, with much freedom existing to decide the manner in which **k**-space is traversed. We will presently focus upon blipped-EPI, referred to herein simply as EPI, which is the classic implementation of the technique, and is routinely used in functional MRI and cardiac morphology studies. Alternative EPI sampling strategies are examined in Chapter 4. EPI acquires the entire **k**-space raster in a rectilinear fashion following a single excitation, while using a spin-echo to ensure that off-resonance effects are refocused when the centre of **k**-space is acquired, as shown in Figure 2.18. Note that the variant of EPI shown here uses a hard refocusing pulse, and includes flow compensated slice refocusing, and a flow compensated spoiler. These modifications render the original technique more robust to the presence of flow. Following an initial dephasing in both directions, and a refocusing pulse, EPI traverses the first read direction as quickly as possible in high-gradient strength bursts, while incrementing the second read direction with short, periodic blips (as EPI is a pure frequency encode technique, it does not possess a phase direction). The use of a high spectral width is necessary with EPI such that Fourier coefficients are sampled in close succession during the rapid traversal of **k**-space. In general, EPI is capable of producing only relatively low resolution images as the total imaging time is limited by $T_2^*$.

It is well known that the high temporal resolution of EPI comes at the expense of robust-

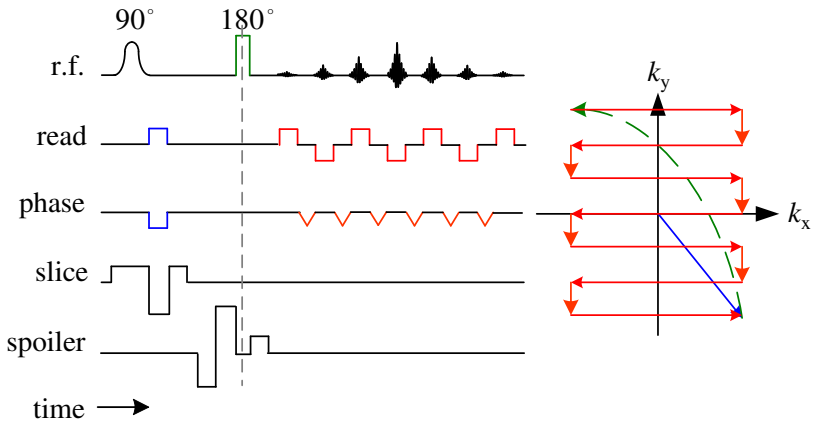


Figure 2.18: Pulse sequence and **k**-space raster for EPI. Note that the sequence shown here is a slight variant of the original EPI sequence, which uses a slice selective refocusing pulse, a broadband refocusing pulse and velocity compensated spoiler, which render the technique more robust to the presence of flow.

ness to off-resonance effects, and a tendency to accrue other artefacts. The most common artefacts associated with EPI acquisitions are demonstrated in Figure 2.19. This figure shows images acquired of a magnetically homogeneous phantom (i.e. $T_2^* \approx T_2$). A reference scan acquired using RARE is given in a), with the two most common artefacts that afflict EPI images shown in b). Firstly, Gibb's ringing is evident in the 'onion peel' rings radiating into the sample in one direction. This effect is caused by the truncation of each line of **k**-space caused by non-ideal gradient behaviour as the corners of the zig-zag path shown in Figure 2.18 are rounded off. This artefact can be corrected by time domain apodisation of each gradient echo with a windowing function (i.e. smoothing), however this comes at the expense of image resolution. The so-called Nyquist ghost is also visible in this image, where a shadow of the phantom, half the field of view out of alignment, can be observed. This artefact is caused by a misalignment of the points sampled in odd and even gradient echoes (which are acquired while traversing **k**-space in opposite directions). The Nyquist ghost can be corrected by acquisition of a reference image with no blips in the second read direction, which allows the gradients to be 'trimmed' such that all echoes are in alignment. Figure 2.19 c) shows an EPI image with the Nyquist ghost corrected.

While Gibb's ringing and the Nyquist ghost are manageable, other, more serious, problems also impact upon EPI images. Figure 2.20 shows the same phantom as above, however now with the inclusion of either a plastic bead of differing magnetic susceptibility (i.e. a localised source of $B_0$ heterogeneity) and a tube of ethanol. Reference images

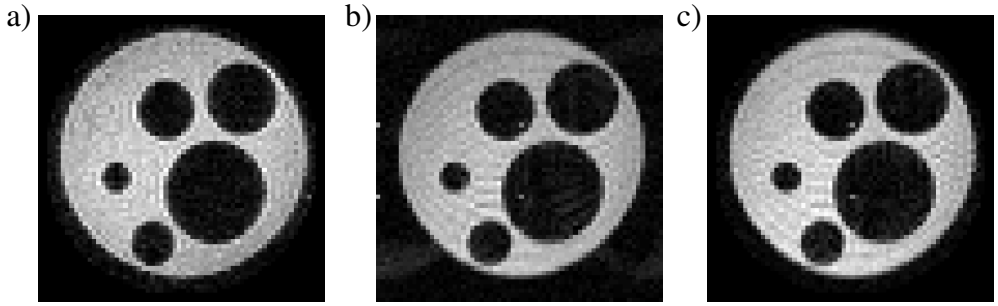


Figure 2.19: Artefacts common to the EPI pulse sequence. a) RARE image of a resolution phantom for reference. b) An EPI image displaying Nyquist ghosting and Gibb's ringing. c) An EPI image with these artefacts corrected. These images were acquired at a $^1$H resonance frequency of 400 MHz, and at a spectral width of 200 kHz, with a field of view of 20 mm $\times$ 20 mm.

acquired using RARE are given in a) and c). The adverse effect of $B_0$ heterogeneity on EPI images is demonstrated in Figure 2.20 b), where localised image distortion and signal misregistration is evident. This occurs as the majority of **k**-space is sampled without off-resonance refocusing in EPI, and hence the images are strongly $T_2^*$ weighted. The effect of chemical shift on EPI images is demonstrated in Figure 2.20 d), where the signal from the ethanol is seen to displace in the second read-direction. Three shadows of the original tube are apparent because of the differing chemical shifts associated with the three peaks of an ethanol spectra. The shift is only seen in one direction because each line of **k**-space is sampled rapidly in the first read direction, whereas sampling of the second read direction is spread over the entire acquisition period. The bandwidth of the image in one direction (200 kHz in the first read direction, but only 3125 Hz (mean) in the second) is therefore of the same order of magnitude as the chemical shift separation of the ethanol peaks relative to the on resonance water peak (2116 Hz for the hydroxyl peak, 1424 Hz for the methylene quartet and 444 Hz for the methyl triplet at a $^1$H frequency of 400 MHz). This leads to the signal from the three ethanol peaks being displaced in the second read direction by 68%, 46% and 14% of the field of view of the image.

### 2.4.4 Ultrafast flow imaging

Flow imaging using MRI is now a well established technique; a comprehensive review of the subject is provided by Fukushima [39]. The earliest instances of flow imaging were 'time-of-flight' measurements [40], wherein a reference grid of saturated magnetisation was prepared, and subsequently imaged as the grid deformed under flow. These techniques have now been largely superseded, however, by so-called 'phase contrast' velocity imaging [41]. As mentioned in Section 2.3, this technique involves imparting a

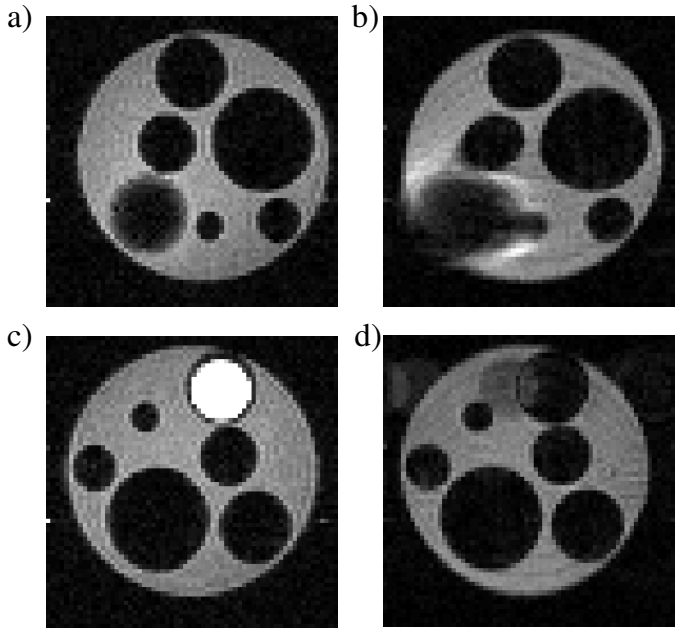


Figure 2.20: The effect of off-resonance spins on EPI images. a) and c) show RARE scans of a phantom with a source of $B_0$ heterogeneity and an NMR tube of ethanol. b) and d) show EPI images of the same systems. The adverse effect of $B_0$ heterogeneity on EPI images is evident, as is a chemical shift artefact in the phase direction.

first moment phase shift to spins undergoing coherent motion, prior to the application of an imaging sequence for spatial resolution. One of the major goals of this thesis is to obtain temporally resolved measurements of velocity fields in the presence of highly unsteady flow. To this end, we seek to combine velocity encoding with a single-shot ultrafast imaging technique. As discussed in Section 2.4.2, single-shot RARE velocity imaging is rendered difficult because of the complicated phase accrual associated with the imaging sequence, however measurements have been successfully performed [37, 38]. Velocity imaging using FLASH is much more readily achieved, and is used routinely for measurements of arterial blood flow [42]. For observation of the most highly transient flowing systems, EPI must be employed. Single-shot EPI velocimetry has been successfully demonstrated several times in the literature [43, 44, 45], and most recently, an EPI based technique known as Gradient Echo Velocity and Acceleration Imaging Sequence (GERVAIS) was described by Sederman *et al.* [46].

GERVAIS is a technique by which three component velocity vectors can be measured. A pulse sequence diagram for GERVAIS is shown in Figure 2.21. Following a slice selective excitation pulse (for which the slice gradient is velocity compensated), GERVAIS uses a train of spin-echoes, with a complete **k**-space raster sampled during each one. Velocity en-

coding is applied around each refocusing pulse, and also acts as a spoiler for these pulses, as described in Section 2.2.3. This velocity encoding is applied in three perpendicular directions, for three sequential images. In this way, as long as the fluid does not move significantly over the course of the acquisition, an 'instantaneous' three-component velocity vector may be reconstructed. Note that hard 180° pulses are used, which allows the excited slice to be refocused irrespective of where it has moved to in the coil: effectively allowing GERVAIS to produce Lagrangian measurements of fluid flow. Two GERVAIS acquisitions are generally acquired: one of the flowing system under examination, and one of a static fluid reference image. Subtraction of the reference image allows both phase shifts due to eddy currents (which are generated by the velocity encoding gradients) and other sources of phase accrual to be removed. After acquisition each sequential image contains the velocity encoded phase information of all previous images, which has been inverted following each refocusing pulse.

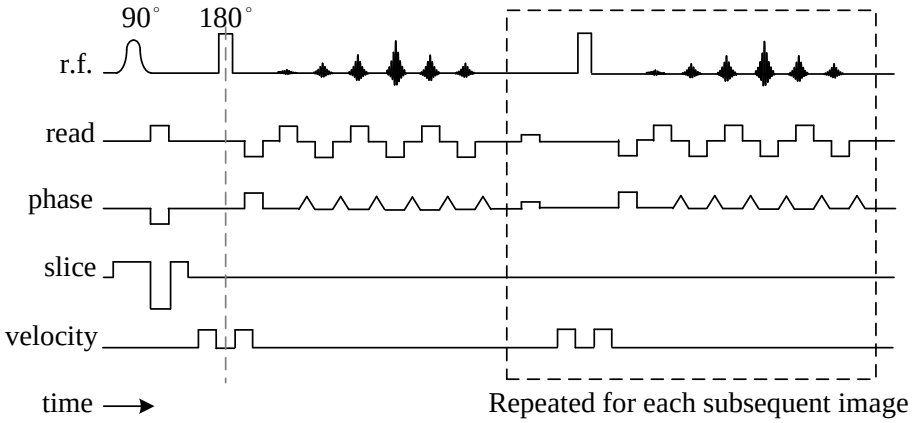


Figure 2.21: Pulse sequence for GERVIAS. A number of sequential velocity encoded EPI images are acquired, using a spin-echo to refocus the magnetisation between each image. For three component velocity vectors, typically three images, velocity encoded in different directions are required.

For three sequential images, velocity encoded in $z$, $x$, and $y$, after subtraction of the reference image the phase of each is given by:

$$\phi_1 = \phi_z$$
$$\phi_2 = \phi_x - \phi_z$$
$$\phi_3 = \phi_y - \phi_x + \phi_z.$$

The velocity proportionate phase in each direction is then given by:

$$\phi_z = \phi_1$$
$$\phi_x = \phi_2 + \phi_1$$
$$\phi_y = \phi_3 + \phi_2.$$

Therefore it can be seen that the velocity proportionate phase for each image can be isolated simply by adding the phase of the preceding image. A particular problem associated with the application of EPI based sequences to flowing systems is that the imaging gradients accumulate significant amounts of first moment phase (because EPI traverses **k**-space unidirectionally in one dimension). In the original application of GERVAIS this problem was avoided by only examining systems in which the transverse plane velocity components would generate errors of less than 5%. For application of EPI to a more heavily mixed system, such as bubbly flow, the effects of first moment accrual during imaging become more problematic. The application of EPI velocimetry to such systems is the subject of Section 3.3.

## 2.5 Compressed sensing

There are several reasons why the acquisition of MRI images is slow: the application of phase encoding is time consuming, acquisition speed during frequency encoding is commonly limited by the bandwidth of the analog-to-digital converter, and magnetisation relaxation must be allowed before repeat excitations. The latter problem is avoided for RARE and EPI by the use of single-shot image encoding, and through the use of low-tip angle excitations for FLASH. The two former constraints, however, can only be addressed by sampling fewer points in **k**-space. The Nyquist-Shannon sampling theorem states that for a digitised signal to be a true representation of the underlying continuous signal, the digital signal must be sampled at twice the highest frequency present in the continuous signal. For images, the sampling rate is set by the desired spatial or temporal resolution, and the Nyquist-Shannon theorem may be translated to state that the number of complex Fourier coefficients sampled must be equal to the number of pixels in the image. Adherence to this principle is important in MRI to prevent a wide range of undersampling artefacts. These artefacts can range from spatial aliasing if only every other data point is sampled (see the demonstration of 'fold-over' in Section 2.2.1) to incoherent noise if the distribution of sampled points is random.

It is well known that MRI acquisition times can be decreased by undersampling. Lustig *et al.* [47] state that there exists three conventional approaches to mitigating undersampling artefacts. Firstly, some techniques sacrifice the signal-to-noise ratio of an image, and aim to produce only incoherent undersampling artefacts [48, 49]. Secondly, it is possible to make use of redundancies in the acquired signal, such as in partial-Fourier imaging [50], where the Hermitian symmetry of **k**-space is exploited to allow the reconstruction of images from only half a **k**-space raster. Lastly, some techniques make use of redundancy in either spatial or temporal characteristics of an image [51, 52]. An alternative approach is to consider more sophisticated image reconstruction strategies by which undersampling artefacts can be eliminated. Compressed sensing is the broad title given to an auspicious approach to this problem, which has recently been successfully demonstrated on MRI data [53].

The fundamental idea of compressed sensing is the exploitation of sparsity in an image. That is, if all features of an image can be represented in relatively few data points (i.e. the image is 'sparse'), it is possible to separate the true image from undersampling artefacts. While some images are naturally sparse, in general it will be necessary to obtain a sparse representation of the image in some other mathematical domain. For example, a sinusoidal signal is represented in the frequency domain by a single point (i.e. the frequency domain is very sparse). If, by some artefact, other frequency components are present in this signal, the original waveform can be separated from the artefact by transforming to the sparse domain, and applying a threshold before performing the inverse transformation. Clearly, it is important that undersampling artefacts are incoherent, such that they do not form structures which may also be sparsely represented. The use of sparsifying transforms and thresholding is well established in the field of image compression, where it is common to store data in a sparse domain such that fewer coefficients need be retained and, as a result, file sizes are smaller.

To mathematically quantify sparsity it is common to employ $l_\mathrm{p}$ space. The $l_\mathrm{p}$ norm of a vector $\mathbf{x}$ is defined for $p \geq 1$ as:

$$\|\mathbf{x}\|_\mathrm{p} = \left( \sum_{i=1}^{n} |x_\mathrm{i}|^p \right)^{1/p} \tag{2.36}$$

and for $0 \leq p < 1$ as:

$$\|\mathbf{x}\|_{\mathrm{p}} = \left( \sum_{i=1}^{n} |x_{\mathrm{i}}|^{p} \right), \tag{2.37}$$

where in this convention $0^0 \equiv 0$. That is, the $l_0$ norm of an image represents the number of non-zero pixels present, while the $l_1$ norm represents sum of pixel magnitudes and the $l_2$ norm the root sum of squares. Sparsity may be enforced by minimisation of the $l_0$ norm, however this is well recognised as being a computationally-expensive approach to solving the problem [54]. Càndes and Wakin state that the minimisation of the $l_1$ norm also promotes sparsity, however can be expressed as a linear program, and thus solved in a computationally efficient manner [55]. Using $l_{\mathrm{p}}$ notation, a generic compressed sensing algorithm can be expressed as [53]:

$$\begin{aligned} &\text{minimise :} && \|\psi\mathbf{M}\|_1 \\ &\text{subject to :} && \|\mathcal{F}\mathbf{M} - \mathbf{K}\|_2 < \epsilon \end{aligned}$$

where the matrix $\mathbf{M}$ is the reconstructed image, $\psi$ is a sparsifying linear operator, $\mathcal{F}$ is a Fourier transform operator, $\mathbf{K}$ is the sampled $\mathbf{k}$-space points, and $\epsilon$ is a threshold level which can be readily set to the noise level of the image. Many approaches have been proposed for solving this minimisation problem, however in the present work we will only apply that of Lustig [20]. Figure 2.22 shows an example of the application of image reconstruction from 50% undersampled data using compressed sensing.

Compressed sensing is one of the most promising avenues of current research by which the speed of MRI acqusitions is being improved, and it is an important tool to be aware of for the imaging of highly transient systems. In the present work, undersampling with a compressed sensing reconstruction will be employed if a fully sampled $\mathbf{k}$-space raster cannot be acquired within the time scales of motion of the systems under examination.

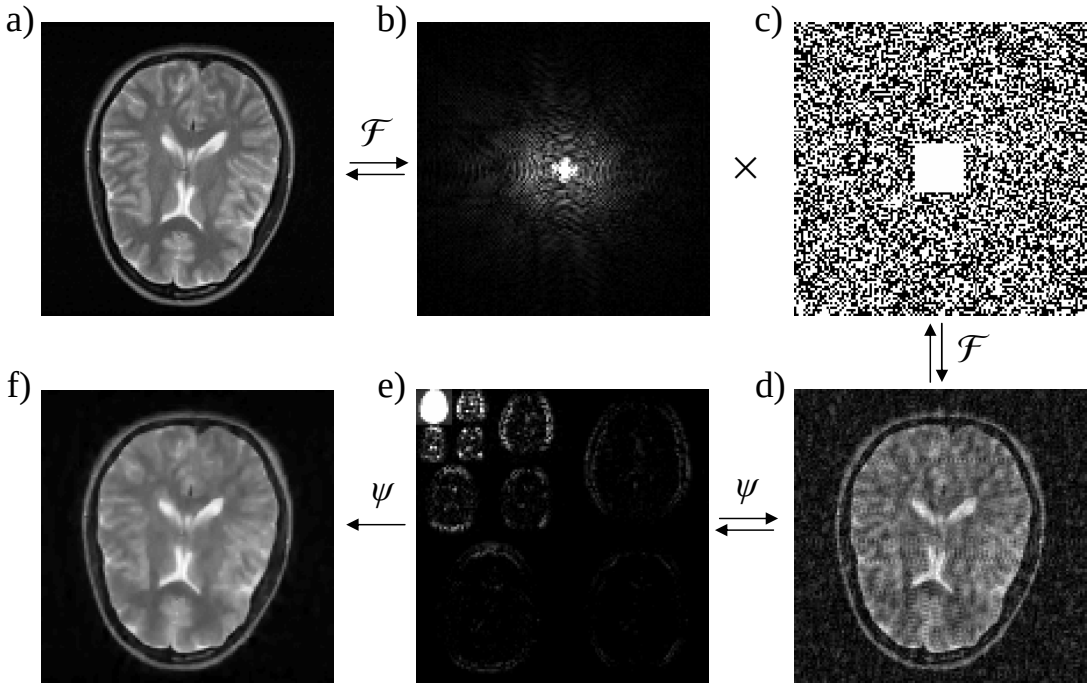


Figure 2.22: Demonstration of a compressed sensing reconstruction from an undersampled data set. Data and compressed sensing algorithm from Lustig sparse MRI package [20]. a) A fully sampled image with b) coresponding **k**-space. c) The undersampled **k**-space is generated by multiplication with a random distribution of pixels. Note that the centre of **k**-space remains fully sampled as the high power Fourier coefficients in this region are critical for any reconstruction to be successful. d) The image with undersampling artefacts. e) The undersampled image rendered sparse by wavelet transform. From this domain it is now possible to solve an optimisation problem that maximises sparsity while minimising deviation from the original **k**-space points. f) After optimisation the undersampling artefact is largely removed, and the original image recovered.

# Bibliography


[1] Purcell, E.M., Torrey, H.C. and Pound, R.V., 1946. Resonance absorption by nuclear magnetic moments in a sold. *Phys. Rev.*, 69, pp. 37–38.

[2] Bloch, F., Hansen, W.W. and Packard, M., 1946. Nuclear induction. *Phys. Rev.*, 69, p. 127.

[3] Lauterbur, P.C., 1973. Image formation by induced local interactions - examples employing Nuclear Magnetic Resonance. *Nature*, 242, pp. 190–191.

[4] Mansfield, P. and Grannell, P.K., 1973. NMR 'diffraction' in solids? *J. Phys. C*, 6, pp. L422–L426.

[5] Mansfield, P., 1977. Multi-planar image formation using NMR spin echoes. *J. Phys. C*, 10, pp. L55–L58.

[6] Callaghan, P.T., 1991. *Principles of nuclear magnetic microscopy.* Clarendon Press, Oxford.

[7] Levitt, M., 2001. *Spin dynamics: basics of nuclear magnetic resonance.* John Wiley & Sons.

[8] Haacke, E.M., Brown, R.W., Thompson, M.R. and Venkatesan, R., 1999. *Magnetic Resonance Imaging Physical Principles and Sequence Design.* John Wiley & Sons.

[9] Fukushima, E. and Roeder, S.B.W., 1981. *Experimental pulse NMR: a nutes and bolts approach.* Addison-Wesley.

[10] Lide, D.R., 1998. *CRC handbook of chemistry and physics.* CRC press, Boca Raton.

[11] Hahn, E.L., 1950. Spin echoes. *Phys. Rev.*, 80, pp. 580–594.

[12] Carr, H.Y. and Purcell, E., 1954. Effects of diffusion on free precession in nuclear magnetic resonance experiments. *Phys. Rev.*, 94(3), pp. 630–638.

[13] Meiboom, S. and Gill, D., 1959. Modified spin-echo method for measuring nuclear relaxation times. *Rev. Sci. Instrum.*, 29, p. 688.

[14] Hennig, J., 1991. Echoes-how to generate, recognize, use or avoid them in MR-imaging sequences. Part I: fundamental and not so fundamental properties of spin echoes. *Concept Magnetic Res.*, 3, pp. 125–143.

[15] Keeler, J., 2005. *Understanding NMR spectroscopy.* Wiley.

[16] Hoult, D.I. and Richards, R.E., 1975. Critical factors in design of sensitive high-resolution nuclear magnetic resonance spectrometers. *Proc. R. Soc. London Ser. A*, 344, pp. 311–340.

[17] Bodenhausen, G., Freeman, R. and Turner, D.L., 1977. Suppression of artifacts in two-dimensional J spectroscopy. *J. Magn. Reson.*, 27, pp. 511–514.

[18] Kingsley, P.B., 1995. Product operators, coherence pathways, and phase cycling. part III: phase cycling. *Concepts Magn. Reson.*, 7, pp. 167–192.

[19] Cooley, J.W. and Tukey, J.W., 1965. An algorithm for the machine calculation of complex Fourier series. *Math. Comput.*, 19, pp. 297–301.

[20] Lustig, M. *Sparse MRI reconstruction package.* http://www.stanford.edu/ mlustig/SparseMRI.html.

[21] Edelstein, W.A., Hutchison, J.M.S., Johnson, G. and Redpath, T., 1980. Spin warp NMR imaging and applications to human whole-body imaging. *Phys. Med. Boil.*, 25(4), pp. 751–756.

[22] Haase, A., Frahm, J., Matthaei, D., Hanicke, W. and Merboldt, K., 1986. Flash imaging rapid NMR imaging using low flip-angle pulses. *J. Mag. Res.*, 67, pp. 258–266.

[23] Mao, J., Mareci, T.H. and Andrew, E.R., 1988. Experimental study of optimal selective 180 radiofrequency pulses. *J. Magn. Reson.*, 79, pp. 1–10.

[24] Karger, J. and Heink, W., 1963. The propagator representation of molecular transport in microporous crystallites. *J. Magn. Reson.*, 51, pp. 1–7.

[25] Stejskal, E.O. and Tanner, J.E., 1965. Spin diffusion measurements: spin echoes in the presence of a time-dependent field gradient. *J. Chem. Phys.*, 42, pp. 288–292.

[26] Stevenson, P., Sederman, A.J., Mantle, M.D., Li, X. and Gladden, L.F., 2010. Measurement of bubble size distribution in a gas-liquid foam using pulsed-field gradient nuclear magnetic resonance. *J. Colloid Interface Sci.*, 352, pp. 114–120.

[27] Hollingsworth, K.G., Sederman, A.J., Buckley, C., Gladden, L.F. and Johns, M.L., 2004. Fast emulsion droplet sizing using NMR self-diffusion measurements. *J. Col. Int. Sci*, 274, pp. 244–250.

[28] Weber, D., Mantle, M.D., Sederman, A.J. and Gladden, L.F., 2009. Surface composition and diffusion in catalysts probed by PFG NMR techniques. *Defect Diffus. Forum*, 283-286, pp. 190–193.

[29] Price, W.S., 1997. Pulsed-field gradient nuclear magnetic resonance as a tool for studying translational diffusion: Part I. basic theory. *Concept Magnetic Res.*, 9, pp. 299–336.

[30] Price, W.S., 1998. Pulsed-field gradient nuclear magnetic resonance as a tool for studying translational diffusion: Part II. experimental aspects. *Concept Magnetic Res.*, 10, pp. 197–237.

[31] Mitchell, J. and Johns, M.L., 2009. Rapid measurements of diffusion using PFG: Developments and applications of the difftrain pulse sequence. *Conepts Magn. Reson. A*, 34A, pp. 1–15.

[32] Pope, J.M. and Yao, S., 1993. Quantitative NMR imaging of flow. *Concept Magn. Reson.*, 5, pp. 281–302.

[33] Hennig, J., Nauerth, A. and Friedburg, H., 1986. RARE imaging: a fast imaging method for clinical MR. *Magn. Reson. Med.*, 3, pp. 823–833.

[34] Norris, D.G., Börnert, P., Reese, T. and Leibfritz, D., 1992. On the application of ultra-fast RARE experiments. *Magn. Reson. Med.*, 27, pp. 142–164.

[35] Ahola, S., Perlo, J., Casanova, F., Stapf, S. and Blümich, B., 2006. Multiecho sequence for velocity imaging in inhomogeneous RF fields. *J. Magn. Reson.*, 182, pp. 143–151.

[36] Galvosas, P. and Callaghan, P.T., 2006. Fast magnetic resonance imaging and velocimetry for liquids under high flow rates. *J. Magn. Reson.*, 181, pp. 119–125.

[37] Amar, A., Blümich, B. and Casanova, F., 2010. Rapid multiphase flow dynamics mapped by single-shot MRI velocimetry. *ChemPhysChem.*, 11, pp. 2630–2638.

[38] Sederman, A.J., 2011. Private communication.

[39] Fukushima, E., 1999. Nuclear magnetic resonance as a tool to study flow. *Annu. Rev. Fluid Mech.*, 31, pp. 95–123.

[40] Axel, L., Shimakawa, A. and MacFall, J., 1986. A time-of-flight method of measuring flow velocity by MRI. *Magn. Reson. Imaging*, 4, pp. 199–205.

[41] Moran, P., 1982. A flow velocity zeugmatographic interlace for NMR imaging in humans. *Magn. Reson. Imaging*, 1, pp. 197–203.

[42] Sakuma, H., Kawada, N., Takeda, K. and Higgins, C.B., 1999. MR measurement of coronary blood flow. *J. Magn. Reson. Im.*, 10, pp. 728–733.

[43] Kose, K., 1990. NMR imaging of turbulent structure in a transitional pipe flow. *J. Phys. D.*, 23, pp. 981–983.

[44] Kose, K., 1991. Instantaneous flow-distribution measurements of the equilibrium turbulent region in a circular pipe using ultrafast NMR imaging. *Phys. Rev. A.*, 44, pp. 2495–2504.

[45] Kose, K., 1991. One-shot velocity mapping using multiple spin-echo EPI and its application to turbulent flow. *J. Magn. Reson.*, 92, pp. 631–635.

[46] Sederman, A.J., Mantle, M.D., Buckley, C. and Gladden, L.F., 2004. MRI technique for measurement of velocity vectors, acceleration, and autocorrelation functions in turbulent flow. *J. Magn. Res.*, 166, pp. 182–189.

[47] Lustig, M., Donoho, D.L. and Pauly, J.M., 2007. Sparse MRI: the application of compressed sensing for rapid MR imaging. *Magn. Reson. Med.*, 58, pp. 1182–1195.

[48] Tsai, C.M. and Nishimura, D., 2000. Reduced aliasing artifacts using variable-density $k$-space sampling trajectories. *Magn. Reson. Med.*, 43, pp. 452–458.

[49] Peters, D.C., Korosec, F.R., Grist, T.M., Block, W.F., Holden, J.E., Vigen, K.K. and Mistretta, C.A., 2000. Undersampled projection reconstruction applied to MR angiography. *Magn. Reson. Med.*, 43, pp. 91–101.

[50] McRobbie, D.W., 2003. *MRI from picture to proton.* Cambridge University Press, Cambridge.

[51] Korosec, F.R., Frayne, R., Grist, T.M. and Mistretta, C.A., 1996. Time-resolved contrast-enhanced 3d MR angiography. *Magn. Reson. Med.*, 36, pp. 345–351.

[52] Parasoglou, P., Malioutov, D., Sederman, A.J., Rasburn, J., Powell, H., Gladden, L.F., Blake, A. and Johns, M.L., 2009. Quantitative single point imaging with compressed sensing. *J. Magn. Reson.*, 201, pp. 72–80.

[53] Lustig, M., Donoho, D., Santos, J.M. and Pauly, J.M., 2008. Compressed sensing MRI. *IEEE Signal Proc. Mag.*, 3, pp. 72–82.

[54] Càndes, E.J. and Romberg, J., 2008. Robust uncertainty principles: exact signal reconstruction from highly incomplete frequency information. *IEEE Trans. Inform. Theory*, 52, pp. 489–509.

[55] Càndes, E.J. and Wakin, M.B., 2008. An introduction to compressive sampling. *IEEE Sig. Proc. Mag.*, 3, pp. 21–30.

# Chapter 3

# Ultrafast MRI of unsteady systems

The trade-off between temporal and spatial resolution is an important consideration in the use of any tomographic technique. For the application of MRI to an unsteady system, such as bubbly flow, striking a workable balance between these two factors can be a particular challenge due to the slow data acquisition commonly associated with MRI relative to the time scales of the system under observation [1]. For systems which are unsteady yet periodic in time, conventional, slow MRI techniques can be employed with some form of triggering, such that **k**-space points are only sampled while the system is at a certain point in its cycle. This approach is commonly used in cardiac imaging and angiography, where acquisitions are triggered by electrocardiogram and data are only sampled at a certain point in the cardiac cycle (known as cardiac gating) [2, 3]. A similar technique can be used for imaging of the respiratory system when breath-hold measurements are not suitable [4]. In an engineering context, a similar approach has been adopted for velocity measurements in a mixed cell (where acquisitions are synchronised with impeller position) [5] and for flow driven by a peristaltic pump (where acquisition is triggered for a certain position in the pump cycle) [6]. By comparison with computational fluid dynamics, triggered phase-contrast velocity measurements have been found to contain errors in the range 5% to 12% [7, 8, 9].

If no periodicity exists it becomes necessary to restrict acquisitions to only those protocols capable of acquiring an entire image within the time scales of motion of the system.

This situation is commonly encountered in many systems of engineering interest, and particularly for unsteady flow systems. The advances in imaging systems in this context are reviewed by Gladden [10] until 1994, Fukushima [11] until 1999, Mantle and Sederman [12] until 2003, Gladden *et al.* [13] until 2006 and most recently Gladden and Mitchell [14]. In general, the fastest MRI protocol, echo-planar imaging (EPI), is capable of producing whole images within 10-20 ms, and has been applied to the imaging of turbulent pipe flow in several studies [15, 16, 17, 18]. EPI velocity measurements have been extended towards the acquisition of three component velocity vectors in a sequence known as GERVAIS, which has also been applied to turbulent pipe flow [19]. GERVAIS has also been used to study accelerating flow in a Couette cell [20], mixing in a stirred cell [21] and multiphase flows [22]. Systems which contain many interfaces between phases of differing magnetic susceptibility tend to generate large amounts of $B_0$ heterogeneity, which renders them unsuitable for investigation using EPI (see Section 2.4.3). Generally, in these cases acquisition speed must be sacrificed for robustness to artefacts, with the optimal balance depending greatly on the system under observation. For example, RARE has been found to be sufficiently fast and robust for imaging two-phase flow in a ceramic monolith reactor [23, 24] while the slightly faster FLASH has been used for visualising bubbling and mixing in fluidised beds [25, 26]. There exists limited prior applications of conventional MRI to bubble flow (reviewed in Section 1.4), and the present thesis is the first to apply ultrafast MRI to this highly unsteady system.

In this chapter the application of ultrafast MRI to unsteady systems is explored, with an approach to the imaging of bubbly flow. Due to the significant magnetic susceptibility difference between air and water [27, 28], it is anticipated that air-water bubbly flow will be a magnetically heterogeneous system. As discussed above, this limits the choice of applicable pulse sequences, with faster techniques tending to lack robustness to artefacts. To avoid this restriction, it is possible to dope the continuous phase with a paramagnetic salt such that the magnetic susceptibilities of the two phases are equivalent [29]. Thus, this chapter firstly details a technique for the measurement of the magnetic susceptibility difference between two phases. This technique is then applied to determine the concentration of dopant required to match the susceptibility of water to that of air. The influence of this dopant upon the structure of bubbly flow is investigated using optical bubble size measurements on a low voidage system. Using a magnetic susceptibility matched solution, the three most commonly used fast imaging protocols, (FLASH, RARE and EPI) are applied to a low voidage bubbly flow in order to explore the balance between the timescales of motion in the system and the temporal resolution of each technique. Lastly,

a potential source of systematic error for velocity measurements on unsteady systems is identified. A technique is then proposed by which this error might be negated for EPI acquisitions, and the new experimental methodology is demonstrated on some example unsteady flow systems.

## 3.1 Magnetic susceptibility matching

MRI can typically be made robust to image artefacts by reversing the dephasing caused by off-resonance effects using spin echoes, or by minimising the time for off-resonance dephasing using short, high-bandwidth read-out sequences. It is, however, specifically the absence of these features which enables the high temporal resolution of EPI. As demonstrated in Figure 2.20, this renders EPI highly susceptible to off-resonance effects, with $B_0$ heterogeneity causing localised image distortion, and chemical-shift leading to coherent signal miss-registration. The adverse effect of $B_0$ heterogeneity on EPI images is likely to be problematic for application of the technique to bubbly flow due to the magnetic susceptibility difference between air and water (in terms of volume magnetic susceptibility, $\chi_v = 0.36 \times 10^{-6}$ for air but $\chi_v = -9.05 \times 10^{-6}$ for water [27]). The medical MRI community is very familiar with image artefacts generated by magnetic susceptibility differences; they are particularly problematic for functional MRI in the vicinity of the nasal passage [30]. Surrounding the sample with a medium of similar magnetic susceptibility has resulted in some artefact reduction (this technique was, in fact, employed in the original work of Laturbur, who imaged two tubes of $H_2O$ surrounded by $D_2O$ [31]), however cannot help to correct for $B_0$ heterogeneity generated internally.

A potential solution to this problem exists in that it is possible to alter the magnetic susceptibility of a liquid phase by doping it with a paramagnetic salt [27]. If the condition of equivalent magnetic susceptibility between dispersed and continuous phases can be enforced in this way, the system will be magnetically homogeneous, and no localised $B_0$ field variations will be introduced by the bubbles. EPI measurements on such a magnetic susceptibility matched system would therefore contain no artefacts arising from field inhomogeneity. Magnetic susceptibility matching by addition of paramagnetic dopants has been previously examined by Chu *et al.* [29], who related the magnetic susceptibility of paramagnetic solutions of varying concentration with the frequency shift caused by the addition of the dopant. This technique was later applied by Bakker and de Roos [32], who examined the dopant concentration required for a solution magnetic susceptibility matched to air. They suggested that Wiedemann's additivity law for the susceptibility of

mixtures [33] may be used to provide an estimate of the concentration of paramagnetic required to induce the desired change in susceptibility. This law states that the magnetic susceptibility of a mixture containing $N$ components is given by:

$$\chi = \sum_{n=1}^{N} p_n \chi_n \tag{3.1}$$

where $p$ is mole fraction and $\chi$ is molar susceptibility. Note that molar susceptibilities are often quoted in the literature in cgs units, which must be multiplied by a factor of $4\pi$ for conversion to the SI units system. The molar susceptibility is related to the volume susceptibility according to:

$$\chi_{\mathrm{v}} = \frac{\rho}{MW}\chi \tag{3.2}$$

where $\rho$ is mass density and $MW$ is molar mass. For a binary mixture, when expressed in terms of volume magnetic susceptibility and assuming the concentration of one component to be small relative to the other (valid for dilute paramagnetic solutions), equation (3.1) gives [32]:

$$\chi_{\mathrm{v}} = \chi_{\mathrm{v}1} + \frac{c_2 \chi_{\mathrm{v}2}}{c_1} \tag{3.3}$$

where $c$ is molar concentration. Table 3.1 was produced using this relationship to estimate the concentration of a variety of paramagnetic dopants that will produce a solution with a magnetic susceptibility equivalent to that of air. Density, molecular mass and molar susceptibility data for each examined dopant were obtained from the literature [28]. Note that data were not available for the molar susceptibility of each dopant in its ionised form, so the susceptibility of a compound containing the paramagnetic was used as an approximation. This approach is valid for obtaining an estimate as the magnetic susceptibility of each species is strongly dominated by the paramagnetic atom.

Table 3.1: Volume susceptibility of common paramagnetic ions and concentration of those ions required for a solution magnetic susceptibility matched to air (estimated using equation (3.3)). Data for these calculations were obtained from the literature [28].

| Paramagnetic ion | $\chi_{\mathrm{v}}$ (estimated) | Concentration (mM) |
|---|---|---|
| $Dy^{3+}$ | $29.00 \times 10^{-3}$ | 17.88 |
| $Ho^{3+}$ | $29.54 \times 10^{-3}$ | 17.55 |
| $Gd^{3+}$ | $16.79 \times 10^{-3}$ | 30.87 |
| $Mn^{2+}$ | $23.96 \times 10^{-3}$ | 21.63 |
| $Cu^{2+}$ | $1.91 \times 10^{-3}$ | 272.09 |

Bakker and de Roos [32] only experimentally investigated holmium, and found the concentration of paramagnetic required for an air-equivalent solution to be $16.6 \pm 0.1$ mM, in modest agreement with Table 3.1. The only other body of work to examine magnetic susceptibility matching with air is that of Sains [22], who used an imaging based approach to determine the frequency shift at the interface between two phases. Sains, who examined dysprosium, found a 15 mM solution to be approximately equivalent to air, in moderate agreement with the theoretical prediction.

As the presence of paramagnetic ions will also reduce $T_1$ and $T_2$ relaxation times, care must be taken in the selection of a dopant to ensure that the relaxation times are not rendered prohibitively short for imaging. The literature notes that both dysprosium and holmium, the two most paramagnetic dopants considered, reduce $T_1$ and $T_2$ approximately equivalently, with an air-equivalent dysprosium solution exhibiting relaxation times of 88 ms [22], compared to 130 ms for holmium [32]. These relaxation times are suitable for single-shot imaging (which requires approximately 10 ms to 100 ms), with the slightly faster relaxation of the dysprosium solution being advantageous for increased repetition rates without the introduction of relaxation weighting. It is known that the effect of gadolinium, manganese and copper ions on relaxation is approximately an order of magnitude greater than the more strongly paramagnetic ions [34], and that gadolinium and manganese influence $T_2$ much more strongly than $T_1$ [35]. When these factors are combined with the relatively large concentration of paramagnetic required for magnetic susceptibility matching, this will likely result in relaxation times on the order of 1 ms to 10 ms. For multishot sequences, where high repetition rates are desirable for fast imaging, the use of these dopants may therefore be highly advantageous.

As discussed in Section 1.2, even small amounts of inorganic material present in the continuous phase can significantly alter the behaviour of a bubbly flow system. In particular, Jamialahmadi and Müller-Steinhagen [36] demonstrated that the gas holdup for a 6 mM potassium chloride is significantly increased compared to that of pure water. They claim that the inclusion of salt led to the formation of smaller bubbles, and stabilised the gas-liquid films, allowing homogeneous bubbly flow to be maintained at much higher gas fractions than those achievable in pure water. This behaviour is explained as being due to the formation of ionic forces between water and the ions in the system rendering gas-liquid films more cohesive [37]. While no previous work exists investigating the effect of paramagnetic salts in particular on bubbly flow, it is possible that they will have a similar effect to the diamagnetic salts examined in the literature. Given that one of the

primary goals of this study is to test the application of MRI to high voidage systems, the inclusion of a paramagnetic salt, which may render the system stable at higher voidages, may be highly beneficial, particularly if the presence of this salt also renders the system more amiable to fast imaging using MRI.

In the present section the technique of Sains [22] is applied to quantify the magnetic susceptibility difference between paramagnetic solutions and air. Both dysprosium and gadolinium ions are considered to provide for the eventual use of either single or multishot imaging. The influence had by the presence of these dopants upon the structure of a bubbly flow system is also investigated.

### 3.1.1 Experimental

The magnetic susceptibility of two phases may be matched using a modified version of the spin-warp pulse sequence (see Section 2.2.1), as shown in Figure 3.1. The main alteration to the sequence consists of the addition of a low-bandwidth (150 Hz) slice-selective 90° pulse, perpendicular to the imaging plane, prior to each excitation of the imaging sequence. This additional pulse has the effect of saturating a line of constant frequency through the sample. If $B_0$ is rendered homogeneous for a single phase sample, upon the introduction of a phase interface (i.e. by removing half the water from a test-tube) the line of saturated magnetisation will bend to reveal the frequency shift generated by the differing magnetic susceptibility of the two phases. Thus by varying the concentration of paramagnetic salt within the solution until the saturated line is undeflected across the interface, the amount of dopant required for a magnetic susceptibility matched solution may be quantified.

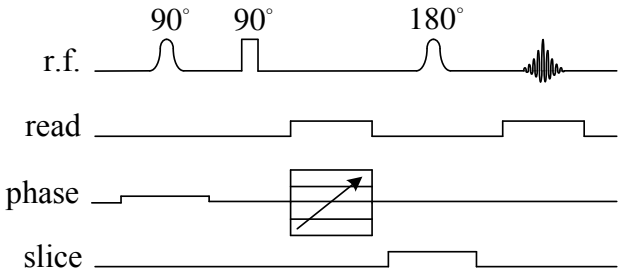


Figure 3.1: Modified spin-warp pulse sequence for the quantification of frequency shift due to magnetic susceptibility miss-match at a phase interface.

In the present study we consider the use of two paramagnetic salts: dysprosium chloride and gadolinium chloride. The magnetic susceptibility difference between air and solutions of these two salts up to concentrations of 30 mM were measured as described above. These

measurements were performed on a Bruker DMX-200 super wide-bore spectrometer operating at a $^1$H frequency of 199.7 MHz, and using a 13.9 G cm$^{-1}$ 3-axis shielded gradient system and 64 mm diameter birdcage coil. The phantom used was a glass jar of inside diameter 28 mm, either filled or half-filled with the solution under examination. The gradient strength used for the initial 90° slice selective pulse was 0.07 G cm$^{-1}$, for generation of a 5 mm thick slice of saturated magnetisation. Images were acquired at a field of view (FOV) of 3.0 cm × 3.0 cm, and a spatial resolution of 117 μm × 117 μm.

The influence had by these dopants upon the structure of bubbly flow was also investigated by means of bubble size distributions measured optically for a low voidage system ($\varepsilon = 3.5\%$) before and after the addition of paramagnetic salt. Bubbles were generated using a foamed rubber cylinder with pores of relaxed diameter 50 μm, which as discussed in Section 1.1, can be used for the production of highly uniform bubble size distributions. The dimensions of this device are shown in Figure 3.2 b). A gas flow rate of 100 cm$^3$ min$^{-1}$ was used for all experiments, which was regulated by an Omega FMA3200ST mass flow controller.

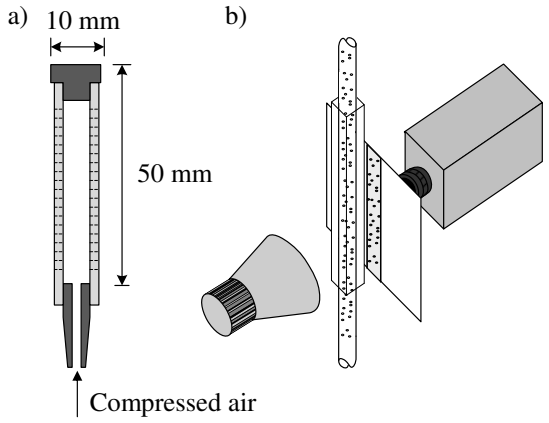


Figure 3.2: a) Dimensions of porous rubber cylinder used for bubble generation in these experiments b) Schematic of experimental setup for measuring shadowgraphs of bubbly flow.

Measurements of bubble size were extracted from shadowgraphs of the column, which maintain a constant focal length for all bubbles by observing projected shadows rather than reflections as in direct photography, and thus are not influenced by the position of a bubble within the column. Additionally, the column was surrounded by a transparent Perspex box, filled with water, which prevented distortion of the bubbles due to the curvature of the column (by ensuring equal and opposite amounts of refraction on both the interior and exterior face of the column walls). A schematic demonstrating this

principle is given in Figure 3.2 b). The shadowgraphs were recorded using a Photron Fastcam SA-1 model 120K-M2 high-speed imaging system. Bubble sizes were measured from the shadowgraphs by thresholding the images at a level sufficient to separate the bubbles from the background, and by fitting ellipses to the segmented bubbles using the procedure of Fitzgibbon [38]. To check for surfactant contamination, surface tension measurements were also performed on both distilled water (as a control) and a magnetic susceptibility matched solution using a pendant drop tensiometer (Krüss DSA100).

### 3.1.2 Results

#### Concentration of paramagnetic dopants

Example images obtained using the magnetic susceptibility difference visualisation sequence are shown in Figure 3.3 for dysprosium chloride solutions of varying concentration. The line of saturated magnetisation is clearly visible in these images, initially bending right, before beginning to straighten at a dysprosium concentration of 15 mM (in accordance with Sains [22]), and bending left at higher paramagnetic concentrations. The direction of this deflection reflects the sign of the magnetic susceptibility difference between the two phases: undoped water has a negative magnetic susceptibility, which is gradually reduced to zero before becoming positive with the addition of the paramagnetic ions. The slice gradient present during the application of the saturation pulse gave rise to a frequency distribution of 298 Hz $cm^{-1}$. A deviation of $1.34 \pm 0.02$ cm from the undeflected line, as present in the undoped sample, is therefore equivalent to a frequency shift of $399 \pm 6$ Hz.

The frequency shift present at the interface is shown as a function of paramagnetic concentration in Figure 3.4 a), while the effect of the dopants on the relaxation times of the solution are shown in b). As expected, dysprosium ions are seen to have a stronger effect upon the magnetic susceptibility than gadolinium, with a magnetic susceptibility matched solution being reached at a concentration of $16.86 \pm 0.02$ mM, compared with $27.70 \pm 0.02$ mM for the gadolinium. The relaxivity (inverse relaxation constant) of both solutions scaled linearly with salt concentration, with gadolinium having a significantly stronger effect than dysprosium. A magnetic susceptibility matched dysprosium chloride solution was chosen for the present experiments because of its favourable relaxation properties for single-shot measurements ($T_1 = 88$ ms, $T_2 = 71$ ms). Gadolinium has a much stronger influence upon the relaxation rates, which renders gadolinium doped solutions more appropriate for use with multi-shot, short readout sequences. A 16.86 mM

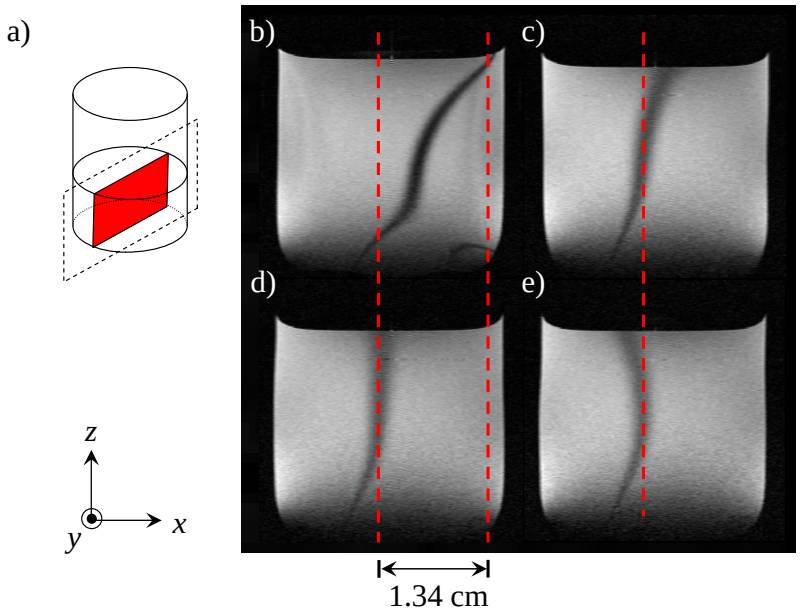


Figure 3.3: Demonstration of magnetic susceptibility matching procedure. a) schematic b) undoped water c) 10 mM $DyCl_3$ d) 15 mM $DyCl_3$ e) 20 mM $DyCl_3$. These images were acquired with a field-of-view of 3.0 cm × 3.0 cm, and a spatial resolution of 117 µm × 117 µm.

dysprosium chloride solution is used for the continuous phase in all further gas-liquid experiments in the present thesis.

The slight difference between the measured air-equivalent paramagnetic concentrations and those given in Table 3.1 is likely due to the theoretical concentrations being calculated using the magnetic susceptibilities for the paramagnetics as a salt, rather than as ions. It is clear, therefore, that this approach is valid only for an approximation. Using equation (3.3) and the experimental values for magnetic susceptibility matched solutions, it is possible to calculate magnetic susceptibilities specifically for the paramagnetic ions. These values are given in Table 3.2. By comparison of these values with Table 3.1, it is clear that the approximated magnetic susceptibilities contained errors in the range 5-10%.

### Influence of dopants on bubbly flow

As discussed in Section 1.2, it is well known that the inclusion of even millimolar concentrations of a salt in the continuous phase can lead to the formation of smaller bubbles, retard bubble coalescence, and thus lead to higher gas-fractions. This behaviour would be beneficial for the present study, which seeks to apply MRI to bubbly flow across a broad

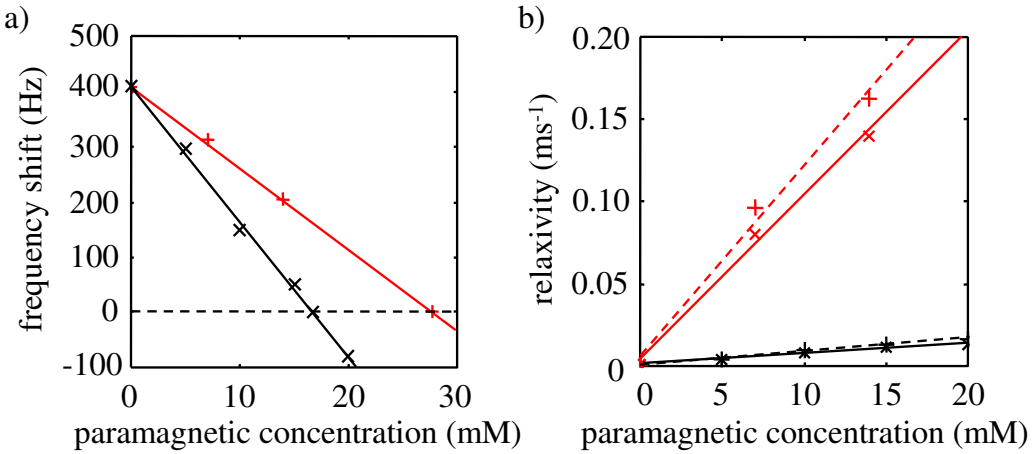


Figure 3.4: Effect of dysprosium chloride (black) and gadolinium chloride (red) on a) frequency shift at an air-water interface due to magnetic susceptibility difference, and b) relaxation properties of the solution. In b), the solid lines correspond to $1/T_1$ while the dotted lines represent $1/T_2$.

Table 3.2: Experimentally measured paramagnetic concentration required for a solution magnetic susceptibility matched to air, and volume magnetic susceptibilities calculated from the experimentally measured concentrations. Note that the experimental concentration for holmium was taken from the literature [32].

| Paramagnetic ion | Concentration (mM) | $\chi_v$ |
|---|---|---|
| $Dy^{3+}$ | $16.86 \pm 0.02$ | $30.74 \times 10^{-3} \pm 0.04 \times 10^{-3}$ |
| $Ho^{3+}$ | $16.60 \pm 0.10$ | $31.23 \times 10^{-3} \pm 0.20 \times 10^{-3}$ |
| $Gd^{3+}$ | $27.70 \pm 0.02$ | $18.71 \times 10^{-3} \pm 0.04 \times 10^{-3}$ |

range of voidages. To check whether the paramagnetic salt has the desired effect, bubble size shadowgrams were obtained of low voidage ($\varepsilon \approx 3.5\%$) bubbly flow for the same solution before and after the addition of dysprosium chloride. Example shadowgrams for each case are shown with the fitted ellipses in Figure 3.5.

From these images it is immediately apparent that the addition of the dopant has strongly affected the produced bubble sizes. Further, qualitative observations were made regarding the maximum voidage for which bubbly flow could be maintained for each system. Whereas the pure system became unstable at a voidage of approximately 18% (estimated from the height difference between the aerated and non-aerated systems), following the addition of paramagnetic stable bubbly flow could be maintained up to a voidage of 40%. To quantify the change caused by the addition of the dopant, bubble size distributions were extracted from approximately 300 bubbles characterised by the shadowgram data. A comparison of the two size distributions is shown in Figure 3.6. Note that fore-aft

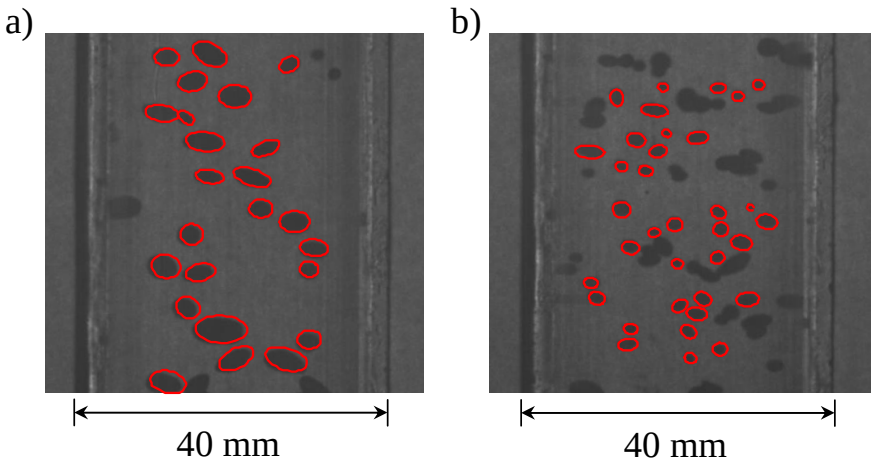


Figure 3.5: Example shadowgrams acquired of low voidage ($\varepsilon \approx 3.5\%$) bubbly flow in a) distilled water and b) 16.86 mM dysprosium chloride solution. Ellipses fitted to the bubbles are shown in red. Note that where uncertainty existed due to overlapping bubbles no shape was fitted.

symmetry of the bubbles has been assumed for the calculation of spherically equivalent bubble radii.

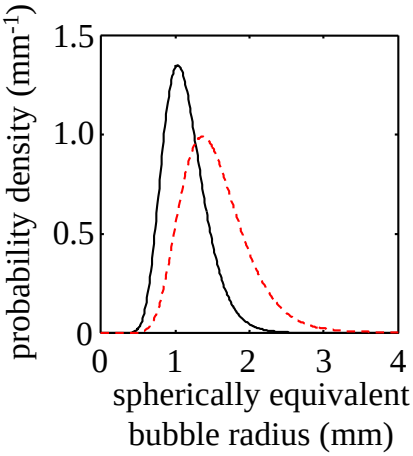


Figure 3.6: Bubble size distributions measured for pure water (red dotted line) and 16.86 mM dysprosium chloride solution (black solid line). The influence of the dopant on the structure of the bubbly flow system is evident.

As observed qualitatively, it is clear that the salt substantially decreases the mean bubble size while narrowing the distribution. These observations are in accord with those made in the literature [36, 39, 40, 41]. The surface tension of a 16.86 mM dysprosium chloride solution was also measured, and found to be $73.2 \pm 0.4$ N m$^{-1}$, as opposed to $74.2 \pm 0.4$ N m$^{-1}$ for pure water. This minor change to the surface tension was as expected from the literature. It appears, then, that the paramagnetic dopants used in the present

study behave congruously with the electrolytes previously described, and may be used for the triple purpose of magnetic susceptibility matching, reducing relaxation times and stabilising bubbly at higher voidages.

## 3.2 MRI of bubbly flow

If bubbly flow is to be successfully imaged using ultrafast MRI it is critical that a workable balance be struck between spatial and temporal resolution. The required spatial resolution is determined by the size of the smallest feature in the image that needs to be resolved. In the present work we will consider only bubbles in the size range $d_e > 0.5$ mm. Due to the fold-over artefact intrinsic to MRI (discussed in Section 2.2.1), the field-of-view of an image is fixed by the diameter of the column under observation, which in the present work is limited to a maximum of 35 mm by the bore size of our magnet. This implies that a minimum 64 pixel $\times$ 64 pixel image is necessary for the resolution of individual bubbles. At a spectral width of 200 kHz, FLASH is capable of producing an image with these dimensions in approximately 65 ms, as opposed to 125 ms for RARE and 28 ms for EPI. The fundamental difference between these techniques is that FLASH samples **k**-space using multiple excitations with short read-out sequences, while RARE acquires all of **k**-space following a single excitation using a combination of spin echoes and gradient echoes. EPI is also a single-shot technique, however it samples **k**-space using solely gradient echoes. While these differences render FLASH and RARE much more robust to off-resonance effects than EPI, as a solution magnetic susceptibility matched to air has already been chosen as the continuous phase for this study, off-resonance artefacts are not anticipated to be problematic in the present experiments. In this section preliminary images of bubbly flow acquired using the FLASH, RARE and EPI pulse sequences are examined. As discussed in Section 1.4, no previous application of ultra-fast MRI to bubbly flow exists in the literature.

### 3.2.1 Experimental

The present experiments were carried out in a Perspex column 2 m in length, and of internal diameter 31 mm. This column was erected inside a vertical bore NMR spectrometer, with the imaging region located 50 cm from the bubble sparger. A 16.86 mM dysprosium chloride solution (i.e. magnetic susceptibility matched to air) was used for the continuous phase. Bubbles were generated by sparging air through a porous foam-rubber frit (of the geometry shown in Figure 3.2 a)). This sparger was selected with the goal of producing highly uniform bubble size distributions, which can enable stable bubble flow to be

maintained for very high voidages [42, 43]. The gas flow rate was regulated by an Omega FMA3200ST mass flow controller up to 1 L $min^{-1}$, and a rotameter and needle valve for higher flow rates. In the first instance, however, only gas flow rates up to 200 $cm^3$ $min^{-1}$ are considered. The voidage for each flow rate was determined from the magnitude of the first point sampled in a pulse-acquire experiment (i.e. the total signal) of the bubbly flow system relative to a single-phase system. A flow loop was connected to the top of the column such that a constant liquid height could be maintained, with overflow liquid transported to a reservoir. A schematic of the flow loop is shown in Figure 3.7 b).

FLASH, RARE and EPI images of a 1 mm thick slice of fluid were obtained at a spectral width of 200 kHz. The slice selective and spoiler gradients used for these sequences were velocity compensated, as discussed in Section 2.3.2. The acquisition time for the images was 65 ms for FLASH, 128 ms for RARE and 28 ms for EPI. All slice selective pulses were Gaussian in shape and 512 μs in duration. For all images, the field of view was 3.5 cm × 3.5 cm, with a spatial resolution of 540 μm × 540 μm. A Bruker AV-400 ultrashield spectrometer operating at a $^1$H resonance frequency of 400.25 MHz was used. This apparatus is fitted with a 3-axis gradient system capable of a maximum magnetic field strength of 30.6 G $cm^{-1}$. A 38 mm diameter birdcage coil was used for r.f. excitation and signal detection.

### 3.2.2 Results

In the first instance, FLASH, RARE and EPI were applied to low voidage bubbly flow ($\varepsilon < 1\%$) in order to explore the balance between the temporal resolution of each technique, and the timescales of motion of a bubbly flow system. Example images obtained with each of the three techniques are shown in Figure 3.8.

From these images it is immediately apparent that the three different imaging protocols produced highly dissimilar depictions of bubbly flow. Firstly, no bubbles are visible at all in the FLASH image. This reflects that slice selection is averaged over the entire acquisition period in FLASH, and that the bubbles have risen a significant distance during the acquisition period (1.28 cm assuming a bubble rise velocity of 20 cm $s^{-1}$), leading to temporally averaged images with no bubbles evident. This temporal averaging effect has also manifested in the RARE image, although in a slightly different way. While RARE is a single-shot technique, the refocusing pulses used for each line of **k**-space are slice selective. Thus, excited fluid which has moved out of the imaging plane will not be refocused, giving rise to the dark swirls where unexcited fluid has been mixed through

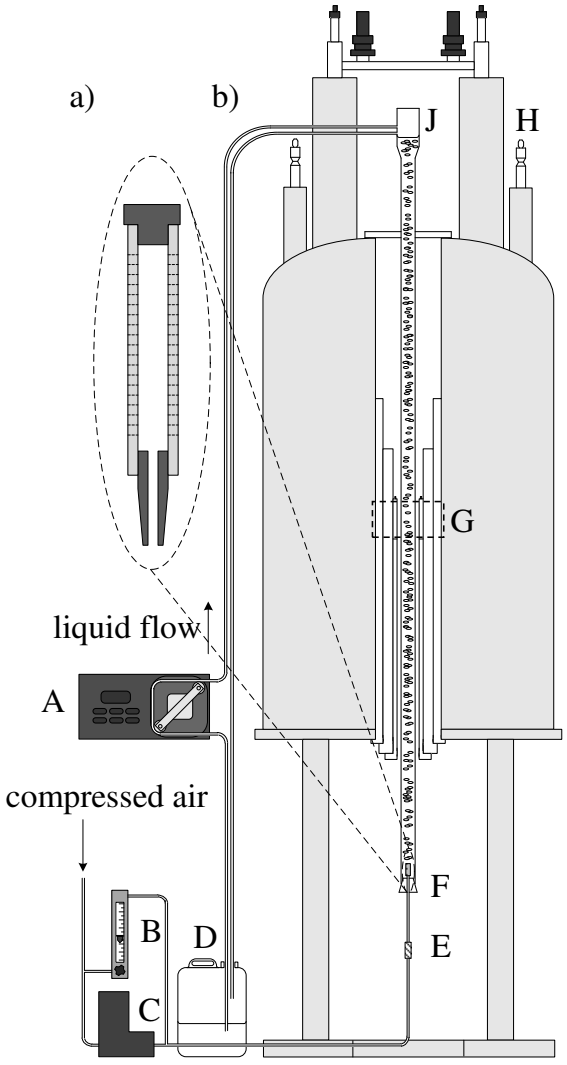


Figure 3.7: a) detail of bubble sparger employed in the present study b) Schematic of the experimental setup. A. Peristaltic pump. B. Rotameter and needle valve, C. Mass flow controller. D. Liquid reserviour. E. Non-return valve. F. Sparger G. Imaging region. H. MRI spectrometer. J. Column overflow vessel.

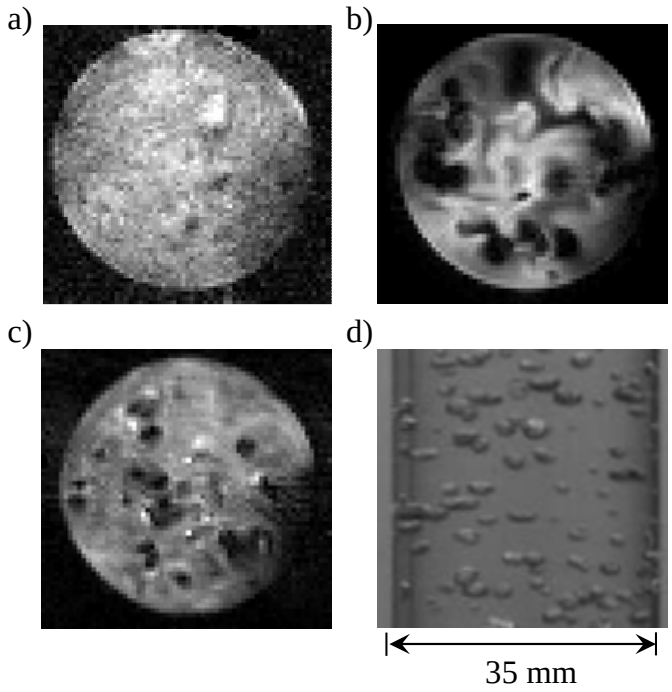


Figure 3.8: First instance horizontal plane MRI images acquired of low voidage ($\varepsilon \approx 0.6\%$) bubbly flow using a) FLASH b) RARE and c) EPI. The field of view of these images is 3.5 cm $\times$ 3.5 cm, with a spatial resolution of 540 μm $\times$ 540 μm, and acquired at a spectral width of 200 kHz. The acquisition time was 64 ms for FLASH, 125 ms for the RARE and 28 ms for the EPI. The signal attenuation at the lower right corner of each image is associated with $B_1$ heterogeneity. A photograph of the column is shown in d) for comparison.

the imaging plane. The signal modulation across the whole image likely reflects bulk convection, where fluid has been displaced downward at the column walls and partially removed from the imaging plane. While temporal averaging associated with slice selection can be marginalised by use of a thicker slice, bubble transverse plane motions over the acquisition period of both FLASH and RARE will remain significant, leading to spatial blurring. Further, as the projection volume is increased so does the likelihood of bubble overlap occurring. The EPI image appears rather more promising, with bubble boundaries clearly visible. This image, too, is affected by artefacts, however, with local bright spots and signal attenuation present. These artefacts indicate that some erroneous phase accrual has occurred during the imaging sequence, leading to localised signal misregistration.

It is clear from Figure 3.8, that little prospect exists for successfully imaging bubble flow using either FLASH or RARE. On the other hand, while EPI still bears some artefacts, it exhibits a temporal resolution sufficient for the identification of individual bubbles, and

so remains a possibility. EPI images have been obtained of bubbly flow up to a voidage of 3.5%, as shown in Figure 3.9. Photographs are shown of the same system for comparison.

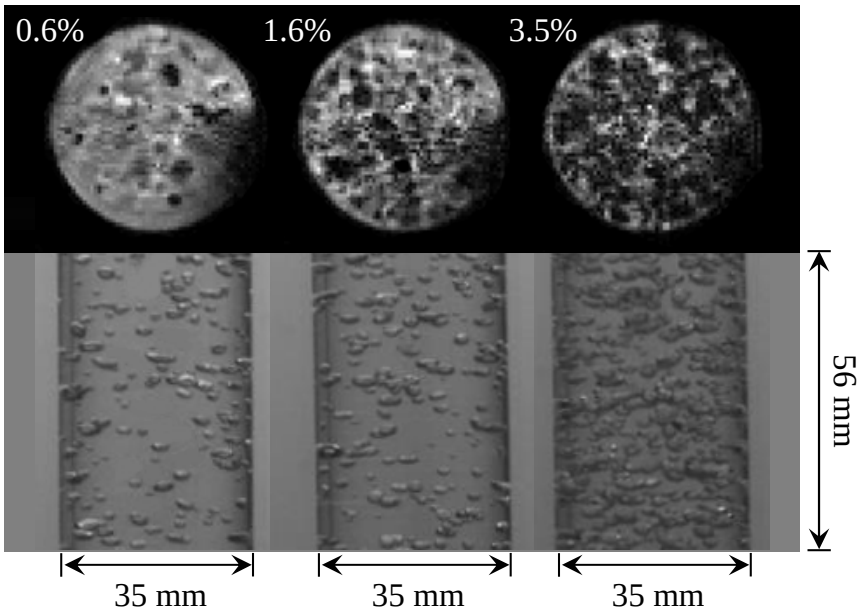


Figure 3.9: Example images of bubble flow at three voidages obtained using EPI. Large amounts of signal attenuation are evident at all but the lowest voidage. The field of view of the MRI images is 3.5 cm × 3.5 cm, with a spatial resolution of 540 μm × 540 μm, and an acquisition time of 28 ms.

It is evident in Figure 3.9 that the local signal attenuation effect observed in Figure 3.8 increases with increasing voidage, until individual bubbles can no longer be resolved for a system of gas-fraction 3.5%. It is well known that heavy fluid mixing in the presence of a magnetic field gradient (either due to $B_0$ inhomogenity [44] or imaging gradients [45]) leads to localised signal attenuation, and it is likely this effect which emerges in application of EPI to bubbly flow. The effect of shear on EPI images was examined by Gatenby and Gore [46, 18], who used the shear-attenuation effect to study single-phase turbulent flow. They explain that as EPI traverses one dimension in **k**-space in a unidirectional manner, significant first moment phase is accrued by the time the centre of **k**-space is reached. For high-shear systems, in which highly dissimilar velocities exist in close proximity to each other, this leads to spin isochromats with very different phases being close together. In heavily mixed systems, these isochromats will be dispersed and the net signal for each voxel will decrease as phases add destructively. It is thus possible to see that the artefact demonstrated in Figure 3.9 is intrinsic to EPI.

In addition to this phase dispersion effect, the first moment phase accrued during EPI imaging also undermines the quantitative nature of EPI-based phase-contrast velocity measurements when applied to low-shear, non-steady state systems. This occurs as the first moment imaging phase cannot be quantified and removed for these systems, and thus acts as a significant potential source of error. Nevertheless, EPI still holds several advantages as the basis for a velocity measurement technique for these systems. In particular, as EPI avoids the use of spin-echos quadrature is preserved throughout the imaging sequence. If the accrual of first moment phase during imaging could be quantified and removed from the velocity-encoded phase, EPI would provide a promising basis for velocity measurements on unsteady systems. The development of an EPI velocity measurement technique which addresses this problem is discussed in Section 3.3.

For the successful imaging of bubbly flow, it is necessary to consider alternate **k**-space sampling trajectories that minimise the accrual of first moment phase during imaging. This subject is considered in Chapter 4.

## 3.3 Single-shot velocity imaging using EPI

As discussed above, it is well known that blipped-EPI accrues a significant amount of velocity proportionate phase during imaging [46]. For application to fast flows, this can introduce significant image artefacts, and undermines the quantitative nature of phase-contrast velocimetry. For application to steady state flow systems, the latter problem can be overcome by acquisition of two images; each with a different degree of velocity encoding such that the velocity proportionate phase shift may be isolated for a specific pixel within the spatial image. This method fails, however, for systems in which no stationary or periodic geometry exists, or when examining a system with an unsteady flow as the reference and velocity encoded images will not be exposed to the same velocity field. This is a particular problem for velocity imaging of multiphase flows, where the dynamic system geometry and chaotic nature of the flow prevents the acquisition of accurate phase reference data. While it has been demonstrated in Section 3.2 that EPI is fundamentally unsuitable for application to bubbly flow, for other unsteady flow systems which are not so heavily mixed, EPI may yet provide a suitable basis for a velocity measurement technique.

EPI velocimetry was originally implemented by Firmin *et al.* [47], who measured a single velocity component perpendicular to the imaging plane. These measurements were further explored by Kose [15, 16], who applied the technique to the visualisation of turbulent

flow in a pipe. In his subsequent work, Kose [17] acquired two perpendicular velocity components from a single excitation to yield a 2D velocity map of turbulent flow. More recently, Sederman *et al.* [19] extended the later work of Kose to the acquisition of 2D velocity maps containing 3-component velocity vectors and named the sequence GERVAIS (Gradient Echo Rapid Velocity and Acceleration Imaging Sequence). As discussed in Section 2.4.4, their approach was to acquire 3 velocity encoded images from a single excitation using a spin-echo to refocus the remaining magnetisation prior to each imaging sequence. The velocity proportionate phase shift was isolated by comparison with a previously acquired zero-flow reference phase map. In the present section, we seek to extend GERVAIS to include the acquisition of the phase reference maps and velocity encoded images from the same excitation. In this way, both phase reference and velocity encoded data are exposed to similar velocity fields, allowing first moment phase accrued during imaging to be removed. As an instantaneous measurement of the velocity field of a system with changing geometry can be acquired, this pulse sequence is referred to as snap-shot GERVAIS (ssG).

### 3.3.1 Theoretical

The pulse sequence for ssG is shown in Figure 3.10. Five images (acquired from a single excitation) are required for the generation of a 3-component velocity map. These are composed of two velocity unencoded images followed by those encoded in $z$, $x$ and $y$ directions. Both unencoded images are required as the phase of the spins is inverted following each 180° pulse, which introduces an asymmetry into the accumulated phase data between odd and even echo trains (i.e. the relative phases of the $2^{\text{nd}}$ and $4^{\text{th}}$ images are shifted from those of the $1^{\text{st}}$, $3^{\text{rd}}$ and $5^{\text{th}}$ images). The two velocity unencoded images provide all the information required to isolate the phase-shift due to velocity encoding in the subsequent images. In this section we show the acquisition of 3 successive images to produce a 3-component velocity vector, though the acquisition is not restricted to three images, and multiple images may be acquired for either a single or multiple components.

ssG is fundamentally similar to GERVAIS; using a train of EPI imaging sequences preceded by a velocity encoding module (where appropriate) and separated by 180° refocusing pulses. GERVAIS acquisitions are, however, dependent upon the velocity encoding gradients (absent in the first two scans in ssG) to spoil residual transverse magnetisation remaining from the 180° pulse. To counter this, a flow compensated homospoil is included in ssG in the slice direction around each 180° pulse, simultaneous to the velocity gradients, to ensure that no coherent magnetisation is present at the start of each

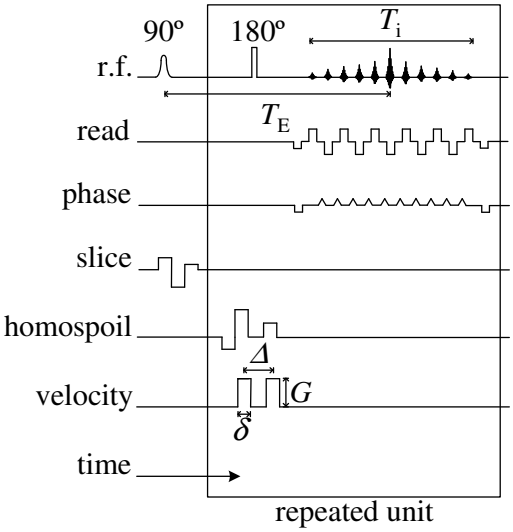


Figure 3.10: Snap-shot GERVAIS pulse sequence. $T_E = 24.8$ ms, $T_i = 18.9$ ms, $\delta = 1.08$ ms, $\Delta = 2.35$ ms, $G = 0$ in first two scans, and set to maximise phase shift within a $2\pi$ window for each scan thereafter. $G$ is typically applied in 3 orthogonal directions in the $3^{rd}$, $4^{th}$ and $5^{th}$ images.

subsequent scan. The ratio of the amplitudes of lobes of this spoiler (-1:3:2 sequentially) was set such that the first moment of the gradient wave form was zero, as described in Section 2.2.3.

The velocity dependent phase shift may be isolated from phase information used in imaging by considering the phase accumulation as the sequence progresses, whilst remembering that the existing phase is inverted following every 180° pulse. For example, if we assume the phase accrued due to the imaging sequence is identical for odd and even groups of spin-echoes, and apply gradients in the $z$, $x$ and $y$ directions for the $3^{rd}$, $4^{th}$ and $5^{th}$ images, respectively:

$$\phi_1 = \phi_{\text{odd}}$$
$$\phi_2 = \phi_{\text{even}}$$
$$\phi_3 = \phi_{\text{z}} + \phi_{\text{odd}}$$
$$\phi_4 = \phi_{\text{x}} - \phi_{\text{z}} + \phi_{\text{even}}$$
$$\phi_5 = \phi_{\text{y}} - \phi_{\text{x}} + \phi_{\text{z}} + \phi_{\text{odd}}$$

where $\phi_n$ ($n = 1-5$ for the acquisition of 3-component velocity vectors) is the cumulative phase shift of the $n^{th}$ image, $\phi_{odd}$ and $\phi_{even}$ are the phases imparted during acquisition of odd and even images, respectively, and $\phi_{x,y,z}$ is the velocity dependent phase shift. That

is:

$$\phi_{\mathrm{z}} = \phi_3 - \phi_1$$
$$\phi_{\mathrm{x}} = \phi_4 + \phi_3 - \phi_2 - \phi_1$$
$$\phi_{\mathrm{y}} = \phi_5 + \phi_4 - \phi_2 - \phi_1.$$

With the velocity dependent phase shifts isolated as above, the linear velocity in each direction is given by equation (2.32), which is restated here:

$$v_{\mathrm{i}} = \frac{\phi_{\mathrm{i}}}{G_{\mathrm{i}}\gamma\delta\Delta} \tag{3.4}$$

where $i$ represents the examined direction ($x$, $y$ or $z$).

### 3.3.2 Experimental

The technique was first applied to a stagnant water phantom, 26 mm in diameter, to verify that no unquantifiable phase shift was occurring for a static (excepting diffusion) system. In order to demonstrate that quantitative velocity measurements are being obtained in the axial direction, ssG was then applied to the measurement of fully-developed laminar flow in a 2 m long, 10 mm diameter Perspex tube. The Reynolds number in these experiments was 300 (corresponding to a mean fluid velocity of 3 cm $s^{-1}$). To ensure the results produced are quantitative in the transverse plane, ssG was also applied to flow in a 19 mm inner diameter, 26 mm outer diameter polyetheretherketone (PEEK) Couette cell rotating at 36 rpm (equivalent to a fluid velocity at the inner wall of 0.57 cm $s^{-1}$ assuming a no-slip boundary condition). To demonstrate the applicability of the present technique to dynamic systems, MRI velocity images were acquired of flow around a PEEK impeller in a 26 mm diameter mixing cell. Triggered velocity encoded spin-warp (i.e. time averaged measurements) and standard GERVAIS images were also acquired of this system for comparison. Finally, velocity images were acquired of approximately 10 mm diameter droplets of decane rising through stagnant distilled water in a 12 mm diameter column. These experiments included an additional water-suppressive 1.9 ms Gaussian soft pulse offset by a frequency of 2.8 ppm relative to the oil resonance as a precursor to the sequence shown in Figure 3.10. Droplets were injected using a syringe pump (Harvard Apparatus 22) connected to a 5 mm diameter glass pipette. The shape oscillations of these droplets were recorded outside of the magnet by highspeed photography using a Photron SA-3 imaging system operating at 2000 frames per second.

The acquisition parameters for each of the experiments described above are summarised in Table 1. The experiments on the static tube of water, Couette cell and impeller systems were performed on a Bruker DMX-200 super wide-bore spectrometer operating at a $^1$H frequency of 199.7 MHz, and using a 13.9 G cm$^{-1}$ 3-axis shielded gradient system and 64 mm diameter birdcage coil. The laminar flow and oil droplet experiments were carried out on a Bruker AV-400 spectrometer, operating at a $^1$H frequency of 400.25 MHz. A 25 mm diameter birdcage coil was used to transmit and receive r.f. and a 146 G cm$^{-1}$ 3-axis shielded gradient system was employed for spatial resolution and velocity encoding. For all experiments the flow encoding time ($\delta$) was 1.08 ms and the flow contrast time ($\Delta$) was 2.35 ms. The key timings for ssG, as shown in Figure 1, were as follows: echo time ($T_{\mathrm{E}}$) of 24.8 ms and imaging time ($T_{\mathrm{i}}$) of 18.9 ms, leading to a total acquisition time of approximately 125 ms for acquisition of the 5 images necessary to characterise a 3D velocity vector map.

Table 3.3: Experimental details

| Experiment | Spectral width (kHz) | Field of view (mm) | Resolution (μm) | Velocity encoding gradient strength (T m$^{-1}$) |
|---|---|---|---|---|
| Static phantom | 175 | 30 × 30 | 469 × 938 | 0.0695 |
| Poiseuille flow | 200 | 15 × 15 | 234 × 469 | 0.2920 |
| Couette Flow | 175 | 30 × 30 | 469 × 938 | 0.0556 |
| Mixing Cell | 175 | 30 × 30 | 469 × 938 | 0.0556 |
| Rising oil drop | 500 | 15 × 15 | 117 × 234 | 0.2920 |

In the application of ssG it must be kept in mind that as it is a technique based upon EPI a homogeneous $B_0$ field is a necessity. In the observation of multiphase systems, disparity in magnetic susceptibility can be a significant source of $B_0$ heterogeneity that is difficult to counter by shimming due to the dynamic nature of the system geometry. This was not greatly problematic in the present experiments as both PEEK and decane have a magnetic susceptibility similar to that of water.

### 3.3.3 Results and discussion

As a control experiment, ssG was applied to a reference sample consisting of a 30 mm diameter tube of stagnant water. Despite the absence of flow, substantial zero and first order phase shifts were present in the velocity encoded images, as shown in Figure 3.11. The magnitude of these phase shifts was noted to be proportional to the strength of the magnetic field gradients used for velocity encoding, which indicates that eddy currents generated by these gradients are responsible. This observation highlights the principle

weakness of ssG: by obtaining phase reference data without velocity encoding present, eddy currents induced by the velocity encoding gradients remain unaccounted for. This is in direct contrast to GERVAIS, where the phase reference data are acquired from scans exposed to identical magnetic field gradients as those experienced by the velocity encoded scans. This artefact may be corrected by including stationary fluid around the region of interest to act as a reference zone fluid by which phase shift due to eddy currents can be quantified and eliminated. For example, by attaching NMR tubes of the fluid under observation to the outside of the examined cell, an eddy-induced phase map was generated and subtracted from the region of interest, as demonstrated in Figure 3.11. As it is evident that the eddy-induced phase shifts vary linearly across a sample, a phase correction map was created by linear interpolation between each of the stationary phase reference points. In this case, a minimum of three phase reference points are required to generate a phase-correction plane, however four were included to ensure that a linear phase correction map was sufficient to entirely correct the artefact. It is convenient to note that for a cylindrical sample, these reference points may be placed in the 'corners' of the imaging region, such as to not impose upon the minimum achievable field-of-view. It is likely that the application of this procedure will only be necessary for examination of low flow-rates where large velocity encoding gradients are required. It is clear from Figure 3.11 that the proposed scheme was successful in correcting the artefact, with a final mean deviation from the expected phase shift of zero of less than 1.5% in all images. The correction process was similarly successful when applied to images velocity encoded in $x$ and $y$ directions.

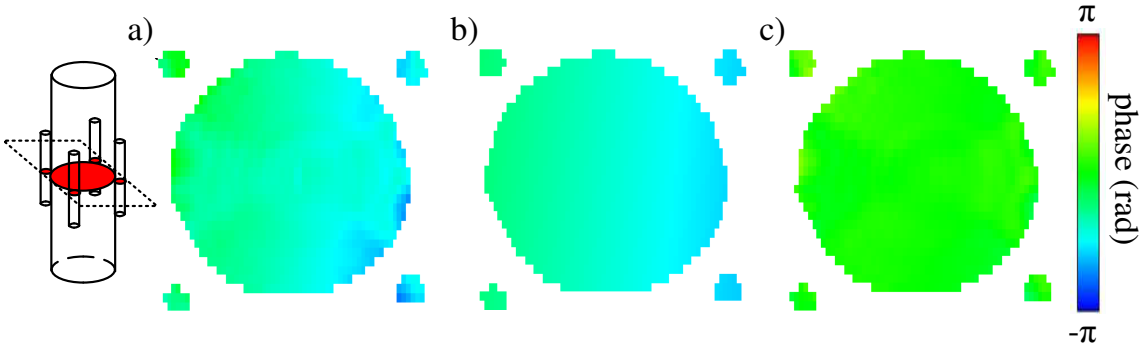


Figure 3.11: a) Effect of eddy-current induced phase shift upon a stagnant water phantom for $G_z = 0.56$ T m$^{-1}$. b) phase correction plane generated from stationary phase reference points. c) corrected image. The field of view in these images is 30 mm $\times$ 30 mm with a resolution of 469 µm $\times$ 938 µm.

**Validation against fluid mechanics for simple systems**

In order to demonstrate that quantitative velocity information is being produced from ssG it was applied to the measurement of laminar flow in a pipe and tangential flow in a Couette cell. Solutions to the Navier-Stokes equations may be readily obtained for laminar flow in a pipe and Couette flow of a Newtonian fluid. For laminar pipe flow there ought to be no transverse plane velocity component, and the axial flow profile will be described by the Hagen-Poiseuille equation. That is, a parabolic velocity profile must be present as described by:

$$v_{\mathrm{r}} = v_{\max}\left(1 - \frac{r^2}{a^2}\right) \tag{3.5}$$

where $v_{max}$ is the maximum velocity in the pipe (twice the average velocity in the pipe, which can be estimated volumetrically), $r$ is radial position and $a$ is the radius of the pipe. For flow in a Couette cell with a stationary outer wall and a marker fluid in the inner cylinder, the tangential velocity profile in the cell is given by:

$$v_\theta = \omega r \qquad 0 < r < R_1 \tag{3.6}$$

$$v_\theta = \frac{\omega R_1^2}{r}\frac{(R_2^2 - r^2)}{R_2^2 - R_1^2} \qquad R_1 \leq r < R_2 \tag{3.7}$$

where $\omega$ is the frequency of rotation of the inner cylinder and $R_1$ and $R_2$ are the inner and outer radii of the cell geometry.

Figure 3.12 shows a comparison of flow profiles for laminar and Couette flow with the theory. It is evident from this comparison that very good agreement exists between the new experimental technique and the theory, with the non-zero wall velocities likely due to partial volume effects. As expected, no velocity component was apparent in the transverse plane for laminar flow. The Couette flow profile also behaved as expected, with rotationally symmetrical flow patterns being produced. The higher noise level present in the Couette cell profile relative to the laminar flow data is most likely due to the increased $T_2$ weighting of the later images acquired in the series. The eddy-phase effect, described above, was present in the Couette cell images, which necessitated the use of phase reference points. The eddy-phase effect was not apparent for the laminar flow image due to the higher coherent flow velocities present in this system permitting the use of weaker velocity gradients. This suggests that the eddy-phase artefact may be reduced by increasing the velocity encoding ($\delta$) and observation ($\Delta$) times, while keeping

$\delta\Delta G$ constant, within the constraints imposed by the relaxation of the magnetisation and the time scales of the fluid phenomena under observation. The mean error (relative to the analytical result) for the laminar flow experiments was 3.5% and 5.6% for the Couette cell profile: both within the 5-10% accuracy range of EPI velocimetry previously established [48].

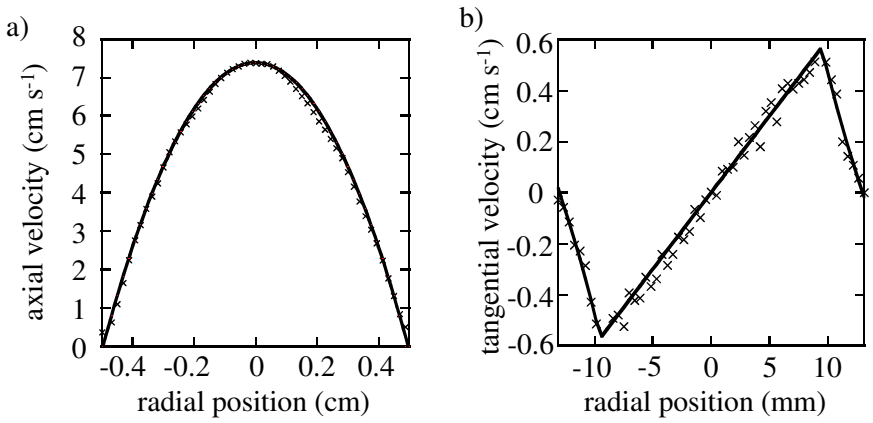


Figure 3.12: Comparison of measurements obtained using ssG (×) with fluid dynamics theory (line) for a) laminar flow in a 1 cm diameter pipe and b) laminar flow in a Couette cell with marker fluid where $R_1 = 9$ mm, $R_2 = 15$ mm.

### Velocity imaging of a mixing cell with impeller

The principle advantage of ssG is its ability to rapidly capture velocity fields in situations where acquiring a separate reference phase map is impractical or impossible. For example, attempting to visualise the velocity field in a stirred cell is difficult due to the moving geometry of the system associated with the rotating impeller. Moser *et al.* [5] demonstrated that it is possible to acquire velocity encoded images for a given impeller position by synchronising the acquisition with the impeller rotation. This approach, however, requires a perfectly periodic system and may not always be practical to implement. It is substantially more straightforward to image this system using a snap-shot technique.

To illustrate this point, ssG images were acquired of a 3 cm diameter mixing cell, stirred by an impeller rotating at 36 rpm. For the removal of the eddy-phase artefact, four NMR tubes filled with water were attached to the outside of the vessel. Additionally, optically triggered velocity encoded single spin-echo and GERVAIS images were acquired to demonstrate that the new technique is consistent with conventional MRI velocimetry. A comparison between three images acquired in this manner is provided in Figure 3.13. From comparison of these images it is evident that the snap-shot technique has suc-

cessfully captured all the major features of the flow field around the impeller. In the longitudinal direction, fluid is observed to flow down between the impeller blades and circulate back up at the sides of the vessel. In the transverse plane, the fluid between the blades flows at a speed approximately equivalent to that of the impeller rotation while dropping off to zero at the vessel walls. Like the GERVAIS image, ssG highlights the somewhat asymmetrical nature of the flow in the cell. This is likely to be a temporally local effect as this feature is not apparent in the time averaged, triggered spin-echo velocity image. As expected, ssG is somewhat noisier than the other two techniques, which is largely due to the increased $T_2$-weighting of the sequence.

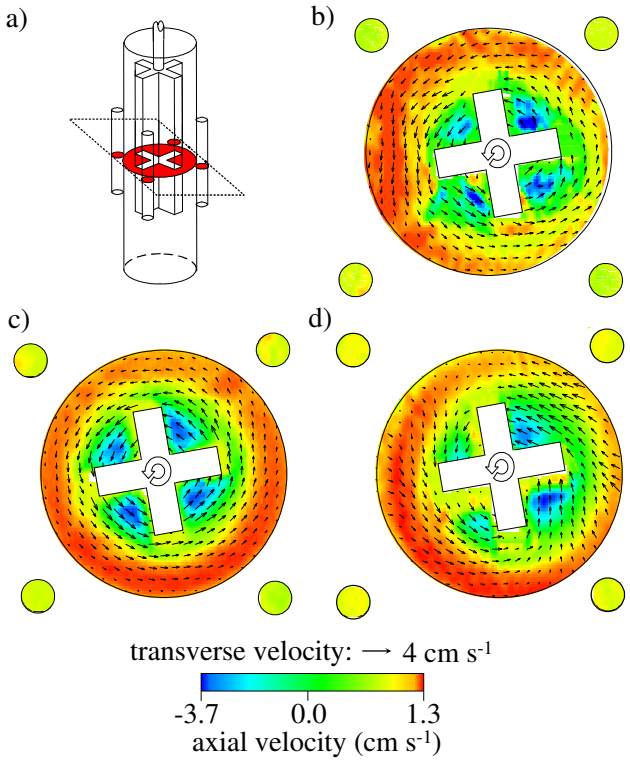


Figure 3.13: Comparison of velocity images for an impeller rotating at 36 rpm in a mixing cell with stationary phase-reference points included showing a) a schematic of the system, b) velocity image acquired with ssG, c) a triggered velocity-encoded single spin-echo acquisition and d) a triggered standard GERVAIS image of the same system. Note that only every second velocity vector in the transverse plane has been shown here for the sake of clarity. A 1 mm thick slice was used. The field of view in these images is 30 mm $\times$ 30 mm with a resolution of 469 $\mu$m $\times$ 938 $\mu$m.

### Flow field within a rising oil drop

Rapidly changing systems which do not exhibit such convenient periodicity as a stirred tank become effectively impossible to obtain velocity images for using conventional MRI

velocimetry. Here we consider an oil-droplet rising through a column of water under its own buoyancy. Characterising the internal flow field of such a droplet is of great interest in the design of liquid-liquid mass transfer units, as is evidenced by the observation that the analytical solution of Kronig and Brink [49] for Stokes-type recirculation within a droplet is known to greatly underestimate the rate of droplet-side mass transfer. Amar *et al.* [50] have recently presented MRI velocity measurements on the internal flow vortices of an oil-drop held static in a contraction against a downward flow. These measurements are, however, limited to a flow-rate such that buoyancy and drag forces acting on the droplet are balanced. Further, large, deformed droplets (Re > 100) undergo shape oscillations and path deviations as they rise (known as secondary motion [51]), which are also neglected in observations of a static droplet. The application of ssG allows the velocity field within a mobile and dynamic oil droplet to be observed by MRI for the first time. Figure 3.14 shows example images of this type for approximately 10 mm cross-sectional diameter droplets of decane as they rise through stagnant distilled water.

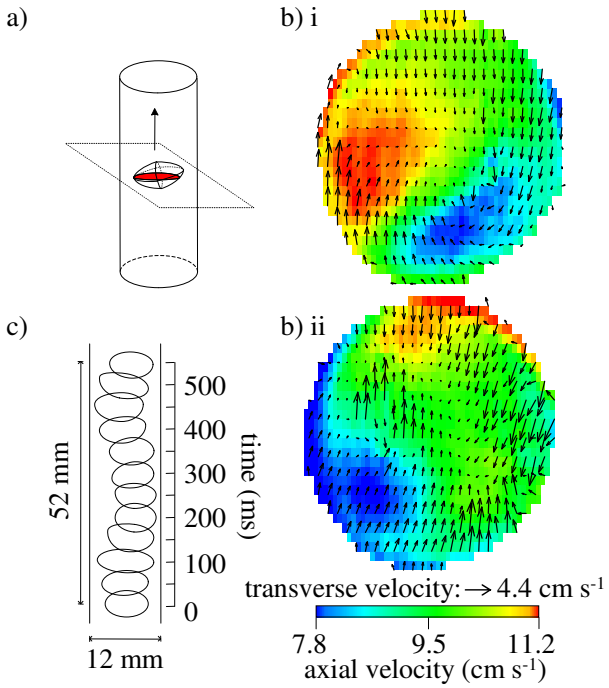


Figure 3.14: a) Schematic of system highlighting the plane being imaged. b) ssG images of the internal flow field of two droplets (i and ii) of decane captured as the drops rose through a column of distilled water. Note that the signal from the water in these images has been suppressed. c) Droplet shape contours extracted from highspeed photography. The field of view in these images is 15 mm × 15 mm with a resolution of 117 µm × 234 µm.

Whilst some element of the expected rotational flow is present, the flow-field inside the droplet is asymmetrical. It is important to note here that the droplets were undergoing

significant shape deformation and path instability, as captured by highspeed photography with the column removed from the magnet. Shape contours extracted from these photographs are shown in Figure 3.14 c). The velocity images imply an intimate coupling between the internal flow field of the droplet and its secondary motion, and suggest that the shape oscillations of a rising drop may be the dominant factor in determining the internal velocity field. The net axial velocity of the droplet measured from the velocity images in Figure 3.14 is $9.48 \pm 0.03$ cm s$^{-1}$. This is in excellent agreement with the droplet rise velocity extracted from the highspeed photography data, of $9.45 \pm 0.01$ cm s$^{-1}$. This rise rate is equivalent to a shift of 1.2 cm over the course of the acquisition period. Spatial averaging over this length is, however, minimised as the data produced by ssG are effectively Lagrangian (i.e. only spins disturbed from equilibrium in the original slice-selective excitation emit a signal for the duration of the pulse-sequence, irrespective of where in the r.f. coil they are transported to).

ssG somewhat overcomes the problem of first moment accrual during imaging, which has previously limited the usefulness of EPI based velocity measurements in application to unsteady flow systems. ssG achieves this by acquiring both phase reference and velocity encoded images in close succession. By acquiring phase reference data in the presence of similar fluid velocities to those present in the velocity encoded scans, the velocity encoding associated with the imaging phase gradient is removed when the imaging phase is subtracted. Thus, ssG reduces the consequences of applying a non-velocity compensated imaging sequence to a flowing system, thereby enabling the measurement of higher transient velocities than those previously attainable. This problem could be alternatively addressed by velocity compensating each phase blip, which substantially increases imaging time, or by limiting the application of EPI and EPI-based velocimetric techniques to systems exhibiting relatively low velocities in the phase direction.

Examples of other dynamic systems which may now be examined by fast MRI velocimetry include: droplet formation, break-up and coalescence; and unsteady climbing flows and falling films. In applications beyond those in the physical sciences, EPI velocimetry has been employed in breath-hold and synchronised acquisitions for the study of blood flow in the human body [47]. The present technique, however, may be able to broaden the scope of such studies; allowing for patient motion or other irregularities. In fact, the present technique permits the application of MRI velocimetry to any unsteady system which changes at a rate slowly enough that spatial blurring is acceptable within the 125 ms acquisition time.

## 3.4 Conclusions

In this chapter, the application of ultra-fast MRI to unsteady systems was investigated, with an approach to the successful imaging of bubbly flow. In doing this, magnetic susceptibility matching between two phases was firstly investigated, on the basis that the fastest MRI protocol, EPI, suffers from a lack of robustness to off-resonance effects. A technique for measuring the phase shift at an interface due to magnetic susceptibility difference was described, and applied to determine that 16.86 mM of dysprosium chloride is needed for a solution with an magnetic susceptibility equivalent to of air. By optical measurements of bubble size distributions of low voidage ($\varepsilon \approx 3.5\%$) bubbly flow before and after the addition dopant, the paramagnetic salt was noted to have a significant effect upon the structure of bubbly flow, decreasing bubble sizes and stablising the flow at higher voidages. As the goal of the present study is the application of MRI to high voidage bubbly flow, these effects were deemed beneficial.

Conventional ultra-fast MRI sequences were tested for their applicability to bubbly flow. It was firstly shown that FLASH and RARE, which average slice selection across the entire acquisition period, are incapable of producing instantaneous images of the system. While EPI successfully produced 'snap-shots' bubbly flow at low voidage ($\varepsilon < 1\%$), for marginally higher voidages ($\varepsilon = 3.5\%$) the images were seen to suffer from heavy localised signal attenuation. This effect stems from the accrual of first moment phase during imaging, which fundamentally renders EPI unsuitable for application to high shear systems such as bubbly flow. Further work will now focus upon EPI-style acquisitions which minimise the amount of first moment phase accrued during imaging.

The accrual of first moment imaging phase also undermines velocity measurements of unsteady flow systems using EPI. While EPI cannot be applied to bubbly flow, it may still be a useful basis for velocity measurements of less heavily mixed systems. Thus, an EPI velocity imaging sequence which somewhat overcomes the phase contrast errors associated with first moment accrual during imaging was proposed. This technique, dubbed ssG, acquires both phase reference and velocity encoded data following a single excitation, which are therefore exposed to similar velocity fields, and thus allowing the velocity encoding to be isolated from the velocity proportionate phase accrued during imaging. ssG was validated against the theory for laminar flow in a pipe and a Couette cell. 3-component velocity images were obtained in approximately 125 ms, rendering the technique suitable for application to systems that change at a rate slow enough for acceptable spatial blurring over this period. ssG was firstly demonstrated on a dynamic

yet periodic system for validation against standard MRI velocimetric techniques. Velocity fields were measured around a rotating impeller, and compared with triggered acquisition velocity encoded spin-warp and GERVAIS images of the same system. Whilst good agreement between the measurement techniques was evident, the one shot technique developed in the present work was substantially less complicated to implement. For slow flows that require high velocity encoding gradients, eddy currents can be a source of significant error for the ssG technique as the phase reference maps are exposed to different magnetic field gradients than those experienced by the velocity encoded images (this is in contrast to GERVAIS, where the effects of eddy currents are minimised by identical gradient application for the flowing and non-flowing images). The effect of eddy currents was minimised by acquiring phase-reference points surrounding the region of interest. These reference points allowed the generation of an eddy-induced phase correction map. This procedure, however, was only necessary for the examination of low velocities, in our case less than 2 cm $s^{-1}$, due to the relatively high strength velocity encoding gradients required for velocity resolution in this range. New experimental data for the flow field within a rising droplet of decane were also presented. These snap-shot images of a mobile droplet are the first of their type existing in the literature and demonstrate the great potential of ssG for the velocimetric characterisation of multiphase flow systems.

# Bibliography


[1] Chaouki, J., Larachi, F. and Dudukovic, M.P., 1997. Noninvasive tomographic and velocimetric monitoring of multiphase flows. *Ind. Eng. Chem. Res.*, 36, pp. 4476–4503.

[2] Lenz, G.W., Haacke, E.M. and White, R.D., 1989. Retrospective cardiac gating: a review of technical aspects and future directions. *Magn. Reson. Im.*, 7, pp. 445–455.

[3] Gatehouse, P.D., Keegan, J., Crowe, L.A., Masood, S., Mohiaddin, R.H., Kreitner, K.F. and Firmin, D.N., 2005. Applications of phase-contrast flow and velocity imaging in cardiovascular MRI. *Eur. Radiol.*, 15, pp. 2172–2184.

[4] Ehman, R.L., McNamara, M.T., Pallack, M., Hricak, H. and Higgins, C.B., 1984. Magnetic resonance imaging with respiratory gating: techniques and advantages. *Am. J. Roentgenol.*, 143, pp. 1175–1182.

[5] Moser, K.W., Raguin, L.G. and Georgiadis, J.G., 2003. Synchronized EPI phase contrast velocimetry in a mixing reactor. *Magn. Reson. Imaging.*, 21, pp. 127–133.

[6] Shiko, G., Gladden, L.F., Sederman, A.J., Connolly, P.C. and Butler, J.M., 2011. MRI studies of the hydrodynamics in a USP 4 dissolution testing cell. *J. Pharm. Sci.*, 100, pp. 976–991.

[7] Frayne, R., Steinman, D.A., Rutt, B.K. and Ethier, C.R., 1995. Accuracy of MR phase contrast velocity measurements for unsteady flow. *J. Magn. Reson. Im.*, 5, pp. 428–431.

[8] Robertson, M.B., Köhler, U., Hoskins, P.R. and Marshall, I., 2001. Quantitative analysis of PC MRI velocity maps: pulsatile flow in cylindrical vessels. *Magn. Reson. Im.*, 19, pp. 685–695.

[9] Papaharilaou, Y., Doorly, D.J. and Sherwin, S.J., 2001. Assessing the accuracy of two-dimensional phase-contract MRI measurements of complex unsteady flows. *J. Magn. Reson. Im.*, 14, pp. 714–723.

[10] Gladden, L.F., 1994. Nuclear magnetic resonance in chemical engineering: principles and applications. *Chem. Eng. Sci.*, 49(20), pp. 3339–3408.

[11] Fukushima, E., 1999. Nuclear magnetic resonance as a tool to study flow. *Annu. Rev. Fluid Mech.*, 31, pp. 95–123.

[12] Mantle, M.D. and Sederman, A.J., 2003. Dynamic MRI in chemical process and reaction engineering. *Prog. Nucl. Mag. Res. Spec.*, 43, pp. 3–60.

[13] Gladden, L.F., Akpa, B.S., Anadon, L.D., Heras, J.J., Holland, D.J., Mantle, M.D., Matthews, S., Mueller, C., Sains, M.C. and Sederman, A.J., 2006. Dynamic MR imaging of single- and two-phase flows. *Chem. Eng. Res. Des.*, 84(A4), pp. 272–281.

[14] Gladden, L.F. and Mitchell, J., 2011. Measuring adsorption, diffusion and flow in chemical engineering: applications of magnetic resonance to porous media. *New J. Phys.*, 3, p. 035,001.

[15] Kose, K., 1990. NMR imaging of turbulent structure in a transitional pipe flow. *J. Phys. D.*, 23, pp. 981–983.

[16] Kose, K., 1991. Instantaneous flow-distribution measurements of the equilibrium turbulent region in a circular pipe using ultrafast NMR imaging. *Phys. Rev. A.*, 44, pp. 2495–2504.

[17] Kose, K., 1991. One-shot velocity mapping using multiple spin-echo EPI and its application to turbulent flow. *J. Magn. Reson.*, 92, pp. 631–635.

[18] Gatenby, J.C. and Gore, J.C., 1996. Echo-planar-imaging studies of turbulent flow. *J. Magn. Reson.*, 121, pp. 193–200.

[19] Sederman, A.J., Mantle, M.D., Buckley, C. and Gladden, L.F., 2004. MRI technique for measurement of velocity vectors, acceleration, and autocorrelation functions in turbulent flow. *J. Magn. Res.*, 166, pp. 182–189.

[20] Davies, C.J., Sederman, A.J., Pipe, C.J., McKinley, G.H., Gladden, L.F. and Johns, M.L., 2010. Rapid measurement of transient velocity evolution using GERVAIS. *J. Magn. Reson.*, 202, pp. 93–101.

[21] Stevenson, R., Harrison, S.T.L., Mantle, M.D., Sederman, A.J., Moraczewski, T.L. and Johns, M.L., 2009. Analysis of partial suspension in stirred mixing cells using both MRI and ERT. *Chem. Eng. Sci.*, 65, pp. 1385–1393.

[22] Sains, M., 2006. *Ultra-fast visualisation of unsteady flow using magnetic resonance imaging*. Ph.D. thesis, University of Cambridge.

[23] Mantle, M.D., Sederman, A.J., Gladden, L.F., Raymahasay, S., Winterbottom, J.M. and Stitt, E.H., 2002. Dynamic MRI visualisation fo two-phase flow in a ceramic monolith. *AIChE J.*, 48, pp. 909–912.

[24] Heras, R., 2006. *Ultra-fast imaging of two-phase flow in structured monolith reactors; techniques and data analysis*. Ph.D. thesis, University of Cambridge.

[25] Müller, C.R., Davidson, J.F., Dennis, J.S., Fennell, P.S., Gladden, L.F., Hayhurst, A.N., Mantle, M.D., Rees, A.C. and Sederman, A., 2006. Real-time measurement of bubbling phenomena in a three-dimensional gas-fluidized bed using ultrafast magnetic resonance imaging. *Phys. Rev. Lett.*, 96(15), pp. 154,504/1–154,504/4.

[26] Fennell, P.S., Davidson, J.F., Dennis, J.S., Gladden, L.F., Hayhurst, A.N., Mantle, M.D., Müller, C.R., Rees, A.C., Scott, S.A. and Sederman, A.J., 2005. A study of the mixing of solids in gas-fluidized beds, using ultra-fast MRI. *Chem. Eng. Sci.*, 60, pp. 2085–2088.

[27] Schenck, J.F., 1996. The role of magnetic susceptibility in magnetic resonance imaging: MRI magnetic compatibility of the first and second kinds. *Med. Phys.*, 23, pp. 815–850.

[28] Lide, D.R., 1998. *CRC handbook of chemistry and physics*. CRC press, Boca Raton.

[29] Chu, K.C., Xu, Y., Balschi, J.A. and Springer, C.S., 1990. Bulk magnetic susceptibility shift in nmr studies of compartmenalized samples: use of paramagnetic reagents. *Magn. Reson. Med.*, 13, pp. 239–262.

[30] Ojemann, J.G., Akbudak, E., Snyder, A.Z., McKinstry, R.C., Raichle, M.E. and Conturo, T.E., 1997. Anatomic localization and quantitative analysis of gradient refocused echo-planar fMRI susceptibility artefacts. *Neuroimage*, 6, pp. 156–167.

[31] Lauterbur, P.C., 1973. Image formation by induced local interactions - examples employing Nuclear Magnetic Resonance. *Nature*, 242, pp. 190–191.

[32] Bakker, C.J.G. and de Roos, R., 2006. Concerning the preparation and use of substances with a magnetic susceptibility equal to the magnetic susceptibility of air. *Magn. Reson. Med.*, 56, pp. 1107–1113.

[33] Kuchel, P.W., Chapman, B.E., Bubb, W.A., Hansen, P.E., Durrant, C.J. and Hertzberg, M.P., 2003. Magnetic susceptibility: solutions, emulsions, and cells. *Concepts Magn. Reson.*, 18A, p. 5671.

[34] Conger, R.L. and Selwood, P.W., 1952. Proton relaxation in paramagnetic solutions. *J. Chem. Phys.*, 20, p. 383387.

[35] Bloembergen, M., 1957. Proton relaxation times in paramagnetic solutions. *J. Chem. Phys.*, 27, pp. 572–573.

[36] Jamialahmadi, M. and Müller-Steinhagen, 1992. Effect of alcohol, organic acid and potassium chloride concentration on bubble size, buble rise velocity and gas hold-up in bubble columns. *Chem. Eng. J.*, 50, pp. 47–56.

[37] Zieminski, S.A. and Whittemore, R.C., 1971. Behavior of gas bubbles in aqueous electrolyte solutions. *Chem. Eng. Sci.*, 26, pp. 509–520.

[38] Fitzgibbon, A., Pilu, M. and Fisher, B., 1999. Direct least squares fitting of ellipses. *IEEE T. Pattern. Anal.*, 21, pp. 476–480.

[39] Ribeiro, C.P. and Mewes, D., 2007. The influence of electrolytes on gas hold-up and regime transition in bubble columns. *Chem. Eng. Sci.*, 62, pp. 4501–4509.

[40] Růžička, M.C., Vecer, M.M. and Drahoš, O.J., 2008. Effect of surfactant on homogeneous regime stability in bubble column. *Chem. Eng. Sci.*, 63, pp. 951–967.

[41] Orvalho, S., Růžička, M. and Drahoš, J., 2009. Bubble columns with electrolytes: gas holdup and flow regimes. *Ind. Eng. Chem. Res.*, 48, pp. 8237–8243.

[42] Harteveld, W., 2005. *Bubble columns: structures or stability?* Ph.D. thesis, Delft University of Technology.

[43] Rice, R.G., Tupperainen, J.M.I. and Hedge, R.M., 1981. Dispersion and hold-up in bubble columns - comparison of rigid and flexible spargers. *Can. J. Chem. Eng.*, 59, pp. 677–687.

[44] De Gennes, P.G., 1969. Theory of spin echoes in a turbulent fluid. *Phys. Lett. A*, 29, pp. 20–21.

[45] Fukuda, K. and Hirai, A., 1979. A pulsed NMR study on the flow of fluid. *J. Phys. Soc. Jpn.*, 47, pp. 1999–2006.

[46] Gatenby, J.C. and Gore, J.C., 1994. Characterization of turbulent flows by NMR measurements with pulsed gradients. *J. Mag. Res.*, A110, pp. 26–32.

[47] Firmin, D.N., Klipstein, R.H., Hounsfield, G.L., Paley, M.P. and Longmore, D.B., 1989. Echo-planar high-resolution flow velocity mapping. *Magn. Reson. Med.*, 12, pp. 316–327.

[48] Moser, K.W., Georgiadis, J.G. and Buckius, R.O., 2000. On the accuracy of EPI-based phase contrast velocimetry. *Magn. Reson. Imaging.*, 18, pp. 1115–1123.

[49] Kronig, R. and Brink, J.C., 1951. On the theory of extraction from falling droplets. *Appl. Sci. Res.*, A2, pp. 142–154.

[50] Amar, A., Gross-Hardt, E., Khrapitchev, A.A., Stapf, S., Pfennig, A. and Blümich, B., 2005. Visualizing flow vortices inside a single levitated drop. *J. Mag. Res.*, 177, pp. 74–85.

[51] Clift, R., Grace, J.R. and Weber, M.E., 1978. *Bubbles, drops, and particles.* Acadamic Press, New York.

# Chapter 4

# Spiral imaging of high-shear systems

One of the major advantages of EPI-style acquisitions is the great amount of freedom that exists to decide the manner in which **k**-space is traversed. As discussed in Chapter 3, conventional blipped-EPI cannot be successfully applied to bubbly flow because of the combination of the first moment phase accrual due to the imaging gradients, and the high-shear, heavily mixed nature of the system. Additionally, the accrual of first moment phase during imaging undermines the quantitative nature of phase-contrast velocity imaging when applied to unsteady flow systems, as the velocity encoded phase shift cannot be isolated by subtraction of an image with increment in the amount of velocity encoding. While an EPI-based velocity measurement technique that overcame this latter problem, dubbed 'snap-shot GERVAIS' (ssG), was proposed in Section 3.3, the acquisition time of this technique is in excess of 100 ms, which limits its applicability. The flow compensation of each individual increment in phase gradient has also been demonstrated for EPI [1], however this alteration leads to a significant increase in acquisition time, which undermines the usefulness of the technique for application to highly unsteady systems. Thus, it seems sensible to explore the use of **k**-space sampling schemes that minimise the accrual of first moment imaging phase in the first place.

A technique known as spiral imaging may be optimal for the refocusing of first moment imaging phase. Spiral imaging, which was first described by Ahn *et al.* [2], samples all of **k**-space following a single excitation in a spiral trajectory extending outwards from the

zero frequency point. This approach holds several advantages [3]: the centre of **k**-space is sampled at the start of the sequence, which provides a high signal-to-noise ratio and minimises off-resonance phase shifts for the high-power, low spatial-frequency Fourier coefficients; gradient slew rate can be readily controlled, which enables efficient gradient performance; and all four quadrants of **k**-space are sampled in an interleaved fashion, which acts to somewhat compensate for the accumulation of first moment imaging phase. While spiral imaging has never been widely adopted in clinical use, with EPI remaining the preferred technique for applications where temporal resolution is important [4], it has featured in several studies in functional MRI [5, 6] and cardiac morphology [7, 8]. Spiral imaging has not yet been employed at all in studies outside of a medical context. The major reason that spiral imaging has not found widespread use is due to complexities in its implementation. In particular, as spiral imaging does not sample **k**-space to a rectilinear raster, the sampled data must be either regridded prior to reconstruction by fast Fourier transform, or reconstructed by the computationally intensive discrete Fourier transform (DFT). While regridding algorithms such as the Kaiser-Bessel convolution kernel are now well accepted [9, 10] and the DFT remains a viable option for images of size less than 64 pixels $\times$ 64 pixels, the challenge lies in obtaining exact knowledge of the location of the points sampled in **k**-space. This information is necessary as the incidence of gradient non-idealities and eddy currents slightly alters the location of the sampled **k**-space points, leading to significant blurring and distortion if the image is reconstructed using the input gradient waveform [3]. To overcome this problem, several approaches have been developed for measurement of magnetic field gradient waveforms, which have been combined with spiral imaging for the production of high quality images [11, 12].

As highlighted in Chapter 3, if bubbly flow is to be successfully visualised, it is critical that minimal first moment phase is accrued during imaging. Previous analyses of spiral imaging have noted that the early sampling of the centre of **k**-space, and the periodic return of all moments of the imaging gradients to zero, leads to the minimal accrual of velocity proportionate phase during imaging [13]. More recently, however, several studies have high-lighted significant image artefacts associated with spiral imaging of flowing systems, and have called into doubt the commonly cited claim that spiral imaging is highly robust to flow [14, 15, 16]. The extent of these flow artefacts remains to the quantified in detail before spiral imaging can be applied with confidence to a fast-flowing, heavily mixed system such as bubbly flow, or before it can be applied to unsteady flow systems for the measurement of quantitative velocity information.

The implementation of spiral imaging and its application to unsteady flow systems is the subject of the present chapter. Two common approaches to gradient waveform measurement are firstly evaluated, and a methodology for the measurement of gradient waveforms for use with spiral imaging is established. The application of spiral imaging to unsteady flow is then considered, and the flow artefacts associated with spiral imaging are quantified using both simulated acquisitions and experiments. Finally, the quantitative measurement of velocity fields for some highly transient unsteady flow systems is demonstrated, as is the combination of compressed sensing and spiral imaging for high temporal resolution velocity imaging. The application of spiral imaging to bubbly flow is considered in Chapter 5.

## 4.1 Implementation of spiral imaging

In this section the implementation of spiral imaging is considered. The path followed in **k**-space during acquisition is given by the algorithm of Glover [17], and is shown in Figure 4.1. Two techniques for the measurement of these gradient waveforms are firstly examined. Following this, the effect of $B_0$ inhomogeneity and chemical shift on spiral imaging are considered with comparison to EPI. The effect of flow on spiral imaging is examined in detail in Section 4.2.

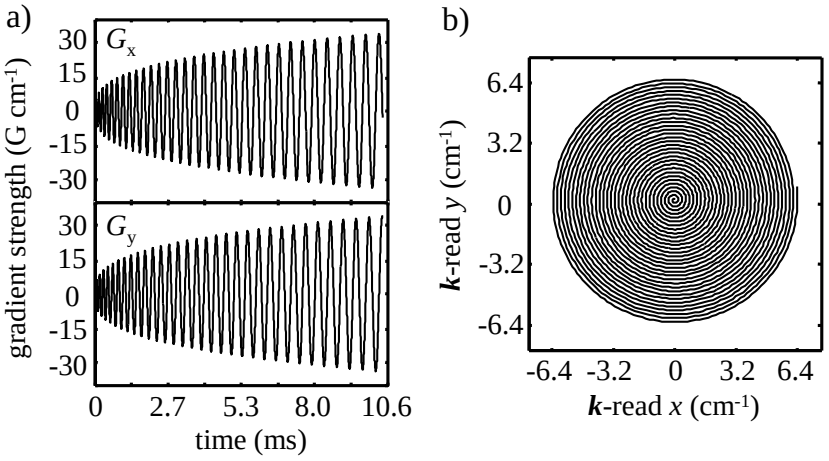


Figure 4.1: a) Spiral gradient waveforms and b) corresponding **k**-space trajectory used in this chapter.

### 4.1.1 Gradient trajectory measurement

High temporal resolution EPI-type acquisitions involve strong read gradient strengths and fast gradient switching. Inevitably this behaviour gives rise to eddy currents in the sample

and non-ideal gradient waveforms. In setting up EPI it is common to acquire a reference scan with the phase gradient switched off [18], prior to 'trimming' the read gradient until all echoes in the train are identical, or applying a 1$^{st}$ order phase correction to every other line in the frequency domain (which is equivalent to a translational shift in **k**-space). In this way, deviations from the input waveform are corrected, and artefacts such as the Nyquist ghost are removed. Errors in the phase direction are generally considered minimal in EPI as the phase gradient waveform consists of only low gradient strength 'blips'. Spiral imaging, on the other hand, involves strong read-out gradients and fast gradient switching in two directions simultaneously. Correcting for imperfect gradient behaviour is therefore significantly more complicated than it is for EPI. Additionally, as **k**-space is not being sampled along a rectilinear grid in spiral imaging, knowledge of the exact gradient waveforms becomes more important. To this end, several techniques have been proposed in the literature for the measurement of gradient waveforms. These procedures may be broadly separated into two categories: the use of magnetic field monitors [19, 20] and imaging based techniques [21, 12]. In the present section a technique from each group is implemented and evaluated. In both approaches it is desirable to only receive signal from a point source at a known offset from the gradient isocentre. Magnetic field monitors use a small reference sample to physically isolate this signal, while imaging based approaches use volume selective excitations. The gradient field strength experienced at the point source is related to the phase of the measured signal according to [21]:

$$\theta = \gamma G_{\mathrm{z}} t_{\mathrm{p}} z_0 \tag{4.1}$$

where $G_{\mathrm{z}}$ is the gradient strength in direction $z$, $t_{\mathrm{p}}$ is phase encoding time and $z_0$ is the offset of the point source from the gradient isocentre. From measured values of $G_z$, the corresponding **k**-space points can be determined using equation (2.22). All measurements in this section were performed on a Bruker AV-400 spectrometer, equipped with 3-axis gradients of maximum strength 146 G cm$^{-1}$, and (unless otherwise noted) a 25 mm diameter birdcage r.f. coil.

### Magnetic field monitors

Magnetic field monitors (MFM) use a small reference phantom to isolate the signal from a single spatial location. The technique presently explored is that described by Han *et al.* [22], however other, similar approaches exist [19, 20]. This pulse sequence uses low tip-angle single point imaging [23] to sample a given gradient waveform, as shown in Figure 4.2. An arbitrary gradient waveform is applied simultaneously to a train of low

tip angle pulses ($\alpha = 15°$). One data point is sampled at a time $t_p$ after excitation. As long as signal is only being emitted from a point source phantom (the position of which was measured from a 1D projection), the mean gradient over the phase encode time can be determined using equation (4.1). The phantom used is heavily doped with gadolinium chloride ($T_1 = T_2 = 100$ μs) such that full magnetisation recovery is possible between each excitation. In the present experiments, the point source used was an NMR bulb of inside diameter 1 mm. The phase encode time used was 10 μs, with a repetition time, $t_r$, of 50 μs.

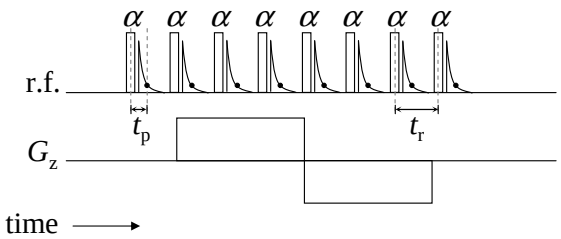


Figure 4.2: Pulse sequence for gradient trajectory measurement using a magnetic field monitor. Small tip angle, broadband excitation pulses are used to elicit signal from a point source phantom. One point for each excitation is acquired after the phase encoding time, $t_p$. This process is repeated rapidly to allow the evolution of phase at a single point in space to be measured.

In initial investigations, it was attempted to measure a simple bi-polar gradient waveform, the results of which are shown in comparison to the input waveform in Figure 4.3 a). From this comparison it is clear that the technique predicts a substantially different waveform from that expected, with one lobe of the measured curve significantly underpredicting the input waveform. This level of deviation from the input waveform seems unrealistic given the well established accuracy of bipolar gradients as used in phase contrast velocimetry. It is important to note that an imaging coil was used in obtaining the measurements shown in Figure 4.3 a). The short $T_2$ of the MFM phantom is comparable with that of the teflon lining of the coil used. Thus it seems likely that the sequence was eliciting signal from the coil itself in addition to the sample. In order to test this hypothesis, the measurement was repeated using a glass-lined NMR coil, as shown in Figure 4.3 b). It is clear that the technique produced a more accurate measurement in this case. Thus it seems apparent that the use of a magnetic field monitor is inappropriate while using a plastic lined imaging coil. It is interesting to note that in the work of Han *et al.* [22], a small saddle coil which surrounds the sample was used. This coil was in turn surrounded by an r.f. shield, thus preventing the problem associated with signal emitted by the coil materials from being apparent.

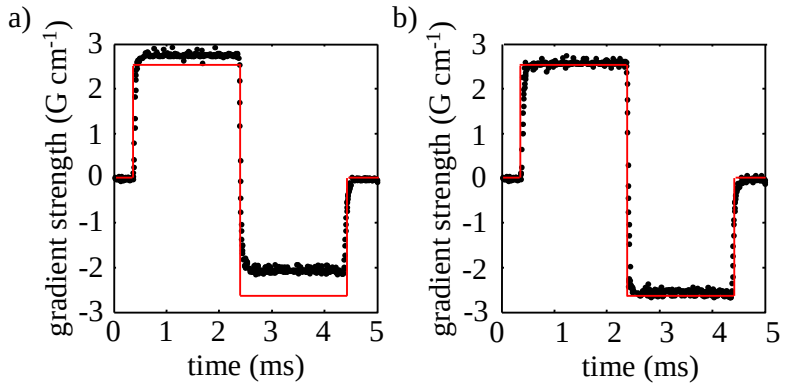


Figure 4.3: Measurement of a bipolar gradient using MFM in a) a teflon lined imaging coil and b) a glass lined NMR coil. The input waveform is represented by the red line. It is clear that signal being received from the lining of the imaging coil prevented the successful application of the technique. Note that no gradient ramping was used in the examined gradient waveforms.

### Imaging based gradient waveform measurement

As an alternative to the use of magnetic field monitors, several techniques have been proposed that make modifications to imaging sequences for the measurement of a gradient waveform. The technique of Duyn *et al.* [11] is presently considered. In this technique, the gradient waveform for a spin-echo based sequence may be measured in one direction by rendering both pulses used for echo formation to be slice selective in two planes orthogonal to the direction of image encoding (such that the excited 'line' of magnetisation is effectively a 'point-source' relative to the changing imaging gradient). Note that some frequency off-set is required for one of the slice selective pulses to distance the point-source from the gradient isocentre. A reference scan with no imaging gradient is also acquired such that background phase evolution due to off-resonance effects can be removed. A two-dimensional gradient waveform can be produced by repeating this process for both imaging directions separately, and substituting the phase of the measured signal into equation (4.1). We presently make a minor modification to the technique of Duyn *et al.*, wherein a third slice selective pulse is added prior to the sequence, such that the technique becomes volume selective, which, while sacrificing signal-to-noise, improves the robustness of the technique to $B_0$ and $B_1$ inhomogenities. A pulse sequence for the modified technique of Duyn *et al.* is shown in Figure 4.4.

The technique was firstly applied to the measurement of a bipolar gradient waveform identical to that used in Figure 4.3. The sample used was a 10 mm test-tube filled with 16.86 mM dysprosium chloride solution. All pulses were 512 μs in duration, and

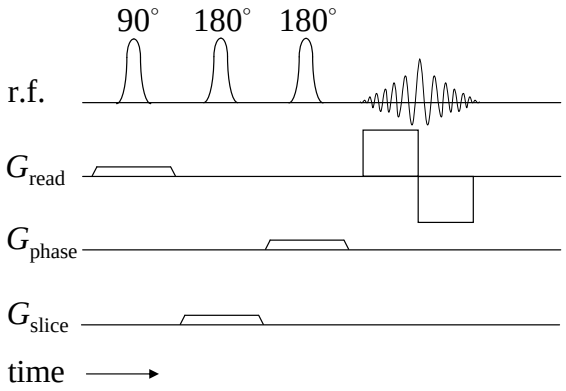


Figure 4.4: A pulse sequence diagram for the gradient waveform measurement technique of Duyn *et al.* [11]. Note that this sequence is slightly modified to render it volume selective, which improved robustness in systems with substantial $B_0$ heterogeneity.

Gaussian in shape. The three excited slices were 0.2 mm in thickness, with the slice offset in the $z$-direction set to 5 mm. The repetition time, $t_r$ was set to 250 ms. Two images were acquired; one with imaging gradients and one without. The subtraction of this reference phase baseline removed phase shifts due to off-resonance effects. A nested, 16 step exorcycle phase cycle [24] (see Section 2.1.7) was used to suppress the formation of undesired phase coherences. The results of this scan are shown in Figure 4.5. It is clear from these data that the imaging based approach produced an accurate measurement of the gradient waveform even when acquired using an imaging coil.

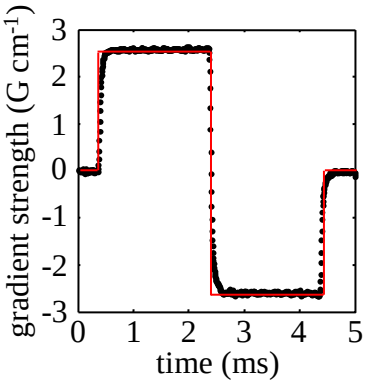


Figure 4.5: Measurement of a bipolar gradient waveform using the technique of Duyn *et al.* [11]. The input waveform is represented by the red line. Note that no gradient ramping was used in the examined gradient waveforms.

The technique was then used to acquire a waveform for a spiral trajectory. The input trajectory used is shown in Figure 4.1. The read and phase gradients were measured separately, and combined to produce a two-dimensional trajectory. While this approach does not account for cross-talk between the gradients during imaging, it is anticipated

that these effects will be small. The phantom examined in Figure 2.19 was reemployed to provide a basis for comparison between spiral imaging and EPI. The spiral trajectory examined had a duration of 19.7 ms, and was acquired at a spectral width of 200 kHz. The field of view of this trajectory corresponded to 20 mm $\times$ 20 mm, with a resolution of 312.5 µm $\times$ 312.5 µm. All other acquisition parameters were identical to those used for the bipolar gradient waveform, described above.

Figure 4.6 shows a comparison of a) input and b) measured spiral trajectories. Images which were reconstructed by non-uniform fast Fourier transform [25] with either trajectory are shown in c) and d). It is clear that while the resolution in the image reconstructed using the ideal trajectory is preserved, there exists significant signal modulation across the image. Comparatively, signal in the image reconstructed using the measured trajectory is fairly homogeneous. This reflects that significant gradient deviations are occurring during the acquisition of the central **k**-space points, which is unsurprising given that this region corresponds to the fastest gradient switching. The slight blurring artefact at the side of Figure 4.6 is caused by local $B_0$ heterogeneity in that region. This artefact highlights one potential source of error with any point-source based approach to gradient trajectory measurement: whether the phase accrual in the excited volume is representative of that at every location in the sample. For systems with a significant proportion of off-resonant spins, more sophisticated gradient trajectory measurement techniques are required. Such a technique has been examined by Barmet *et al.* [26], who demonstrated the use of multiple simultaneous magnetic field monitors. As all systems examined in the present study are susceptibility matched and do not exhibit chemical shift, however, these more complex techniques are not considered necessary. For all further experiments using spiral imaging in this thesis, the images are reconstructed using gradient trajectories measured using the modified technique of Duyn *et al.* [11].

### 4.1.2 Spiral imaging with off-resonance effects

To demonstrate the influence of off-resonance effects on spiral imaging, spiral images were acquired of a phantom containing sources of $B_0$ inhomogeneity and chemical shift. All acquisition parameters are identical to those described for the demonstration of the technique of Duyn *et al.* in Section 4.1.1. Images were reconstructed using a **k**-space trajectory measured described as above, and a non-uniform fast-Fourier transform [25].

Spiral images containing $B_0$ heterogeneity and chemical shift are juxtaposed with images of the same systems acquired using RARE and EPI in Figure 4.7. The phantom includes a

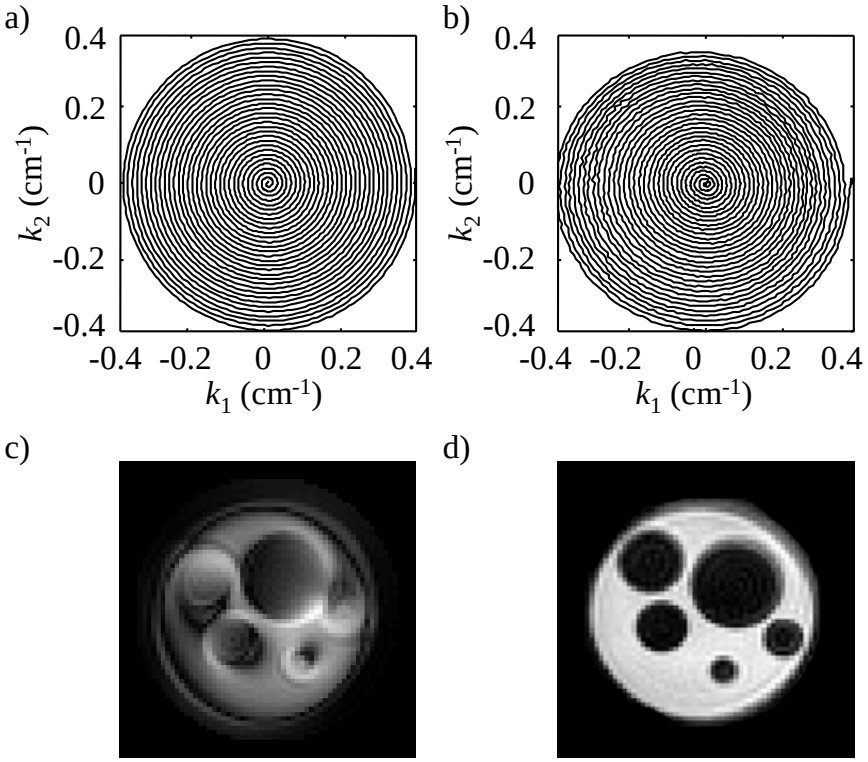


Figure 4.6: Comparison of a) input and b) measured spiral gradient trajectories. Also shown are images of a resolution phantom reconstructed with c) input trajectory and d) measured trajectory. The necessity for a measured **k**-space trajectory for image reconstruction is evident. The field of view of these images is 20 mm × 20 mm, with a resolution of 312.5 μm × 312.5 μm.

plastic bead (source of $B_0$ heterogeneity) in images d) - f) and an NMR tube of ethanol in images h) - i). It is clear from these images that both $B_0$ heterogeneity and chemical shift have an adverse effect on spiral images. In fact, both effects are substantially worse than those exhibited by EPI. The reason for this is related to the non-linear **k**-space sampling strategy employed by spiral imaging, with the available gradient slew rate limiting the image bandwidth in each direction (for these images 5 kHz at the centre of **k**-space decreasing to approximately 1 kHz at the edge). Conversely, EPI samples one direction at the spectral width of the image (200 kHz), while the bandwidth of the perpendicular direction is much lower (a mean of 3125 Hz). Thus, while EPI images only tend to suffer distortion and chemical shift artefacts in one direction, the effect upon spiral images is two dimensional, and much more significant. Nevertheless, as the bubbly flow system under examination in the present study has been rendered magnetically homogeneous by magnetic susceptibility matching in Chapter 3, and contains only a single NMR peak, spiral imaging may still be successfully applied.

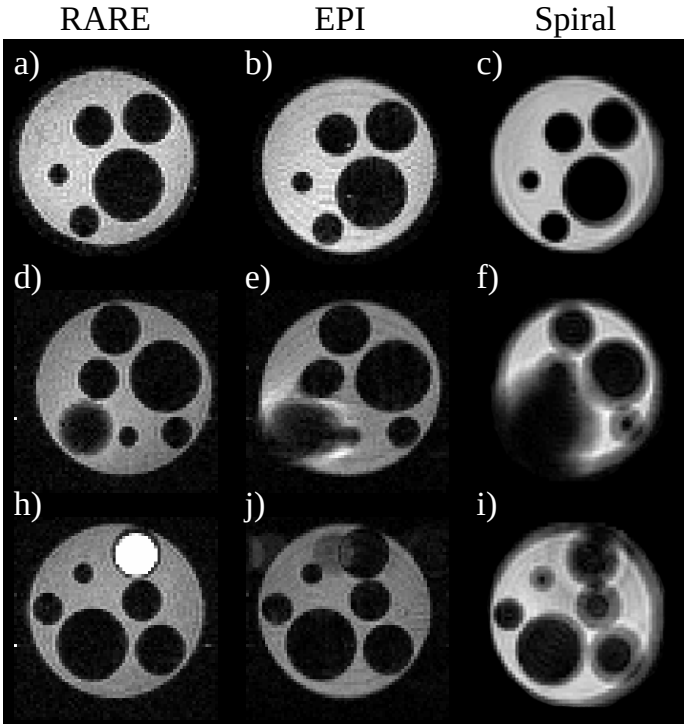


Figure 4.7: Comparison of the effect of off-resonance effects on RARE images (a,d,h), EPI images (b,e,j) and spiral images (c,f,i). Shown is a magnetic susceptibility matched resolution phantom (a,b,c), with a plastic bead of differing magnetic susceptibility included (d,e,f) and with a tube of ethanol included (h,j,i). The field of view of these images is 20 mm $\times$ 20 mm, with a resolution of 312.5 μm $\times$ 312.5 μm.

## 4.2 Velocity imaging of unsteady flow systems

Velocity encoded, single-shot spiral imaging was first implemented by Gatehouse *et al.* [14], almost simultaneously with Pike *et al.* [27] who investigated multi-shot interleaved spiral velocimetry. Both sets of researchers verified the measured average flow rate to be quantitative, prior to applying their respective techniques to the *in vivo* measurement of arterial blood flow. Subsequent to these early works, phase contrast spiral imaging has been employed in several medical studies, primarily centred upon applications in cardiology [28, 29, 30, 31, 32, 33, 34]. Early studies of the effect of flow on spiral imaging noted that the early sampling of the centre of k-space, and the periodic return of all moments of the imaging gradients to zero, rendered the technique highly robust to flow artefacts [13]. Subsequently, however, Butts and Riederer [15] and Gatehouse and Firmin [16] noted that despite it being commonly acknowledged that spiral imaging demonstrates excellent resistance to flow artefacts, fast ($> 50$ cm s$^{-1}$) in-plane flows have an adverse effect upon the point spread function (PSF). The PSF is seen to shift in the direction of flow, split into multiple peaks and broaden over several pixels. This

behaviour is congruent with the experiments and simulations of Gatehouse *et al.* [14], who noted that their images fringe and blur respectively in the direction of flow where their flow phantom entered and left the imaging plane, which they identified as being due to the motion of spin isochromats between the start of the sequence, when all low spatial frequencies are sampled, and at its end, when high-resolution information is obtained. Nishimura *et al.* [35] also simulated acquisitions of spiral imaging in the presence of flow, however they reported that spiral imaging demonstrates minimal flow artefacts even for in-plane velocities in excess of 2 m $s^{-1}$. This disparity with other studies appears to be due to their simulation of a unidirectional flow phantom of infinite length.

In the present section the applicability of spiral imaging towards the quantification of velocity fields for unsteady flow systems is explored. In doing this, simulated acquisitions and experiments are used to investigate the impact of in-plane flow. With the flow artefacts associated with spiral imaging thereby quantified, the use of spiral imaging for the measurement of velocity fields is demonstrated on some example unsteady flow systems.

### 4.2.1 Theoretical

For application to unsteady flow systems, it is important that the accrual of first moment phase during imaging is minimal. Recall from equation (2.30) that the phase accrued while traversing a given gradient waveform is given by:

$$\phi(r,t) = \gamma r \int_0^t G(t)dt + \gamma v \int_0^t tG(t)dt + \emptyset(t^3) \tag{4.2}$$

where $\gamma$ is the gyromagnetic ratio, $G(t)$ is the gradient waveform, $r$ is position in real space and $v$ is the velocity component in the direction of the applied magnetic field gradient. The first term in this equation represents the zeroth moment phase, which is used for spatial encoding. The second term is the first moment phase, which, if accrued during imaging, gives rise to flow artefacts. Phase due to higher order terms (e.g. acceleration) may also be accrued, however it is generally small in proportion to the first moment phase. For example, Sederman *et al.* [36] noted that for single phase pipe flow at a Reynolds number of 5,000 (a liquid velocity of 15.1 cm $s^{-1}$ in their system), the maximum fluid acceleration associated with vortex formation was on the order of 40 cm $s^{-2}$. For an image acquired over 10 ms, the phase accrued due to acceleration is therefore 2.6% of that accrued due to velocity. In the present analysis, phase accrual due to higher moments is considered negligible.

The first moment phase accrued for during the traversal of the trajectory shown in Figure 4.6 is shown in Figure 4.8, together with that accrued during an equivalent EPI sequence. This figure was generated using equation 4.2 and assuming a field of view of 2.5 cm × 2.5 cm, a spectral-width of 400 kHz and a uniform flow field of 20 cm $s^{-1}$ in the direction of the gradients. Modulus time-domain signals for typical acquisitions are also shown in Figure 4.8 c). These curves demonstrate that the velocity proportionate phase accrued during spiral imaging is periodically refocused in both directions, unlike that accrued in the second read direction during EPI. This feature is commonly acknowledged as being the source of the robustness to flow demonstrated by spiral imaging [13]. Further, it is clear that little or no first moment weighting exists when the majority of the power is acquired in spiral imaging, again unlike the EPI image which contains substantial first moment phase by the time the centre of **k**-space is reached.

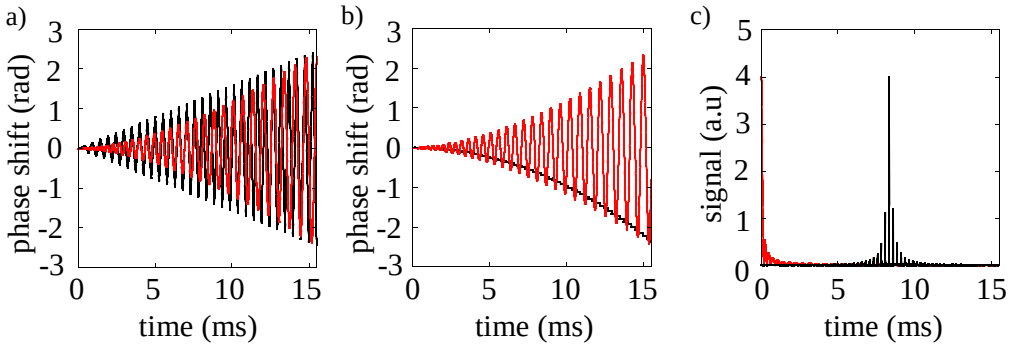


Figure 4.8: The first moment phase accumulated during imaging for spiral (red) and EPI (black) in a) the first read direction and b) the second read direction. In this calculation a field of view of 5 cm was assumed, as was a spectral width of 200 kHz and a uniform velocity of 20 cm $s^{-1}$ in both directions. Typical modulus time-domain signals for both acquisitions are shown in c). Note that significant first moment weighting exists by the time the centre of **k**-space is reached for the EPI acquisition, but not for spiral imaging.

It is difficult to analytically quantify the accrual of first moment phase for an entire image because the spiral trajectories used in practice are complex functions of the maximum gradient amplitude and slew rate available [4]. Instead, simulated acquisitions are used to numerically reproduce the flow artefacts associated with spiral imaging in Section 4.2.2.

### 4.2.2 Simulations

In this section the extent of flow artefacts is quantified for a two dimensional image acquired using a realistic spiral trajectory by simulating the acquisition of spiral images with additional phase accrual originating from the first moment of the imaging gradients.

All simulations assumed a spectral width of 357 kHz for a 64 pixel $\times$ 64 pixel image with a 5 cm $\times$ 5 cm field of view yielding a resolution of 0.78 mm $\times$ 0.78 mm. For a given image geometry and velocity field, equation (4.2) was used with the trajectory shown in Figure 4.1 to generate a first moment phase map for every sampling increment. A set of **k**-space signals was then generated by application of an inverse non-uniform fast Fourier transform [25] to these phase maps and the original modulus image. A simulated signal, complete with flow artefacts, was then constructed by concatenation of the complex data point for each time increment.

To demonstrate the effect of flow upon the modulus of the PSF for spiral imaging, the distortion of a single pixel was simulated for a range of flow rates. In examining these data it is convenient to adopt a dimensionless velocity, defined as:

$$v^* = \frac{v t_{\mathrm{i}} N_{\mathrm{p}}}{res}, \tag{4.3}$$

where $v$ is velocity, $t_{\mathrm{i}}$ is the sampling increment, $N_{\mathrm{p}}$ is the number of pixels in one spatial dimension and $res$ is the image resolution. It is important to note that, even for a unidirectional flow, the effect upon the PSF for spiral imaging will be two dimensional. This is shown in Figure 4.9 a) for a velocity of 50 cm s$^{-1}$ in the $x$ direction (equivalent to a dimensionless velocity of 1.15 $\times$ $10^{-1}$). The PSF is seen to spread in the direction of flow, while also splitting and spreading symmetrically in the perpendicular direction. This splitting is likely responsible for the ringing and fringing of spiral modulus images observed by previous researchers [14]. To quantify the extent of these flow artefacts, the two-dimensional PSF was simulated for a range of velocities, and was then integrated in one direction. These results are shown for the $x$ and $y$ directions in Figure 4.9 b) and c), respectively. The asymmetrical blurring in the flow direction is seen to always be in excess of that in the direction perpendicular to flow, and thus can be solely considered for a conservative estimate of the extent of blurring for spiral imaging of flow. A linear fit to the blurred edge of Figure 4.9 b) yields the relationship:

$$x_b = 2.17 v t_{\mathrm{read}} \tag{4.4}$$

where $x_{\mathrm{b}}$ is the length over which blurring will take place in the image and $t_{\mathrm{read}}$ is the image read-out time (equivalent to $N_p^2 t_i$ for a fully sampled, rectilinear **k**-space raster). Clearly the extent of acceptable blurring depends upon the pixel resolution of an image. This implies that, for images such as those simulated herein (0.78 mm resolution), velocities greater than 3 cm s$^{-1}$ cannot be exceeded without interpixel blurring. For studies

in a medical context, however, where resolutions on the order of 5 mm are common, in plane flows of up to 20 cm $s^{-1}$ may be examined with all blurring contained within a single pixel.

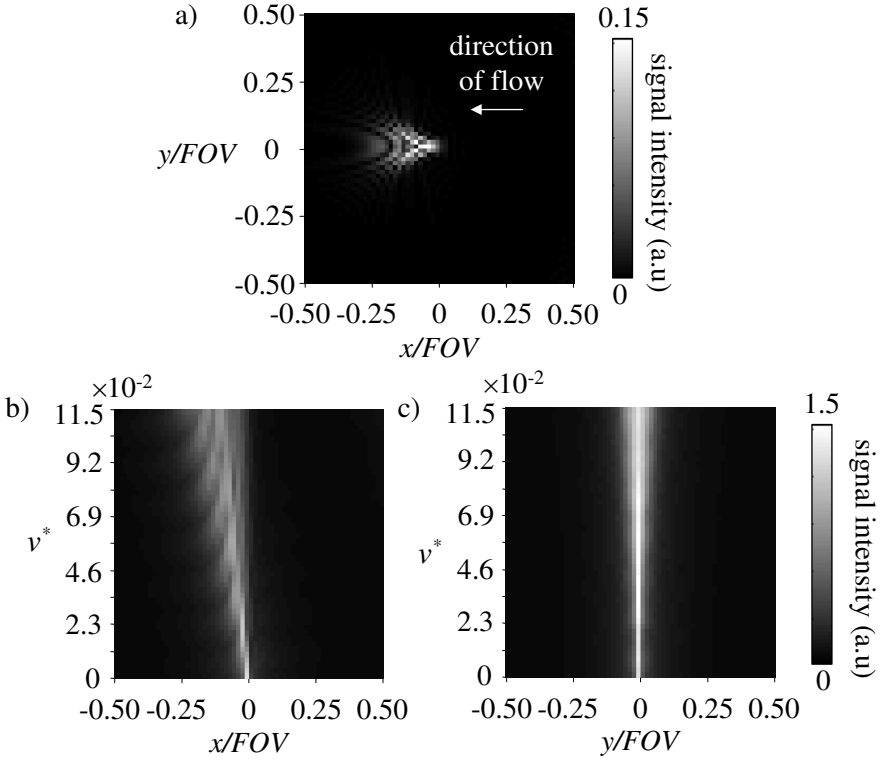


Figure 4.9: a) The effect of flow upon the modulus PSF for spiral imaging for a system with uniform dimensionless velocity, $v^*$, of 0.115 (spectral width of 357 kHz, $64 \times 64$ pixel image with a 5 cm $\times$ 5 cm field of view, flow velocity of 50 cm $s^{-1}$). b) The blurring of the PSF as a function of flow velocity, integrated in the $x$ direction. c) The blurring of the PSF as a function of flow velocity, integrated in the $y$ direction.

To demonstrate the effect of flow artefacts in a system of more general interest, a more complex geometry and flow field can be simulated. In particular, Stokes flow around a sphere in an infinite medium is presently examined, for which the velocity field is given for $r > a$ by [37]:

$$u_r = u_\infty \cos\theta \left(1 - \frac{3}{2}\frac{a}{r} + \frac{1}{2}\frac{a^3}{r^3}\right) \tag{4.5}$$

$$u_\theta = -u_\infty \sin\theta \left(1 - \frac{3}{4}\frac{a}{r} - \frac{1}{4}\frac{a^3}{r^3}\right) \tag{4.6}$$

where $r$ and $\theta$ are polar coordinates, and $u_\mathrm{r}$ and $u_\theta$ are the radial and tangential velocities, respectively. The radius of the sphere is given by $a$, and $u_\infty$ is the unidirectional velocity of the fluid an infinite distance away from the sphere. Figure 4.10 a) shows the input

geometry and velocity field, while b) and c) show the resultant modulus and phase images. Data are shown for a 50 cm $s^{-1}$ flow around a 0.8 cm radius sphere with image resolution of 780 µm $\times$ 780 µm.

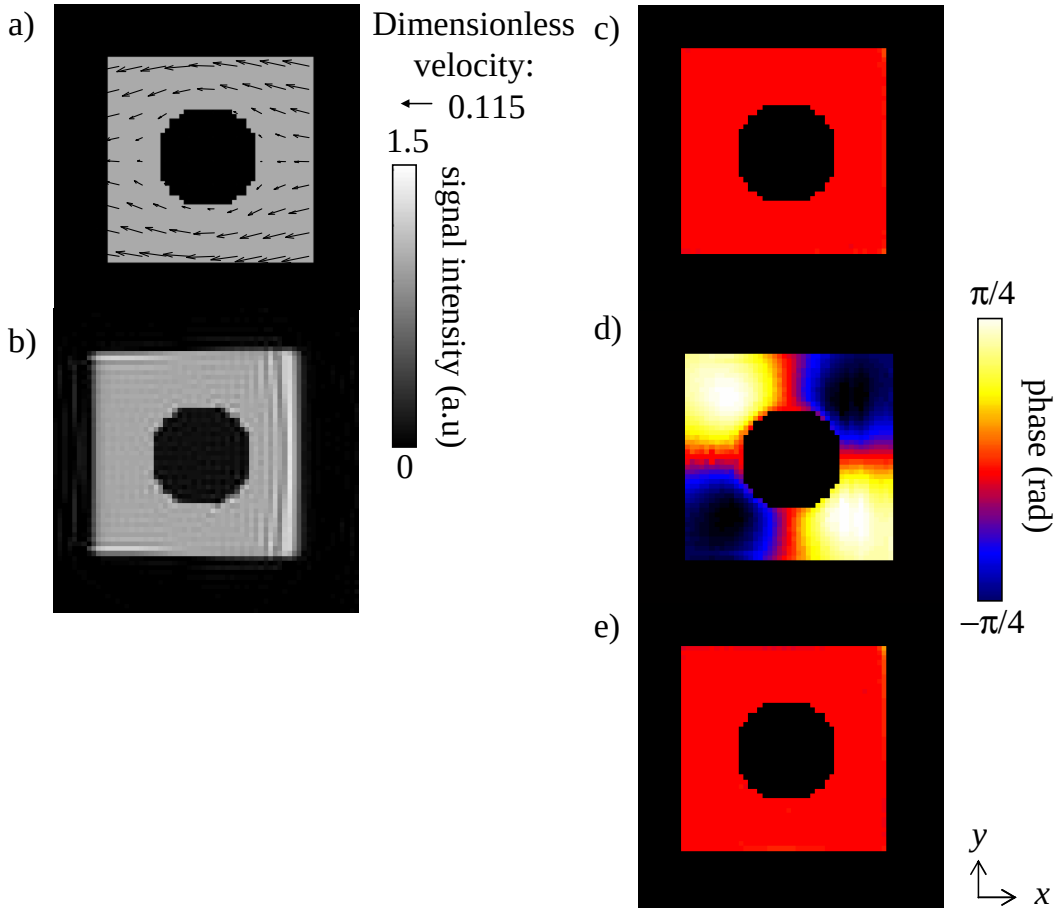


Figure 4.10: a) Input geometry and velocity field for Stokes flow around a 0.8 cm radius sphere in a 3.5 cm $\times$ 3.5 cm box of fluid with a far-field dimensionless velocity of 0.115. b) Modulus and c) phase images for a simulated acquisition with flow artefacts. d) Phase map for an image with simulated velocity encoding in the y-direction and e) difference image for pre- and post-acquisition phase maps.

As expected, the substantial in-plane flow present in this simulation has an adverse effect upon the modulus image (b). The whole image is seen to shift in the direction of flow, concurrent with the behaviour of the PSF. A ringing artefact, caused by the oscillations of the PSF, is most clearly visible at the inflowing edge of the simulated phantom where the dispersed signal from the edge adds constructively with the non-displaced signal in the centre. The outflowing edge of the simulated phantom appears blurred, with high-resolution signal from that region displaced off the edge of the simulated region. These artefacts occur over a distance of approximately one quarter of the field of view of the

image, in accordance with equation (4.4). The same artefacts are not visible on the fore and aft sides of the sphere because the flow field is derived with a no-slip condition on this boundary. This point has important implications for real systems, where velocities near a boundary are generally significantly decreased from those in the bulk (even for liquid-liquid or gas-liquid interfaces where some slip exists). Because the distortion of the PSF is largely limited to signals sampled in the high spatial frequency edges of **k**-space (i.e. those pixels next to an edge in image space), for systems in which fast flows are limited to regions in the bulk fluid (and are therefore represented by low spatial frequency Fourier coefficients), substantially less distortion of the image should be expected. Additionally, the flow artefacts present on the inflowing and outflowing edges of a sample may be minimised by $B_1$ heterogeneity in that region, which will result in a gradually attenuated edge to the image. Thus, the practical implementation of spiral imaging (particularly to those systems which lack high resolution flow features) is likely to be more robust to flow than suggested by the PSF.

The effect of flow upon the phase image is demonstrated in Figure 4.10 c). It is clear that no significant first moment phase accrued during imaging is transmitted through to the phase image. In simulations extending the range of flow rates examined, no significant error or artefact was visible in the phase image for velocities in excess of 2 m $s^{-1}$. To test the effect of including higher resolution features in the phase image, we simulated a velocity encoded acquisition. This was done by providing an initial phase map in proportion to the $y$-velocity component, shown in Figure 4.10 d), prior to performing the simulated acquisition. A difference map between the initial and final phase maps is shown in Figure 4.10 e). It is clear that the ringing and blurring artefacts visible in the modulus image are not present in the phase image. The lack of sharp structures in the flow is representative of many real physical systems, for which velocity images will be very robust to flow artefacts. If high spatial resolution velocity features are to be imaged, the PSF must be considered and blurring will be described by equation (4.4). Within these considerations it is thus evident that spiral imaging is capable of producing quantitative velocity-proportionate phase even in the presence of high in-plane velocities. This is verified experimentally in Section 4.2.4. The robustness of the phase image to error suggests that, as long as other sources of phase error are small, spiral imaging does not intrinsically require the subtraction of a reference image. For the removal of phase accrued due to off resonance effects, eddy currents and reconstruction error it has been previously suggested that phase reference data may be generated from stationary fluid included in the imaging region [38, 39].

As a final note, if flow artefacts are judged too severe they can be further reduced by the implementation of a variable density spiral sampling trajectory. To demonstrate this, Figure 4.11 shows a simulation of a 50% undersampled spiral, otherwise identical to the simulations shown in Figure 4.10, with the image reconstructed using an iterative compressed sensing procedure [40]. The flow artefacts at the image boundaries in the modulus image shown in Figure 4.11 b) are greatly decreased from those exhibited by the fully sampled spiral given in Figure 4.10 b). Note that the application of a compressed sensing reconstruction for velocity encoded images has been previously demonstrated [41, 42, 43], and is discussed in detail in Section 4.3.

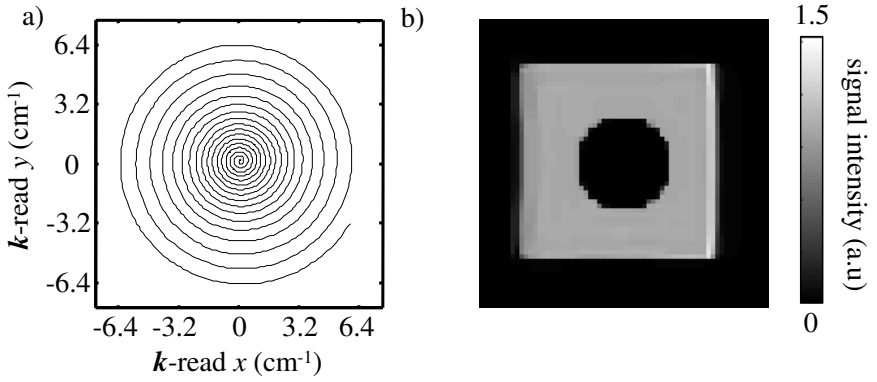


Figure 4.11: a) 50% undersampled spiral image trajectory and b) modulus of image reconstructed using compressed sensing. Note the flow artefacts are greatly decreased compared to those acquired using a full spiral.

### 4.2.3 Experimental

The pulse sequence for phase contrast spiral imaging is shown in Figure 4.12. The slice selection gradient was flow compensated [44], and the velocity encoding lobes (where employed) were applied simultaneously to the slice gradient flow compensation. The image readout gradients followed the maximum gradient limited spiral trajectory, determined as described by Glover *et al.* [17]. The total acquisition time, $AQ$, was 12.5 ms obtained at a rate of 55 frames per second (fps) for $64 \times 64$ pixel images and 5.4 ms at a rate of 91 fps for $32 \times 32$ pixel images (a minimum recycle time of 5.5 ms was imposed by the spectrometer software). The liquid phase used in all experiments was distilled water doped with a paramagnetic salt to render the solution magnetic susceptibility matched to air (as described in Section 3.1.1), and to shorten the relaxation times of the solution (in the present experiments $T_1 = 61$ ms and $T_2 = 50$ ms at $B_0 = 9.4$ $T$). All images

were acquired using a low tip-angle 512 μs Gaussian excitation pulse (5.6° for 32 × 32 pixel images and 11.25° for 64 × 64 pixel images). This low tip-angle permitted rapid repeat acquisitions with minimal relaxation weighting. To verify that no coherent first moment phase was being accrued during imaging, $x$-$z$ plane spiral images (where the $z$-coordinate is aligned with the direction of flow) were acquired of laminar flow in a 3 mm tube for comparison with fluid mechanics theory. In a pipe of this diameter laminar flow is achievable for centreline velocities up to 133 cm $s^{-1}$ (Re = 2,000), although to maintain fully developed laminar flow we only examined centreline velocities up to 60 cm $s^{-1}$ (Re = 900). This flow was gravity driven, and controlled using a rotameter and needle valve. In order to quantify the signal attenuation associated with intravoxel phase dispersion, spiral images without velocity weighting were acquired of flow in a pipe of diameter 16 mm for the range Re = 500 to 12,000 (equivalent to superficial velocities in the range 3.1 cm $s^{-1}$ to 75.0 cm $s^{-1}$). Non-velocity encoded EPI images were also acquired. In addition, velocity encoded images were acquired of flows in this range to demonstrate the usefulness of spiral imaging for characterising the transient instabilities associated with turbulent flow. In all experiments, reference phase maps were acquired of non-flowing systems, and subtracted from the images of flowing systems for the removal of image reconstruction, eddy-current and $B_0$ inhomogeneity phase errors.

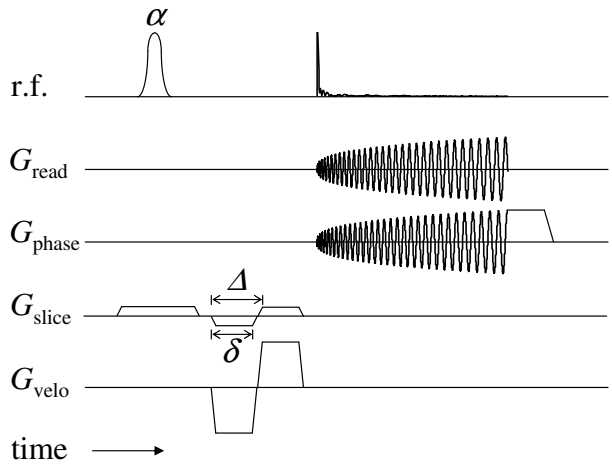


Figure 4.12: Pulse sequence for low-angle, snap-shot spiral imaging. For a 32 × 32 pixel image $\alpha = 5.6°$, and for a 64 × 64 pixel image $\alpha = 11.25°$.

All measurements were performed on a Bruker AV-400 spectrometer, operating at a $^1$H resonance frequency of 400.25 MHz. A three-axis, shielded micro-imaging gradient system with a maximum strength of 146 G $cm^{-1}$ was used for zeroth and first gradient moment encoding, and a 25 mm diameter birdcage r.f. coil was used for excitation and signal reception. For all experiments involving velocity encoding, the flow encoding

time ($\delta$) was 416 μs, and the flow contrast time ($\Delta$) 516 μs. The **k**-space trajectory followed during acquisition was measured using a modified version of the technique of Duyn et al. [11], as described in Section 4.1.1. To correct for the disparity in the sampling density of **k**-space associated with spiral imaging, all acquired data were weighted using a Voronoi sampling-density compensation function [45] prior to image reconstruction using a non-uniform fast Fourier transform [25].

### 4.2.4 Results

The simulations provided in the previous section predicted minimal error in the phase image due to in-plane flow for spiral imaging. We presently validate this hypothesis experimentally. Additionally, we explore the degree to which spiral imaging is afflicted by signal attenuation caused by shear induced turbulence, which is another significant flow artefact commonly associated with echo-planar type sequences. The error in modulus and phase images acquired using EPI and spiral imaging are then compared. Finally, we demonstrate some examples of spiral imaging based velocity measurements on high-shear, unsteady flow systems.

#### Error in the phase image

The theory and simulations suggest that the accrual of first moment imaging phase should not introduce substantial errors into the phase image. We have validated this assertion experimentally by acquiring longitudinal plane spiral images, with and without velocity encoding, for laminar flow in a pipe. By using a small diameter pipe (3 mm) we were able to maintain laminar flow up to a centreline velocity of 60 cm $s^{-1}$ (Re = 900). Figure 4.13 shows both a phase profile extracted from a non-velocity encoded image and a comparison of a velocity profile at this flowrate with the theoretical result of Hagen-Poiseuille [46]. That no significant phase shift is present in the former, while good agreement between experiment and theory is evident in the latter, reinforces that no significant systematic error due to the imaging gradients is present in the phase image. A small phase offset of approximately 0.05 radians was noted in the velocity unencoded profile, and also for images of stationary systems; the origin of this error is most likely to be phase accrual due to off-resonance effects. The noise level in the profile corresponds to a measurement error of approximately 2%.

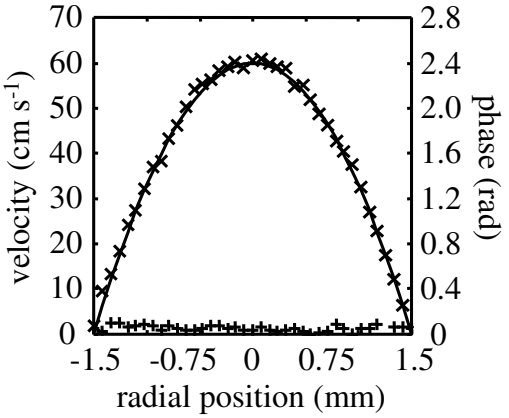


Figure 4.13: Velocity profile obtained from a phase image for a system with high in-plane flow with (×) and without (+) flow encoding gradients. The velocity profile expected from fluid mechanics theory for laminar flow is also shown (line). These images were obtained with a 5 mm field of view and a resolution of 78 μm. The lack of phase in the image without flow encoding gradients and the good agreement between theory and experiment when the flow encoding gradients are turned on suggests that no significant velocity encoding is occurring due to the imaging gradients and that flow measurement is quantitative.

### Signal attenuation due to high-shear

It is well known that turbulent flow in the presence of a magnetic field gradient (either due to $B_0$ inhomogenity [47] or applied gradients [48]) leads to localised signal attenuation. This occurs due to the presence of substantially different velocities in close proximity to each other, which when combined with some degree of first moment phase accrual, leads to different phases mixing within individual voxels. These phases add destructively to attenuate the net signal for a particular voxel. It is clear from the distortion of the PSF, as shown in Figure 4.9, that the accumulation of first moment imaging phase can have a significant effect upon the modulus image, and in this section we seek to quantify the signal attenuation due to intravoxel phase dispersion. In doing this, non-velocity encoded cross-sectional plane images were acquired of turbulent flow in a 16 mm diameter pipe up to a Reynolds number of 12,000. By comparing the modulus of these images with a reference image of stagnant liquid, a measurement of signal attenuation as a function of Reynolds number was extracted. These data are shown in Figure 4.14. The mean error present at Re = 0 represents a measurement error due to noise of 0.6%. It is evident that shear induced signal attenuation is insubstantial for spiral imaging, with a mean error of approximately 3.5% for a Reynolds number of 12,000. The reason this error is so small is likely due to the centre of **k**-space (and hence the bulk of the signal intensity) being acquired at the start of the sequence, when little or no first moment imaging phase

exists. Thus spiral imaging overcomes the shear artefact which afflicts EPI images, and is a propitious basis for the visualisation of bubbly flow. The application of spiral imaging to our model bubbly flow system is examined in Chapter 5.

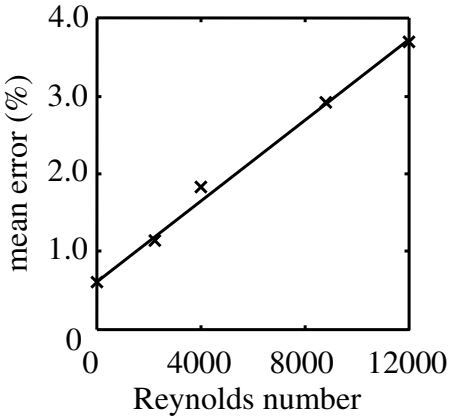


Figure 4.14: Error in the signal modulus as a function of Reynolds number for spiral imaging of single phase flow in a pipe of diameter 16 mm. A linear trend fitted to the data is shown to guide the eye.

**Comparison of spiral imaging and EPI in application to unsteady flow systems**

Given the minor accrual of first moment imaging phase, spiral imaging seems an auspicious basis for snap-shot velocity imaging of unsteady flow. Spiral imaging is advantageous compared to EPI in this application, as it removes the systematic error in the phase image associated with the imaging gradients. This is demonstrated in Figure 4.15, which shows a comparison of non-velocity encoded blipped-EPI and spiral images of turbulent flow in a pipe at a Reynolds number of 8,800. Both modulus and phase images are shown. It is clear that while significant shear attenuation is present in the modulus EPI image (mean error of 24.8%), the spiral image is much more robust (mean error of 2.8%; in accordance with Figure 4.15). Furthermore, significant coherent structures exist in the EPI phase image, reflecting that flow encoding has occurred in one direction due to the imaging gradients. Conversely, no phase exists in the spiral image, which reflects the robustness of the technique to flow. The degree of error present in the EPI images is, of course, a function of the imaging gradient strength used and transverse plane velocity components. Of course, EPI may still be appropriate for application to unsteady flow systems as long as the accrual of error within the bounds of these parameters is acceptable.

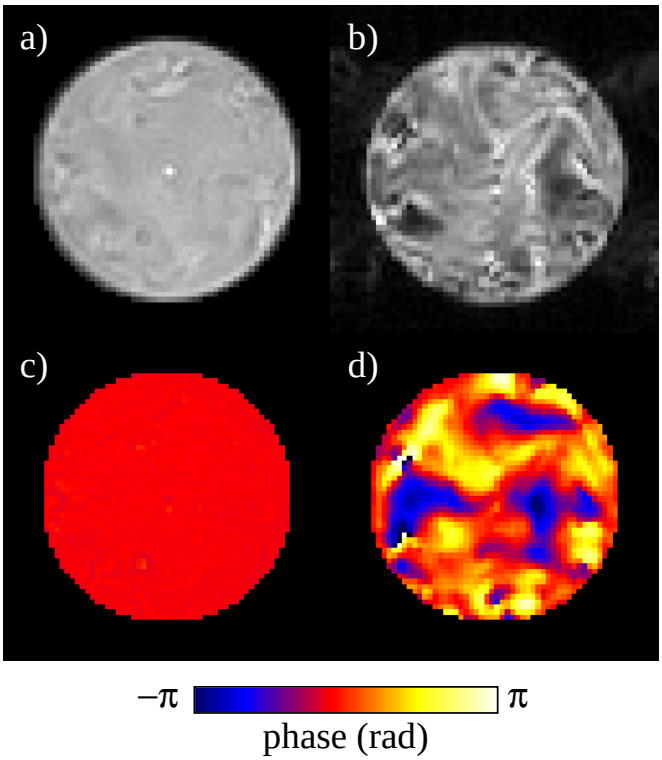


Figure 4.15: Comparison of non-velocity encoded spiral and EPI images of turbulent pipe flow at a Reynolds number of 8,800 in a pipe of inside diameter 16 mm. Modulus images are shown for a) spiral imaging and b) EPI. Phase images are shown for c) spiral imaging and d) EPI. The in-plane shear and velocity result in attenuation of the signal and the accrual of significant phase shifts during EPI, but not spiral imaging. Note that the slice selection gradients were velocity compensated for both imaging techniques. The spatial resolution is 313 μm ×313 μm for a field of view of 20 mm × 20 mm.

### Application of spiral imaging to unsteady flow systems

Given the minor accrual of first moment imaging phase, spiral imaging seems an auspicious basis for snap-shot velocity imaging of unsteady flow. Spiral imaging holds several advantages over EPI in this respect: as discussed it removes the systematic error in the phase image associated with the imaging gradients, and it also acquires an image directly from an FID, which significantly decreases the acquisition time and allows smaller tip angles to be used; permitting rapid repeat excitations without relaxation weighting. This latter point allows some highly transient flow features to be imaged for the first time. Consider, for example, Figure 4.16, which shows a number of time sequential velocity images of unsteady flow in a pipe (Re = 4500). Attention is drawn to the wall region, where an instability is visible extending from the wall; snaking to and fro in the main body of the fluid. The acquisition rate of these images (91 Hz) is just sufficient to characterise this highly transient fluid phenomenon.

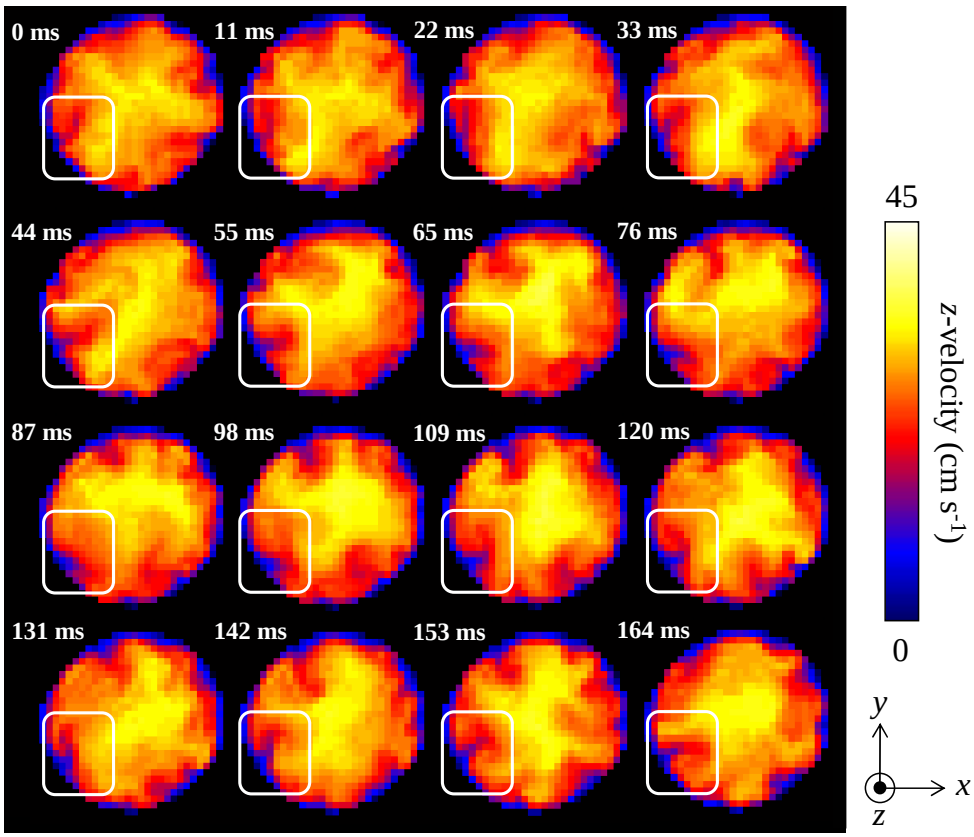


Figure 4.16: Cross-sectional maps of the z-velocity of unsteady flow acquired using spiral imaging (Re = 4,500). The transient behaviour of a wall instability is highlighted. The acquisition rate of these images is 91 fps. The times shown on the images refer to the start of the acquisition. The spatial resolution is 625 μm × 625 μm for a field of view of 20 mm × 20 mm.

An interesting juxtaposition exists between these data and those of Sederman *et al.* [36], who acquired multiple sequential images of turbulent flow from the same excitation using EPI. Whereas they noted the turbulent structures to be relatively constant over an 80 ms period, from the present images it is clear that the flow field changes substantially over the course of 10 ms. The reason for this disparity is that the present images (which were each acquired from a fresh excitation) show an Eulerian velocity represented in an Eulerian frame of reference, whereas those acquired by Sederman *et al.* depict an Eulerian velocity however now in the Lagrangian frame. The difference between these two measurements lies in the way they observe changes to the flow field; while the sequence of velocity measurements obtained using spiral imaging are acquired at a fixed spatial location, the measurements of Sederman *et al.* were acquired from repeatedly refocused magnetisation and therefore yield signal from a mobile packet of fluid. To demonstrate this difference,

consider Figure 4.17, which shows longitudinal plane velocity images of the turbulent flow system examined above. It is clear from these images that the unsteady features (that is the regions of fast and slow moving fluid immediately adjacent to each other) are transmitted along the pipe as coherent and relatively slowly evolving structures. These structures are seen to move along the pipe at approximately the superficial velocity of the fluid, and in this context are stable for approximately 80 ms; this observation is consistent with the findings of Sederman *et al.* [36]. Figure 4.17 also demonstrates the successful application of spiral imaging for velocity measurements on a system which contains high in-plane flows. According to equation (4.4), blurring of the PSF can be expected over a maximum of 10 mm (approximately 10 pixels) in this image in the direction of flow. This blurring is substantial, and can only be decreased by shortening the acquisition time. The combination of undersampled, velocity-encoded spiral imaging and compressed sensing for high temporal resolution velocity imaging of unsteady flow systems is examined in Section 4.3.

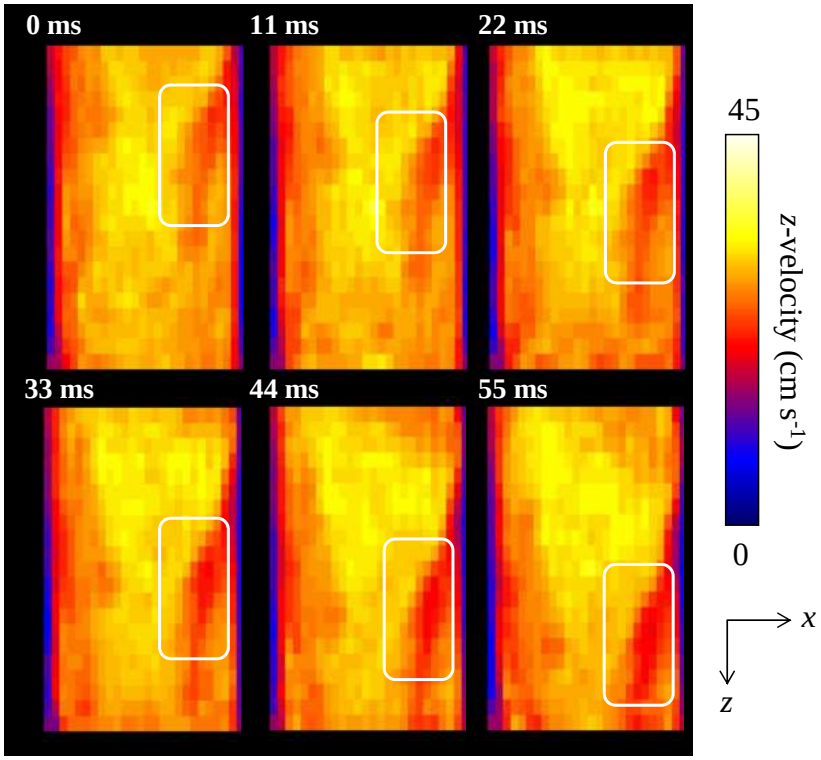


Figure 4.17: Longitudinal maps of the $z$-velocity of fully developed turbulent flow acquired using spiral imaging (Re = 4,500). A slowly evolving turbulent structure is highlighted by the rounded white box. The acquisition rate of these images is 91 fps. The times shown on the images refer to the start of the acquisition. The spatial resolution is 625 µm × 984 µm for a field of view of 20 mm × 31.5 mm.

While in the present work unsteady single phase pipe flow is used as a convenient test case

for the demonstration of velocity encoded spiral imaging, these data do hold significant scientific merit. The transition from laminar to turbulent flow is an area of active research in fluid mechanics [49, 50], and quantitative velocity measurements that represent the formation of turbulent instabilities are insightful for the formulation of models, and necessary for the validation of computational fluid dynamics codes. MRI holds several unique advantages over other techniques for the measurement of this type of information, such as particle imaging velocimetry (PIV) [51] or laser Doppler anemometry (LDA) [52]. In particular, both PIV and LDA require the introduction of tracers or particles to the system, and assume that motion of these particles accurately represents that of the fluid. MRI, on the other hand, is completely non-invasive, and obtains a measurement directly from the fluid. Further, as discussed above, MRI can yield measurements in either an Eulerian or Lagrangian frame of reference. Finally, being non-optically based, MRI is capable of producing measurements in opaque systems, and at any orientation.

## 4.3 High temporal resolution velocity imaging using compressed sensing

The images shown in Figures 4.16 and 4.17 demonstrate the potential for spiral imaging to quantitatively characterise highly transient flow features for unsteady systems. These data, however, represent only single component velocity maps, are of quite low spatial resolution (at best, 625 μm), and suffer from substantial blurring caused by in-plane flow (particularly for the vertical plane images, which were blurred over 10 mm). As discussed in Section 2.5, it is possible to decrease image acquisition times by undersampling, and as long as the undersampling artefacts are rendered noise-like, they can be removed by enforcing sparsity in some transform domain. This process is known as compressed sensing, which has been recently demonstrated as a promising avenue for decreasing MRI data acquisition times [40, 53]. Spiral imaging lends itself well to the implementation of undersampling schemes, as the density of the spiral revolutions can be tuned to fully sample the centre of **k**-space, while sparsely sampling the outer edges. Further, the non-idealities associated with fast spiral trajectories (which necessitate the use of gradient trajectory measurement, as discussed in Section 4.1.1) introduce a stochastic element to the sampled points, which helps maintain the incoherence of the undersampling artefacts. In this section, compressed sensing is applied to speed up velocity encoded spiral acquisitions: enabling higher spatial and temporal resolutions, and permitting more velocity information to be obtained. The only previous studies to combine compressed sensing with velocity encoded acquisitions are those of Gamper *et al.* [41], Holland *et al.* [42] and

Bajaj *et al.* [43].

### 4.3.1 Experimental

Undersampled, velocity encoded spiral images have been acquired of flow in a 16 mm internal diameter pipe at Reynolds numbers of 500 and 4,500. The solution used in these experiments was 16.86 mM dysprosium chloride. The trajectory used in these experiments is shown in Figure 4.18. The density of this spiral is weighted by a Gaussian function such at the central points are almost fully sampled while the outer edges of **k**-space are sampled progressively more sparsely. Only 1175 complex data points are sampled on this trajectory, which is 28.7% of those required for a fully sampled 64 pixel × 64 pixel image.

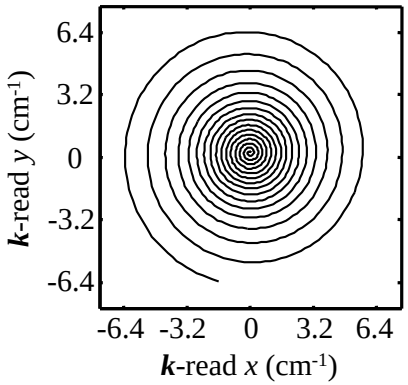


Figure 4.18: Variable density spiral used for undersampled acquisitions. This trajectory samples 1175 complex datapoints, which is 28.7% of those required for a fully sampled 64 pixel × 64 pixel image.

The read-out time of the images was 2.94 ms. To further increase acquisition speed, the excitation pulse length was decreased to 256 μs, with the flow encoding and contrast times of 368 μs and 388 μs, respectively. This provides a total time for each image of 5.30 ms. Further, following upgrades to the spectrometer software, the previous minimum recycle time was removed, and images were acquired at a rate of 188 fps. The tip-angle used in all experiments was 5.6°. All other experimental parameters were identical to those described in Section 4.2.3. Gradient trajectories were measured as described in Section 4.1.1. Initial image reconstructions were performed using a non-uniform fast-Fourier transform [25] with a Voronoi density compensation function [45]. A compressed sensing reconstruction was performed using the MATLAB package of Lustig [54], with image sparsity enforced in the wavelet domain using the wavelet toolbox of Donoho *et al.* [55]. Note that the compressed sensing reconstruction was performed on the real and imaginary components of the image separately, prior to the calculation of a phase image.

### 4.3.2 Results

To demonstrate that quantitative velocity information is preserved throughout the compressed sensing reconstruction, images were firstly acquired of laminar pipe flow (Re = 500). A flow encoded image is shown in Figure 4.19 a), and an extracted profile in comparison to the model of Hagen-Poiseuille in b). No undersampling artefact is evident in a), and good agreement is between theory and experiment is evident in b), which suggests that the true image is being recovered by the compressed sensing reconstruction procedure, and quantitative phase information is being retained.

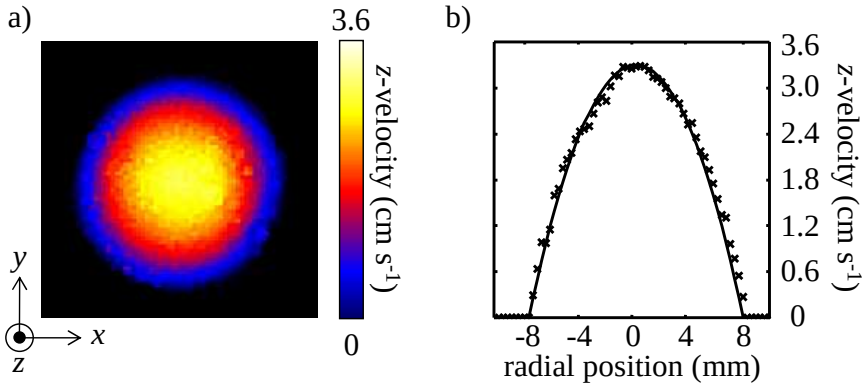


Figure 4.19: a) An undersampled velocity image reconstructed using compressed sensing. b) A velocity profile extracted from a) in comparison with fluid mechanics theory. It is clear that the quantitative phase map is being recovered by the compressed sensing procedure. The spatial resolution is 312.5 μm × 312.5 μm for a field of view of 20 mm × 20 mm.

High-spatial (312.5 μm × 312.5 μm) and temporal (188 fps) single component velocity images of unsteady flow at a Reynolds number of 4,500 are shown in Figure 4.20. Horizontal plane images are shown in a), and vertical plane in b). The flow features here are resolved in much greater detail than in Figures 4.16 and 4.17; particularly in the vertical plane. This is aided by both the increased spatial resolution, and reduced blurring associated with the shortened acquisitions time. All of the flow features present in the fully sampled images are evident, including the fingering wall instabilities and more slowly evolving turbulent structures. According to equation (4.4), blurring is expected over a maximum of 2.9 mm in the vertical plane images, which corresponds to 6 pixels. This represents a significant improvement over the fully sampled images, and is considered acceptable given the inevitability of some blurring when imaging fast in-plane flows.

Little change is evident in the horizontal plane data over any three sequential images shown in Figure 4.20 a). To quantify the change between these images it is possible to

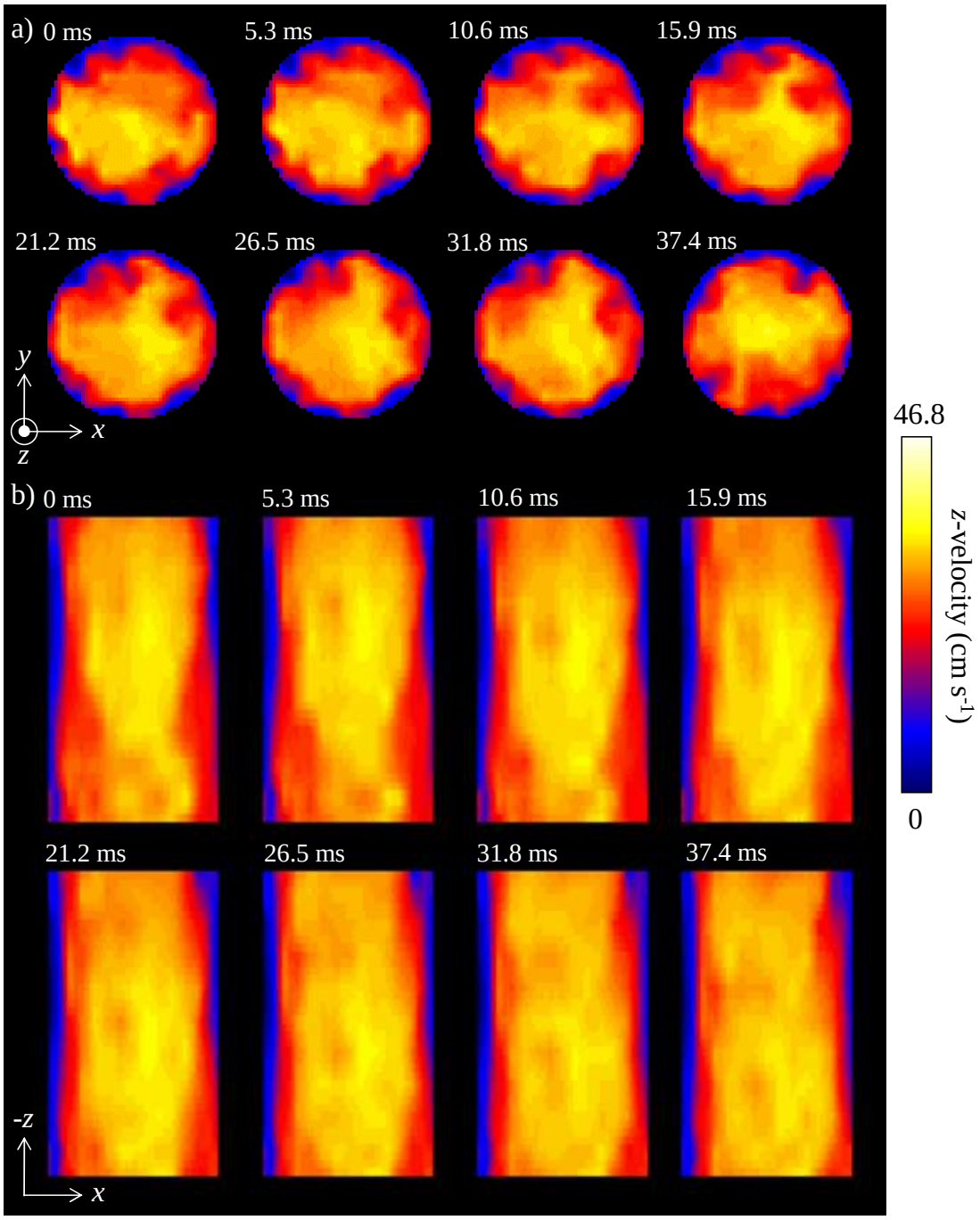


Figure 4.20: a) Horizontal and b) vertical plane velocity images of unsteady flow at Re = 4,500. The spatial resolution is 312.5 μm × 312.5 μm for a field of view of 20 mm × 20 mm in the horizontal plane images, and 312.5 μm × 492 μm for a field of view of 20 mm × 31.5 mm in the vertical plane images. The indicated times represent the start of each acquisition.

calculate a velocity auto-correlation function (VACF) [56, 36]:

$$R_{\mathrm{v}}(t_2) = \frac{\langle v(t_1)v(t_2)\rangle}{\langle v(t_1)^2\rangle} \tag{4.7}$$

where $v$ represents the instantaneous velocity at a given time. Velocity autocorrelation maps for images acquired between $t_1 = 0$ ms and $t_2 = 15.9$ ms are shown in Figure 4.21.

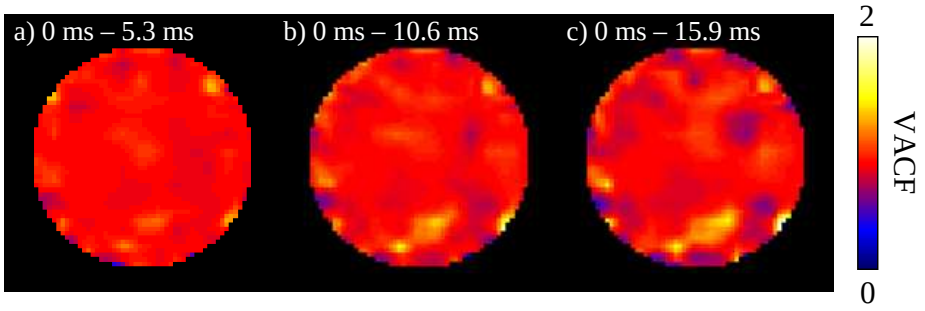


Figure 4.21: Velocity autocorrelation functions demonstrating the difference between images acquired at a) 0 ms and 5.3 ms, b) 0 ms and 10.6 ms and c) 0 ms and 10.9 ms.

It is clear from Figure 4.21 that at most 15% difference exists between images acquired at 0 ms and 10.6 ms, and in general much less than this. This suggests that by acquiring images velocity encoded in the $z$, $x$ and $y$ directions sequentially, that three component velocity images may be produced that represent an effectively instantaneous 'snap-shot' of the flow. Horizontal plane data of this type are shown in Figure 4.22 a). The formation of vortices in the transverse plane data may clearly be observed at the walls of the column, and is seen to be coupled with the fingering instabilities previously observed. While the development and evolution of in-plane flow structures may be observed in the wall region, fewer coherent velocity structures are visible from image-to-image in the bulk flow. This is to be expected as the greater through-plane flow in this region conveys the fluid out of the imaging plane from frame-to-frame.

Vertical plane, three-component velocity maps are shown in Figure 4.22 b). The superficial liquid velocity has been subtracted from this image, and $z$-component of the velocity vectors are scaled back to 8% of their original magnitude in order to render the in-plane flow features visible. It is clear that recirculating vortices were present in the longitudinal plane as well as the transverse plane, and were conveyed down the column at the superficial velocity of the liquid. The vortices are seen to accompany through-plane motion, which in these images correspond to the transverse plane vortices seen in Figure 4.22 a). This reflects the three dimensional nature of the vortical structures exhibited

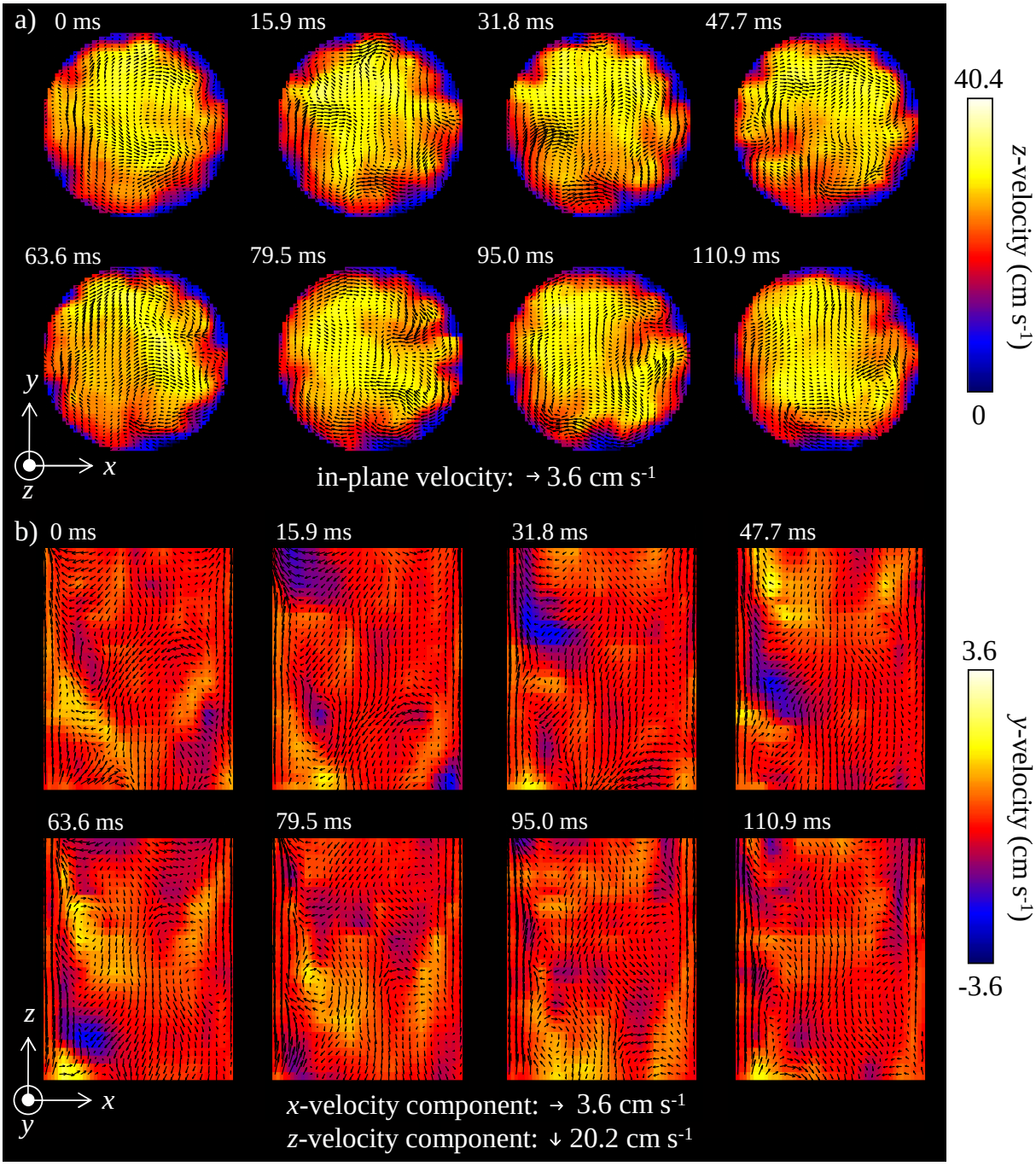


Figure 4.22: a) Horizontal and b) vertical plane velocity three-component velocity images of unsteady flow at Re = 4,300. Note that the magnitude of the $z$-component of the velocity vectors is reduced to 8% of the true length, and the mean liquid flow rate has been subtracted, to enhance the clarity of the flow features. The spatial resolution is 312.5 µm × 312.5 µm for a field of view of 20 mm × 20 mm in the horizontal plane images, and 312.5 µm × 492 µm for a field of view of 20 mm × 31.5 mm in the vertical plane images. The indicated times represent the start of each acquisition.

by turbulent flows. The through plane velocity map in Figure 4.22 b) also reveals some information about the evolution of turbulent vortices. The vortices are seen to begin extended far out into the bulk fluid, before becoming skewed as different parts of the vortex are conveyed down the tube at different rates. This leads to a long tail of rotating fluid near the wall, and a 'puff' of turbulence being conveyed along the tube. Turbulent puffs such as this are commonly associated with transitional flows [57], and these data may provide an interesting new insight into their origin.

These data demonstrate the great potential held by undersampling and compressed sensing for the characterisation of highly transient systems. While further undersampling of these images was found to introduce artefacts which could not be corrected using compressed sensing, additional increases to the temporal resolution of the technique may yet be possible. This may be achieved by employing a three-dimensional compressed sensing reconstruction using time as a psuedo-spatial third dimension. It is noted by Càndes [58] that sparsity tends to increase with the amount of dimensions sampled, which will be particularly true for the present system where only very minor changes exist from frame-to-frame. Thus with further undersampling, and a multidimensional compressed sensing reconstruction procedure, the spatio-temporal balance of velocity encoded spiral imaging may be further improved, which will broaden the applicability of the technique.

## 4.4 Conclusions

Spiral imaging has been assessed as a technique for acquisition of temporally resolved images of high-shear systems, and for the measurement of quantitative velocity fields of unsteady flow. In the implementation of fast spiral imaging it is necessary that gradient trajectories be measured, and used in image reconstruction. Two approaches were assessed for the measurement of these gradient waveforms: magnetic field monitors and imaging based techniques. The former proved to be unsuitable for use with a plastic-lined imaging coil, however good results were obtained with the latter. Spiral imaging was shown to be more susceptible than EPI to off-resonance effects, which was attributed to the low effective image bandwidth in both read directions, however as the examined systems are magnetic susceptibility matched, this was not judged to be problematic for the present study.

The effect of flow on spiral images was examined in detail. In particular, extent of the distortion of the PSF due to flow was quantified using simulated acquisitions, however it

was noted that the impact of this artefact is minimal for many physical systems. This is because flows near an edge in image space (i.e. corresponding to heavily first moment weighted high-frequency Fourier coefficients) are boundary affected and thus are often significantly decreased from the bulk fluid velocity. The shear induced, localised attenuation in the modulus image was also quantified, and errors found to be less than 3.5% for flows up to a Reynolds number of 12,000 for single phase flow in a pipe. These errors are likely so small due to the early sampling of the centre of **k**-space associated with spiral imaging. Non-velocity encoded images acquired using both EPI and spiral imaging of turbulent pipe flow were compared, with significant errors in the modulus and velocity proportionate phase present in the EPI images. Conversely the spiral images were relatively robust in both the modulus and phase images. This demonstrates the superiority of spiral imaging for the measurement of quantitative velocity fields of unsteady systems. The acquisition of velocity fields using spiral imaging was then demonstrated on some example unsteady flow systems. Turbulent flow in a pipe was imaged at a time resolution of 91 fps, and the behaviour of highly transient wall instabilities were captured using MRI for the first time.

To reduce blurring and improve the spatio-temporal resolution of these measurements, compressed sensing was applied to undersampled acquisitions. It was firstly shown that quantitative velocity information is retained throughout the compressed sensing reconstruction by application of the technique to laminar flow in a pipe, with good agreement with fluid mechanics theory evident. Images sampled at 28.7% of the data required for a fully sampled **k**-space raster were then acquired of turbulent flow at a Reynolds number of 4,300. These data were acquired at 188 fps, and at twice the spatial resolution of the fully sampled images. At this temporal resolution, it was clear that only minor changes to the flow structure occur over any three subsequent images, which allowed three images, each with velocity encoding in a different direction, to be acquired for the reconstruction of three component velocity vectors that represent an effective instantaneous 'snap-shot' of the flow. Spiral imaging, particularly when accelerated using compressed sensing, was thus shown to be a very promising basis for the acquisition of temporally resolved velocity maps of unsteady systems. The application of spiral imaging to bubbly flow is considered in the following chapter.

# Bibliography


[1] Duerk, J.L. and Simonetti, O.P., 1991. Theoretical aspects of motion sensitivity and compensation in echo-planar imaging. *J. Magn. Reson. Im.*, 1, pp. 643–650.

[2] Ahn, C.B., Kim, J.H. and Cho, Z.H., 1986. High-speed spiral scan echo planar NMR imaging - I. *IEEE T. Med. Imaging*, 5, pp. 2–5.

[3] Delattre, B.M.A., Heidemann, R.M., Crowe, L.A., Vallee, J.P. and Hyacinthe, J.N., 2010. Spiral demystified. *Magn. Reson. Im.*, 28, pp. 862–881.

[4] Block, K.T. and Frahm, J., 2005. Spiral imaging: a critical appraisal. *J. Magn Reson. Im.*, 21, pp. 657–668.

[5] Klarhofer, M., Barth, M. and Moser, E., 2002. Comparison of multi-echo spiral and echo planar imaging in functional MRI. *Magn. Reson. Imaging*, 20, p. 359364.

[6] Truong, T. and Song, A., 2009. Single-shot dual-z-shimmed sensitivity encoded spiral-in/out imaging for functional MRI with reduced susceptibility artifacts. *Magn. Reson. Imaging*, 59, pp. 221–227.

[7] Nayak, K., Cunningham, C., Santos, J. and Pauly, J., 2004. Real-time cardiac MRI at 3 Tesla. *Magn. Reson. Imaging*, 51, pp. 655–660.

[8] Ryf, S., Kissinger, K.V., Spiegel, M.A., Börnert, P., Manning, W.J., Boesiger, P. and Stuber, M., 2004. Spiral MR myocardial tagging. *Magn. Reson. Imaging*, 51, pp. 237–242.

[9] O'Sullivan, J., 1985. A fast sinc function gridding algorithm for fourier inversion in computer tomography. *IEEE Trans. Med. Imaging*, 4, pp. 200–207.

[10] Jackson, J., Meyer, C.H., Nishimura, D.G. and Macovski, A., 1991. Selection of a convolution function for fourier inversion using gridding. *IEEE Trans. Med. Imaging*, 10, pp. 473–478.

[11] Duyn, J.H., Yang, Y., Frank, J.A. and van der Veen, J.W., 1998. Simple correction method for k-space trajectory deviations in MRI. *J. Magn. Reson.*, 132, pp. 150–153.

[12] Mason, G.F., Harshbarger, T., Hetherington, H.P., Zhang, Y., Pohost, G.M. and Twieg, D.B., 1998. A method to measure arbitrary **k**-space trajectories for rapid mr imaging. *Magn. Reson. Im.*, 38, pp. 462–496.

[13] Meyer, C.H., Hu, B.S., Nishimura, D.G. and Macovski, A., 1992. Fast spiral coronary artery imaging. *Magn. Reson. Med.*, 28, pp. 202–213.

[14] Gatehouse, P.D., Firmin, D.N., Collins, S. and Lonmore, D.B., 1994. Real time blood flow imaging by spiral scan phase velocity mapping. *Magn. Reson. Med.*, 31, pp. 504–512.

[15] Butts, K. and Riederer, S.J., 1992. Analysis of flow effects in echo-planar imaging. *J. Magn Reson. Im.*, 2, pp. 285–293.

[16] Gatehouse, P.D. and Firmin, D.N., 1999. Flow distortion and signal loss in spiral imaging. *Magn. Reson. Med.*, 41, pp. 1023–1031.

[17] Glover, G.H., 1999. Simple analytic spiral k-space algorithm. *Magn. Reson. Med.*, 42, pp. 412–415.

[18] Hu, X. and Le, T.H., 1996. Artifact reduction in EPI with phase-encoded reference scan. *Magn. Reson. Med.*, 36, pp. 166–171.

[19] Zanche, N.D., Barmet, C., Nordmeyer-Massner, J.A. and Pruessmann, K.P., 2008. NMR probes for measuring magnetic fields and field dynamics in MR systems. *Magn. Reson. Im.*, 60, pp. 176–186.

[20] Zhang, Y., Hetherington, H.P., Stokely, E.M., Mason, G.F. and Twieg, D.B., 1998. A novel **k**-space measurement technique. *Magn. Reson. Im.*, 39, pp. 999–1004.

[21] Goodyear, D.J., Shea, M., Beyea, S.D., Shah, N.J. and Balcolm, B.J., 2003. Single point measurements of magnetic field gradient waveform. *J. Magn. Reson.*, 163, pp. 1–7.

[22] Han, H., MacGregor, R.P. and Balcolm, B.J., 2009. Pure phase encode magnetic field gradient monitor. *J. Magn. Reson.*, 201, pp. 212–217.

[23] Emid, S. and Creyghton, J., 1985. High-resolution nmr imaging in solids. *Physica B & C*, 128, pp. 81–83.

[24] Bodenhausen, G., Freeman, R. and Turner, D.L., 1977. Suppression of artifacts in two-dimensional J spectroscopy. *J. Magn. Reson.*, 27, pp. 511–514.

[25] Fessler, J.A. and Sutton, B.P., 2003. Nonuniform fast fourier transform using min-max interpolation. *IEEE T. Signal Proces.*, 51, pp. 560–574.

[26] Barmet, C., M/, D. and Prüssmann, K.P., 2008. Spatiotemporal magnetic field monitoring for MR. *Magn. Reson. Med.*, 60, pp. 187–197.

[27] Pike, G.B., Meyer, C.H., Brosnan, T.J. and Pelc, N.J., 1994. Magnetic resonance velocity imaging using a fast spiral phase contrast sequence. *Magn. Reson. Med.*, 32, pp. 476–483.

[28] Nayak, K.S., Pauly, J.M., Kerr, A.B., S., H.B. and Nishimura, D.G., 2000. Real-time color flow MRI. *Magn. Reson. Med.*, 43, pp. 251–258.

[29] Park, J.B., W., O.E. and Nishimura, D.G., 2003. Rapid measurement of time-averaged blood flow using ungated spiral phase-contrast. *Magn. Reson. Med.*, 49, pp. 322–328.

[30] Nayak, K.S., Hu, B.S. and Nishimura, D.G., 2003. Rapid quantitation of high-speed jets. *Magn. Reson. Med.*, 50, pp. 366–372.

[31] Park, J.B., Santos, J.M., Hargreaves, B.A., Nayak, K.S., Sommer, G., Hu, B.S. and Nishimura, D.G., 2005. Rapid measurement of renal artery blood flow with ungated spiral phase-contrast MRI. *J. Magn Reson. Im.*, 21, pp. 590–595.

[32] Park, J.B., Hu, B.S., Conolly, S.M., Nayak, K.S. and Nishimura, D.G., 2006. Rapid cardiac-output measurement with ungated spiral phase contrast. *Magn. Reson. Med.*, 56, pp. 432–438.

[33] A., C.J.L. and Nayak, K.S., 2007. Rapid quantitation of cardiovascular flow using slice-selective fourier velocity encoding with spiral readouts. *Magn. Reson. Med.*, 57, pp. 639–646.

[34] Harloff, A., Albrecht, F., Spreer, J., Stalder, A.F., Block, J., Frydrychowicz, A., Schllhorn, J., Hetzel, A., Schumacher, M., J., H. and Markl, M., 2009. 3D blood flow characteristics in the carotid artery bifurcation assessed by flow-sensitive 4D MRI at 3T. *Magn. Reson. Med.*, 61, pp. 65–74.

[35] Nishimura, D.G., P., I. and Meyer, C.H., 1995. A velocity k-space analysis of flow effects in echo-planar and spiral imaging. *Magn. Reson. Med.*, 33, pp. 549–556.

[36] Sederman, A.J., Mantle, M.D., Buckley, C. and Gladden, L.F., 2004. MRI technique for measurement of velocity vectors, acceleration, and autocorrelation functions in turbulent flow. *J. Magn. Res.*, 166, pp. 182–189.

[37] Lamb, H., 1895. *Hydrodynamics*. Cambridge University Press, Cambridge.

[38] Tayler, A.B., Sederman, A.J., Newling, B., M.D., M. and Gladden, L., 2010. 'snapshot' velocity vector mapping using echo-planar imaging. *J. Magn. Reson.*, 204, pp. 266–272.

[39] Man, L.C., Pauly, J.M., G., N.D. and Macovski, A., 1999. Nonsubtractive spiral phase contrast velocity imaging. *Magn. Reson. Med.*, 42, pp. 704–713.

[40] Lustig, M., Donoho, D.L. and Pauly, J.M., 2007. Sparse MRI: the application of compressed sensing for rapid MR imaging. *Magn. Reson. Med.*, 58, pp. 1182–1195.

[41] Gamper, U., Boesiger, P. and Kozerke, S., 2009. Compressed sensing in dynamic MRI. *Magn. Reson. Med.*, 59, pp. 365–373.

[42] Holland, D.J., Malioutov, D.M., Blake, A., J., S.A. and Gladden, L.F., 2010. Reducing data acquisition times in phase-encoded velocity imaging using compressed sensing. *J. Magn. Reson.*, 203, pp. 236–246.

[43] Bajaj, V.S., Paulsen, J., Harel, E. and Pines, A., 2010. Zooming in on microscopic flow by remotely detected MRI. *Science*, 19, pp. 1078–1081.

[44] Pope, J.M. and Yao, S., 1993. Quantitative NMR imaging of flow. *Concept Magn. Reson.*, 5, pp. 281–302.

[45] Aurenhammer, F., 1991. Voronoi diagrams - a survey of a fundamental geometric data structure. *Comput. Surv.*, 23, pp. 345–405.

[46] Sutera, S.P. and Skalak, R., 1993. The history of Poiseuille's law. *Annu. Rev. Fluid Mech.*, 25, pp. 1–19.

[47] De Gennes, P.G., 1969. Theory of spin echoes in a turbulent fluid. *Phys. Lett. A*, 29, pp. 20–21.

[48] Fukuda, K. and Hirai, A., 1979. A pulsed NMR study on the flow of fluid. *J. Phys. Soc. Jpn.*, 47, pp. 1999–2006.

[49] Peixinho, P. and Mullin, T., 2006. Decay of turbulence in pipe flow. *Phys. Rev. Lett.*, 93, p. 094,501.

[50] Eckhardt, B., Schneider, T.M., Hof, B. and Westerweel, J., 2007. Turbulence transition in pipe flow. *Annu. Rev. Fluid Mech.*, 39, pp. 447–468.

[51] Adrian, R.J., 1991. Particle-imaging techniques for experimental fluid mechanics. *Annu. Rev. Fluid Mech.*, 23, pp. 261–304.

[52] Buchhave, P., George, W.K. and Lumley, J.L., 1979. The measurement of turbulence with the laser-doppler anemometer. *Annu. Rev. Fluid Mech.*, 11, pp. 443–503.

[53] Lustig, M., Donoho, D., Santos, J.M. and Pauly, J.M., 2008. Compressed sensing MRI. *IEEE Signal Proc. Mag.*, 3, pp. 72–82.

[54] Lustig, M. *Sparse MRI reconstruction package.* http://www.stanford.edu/ mlustig/SparseMRI.html.

[55] Donoho, D., Maleki, A. and Shahram, M. *Wavelab 850.* http://www-stat.stanford.edu/∼wavelab/.

[56] Stapf, S., 2001. Determination of velocity autocorrelation functions by multiple data acquisition in NMR pulsed-field gradient experiments. *J. Magn. Reson.*, 152, pp. 308–312.

[57] Pope, S.B., 2000. *Turbulent flows.* Cambridge University Press, Cambridge.

[58] Càndes, E.J. and Wakin, M.B., 2008. An introduction to compressive sampling. *IEEE Sig. Proc. Mag.*, 3, pp. 21–30.

# Chapter 5

# Characterisation of high-voidage bubbly flow

In this chapter the characterisation of high-voidage bubbly flow is examined. In particular, it is sought to measure the bubble size distribution, interfacial area and liquid phase hydrodynamics. The measurement of these parameters has been the focus of intense research for decades, and many different approaches to the problem have been developed (reviewed in Section 1.3). In general, these experimental techniques may be categorised as invasive, or non-invasive, and optical or non-optical. Previous studies making use of experimental techniques from each category are reviewed by Cheremisinoff [1] and Boyer *et al.* [2]. Typically, both invasive and non-invasive optical techniques (photography [3], particle image velocimetry [4] and laser Doppler anemometry [5]) are limited in application to low voidage bubbly flow ($\varepsilon < 5\%$), as the bubbles in the centre of the column are occluded for higher gas-fractions. Conversely, while non-invasive, non-optical techniques (electrical capacitance or radiography tomographies [6]) are applicable to high-voidage systems, they struggle to find the necessary balance between spatial and temporal resolution, although one exception to this is the electron beam scanning technique recently proposed by Beiberle *et al.* [7]. Finally, invasive, non-optical techniques (local phase probes [8], wire mesh sensors [9], hot wire anemometry [10]) can be applied to low and high gas fraction systems alike, however these must take into account the interference of the probe on the measurement [11, 12]. Despite their invasive nature, local phase probes

are essentially the only technique capable of obtaining measurements in high-voidage systems, and are commonly employed for measurement of bubble size [13, 14] and interfacial area [15, 16], while wire mesh sensors are used for their 2D visualisation capability [17, 18].

The present work is the first to attempt the measurement of these parameters using ultra-fast MRI, with all earlier studies that employ magnetic resonance focusing exclusively on either spatially or temporally averaged measurements. MRI holds several advantages over alternate techniques, including being completely non-invasive, and non-optical. In Chapter 4 it was demonstrated that spiral imaging possesses the spatio-temporal balance required for the resolution of highly transient flow features in some systems, while still being robust to the presence of fluid shear. These properties render spiral imaging a highly auspicious basis for the quantitative imaging of bubbly flow. Previous applications NMR and MRI to bubbly flow were reviewed in full in Section 1.4. Of most relevance to the present study is the work of Lynch and Segel [19], who showed that for pulse-acquire experiments a linear relationship exists between voidage and NMR signal, and Leblond *et al.* [20], who demonstrated the use of propagators for characterising the liquid-phase hydrodynamics of bubbly flow. Leblond *et al.* showed that the velocity distribution for bubbly flow is Lorentzian-like, centred around the superficial velocity of the fluid and broadens with increasing voidage.

In this chapter, methodologies for producing measurements of voidage, bubble size distribution and interfacial area from MRI images are firstly described. Particular focus is given to the automated image processing algorithms needed for data extraction, and the limitations of the MRI technique. Spiral imaging is then demonstrated in application to gas-liquid flow across the whole range of voidages for which stable bubbly flow was possible (up to $\varepsilon = 40.8\%$), and the developed techniques are applied to extract measurements of bubble size distribution and interfacial area density. Finally, both propagators and the quantitative, ultra-fast velocity imaging technique already developed in Section 4.2 are applied to bubbly flow across a range of voidages to provide a spatially and temporally resolved characterisation of the system hydrodynamics. Note that all measurements in this chapter are performed on a magnetic susceptibility matched (16.86 mM dysprosium chloride) solution, which while rendering the system MRI-friendly, has the additional effect of electrolytically stabilising bubbly flow (as discussed in Section 3.1.2). The measurements produced in this chapter are used to close a drift-flux hydrodynamic model of the system in Chapter 7.

## 5.1 Theoretical

### 5.1.1 Measurement of voidage

The major advantage of applying spiral imaging to bubbly flow is that the high-power centre of Fourier space is acquired at the start of the imaging sequence, and is thus free from the influence off-resonance and flow errors. As the total image intensity (which is quantitatively representative of the amount of fluid in the slice [19]) is represented by the central point of **k**-space, the voidage of a bubbly flow system may be readily determined according to [19]:

$$\varepsilon = 1 - \frac{s_{\mathrm{bub}}(0)}{s_{\mathrm{ref}}(0)} \tag{5.1}$$

where $s_{\mathrm{bub}}$ and $s_{\mathrm{ref}}$ are time domain signals acquired of bubbly flow, and single phase reference systems.

### 5.1.2 Measurement of bubble size

As discussed in Section 3.2, in order to obtain a 'snap-shot' of bubbly flow, it is necessary to acquire an image within approximately 20 ms. Using an echo-planar style acqusition, modern MRI hardware is able to acquire a full-Fourier 64 pixel $\times$ 64 pixel image in this time. While for the column under examination (31 mm diameter) this represents a relatively low spatial resolution ($\approx$ 500 $\mu$m), as long as the bubble is represented by several pixels (typically at least three pixels across the diameter), a circle fitted to the bubble outline will yield an interpolated projected bubble size, $r_{\mathrm{p}}$, to a subpixel accuracy [21]. The quantitative nature of the MRI signal also provides extra information that enables a secondary measurement of bubble size. If a bubble is wholly contained within the slice of excited fluid during the acquisition period, the signal loss due to the presence of the bubble will be proportional to the bubble volume. A schematic demonstrating this concept is provided in Figure 5.1.

While for an ideal system it is possible to calculate the signal-volume equivalency directly from equation (2.24), in a real system non-idealities in the hardware introduce errors (such as $B_1$ inhomogeneity) to the amount of signal present in some regions of the image. These errors are, however, consistent from scan to scan, and thus it is possible to quantify the bubble volume by comparison with a single-phase reference image. Thus, a spherically

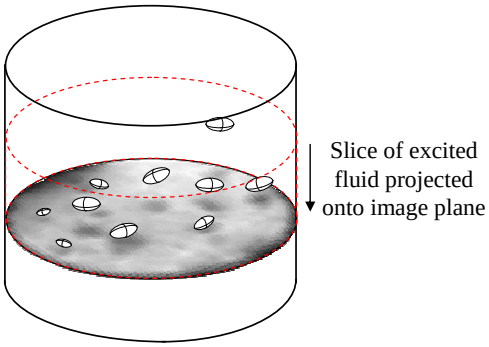


Figure 5.1: Demonstration of the nature of MRI images. A slice of fluid is excited, and spatially encoded in two dimensions perpendicular to the slice plane. The signal from fluid in the perpendicular direction is projected onto the imaging plane. The local signal intensity in an image can thus be rendered proportional to the volume of a bubble.

equivalent bubble radius may be calculated according to:

$$r_{\mathrm{b}} = \sqrt[3]{\frac{3}{4\pi} V_{\mathrm{ref}} \left(1 - \frac{|I_{\mathrm{bub}}|}{|I_{\mathrm{ref}}|}\right)} \tag{5.2}$$

where $V_{\mathrm{ref}}$ is the volume of the fluid voxels contained in the region of an identified bubble, $I_{\mathrm{bub}}$ is the complex image intensity present in this region for the image containing the bubble and $I_{\mathrm{ref}}$ is the complex image intensity for the reference image. By calculating bubble size from a signal ratio, partial volume effects caused by voxels half filled with liquid will be accounted for. Additionally, by directly measuring bubble volume, the influence of bubble shape on the measurement of bubble size is entirely avoided. This effect is particularly advantageous when considered in comparison to alternative techniques for the measurement of BSDs; in addition to being non-invasive and not limited by the optical opacity of the system, the influence of bubble shape upon the measurement of bubble size (which is highly problematical for techniques that measure only a chord length of the bubble [16]) is avoided altogether. In fact, by acquiring two independent measurements of bubble size, some information about bubble shape is also obtained. Assuming the bubble maintains fore-aft symmetry, the aspect ratio of the bubble will be given by:

$$\alpha = \left(\frac{r_{\mathrm{b}}}{r_{\mathrm{p}}}\right)^3 \tag{5.3}$$

where $r_{\mathrm{p}}$ is the radius of the projected bubble.

Note that it is important that the spatial integrations to yield $I_{\mathrm{bub}}$ and $I_{\mathrm{ref}}$ are performed on complex data to minimise errors generated by the signal-to-noise ratio of the image.

That is, when summing complex data, the mean value of the noise is zero and the signal-to-noise ratio scales with $\sqrt{n_\mathrm{p}}$ (where $n_\mathrm{p}$ is the number of summed points), whereas when summing modulus data the noise is always positive in magnitude (with a non-zero mean), which leads to the introduction of greater errors to the signal. This process assumes that no significant phase shift exists from pixel to pixel, which was true for the present case due to the magnetic susceptibility matched system under examination. The error in bubble sizes measured from signal intensity therefore depends upon the number of pixels contained in the bubble region. If the image is segmented into bubble regions in the form of digitised circles of radius $r_\mathrm{s}$, the error in bubble size due to the signal-to-noise ratio of the image, $S$, is given by:

$$\%E = \frac{3}{4}\frac{\sqrt{\lceil \pi r_\mathrm{p}^2 \rceil}\nu}{\pi r_\mathrm{s}^3 S_\mathrm{v}} \times 100 \tag{5.4}$$

where $\nu$ is the variance of the noise in the difference image, and $S_\mathrm{v}$ is the signal per unit volume of fluid. An additional potential source of error exists in that measurements based on the signal intensity are dependent upon the signal remaining quantitative in the presence of large amounts of shear. In Section 4.2.4, it was demonstrated that for spiral imaging errors of less than 3.5% are present in the image intensity for Reynolds numbers up to 12,000, which suggests that errors related to shear attenuation ought to be minor for the present experiments.

It is important to note that a large enough slice thickness must be selected to ensure that the majority of bubbles will be wholly contained within the slice for the duration of the imaging sequence. In dispersed flow, most bubbles do not rise faster than 30 cm $\mathrm{s}^{-1}$ [16]. This is equivalent to a rise of 6 mm over the 20 ms course of our established maximum acquisition time, indicating that the excited slice should be at least 6 mm thick. However, an excessively thick slice should be avoided as the risk of bubbles overlapping within the projected pipe cross-section is increased. Care must also be taken to ensure that the slice excitation profile is rectangular, such that the change in signal intensity due to the presence of a bubble is independent of its longitudinal position within the slice of excited fluid. In the present study, both 7.5 mm and 15 mm thick slices are examined; the radially averaged slice excitation profiles are shown in Figure 5.2.

Possible sources of error in these measurements relate to bubbles which are partially included in the slice during excitation, or bubbles which overlap in the slice of excited fluid. For bubbles which are part included in the excited slice the measured spherically

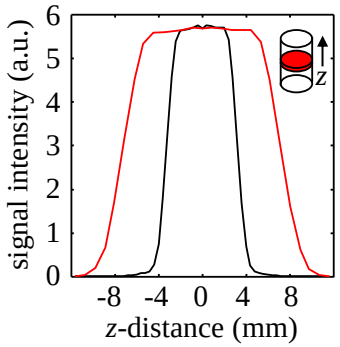


Figure 5.2: Slice excitation profiles for 7.5 mm thick slice (black) and 15 mm thick slice (red) used in the current experiments. Note that a rectangular slice shape is necessary to ensure that the signal loss due to the presence of a bubble is independent of the position of that bubble within the excited slice.

equivalent radius will always be less than that expected for a given projected bubble radius. The opposite is true for bubbles which overlap within the projected slice of fluid, with the bubble volume being in excess of that expected. It is generally true that $0.4 \leq \alpha \leq 1$ for bubbles with Eo $< 10$ [22], where the Eötvös number is defined as:

$$\text{Eo} = \frac{4\Delta\rho g r_b^2}{\sigma} \tag{5.5}$$

where $\Delta\rho$ is the density difference between the two phases, $g$ is acceleration due to gravity and $\sigma$ is surface tension. By discarding bubbles outside of the range $0.4 \leq \alpha \leq 1$, it is possible to minimise the influence of overlapping and part-included bubbles. It is important to note that filtering the data in this manner is a potential source of sampling bias, the influence of which is explored by applying the data analysis procedure to simulated data in Section 5.3.4.

### 5.1.3 Measurement of interfacial area

In this section, the quantification of interfacial area is examined as a function of both vertical and radial position in the column. While the data filtering procedure described above removes a significant source of potential error from the measurement, it also prevents the direct measurement of total interfacial area (as bubbles which are overlapping or part included in the slice will still contribute to the net surface area despite having been removed from the dataset). However as long as the mean interfacial area per bubble and number of bubbles present are known, the total interfacial area can be calculated.

The number of bubbles per unit volume can be determined by the relation:

$$N = \frac{\varepsilon V_{\text{slice}}}{V_{\text{mean}}} \tag{5.6}$$

where $V_{\text{mean}}$ is the mean bubble volume and $V_{\text{slice}}$ is the volume of the excited slice. Assuming the bubbles to remain oblate ellipsoids, the interfacial area of each individual bubble may be calculated by numerical integration of the surface integral:

$$A_{\text{s}} = \int_0^{\phi} \int_0^{2\pi} \sin\theta \sqrt{a^4 \sin^2\theta \sin^2\phi + a^2c^2 \sin^2\theta \cos^2\phi + a^2c^2 \cos^2\theta} d\theta d\phi \tag{5.7}$$

where $a$ and $c$ are the major and minor axes of each bubble, and $\theta$ and $\phi$ are rotated spherical coordinates, as shown in Figure 5.3. For computation of the entire surface area of a bubble, the limit $\phi = \pi$ must be considered. In assigning interfacial area to radial column bins it is not sufficient to simply consider the location of the bubble centroid. Rather, because the surface of different bubbles contribute to the interfacial area at each radial position, it is necessary to quantify the surface area of ellipsoidal segments. This may be achieved by evaluating the above integral up to the limit given by:

$$\phi = \frac{\arctan\left(a\sqrt{1 - \frac{h^2}{c^2}}\right)}{h} \tag{5.8}$$

where $h$ is the distance between the bubble centroid and the division between radial bins, as shown in Figure 5.3.

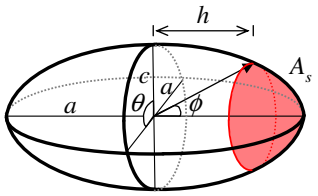


Figure 5.3: Coordinate system employed for the calculation of interfacial area of segments of the bubble. The bubble's major and minor semi-axes are given by $a$ and $c$, respectively, while $h$ is the distance from the bubble centroid to the plane that separates two radial locations in the column.

### 5.1.4 Data analysis

In order to obtain a statistically representative measurement of bubble size and interfacial area, hundreds of images may be required. Clearly, to process this volume of data

some automated analysis procedure is required for bubble identification and image segmentation. There exist multiple techniques to identify shapes within an image, which are explored in detail by Petrou and Bosdogianna [23]. The present application is, however, complicated by the relatively low signal-to-noise ratio associated with ultra-fast MRI. In such cases a Hough transform is conventionally used to produce a 'Hough space': a mathematical domain in which the desired shape features are represented by local maxima. When several maxima are located closely together, however, as in the case with densely clustered bubbles, peak identification can become problematic. To overcome this, it is possible to employ an iterative peak finding procedure. In this technique the global maximum is located, and the corresponding shape removed from the image domain, prior to recalculating the Hough space, such that ambiguity in shape locations is progressively reduced as each bubble is identified and removed. This shape identification procedure is demonstrated in Figure 5.4. An improved contrast image is first prepared by subtraction of a single-phase reference image, prior to the generation of a gradient image for edge-enhancement. A pseudo-Hough space was then generated by normalized cross-correlation with template images of circles of varying diameter. The maximum in this correlogram was identified as described above, which permitted the image to be segmented into approximate bubble locations. Each of these segments was then thresholded at a quarter of its maximum intensity (in order to remove back ground noise) prior to fitting a circle using the procedure of Taubin [24]. This process was repeated until a minimum correlation coefficient of 0.7 was reached. The signal in the segmented region for each bubble was then compared to the signal in the same region of the single phase reference image to determine a spherically equivalent diameter, in accordance with equation (5.2). The projected and volumetric bubble sizes were used to calculate an aspect ratio (as per equation (5.3)), and finally those bubbles identified as having an aspect ratio outside of the range $0.4 \leq \alpha \leq 1$ were removed from the dataset.

## 5.2 Experimental

The present experiments were carried out in a Perspex column 2 m in length ($L = 2$ m), and of internal diameter 31 mm ($R = 15.5$ mm). Magnetic susceptibility matched (16.86 mM dysprosium chloride) solution was used for the continuous phase. Bubbles were generated by sparging air through a porous foam-rubber frit (of the geometry shown in Figure 3.7 a) with the gas flow rate regulated by an Omega FMA3200ST mass flow controller for voidages up to 9%, and with a rotameter and needle valve for higher gas fractions. A flow loop was connected to the top of the column such that a constant

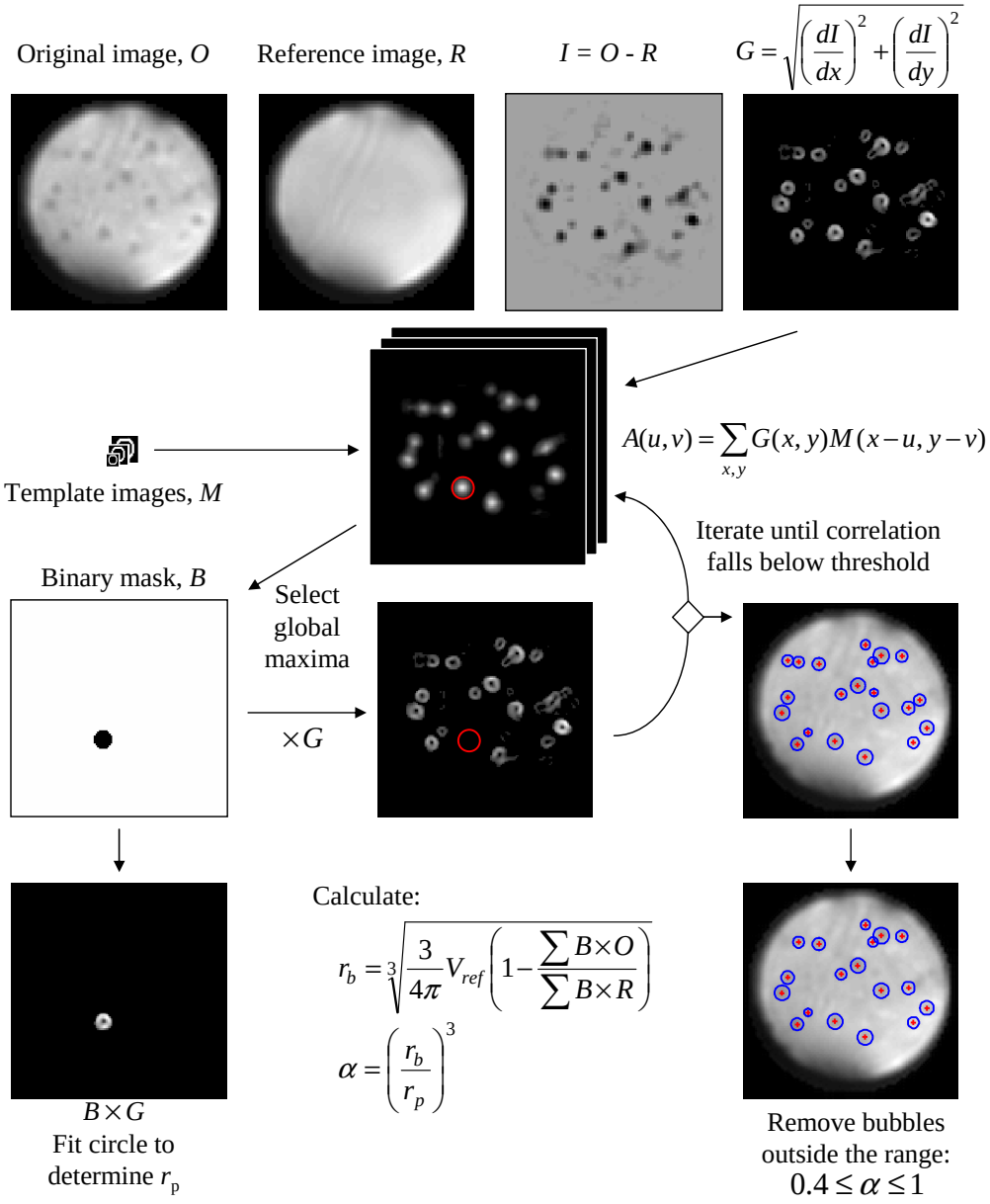


Figure 5.4: Demonstration of data analysis procedure. A single-phase reference image, $R$, is initially subtracted from an image of bubbly flow, $O$, in order to provide an image with improved contrast, $I$. A gradient image, $G$, is then generated by taking finite differences of $I$. The gradient image is segmented into individual bubbles by two-dimensional cross-correlation with template images of circles of varying diameter. The global maximum of the correlogram is then selected, and a binary mask, $B$, generated of the bubble corresponding to that peak. This mask is then used to extract the bubble outline from $G$, from which it is removed, and a circle is then fitted to the isolated bubble to determine the projected radius. The cross-correlation is then repeated to identify the next global maximum, and the process is iterated until a threshold correlation coefficient of 0.7 is reached. From the identified bubble locations, a spherically equivalent bubble diameter is then calculated from the intensity ratio between the original and reference images. An aspect ratio is then calculated using the two measurements of bubble size, and the data are filtered to remove bubbles demonstrating unrealistic proportions.

liquid height could be maintained, with overflow liquid transported to a reservoir. An experimental schematic is shown in Figure 3.7 b).

In order to validate the results produced by the MRI technique, sizes were measured of 9.52 mm diameter Perspex beads settling in the column, and BSDs were measured from a 7.5 mm thick slice at a voidage of 3.5% for comparison with an optical technique. The optical measurements of bubble size were obtained in Section 3.1.2. MRI measurements for the low voidage system were also acquired from a 15 mm thick slice to examine the influence of slice thickness on the produced size distributions.

Spiral images were obtained at 15 increments in superficial gas velocity in the range 4.4 cm $s^{-1}$ to 71.4 cm $s^{-1}$ (corresponding to a maximum voidage of 40.8%, above which stable bubbly flow was not possible). These measurements were performed at a position 25 mm from the sparger ($z/L = 0.0125$, where $z$ is the vertical direction) and at 10 cm increments up to a height of 1025 mm ($z/L = 0.51$). The entire column was shifted vertically with respect to the spectrometer to allow these heights to be examined. Higher positions in the column could not be investigated due to the fixed height of the magnet. The total acquisition time was 15.3 ms for a $64 \times 64$ pixel image acquired at a field of view of 37 mm $\times$ 37 mm (to give a pixel resolution of 578 μm $\times$ 578 μm). The spiral imaging protocol used was as described in Section 4.2.3, with the slight modification that a single spin-echo was used with a Mao refocusing pulse [25] to generate either a 7.5 mm or 15 mm thick slice of excited fluid of rectangular profile. Images were acquired every 300 ms to allow complete magnetisation relaxation, and to give time for the sampled bubbles to leave the imaging region. Two hundred images were acquired for each position and flow rate. High time resolution velocity encoded images were also acquired of bubbly flow at each voidage using a 1 mm thick slice. These images were acquired from an FID, had an acquisition time of 12.5 ms and were obtained at a rate of 55 fps. For $x$-$y$ plane images the field of view and resolution were the same as that described above, however for $x$-$z$ plane images the field of view was 37 mm $\times$ 47 mm for a pixel resolution of 578 μm $\times$ 734 μm. Where velocity encoding was applied the flow encoding time ($\delta$) was 416 μs, the flow contrast time ($\Delta$) 516 μs, and the velocity encoding gradient strength 12.2 G $cm^{-1}$. Longitudinal and transverse plane velocity component propagators were also obtained of the same systems, with 32 increments in velocity encoding gradient between -26 G $cm^{-1}$ and 26 G $cm^{-1}$, and with $\delta = 1$ ms and $\Delta = 1.4$ ms. These measurements were based on a spin-echo with an echo time of 1.5 ms. Repeat experiments were also performed with $\Delta = 5$ ms and $\Delta = 10$ ms.

All MRI experiments were performed on a Bruker AV-400 ultrashield spectrometer operating at a $^1$H resonance frequency of 400.25 MHz. This apparatus is fitted with a 3-axis mini-imaging gradient system capable of a maximum magnetic field gradient strength of 30.6 G cm$^{-1}$. A 38 mm diameter birdcage coil was used for r.f. excitation, and subsequently, signal detection. All images were acquired at a spectral width of 400 kHz. The gradient waveform was determined according to the algorithm of Glover *et al.* [26]. The modified technique of Duyn *et al.* (as described in Section 4.1.1) was used to measure the reciprocal space locations of the sampled points, and these were subsequently used to reconstruct the images using a non-uniform fast Fourier transform [27].

## 5.3 Results

### 5.3.1 Spiral imaging of bubbly flow

Spiral imaging has been used to acquire images of bubbly flow for systems of voidage up to 40.8%, which was just lower than the transition to slug flow. Example images for this range of voidages, with photographs of the same systems, are shown in Figure 5.5. Note that the voidages given as labels in this figure were measured from the MRI signal as per equation (5.1), with the error on these measurements being $\pm 0.1\%$. From these images it is clear that the spatio-temporal resolution of the MRI technique is sufficient for the identification of individual bubbles for the entire range of gas-fractions for which dispersed bubbly flow is possible.

The signal-to-noise ratio of these images is approximately 8:1, for which equation (5.4) predicts an error of 4.7% in the average signal intensity for a circular region of diameter 3 pixels. By measuring the average signal intensity in-between individual bubbles in small regions such as this, and comparing this value to the average intensity sampled in the same location in a reference image of a static system, it is possible to test for the presence of the shear attenuation artefact. In performing this test for images at all voidages, errors of no greater than 5% were found. This suggests that any shear attenuation occurring is small relative to the magnitude of noise in the images. The error in signal intensity, is therefore largely governed by the signal-to-noise ratio of the images for the present experiments, and it is this error which must be considered during the volumetric measurement of bubble size.

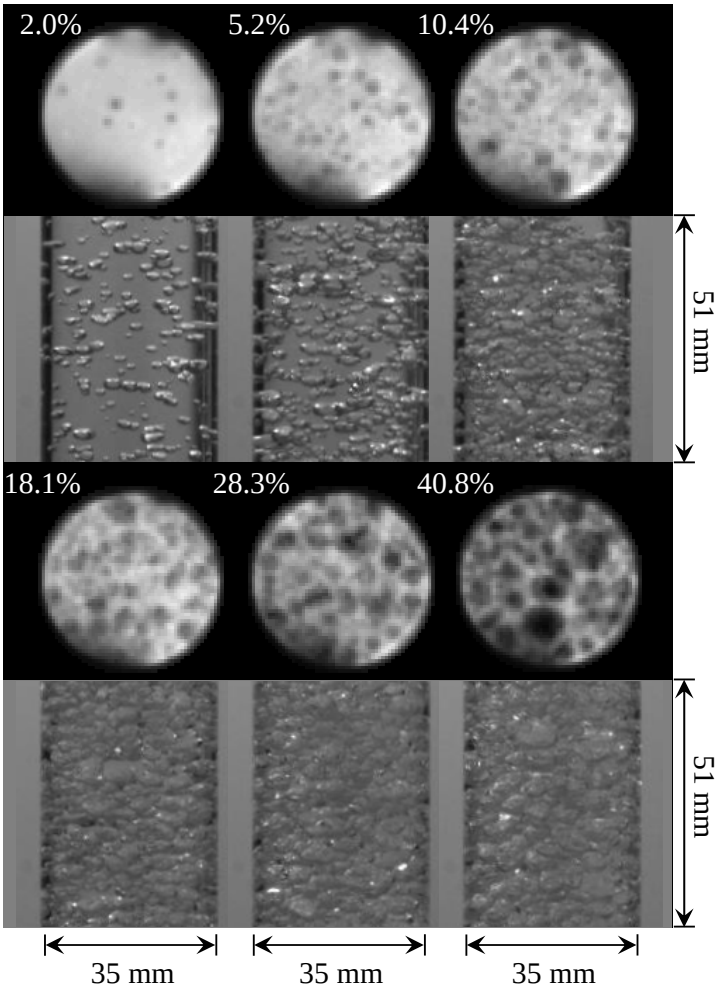


Figure 5.5: Example MRI images and photographs of bubbly flow for the range of voidages examined in the present study. These data were obtained at a vertical position of $z/L = 0.25$. The field of view is 35 mm × 35 mm of the MRI images, and 38 mm × 35 mm for the photographs. The MRI images have a resolution of 578 μm × 578 μm and an acquisition time of 15.3 ms.

### 5.3.2 Gas hold-up response

The voidage as a function of superficial gas velocity for all flow rates examined in the present study is shown in Figure 5.6. The gas-holdup response is seen to be linear for low gas velocities, however begins to curve upwards at higher voidages. A transition in the behaviour of a gas-holdup curve with increasing gas flow-rate is very familiar from the literature [28, 29, 30], however in pure systems this transition is towards a plateau. This turning point has been previously attributed to the transition between homogeneous and heterogeneous bubbly flow, with the greater proportion of larger bubbles present in the latter leading to lower gas hold up [31]. The opposite transition, with increasing

hold-up accompanying higher gas flow-rates, has been previously observed by several authors studying the effect of electrolytes on bubbly flow [32, 33, 34]. In particular, Jamialahmadi and Müller-Steinhagen [32] showed that their system made the transition from a plateauing gas-holdup curve to a convex curve upon the addition of 67 mM potassium chloride. As discussed in Section 1.2 electrolytes have the effect of stabilising the gas-liquid interface without significantly altering the surface tension. It is likely that this stabilising effect retards the formation of large bubbles, and thus leads to higher voidages being maintained at high superficial gas velocities.

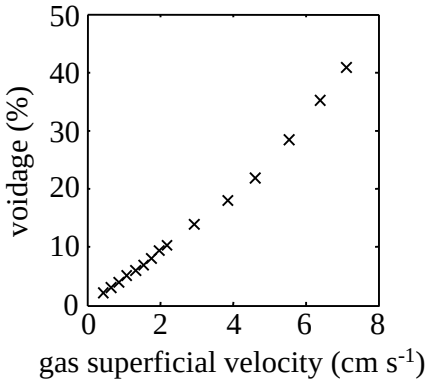


Figure 5.6: Voidage as a function of superficial gas velocity. The convex shape of the curve at high gas flow rates is characteristic of the presence of electrolytes.

### 5.3.3 Distribution fitting

Bubble size distributions generated by spargers with a single pore diameter tend to be unimodal, with a narrow distribution of small bubbles, and a longer tail of larger bubbles, which lends them well to description using the log-normal distribution [8, 35]. A log-normal distribution is defined as:

$$p(r) = \frac{1}{r\sigma\sqrt{2\pi}} \exp\left(\frac{-(\ln r - \mu)^2}{2\sigma^2}\right) \tag{5.9}$$

where $\mu$ and $\sigma$ are the mean and standard deviation of the natural logarithm of bubble size. These parameters may be calculated using maximum likelihood estimators:

$$\mu = \frac{\sum_{\mathrm{n}} (\ln r_{\mathrm{n}})}{N} \tag{5.10}$$

$$\sigma = \sqrt{\frac{\sum_{\mathrm{n}} (\ln r_{\mathrm{n}} - \mu)^2}{N}} \tag{5.11}$$

where $N$ is the number of samples taken. The mean bubble size and variance of the distribution are given by:

$$r_{\text{mean}} = \mathrm{e}^{\mu+\sigma^2/2} \tag{5.12}$$

$$s = (\mathrm{e}^{\sigma^2} - 1) r_{\text{mean}}^2. \tag{5.13}$$

The statistical likelihood that any given distribution is an accurate representation of the underlying dataset may be estimated using Pearson's chi-square test [36]. This test defines a squared sum of differences between an expected population, $P_{\text{e}}$, and an observed population, $P_{\text{o}}$, as being:

$$\chi^2 = \sum_{\text{n}} \frac{(P_{\text{o}} - P_{\text{e}})^2}{P_{\text{e}}}. \tag{5.14}$$

A log-normal distribution (which has 2 parameters), evaluated at 13 increments, has 10 degrees of freedom. In this case a chi-square distribution dictates that if $\chi^2 \leq 3.94$, 95% confidence exists that the fitted distribution is a true representation of the data. A log-normal distribution is shown in comparison with a histogram for a BSD measured at a voidage of 10.4% in Figure 5.7. In this case, $\chi^2 = 0.06$; reflecting that the distribution is an excellent fit to the data. In all experiments in this chapter, $\chi^2$ was found to be less than unity. The mean bubble size and variance of log-normal distributions fitted to the data will be used to describe the measured BSDs in the following sections.

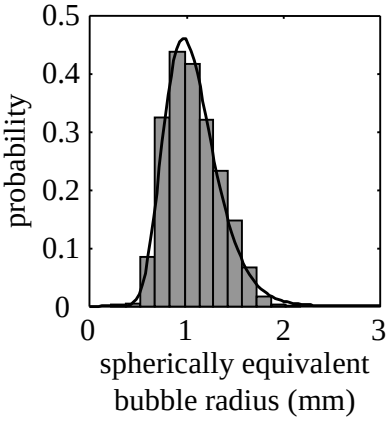


Figure 5.7: Comparison of a BSD measured for a system of voidage 10.4% (histogram) together with a log-normal distribution fitted to these data.

### 5.3.4 Validation of bubble size measurement procedure

Prior to the application of MRI to the measurement of BSDs for high voidage systems it is necessary to demonstrate that the developed techniques are capable of producing an accurate measurement of bubble size. The main possible sources of error in these measurements relate to the localised MRI signal not remaining quantitatively representative of the amount of fluid present, the selection of a sub-optimal slice thickness and the potential for the introduction of sampling bias due to over-lapping bubbles, and bubbles part-included in the slice during excitation. In this section the former is firstly examined by validating the experimental measurements in application to settling particles and in comparison to optical bubble size measurements for a low voidage system. The influence of the chosen slice thickness is then explored by comparing size distributions measured using both thin and thick slices. Finally, the presence of any sampling bias is explored by applying the data analysis procedure to simulated images of bubbly flow at a variety of voidages.

#### Experimental validation

The veracity of the basic principle of quantifying the volume of an object from local signal intensity in MRI was first explored by imaging 9.5 mm diameter spherical PVC beads dropped though a column of water. While the magnetic susceptibility of PVC can vary substantially, these particular beads, fortuitously, had a magnetic susceptibility very close to that of undoped water and thus off-resonance artefacts were not present in the images. The MRI technique produced a measurement of $9.48 \pm 0.23$ mm diameter for the spherically equivalent diameter of the beads, and $9.54 \pm 0.46$ mm on the basis of its projected shape. Thus, within the bounds of experimental error, both measurements of particle size were accurate.

The technique was further validated by comparison between MRI and optically measured BSDs for a low voidage ($\varepsilon = 3.5\%$) bubbly flow system. The distributions produced by the two measurements are shown in Figure 5.8. Comparison is made on the basis of both spherically equivalent bubble diameter in a) and projected axis lengths in b) (the minor axis length was calculated from the MRI measurements using the aspect ratio obtained as per equation (5.3)). Note that while the MRI technique is capable of directly measuring bubble volumes, it was necessary to assume fore-aft symmetry in order to obtain a similar measurement from the optical technique.
While there is a significant difference between the distributions shown in Figure 5.8, this

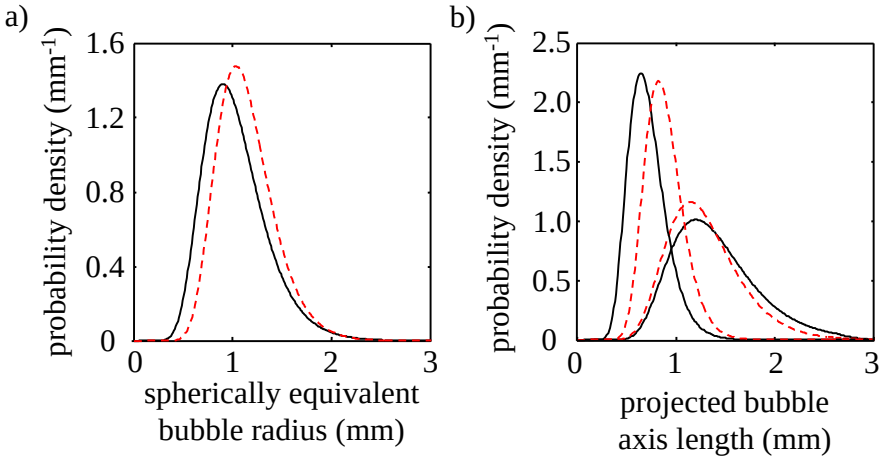


Figure 5.8: Comparison of optical (red dashed line) and MRI (black solid line) measurements of BSD. a) spherically equivalent diameter b) major and minor axes. These data were obtained at a voidage of 3.5% and at a vertical position of z/L = 0.2.

disparity was not unexpected, and does not necessarily reflect a shortcoming of the MRI. The accuracy of the optical technique is undermined by the nature of projections obtained of a three-dimensional object. As discussed by Lunde and Perkins [37], if one of the principle axes of a bubble is not aligned with the focal line of the camera (which is often the case), some error in the projected bubble size is unavoidable. If the bubble is at some other orientation to the camera, the major axis length will tend to be underestimated, while the minor axis is overestimated. These predictions are consistent with the behaviour shown in Figure 5.8 b). The projections obtained using MRI are more forgiving, as two measurements of the major axis length are obtained, and (as long as the angle of attack of the bubble is small) should approach a representative length scale. Additionally, the MRI measured minor axis is calculated using information obtained from a direct measurement of the bubble volume, which decreases the influence of the projected bubble shape, and is thus a more accurate basis for the measurement. With the above considerations taken into account, it seems that the MRI technique is capable of producing accurate measurements of bubble size. Note that MRI measured size distributions shown in Figure 5.8 were generated from measurements extracted from 200 images (corresponding to approximately 1,800 bubbles), which is regarded statistically significant. As noted in Section 5.3.1, the error in the MRI measurement of spherically equivalent bubble size is approximately 4.7%.

### Influence of slice thickness

To explore the influence had by the chosen slice thickness on the produced measurements, BSDs were measured for a low voidage system using two slice thicknesses (7.5 mm and 15 mm). A comparison of these two distributions is shown in Figure 5.9. It is clear from these data that increasing the slice thickness does not have a significant effect upon the produced BSD, with only a minor difference present between the two distributions. The BSD for the larger slice thickness demonstrates a marginally greater proportion of larger bubbles in the system, with a mean bubble size of $1.07 \pm 0.05$ mm, as opposed to $1.05 \pm 0.05$ mm for the thinner slice. This difference is possibly to due to introduction of a sampling bias caused by the removal bubbles part included in the slice during excitation, which will be more significant for data for the thinner slice. As voidage increases, however, the thick slice will exhibit a large proportion of overlapping bubbles, the removal of which from the data set will also introduce a sampling bias. Therefore, given that the difference between the two slice thicknesses lies within the experimental error of the measurements, any sampling bias introduced by the use of the thinner slice is considered marginal. For this reason, a 7.5 mm slice will be used in all further bubble size measurements in the present chapter.

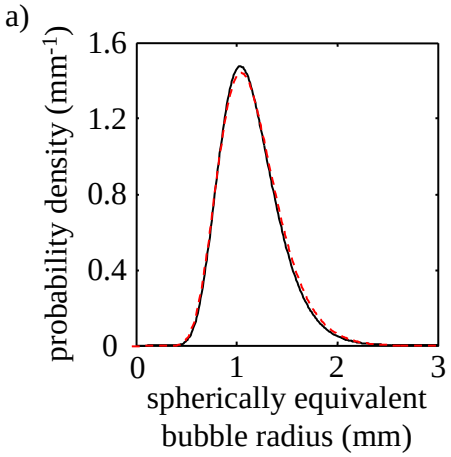


Figure 5.9: Bubble size distributions measured using MRI with a slice thickness of 7.5 mm (black solid line) and 15 mm (red dashed line). These data were obtained at a voidage of 1.5% and at a vertical position of z/L = 0.2.

### Analysis of simulated data

Simulated data have been analysed to explore the possibility of sampling biases introduced while filtering from the data overlapping bubbles and bubbles part included in the

slice during excitation. In generating the simulated data a three-dimensional cylindrical geometry was created using MATLAB, and populated with bubbles generated according to a log-normal size distribution ($r_{\text{mean}} = 1.5$ mm, $s^2 = 0.15$ mm$^2$). It was assumed that all bubbles were ellipsoidal with an aspect ratio of 0.7. The position of the bubbles within the 3D geometry was random, however bubbles were constrained from occupying the same volume as each other. Example images of these simulated data are shown in Figure 5.10.

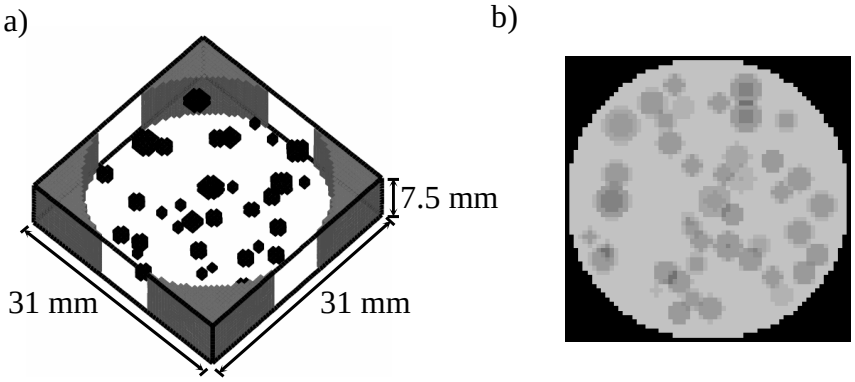


Figure 5.10: Simulated data used for testing the data analysis procedure. a) A 3D geometry is firstly generated, before b) being projected in one direction for the generation of a simulated MRI image. The data shown here correspond to a voidage of 7.0%.

These data were generated for seven increments in bubbly flow up to a maximum voidage of 30.7%. Higher voidages could not be simulated with the chosen size distribution due to the random placement of bubbles preventing the efficient 'packing' of the system. Clearly, at higher voidages, smaller bubbles will tend to occupy the spaces between larger bubbles, and the assumption of a random distribution of bubble positions is no longer valid. The present simulations, therefore, will be used to provide only an estimate of the population of bubbles sampled in a given MRI acquisition. Figure 5.11 a) shows the mean bubble size and variance of size distributions measured from the simulated data as a function of voidage, while c) shows the number of bubbles sampled in each distribution compared with the number of bubbles initially generated.

From these simulations it is clear that the correct mean bubble size and variance were produced by the data analysis procedure up until a voidage of approximately 22%. The number of bubbles sampled in these distributions is seen to slowly diverge from the number of bubbles present in the system, which corresponds to an increasing number of bubbles being identified as overlapping, and being filtered from the data set. That accurate measurements of the mean and variance are still being produced, however, re-

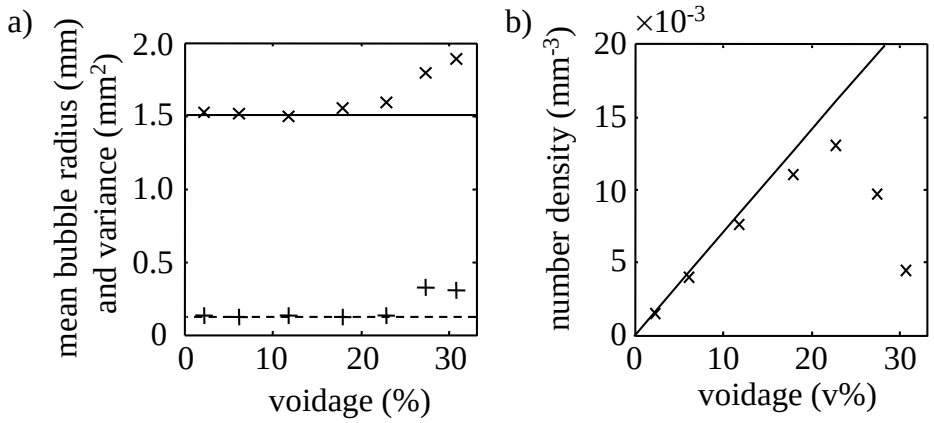


Figure 5.11: a) Mean bubble size (×) and variance (+) measured from simulated MRI images as a function of voidage. The true mean bubble size and variance are shown as solid and dotted lines, respectively. b) The bubble number density for each measured distribution (×) and the true bubble number density (line). Note the decreasing size of the sampled population occurring at a voidage of 22% corresponds to a loss of accuracy of the data analysis procedure, reflecting the introduction of sampling bias to the measurements.

flects that the overlapping bubbles are being drawn proportionately from the number of bubbles of each size present in the BSD. Above a voidage of 22%, the number of bubbles identified in each image begins to decrease, which corresponds to a significant increase in the number of overlapping bubbles in the system. This decrease in the sampled population corresponds to an increase in both the mean and variance of bubble size; reflecting that more small bubbles than large bubbles are now being removed from the data set. In high-enough gas-fraction systems bubbles will begin to overlap irrespective of the slice thickness chosen (assuming that the slice remains thick enough to completely contain the bubbles), and the sampling bias observed here is therefore unavoidable for volumetrically based measurements on high voidage systems.

### 5.3.5 Measurement of bubble size distributions

BSDs have been measured at a position 2.5 cm from the distributor for fifteen increments in voidage. The mean and variance of these distributions is shown in Figure 5.12 a) and b), respectively. Both the mean bubble size and distribution variance are seen to decrease until a voidage of 4.0% is reached, at which point they begin to increase with increasing voidage. The reason for this kink at low voidages is related to the residence time of bubbles on the sparger, with bubbles able to grow for longer before detaching at low gas-flowrates. At the highest gas flow rates, the mean bubble size approaches a plateau.

The mean bubble size as a function of voidage is well fitted in the range $\varepsilon > 4.0\%$ by:

$$r_{\mathrm{b}} = 1.9\varepsilon^{0.23}. \tag{5.15}$$

Figure 5.12 c) shows the bubble number density calculated using equation (5.6), and the number of bubbles identified by the image segmentation algorithm. The number of sampled bubbles is seen to slowly diverge from the total number of bubbles up to a voidage of approximately 20%, at which point the size of the sampled population begins to shrink. This is in good agreement with the behaviour displayed by the simulated data displayed in Figure 5.11, with the cause of the decreasing sample size therefore due to the increasing incidence of bubbles overlapping within the slice, and thus being removed from the dataset. Figure 5.11 demonstrated that this decreasing sample size accompanies the introduction of a sampling bias towards the identification of predominately larger bubbles, with the accuracy decreasing for all volumetric measurements of bubble size at voidages higher than 22%. Other approaches for the measurements of bubble sizes in higher gas fractions systems are possible; for example measurements of bubble cross-section may be obtained by shape identification performed on data obtained using a very thin slice. This approach, however, reintroduces the influence of bubble shape to the measurement of bubble size, which is a standing problem for all techniques which only measure chord lengths or segments of bubbles [16]. The present work will therefore continue with the proposed volumetric sizing methodology, and further analysis in the present work will be limited to a maximum voidage of 22%. Figure 5.12 d) shows the interfacial area per unit volume as a function of voidage. For a uniform distribution of spherical bubbles, it is known that the interfacial area is given by [38]:

$$A_{\mathrm{i}} = \frac{3\varepsilon}{r}. \tag{5.16}$$

The curve corresponding to equation (5.16), calculated from the measured voidage and mean radii, is plotted with the measured interfacial area in Figure 5.12 d). While good agreement is evident for very low voidages, the curves diverge for higher voidages. It is important to note, however, that as the mean bubble size increases (with increasing voidage), the aspect ratio of the bubbles will decrease. Therefore, it is to be expected that the surface area per unit volume of bubbles within the column will be less than that predicted for a uniform array of spheres.

BSDs have been measured for voidages up to 22%, and at 10 cm increments along the column starting from 25 mm above the distributor. Within the bounds of the signal-to-

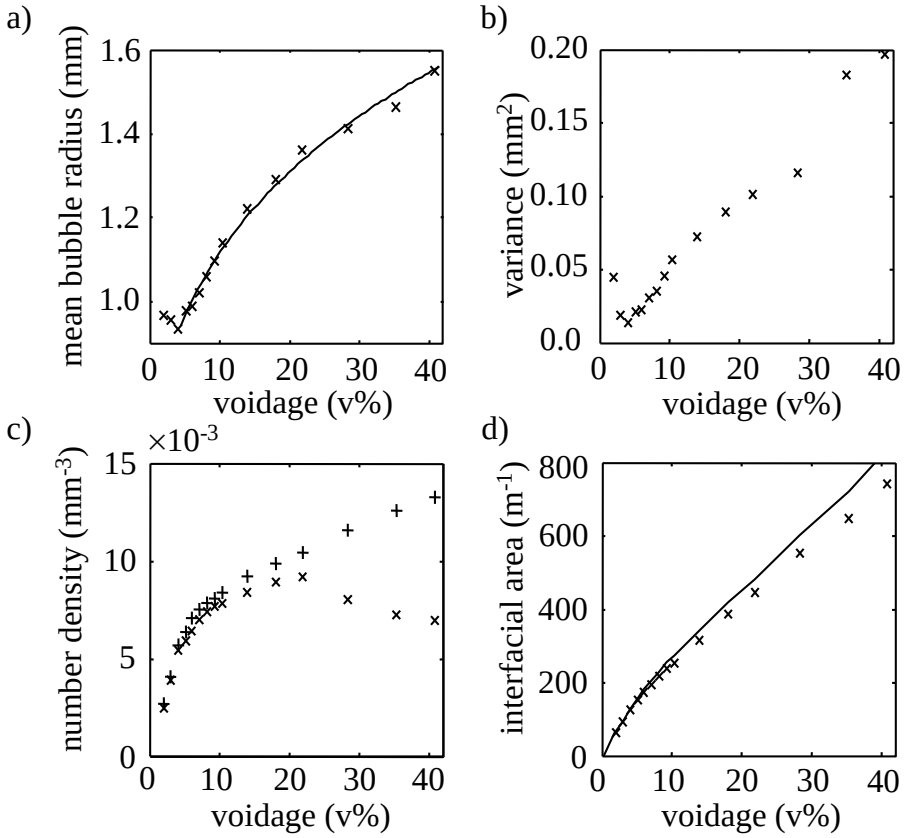


Figure 5.12: a) Mean and b) variance of BSD as a function of voidage. The fit given in equation (5.15) is shown (line) c) Bubble number density calculated from the voidage and mean bubble volume (+) and calculated from the population of bubbles sampled (×). The divergent section above $\varepsilon = 22\%$ is due to an increasing number of overlapping bubbles in the excited slice of fluid. d) Measured amount of interfacial area per unit volume (×) and the amount expected for a uniform distribution of spheres (line).

noise ratio of the measurements, the voidage was found to be independent of position in the column. The mean bubble size and distribution variance are given as a function of vertical position in the column in Figure 5.13 a) and c). By averaging over the column length, enough bubbles were sampled to also produce size distributions as a function of radial position. The mean and variance of these distributions are given in b) and d). The solid lines shown are included only to guide the eye. The dotted line in a) shows the change in bubble size that would be expected due to the changing hydrostatic pressure as the bubbles rise up the column, which was calculated using the ideal gas law and assuming the internal pressure of the bubble is equivalent to the hydrostatic pressure at any given position in the column (which is valid as the Young-Laplace equation dictates that capillary pressure becomes insignificant for bubbles greater than a few hundred micrometres in radius [39]).

Time averaged BSDs, such as these, represent the evolution of bubble size as the bubbles rise up the column, and reflect the changing rates of bubble break-up and coalescence. For the lowest voidage, the bubble size is seen to increase at approximately the rate expected due to the change in hydrostatic pressure, reflecting that little opportunity exists for bubble coalescence in a low voidage system, and that insufficient turbulent shear is present for the instigation of bubble breakup. At higher voidages, an inflection begins to appear, which corresponds to an increasing amount of bubble coalescence giving rise to larger bubbles at higher positions in the column. A plateau is approached for the 18.1% voidage system at a mean bubble radius of 1.6 mm, which represents an equilibrium between bubble break-up and coalescence. The variance is also seen to increase as a function of both voidage and height in the column; particularly favouring the formation of larger bubbles for high voidage systems. For low voidage systems bubble size is seen to be independent of radial position in the column, with the mean and variance relatively constant. As voidage increases, however, the mean bubble size is seen to peak before dropping off sharply near the wall. This occurs as each bubble size has been assigned to the position of the bubble centroid, and thus large bubbles cannot 'fit' immediately adjacent to the wall. Smaller bubbles tend to accumulate in the space between large bubbles near the column wall, and thus gives rise to a narrow size distribution of small bubbles. This observation has important consequences for optical bubble size measurements on high voidage bubbly flow, which will observe only these boundary affected distributions and are demonstrably not representative of the bulk flow.

The measurement of BSDs for high voidage systems is desirable because it enables the prediction of bubble slip velocity, which is necessary for the determination of residence time distribution and for the use of drift-flux analysis in the design and operation of gas-liquid unit operations. For this latter purpose closure models are required for mean bubble size. To provide a set of empirical closures, curves such as that shown in Figure 5.12 a) can be fitted to the data shown in Figure 5.13 a) for each position in the column. Figure 5.14 shows these data together with fitted curves. Power law curves were found to provide an adequate fit up to a voidage of 18.1%. For higher gas-fractions, power law curves only provided a good fit up to a mean bubble size of 1.6 mm, after which the bubble size is seen to increase at a constant rate. This transition corresponds to the equilibrium between bubble break-up and coalescence attained in Figure 5.13 a).

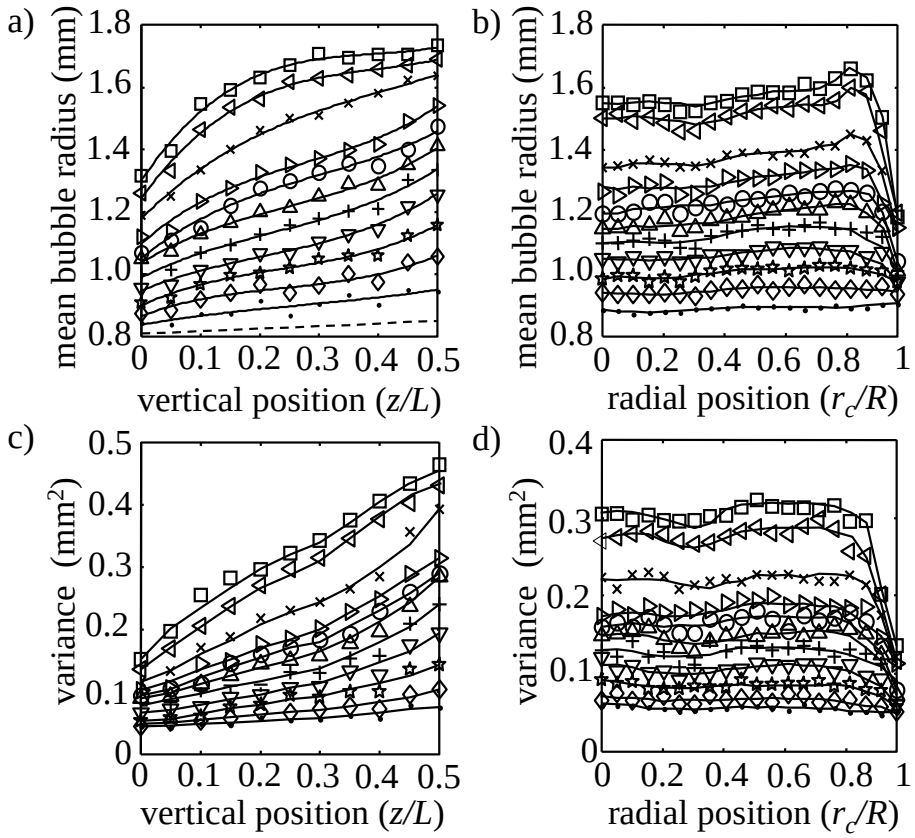


Figure 5.13: Mean bubble size as a function of a) vertical and b) radial position in the column. The dotted line in a) shows the change in bubble size due to decreasing hydrostatic pressure as the bubbles rise up the column. The peak in b) near the wall is likely due to bubbles of size $< 1$ mm (the radial increment size being to large to register bubbles of that size in that region). Also shown is the variance of the size distributions as a function of c) vertical and d) radial position in the column. Voidage key: $\bullet$ 3.1% $\Diamond$ 4.0% $\star$ 5.2% $\triangledown$ 5.9% $+$ 7.0% $\triangle$ 8.1% $\circ$ 9.3% $\triangleright$ 10.4% $\times$ 13.9% $\triangleleft$ 18.1% $\square$ 21.9%.

In Figure 5.14, curves are fitted of the form:

$$r_{\mathrm{b}} = a\varepsilon^{b} \qquad r_{\mathrm{b}} \leq 1.6 \text{ mm} \tag{5.17}$$

$$r_{\mathrm{b}} = a\varepsilon + b \qquad r_{\mathrm{b}} > 1.6 \text{ mm}. \tag{5.18}$$

The coefficients corresponding to the curves fitted in Figure 5.14 are given in Table 5.1.

The measurement of BSDs for high-voidage systems is also useful for the validation of the population balance approach to the modelling of multiphase systems [40]. The population balance equation requires closure models for rates of bubble breakup and coalescence [41]. These closures may be validated on the basis of the evolution of the BSD as a function

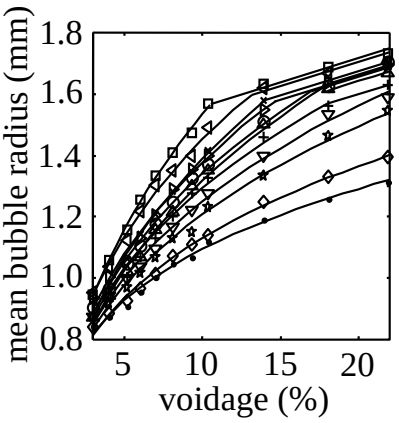


Figure 5.14: Mean bubble size as a function of voidage with fitted curves. A power-law was found to provide an adequate fit for $r_b \leq 1.6$ mm, with the bubble size increasing linearly at all larger sizes. The transition in this behaviour corresponds to an equilibrium between bubble break-up and coalescence being attained. Distance from distributor: • 2.5 cm ◊ 12.5 cm ☆ 22.5 cm ▽ 32.5 cm + 42.5 cm △ 52.5 cm ○ 62.5 cm ▷ 72.5 cm × 82.5 cm ◁ 92.5 cm □ 102.5 cm.

of column height, which can provide a measure of the balance between rates of bubble break-up and coalescence. Alternatively, rates of bubble breakup and coalescence may also be obtained independently of each other by rapid repeat acquisition of ultra-fast MRI images in the vertical plane of the column. Such images possess the temporal resolution sufficient for individual bubbles to be tracked, and for bubble break-up and coalescence events to be observed. Figure 5.15 shows example images of this type for a voidage of 28.3%: a break-up event is evident in a) and bubble coalescence in b). By providing a basis for breakup and coalescence models to be validated in high voidage systems, the MRI technique provides a potential avenue by which the veracity of multiphase models may be tested. The experimental validation of such models is of the utmost importance for confidence to exist in the results of numerical simulations of two-phase flows.

While for the present system MRI has provided the necessary balance between spatial and temporal resolution required for measurements to be extracted of individual bubbles, for systems of larger diameter, or containing smaller bubbles, this may not be the case. The applicability of MRI to a wider variety of bubble flow systems may be improved by implementing a compressed sensing reconstruction procedure (as described in Section 2.5). This technique allows the spatio-temporal balance of an image to be improved by undersampling, with undersampling artefacts then removed using compressed sensing reconstruction. Bubbly flow is an ideal case for the application of compressed sensing as a great deal of *a priori* knowledge exists regarding the shape features present in the

Table 5.1: Coefficients corresponding to fitted curves in Figure 5.14

| Distance from | $r_b \leq 1.6$ mm | | $r_b > 1.6$ mm | |
|---|---|---|---|---|
| distributor (cm) | $a$ | $b$ | $a$ | $b$ |
| 2.5 | 1.90 | 0.24 | - | - |
| 12.5 | 2.11 | 0.27 | - | - |
| 22.5 | 2.46 | 0.31 | - | - |
| 32.5 | 2.63 | 0.32 | - | - |
| 42.5 | 2.75 | 0.33 | 1.59 | 1.28 |
| 52.5 | 3.04 | 0.36 | 1.59 | 1.33 |
| 62.5 | 2.96 | 0.35 | 1.59 | 1.35 |
| 72.5 | 3.08 | 0.35 | 1.59 | 1.34 |
| 82.5 | 3.33 | 0.38 | 1.59 | 1.36 |
| 92.5 | 3.30 | 0.36 | 1.59 | 1.38 |
| 102.5 | 3.93 | 0.41 | 1.59 | 1.40 |

image (i.e. the bubbles are mainly represented by circle or ellipses). An image of bubbly flow may therefore be readily rendered sparse by a shape identification procedure, such as a Hough transform. While this has not been performed for the present study, as fully sampled images sufficiently characterise the examined system, it remains an important consideration for the application of MRI to a wider variety of bubbly flow systems.

### 5.3.6 Measurement of interfacial area

It is only a slight extension of the quantification of bubble size to obtain a measurement of the bubble surface area. This information is valuable as rates of interphase transport phenomena are proportional to the interfacial area. The interfacial area per unit volume has been calculated as described in Section 5.1.3, and is shown as a function of vertical and radial position in the column in Figure 5.16 a) and b). While the interfacial area is relatively homogeneous for lower voidage systems, by comparison with Figure 5.13, it is clear that the proportion of interfacial area decreases with increasing bubble size. This is as expected, as (for the same volume of gas) smaller bubbles possess a greater surface area. The radial distribution of interfacial area displays a more dramatic peak at the wall, which corresponds to the smaller bubbles which tend to accumulate there. An interfacial area wall peak such as this has been observed by previous researchers (see for example Kalkach-Navarro *et al.* [14]). The measurement of interfacial area may be useful for the validation of some approaches to the modelling two-phase flows, such as the interfacial area transport equation of Hibiki and Ishii [41].

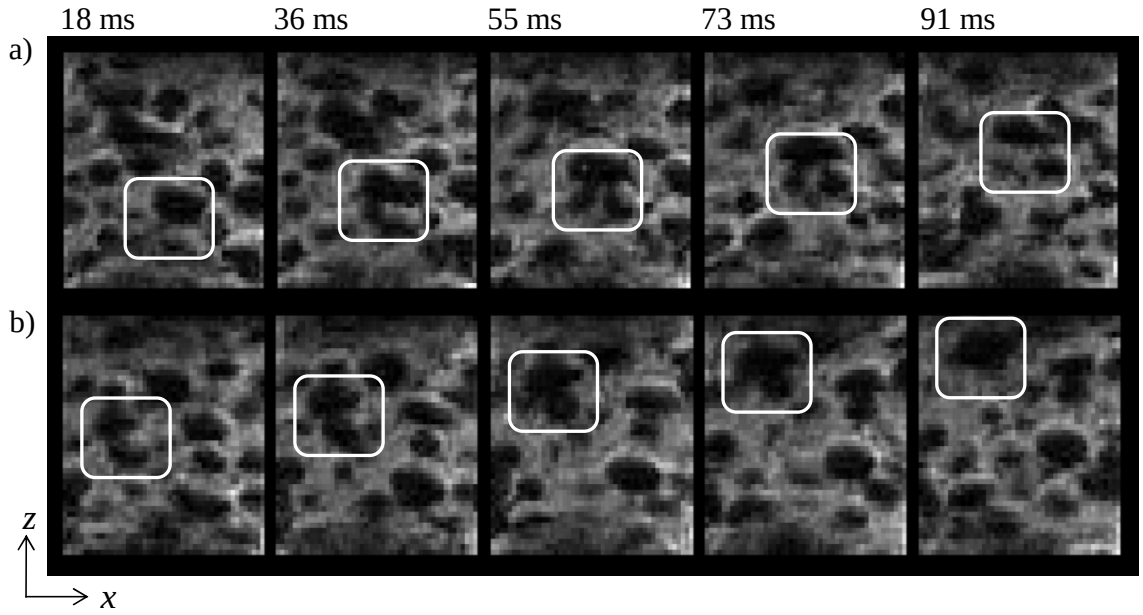


Figure 5.15: High time resolution vertical plane MRI images of bubble flow at a voidage of 28%. A bubble break-up is evident in a) and coalescence in b). These images have a field of view of 37.5 mm × 32 mm and spatial resolution of 578 μm × 580 μm. These data were acquired at a rate of 55 fps.

### 5.3.7 Measurement of liquid phase hydrodynamics

In addition to the characterisation of the dispersed phase structure of the model bubble column, the liquid phase hydrodynamics of the system have also been examined. The hydrodynamics of bubbly flow has been the focus of considerable research, however most conventional techniques for the measurement of liquid phase velocity fields (particle imaging velocimetry, PIV [42] and laser Doppler anemometry, LDA [43]) are optically based, and therefore have only limited utility in application to high voidage systems. The highest voidage system which has been previously examined using optical velocimetry is that of Mudde *et al.* [44] who examined systems of voidage up to 25% voidage using LDA. They were able to measure velocities at only a single point, however, and found their sampling rate to decrease exponentially as the sampled point was shifted further from the column walls. As an alternative, hot-wire anemometry has been applied extensively to study the of high voidage bubbly flow, however it has been shown that the invasive nature of the probe changes the system considerably [12]. The only previous study examining the use of magnetic resonance to characterise bubbly flow hydrodynamics was that of Leblond *et al.* [20], who acquired NMR propagators (described in Section 2.3.1) of bubbly flow up to a voidage of 42%. They noticed the velocity distribution to be approximately Lorentzian about the liquid superficial velocity of the system, with the

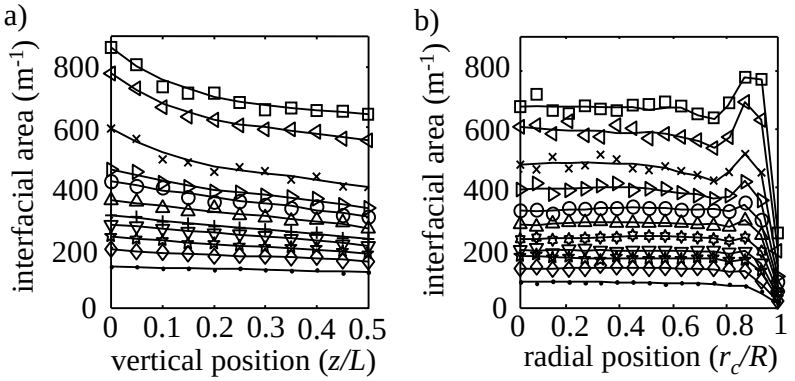


Figure 5.16: Interfacial area as a function of a) vertical position in the column and b) radial position in the column. Voidage key: • 3.1% ◊ 4.0% ☆ 5.2% ▽ 5.9% + 7.0% △ 8.1% ○ 9.3% ▷ 10.4% × 13.9% ◁ 18.1% □ 21.9%.

variance increasing as a function of gas-fraction. Similarly to Leblond *et al.*, propagators have been measured for the present system, and are shown in Figure 5.17.

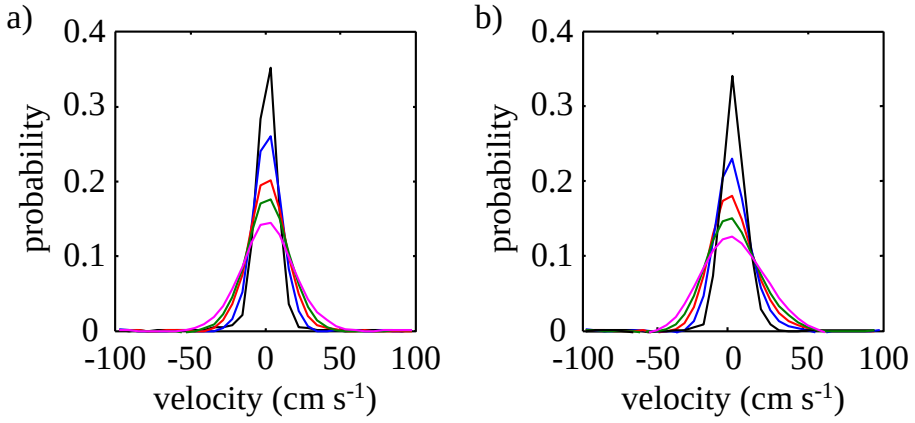


Figure 5.17: a) Longitudinal and b) transverse plane velocity component propagators as a function of voidage. For all measurements $G_z = 26$ G cm$^{-1}$. $\delta = 1$ ms $\Delta = 1.4$ ms. Color key: black $\varepsilon = 2.0\%$, blue $\varepsilon = 5.9\%$, red $\varepsilon = 10.4\%$, green $\varepsilon = 13.9\%$ and pink $\varepsilon = 21.9\%$.

The velocity distributions shown in Figure 5.17 closely resemble those previously reported by Leblond *et al.*; both longitudinal and transverse plane velocity components are symmetrical about zero (the liquid superficial velocity), which reflects adherence to the continuity equation. The flow contrast time for these measurements was 1.4 ms. It is interesting to note that by varying this displacement period different scales of motion in the system may be probed, with the propagator approaching a Gaussian distribution (corresponding to molecular diffusion) for sufficiently long flow contrast times. To test the dependence of propagator shape upon flow contrast time, this parameter was varied

for propagators measured at a voidage of 10.4%. These data are shown in Figure 5.18. It is clear from this figure that increasing the flow contrast time lead to a proportionate broadening of the displacement distribution, which demonstrates that the underlying velocity distribution is relatively independent of the selected flow contrast time.

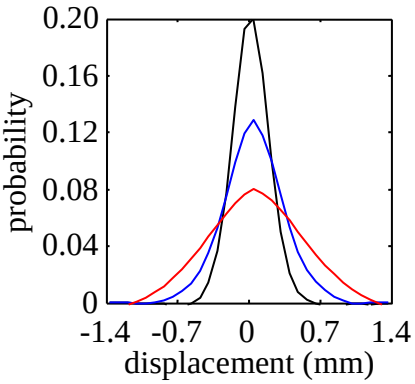


Figure 5.18: Longitudinal velocity component propagators as a function of observation time. All measurements were obtained at a voidage of 10.4%. Colour key: $\Delta = 1.4$ ms black, $\Delta = 2.4$ ms blue, $\Delta = 5.0$ ms red.

While Leblond *et al.* produced only spatially and temporally averaged measurements of the liquid phase hydrodynamics, quantitative 'snap-shot' velocity maps have been acquired of the present system using spiral imaging, as previously demonstrated in Section 4.2. This information is useful as the phenomenological nature of multiphase induced turbulence is still poorly understood, and turbulent shear must be accurately modelled for the prediction of the rate of bubble break-up. Example temporally resolved velocity images obtained for a range of voidages examined in the present work are shown in Figure 5.19. The position of bubbles in the plane of these images has been identified from the modulus images and masked by the filled white ellipses. Liquid is seen to be entrained by the rising bubbles while flowing downwards in channels in regions of bubble sparsity. The large scale circulatory behaviour often associated with bubble columns [45] was not observed in these experiments, most likely due to the small diameter system under examination. The average velocity for each dataset was $0 \pm 1.1$ cm s$^{-1}$ for each experiment (after the bubble regions have been removed by generating a mask using the modulus data), reflecting that mass is being conserved in these measurements. The range of velocities present in these images is in good accord with the propagators shown in Figure 5.17, with large segments of each image being stagnant, and the majority of velocities present constrained to the range $\pm 22.4$ cm s$^{-1}$.

While only single component velocity fields are presented herein, it is possible to use com-

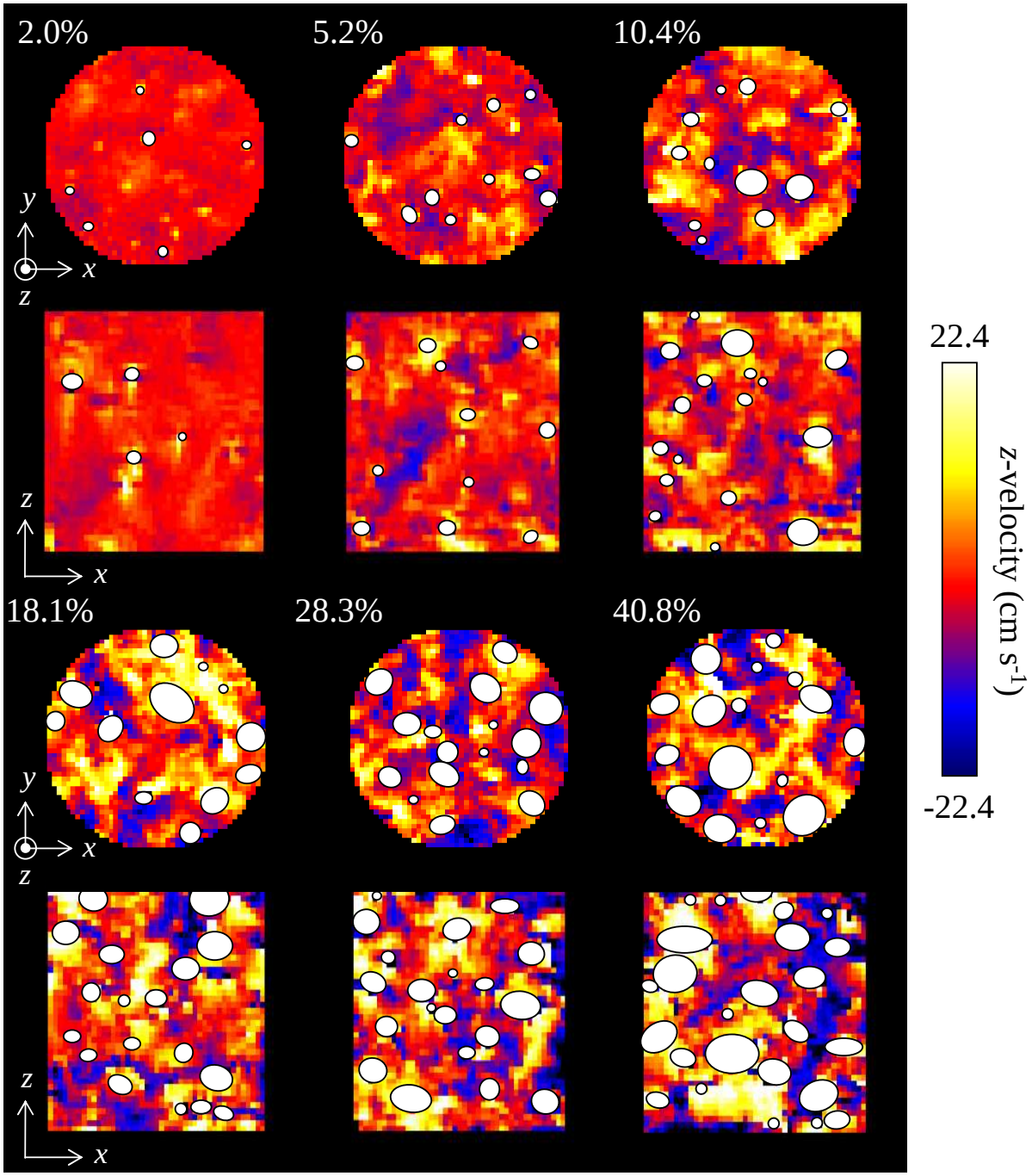


Figure 5.19: Example velocity images of the liquid-phase for different voidages. Cross-sectional plane and vertical images are shown. The slice thickness in these images was 1 mm. The cross-sectional images have a field of view of 37 mm × 37 mm and a resolution of 578 μm × 578 μm. The vertical plane images a field of view of 37 mm × 47 mm and spatial resolution of 578 μm × 734 μm.

pressed sensing to accelerate the image acquisition, and acquire all information required for three component velocity maps, as demonstrated in Section 4.3. Unfortunately, this was not possible for the present system as the mini-imaging gradient set used to accommodate the bubble column lacks a temperature monitoring system, and thus could not safely be used for rapid repeat acquisitions.

## 5.4 Conclusions

High voidage bubbly flow has been imaged using ultra-fast MRI for the first time. Spiral imaging proved to possess the spatio-temporal resolution, and robustness to fluid flow and shear required for high quality images to be obtained for the entire range of voidages for which bubbly flow was possible. Techniques were described for the extraction of two measurements of bubble size from MRI images: one on the basis of projected size, and the other from a direct measurement of the bubble volume. Using these two measurements, a description of bubble shape was inferred, which allowed the quantification of interfacial area. Automated data analysis procedures for the extraction of these parameters were described. All size distributions were found to be well described by log-normal distributions. The measurement technique was validated in application to a settling particle, and in comparison to optical bubble size measurements for a low voidage ($\varepsilon = 3.5\%$) system. Using an extracted measurement of aspect ratio, bubbles which were overlapping or part included in the excited slice during excitation were identified, and removed from the data set. The possibility of sampling bias introduced by this data filtering procedure was explored by application of the data analysis procedure to simulated MRI images, and it was found that the developed techniques are capable of accurately quantifying a size distribution up to a voidage of 22%, with the sampled population decreasing for higher gas-fractions accompanied by considerable sampling bias.

Using the developed methodologies, the bubble size distribution and interfacial area density were measured up to a voidage of 40.8%, the highest gas-fraction system upon which non-intrusive measurements have been performed to date. However, due to the possibility of sampling bias for measurements above 22% voidage, measurements performed on the highest gas-fraction systems cannot be considered accurate. For systems of this voidage and lower, size distributions and interfacial area were obtained as a function of position in a vertical bubble column. The evolution of the BSD due to bubble break-up and coalescence was apparent, with the system reaching an equilibrium size distribution within the examined region of the column at a voidage of 18.1%. Until this equilibrium

was reached the mean bubble size as a function of voidage was found to be well fitted by a power-law, however increased linearly once equilibrium was reached. By fitting these curves a set of numerical closures for bubble size as a function of voidage was provided for use in drift-flux analysis. Temporally resolved images were also obtained, allowing the motion of individual bubbles to be tracked, and bubble break-up and coalescence events to be observed.

The liquid phase hydrodynamics of the model bubble column were also investigated. Propagators were obtained for a range of voidages, and were found to be in good qualitative agreement with similar systems examined using NMR in the literature. Spatially and temporally resolved velocity information was also obtained, although due to hardware limitations only single component velocity fields were measured. These measurements demonstrate the great potential for ultra-fast MRI in the characterisation of gas-liquid flows, and for the validation of computational multiphase fluid dynamics codes.

# Bibliography


[1] Cheremisinoff, N., 1986. Review of experimental methods for studying the hydrodynamics of gas-solid fluidized beds. *Ind. Eng. Chem. Proc. Des. Dev.*, 25, pp. 329–351.

[2] Boyer, C., Duquenne, A. and Wild, G., 2002. Measuring techniques in gas-liquid and gas-liquid-solid reactors. *Chem. Eng. Sci.*, 57(16), pp. 3185–3215.

[3] Tayali, N.E. and Bates, C.J., 1990. Particle sizing techniques in multiphase flows: a review. *Flow. Meas. Instrum.*, 1, pp. 77–103.

[4] Adrian, R.J., 1991. Particle-imaging techniques for experimental fluid mechanics. *Annu. Rev. Fluid Mech.*, 23, pp. 261–304.

[5] Buchhave, P., George, W.K. and Lumley, J.L., 1979. The measurement of turbulence with the laser-doppler anemometer. *Annu. Rev. Fluid Mech.*, 11, pp. 443–503.

[6] Chaouki, J., Larachi, F. and Dudukovic, M.P., 1997. Noninvasive tomographic and velocimetric monitoring of multiphase flows. *Ind. Eng. Chem. Res.*, 36, pp. 4476–4503.

[7] Bieberle, M., Fischer, F., Schleicher, D., Koch, D., Menz, H.J., Mayer, H.G. and Hampel, U., 2009. Experimental two-phase flow measurement using ultra fast limited-angle-type electron beam x-ray computed tomography. *Exp. Fluids*, 47, pp. 369–378.

[8] Saxena, S.C., Patel, D., Smith, D.N. and Ruether, J.A., 1988. An assessment of experimental techniques for the measurement of bubble size in a bubble slurry reactor as applied to indirect coal liquefaction. *Chem. Eng. Comm.*, 63, pp. 87–127.

[9] Prasser, H.M., Bottger, A. and Zschau, J., 1998. A new electrode-mesh tomograph for gas-liquid flows. *Flow Meas. Instr.*, 9(2), pp. 111–119.

[10] Bruun, H.H., 1996. Hot-film anemometry in liquid flows. *Meas. Sci. Technol.*, 7, pp. 1301–1312.

[11] Juliá, J.E., Harteveld, W.K., Mudde, R.F. and Van den Akker, H.E.A., 2005. On the accuracy of the void fraction measurements using optical probes in bubbly flows. *Rev. Sci. Instrum.*, 76, p. 035,103.

[12] Rensen, J., Stefan, L., de Vries, J. and Lhose, D., 2005. Hot-film anemometry in bubbly flow I: bubble-probe interaction. *Int. J. Multiphase Flow*, 31, pp. 285–301.

[13] Magaud, F., Souhar, M., Wild, G. and Boisson, N., 2001. Experimental study of bubble column hydrodynamics. *Chem. Eng. Sci.*, 56, pp. 4597–4607.

[14] Kalkach-Navarro, S., Lahey, R.T., Drew, D.A. and Meyer, R., 1993. Interfacial area density, mean radius and number density measurements in bubbly two-phase flow. *Nuc. Eng. Des.*, 142, pp. 341–351.

[15] Hibiki, T., Goda, H., Kim, S., Ishii, M. and Uhle, J., 2003. Experimental study on interfacial area transport of a vertical downward bubbly flow. *Exp. Fluids*, 35, pp. 100–111.

[16] Kulkarni, A.A., Joshi, J.B. and Ramkrishna, D., 2004. Determination of bubble size distributions in bubble columns using LDA. *AIChE J.*, 50, pp. 3068–3084.

[17] Prasser, H.M., Scholz, D. and Zippe, C., 2001. Bubble size measurement using wire-mesh sensors. *Flow Meas. Instr.*, 12(4), pp. 299–312.

[18] Prasser, H.M., Beyer, M., Carl, H., Gregor, S., Lucas, D., Pietruske, H., Schutz, P. and Weiss, F.P., 2007. Evolution of the structure of a gas-liquid two-phase flow in a large vertical pipe. *Nucl. Eng. Des.*, 237(15-17), pp. 1848–186.

[19] Lynch, G.F. and Segel, S.L., 1977. Direct measurement of void fraction of a 2-phase fluid by nuclear magnetic resonance. *Int. J. Heat Mass Transfer*, 20, pp. 7–14.

[20] Leblond, J., Javelot, S., Lebrun, D. and Lebon, L., 1998. Two-phase flow characterization by nuclear magnetic resonance. *Nucl. Eng. Design*, 184, pp. 229–237.

[21] Chen, F.L. and Lin, S.W., 2000. Subpixel estimation of circle parameters using orthogonal circular detector. *Comput. Vis. Image Und.*, 13, pp. 206–221.

[22] Clift, R., Grace, J.R. and Weber, M.E., 1978. *Bubbles, drops, and particles.* Acadamic Press, New York.

[23] Petrou, M. and Bosdogianni, P., 1999. *Image processing, the fundamentals.* Wiley, West Sussex.

[24] Taubin, G., 1991. Estimation of planar curves, surfaces and nonplanar space curves defined by implicit equations, with applications to edge and range image segmentation. *IEEE T. Pattern. Anal.*, 13, pp. 1115–1138.

[25] Mao, J., Mareci, T.H. and Andrew, E.R., 1988. Experimental study of optimal selective 180 radiofrequency pulses. *J. Magn. Reson.*, 79, pp. 1–10.

[26] Glover, G.H., 1999. Simple analytic spiral k-space algorithm. *Magn. Reson. Med.*, 42, pp. 412–415.

[27] Fessler, J.A. and Sutton, B.P., 2003. Nonuniform fast fourier transform using min-max interpolation. *IEEE T. Signal Proces.*, 51, pp. 560–574.

[28] Akita, K. and Yoshida, F., 1973. Gas hold-up and volumetric mass transfer coefficient in bubble columns. *Ind. Eng. Chem. Process Des. Develop.*, 12, pp. 76–80.

[29] Hikita, H., Asai, S., Tanigawa, K., Segawa, K. and Kitao, M., 1980. Gas hold-up in bubble columns. *Chem. Eng. J.*, 20, pp. 59–67.

[30] Letzel, H.M., Schouten, J.C., Krishna, R. and van den Bleek, C.M., 1999. Gas holdup and mass transfer in bubble columns reactors operated at elevated pressure. *Chem. Eng. Sci.*, 54, pp. 2237–3346.

[31] Krishna, R., Wilkinson, P.M. and van Dierendonck, L.L., 1991. A model for gas holdup in bubble columns incorporating the influence of gas density on flow regime transitions. *Chem. Eng. Sci.*, 10, pp. 2491–2496.

[32] Jamialahmadi, M. and Müller-Steinhagen, 1992. Effect of alcohol, organic acid and potassium chloride concentration on bubble size, buble rise velocity and gas hold-up in bubble columns. *Chem. Eng. J.*, 50, pp. 47–56.

[33] Ribeiro, C.P. and Mewes, D., 2007. The influence of electrolytes on gas hold-up and regime transition in bubble columns. *Chem. Eng. Sci.*, 62, pp. 4501–4509.

[34] Orvalho, S., Růžička, M. and Drahoš, J., 2009. Bubble columns with electrolytes: gas holdup and flow regimes. *Ind. Eng. Chem. Res.*, 48, pp. 8237–8243.

[35] Cartellier, A. and Achard, J.L., 1991. Local phase detection probes in fluid/fluid two-phase flows. *Rev. Sci. Instrum.*, 62, pp. 279–303.

[36] Snedecor, G.W. and Cochran, W.G., 1989. *Statistical methods*. Iowa State University Press, Ames.

[37] Lunde, K. and Perkins, R.J., 1998. Shape oscillations of rising bubbles. *Appl. Sci. Res.*, 58, pp. 387–408.

[38] Coulson, J.M., Richardson, J.F., Harker, J.H. and Backhurst, J.R., 1991. *Chemical engineering volume 2, 4th Edition*. Butterworth-Heinemann, Oxford.

[39] Batchelor, G.K., 1967. *An introduction of fluid mechanics*. Cambridge University Press, Cambridge.

[40] Wang, T. and Wang, J., 2007. Numerical simulation of gas-liquid mass transfer in bubble column with a CFD-PBM coupled model. *Chem. Eng. Sci.*, 62, pp. 7107–7118.

[41] Hibiki, T. and Ishii, M., 2009. Interfacial area transport equations for gas-liquid flow. *J. Comp. Multiphase Flow*, 1, pp. 1–22.

[42] Delnoij, E., Kuipers, J.A.M.and van Swaaij, W. and Westerweel, J., 2000. Measurement of gas-liquid two-phase flow in bubble columns using ensemble correction PIV. *Chem. Eng. Sci.*, 55, pp. 3385–3395.

[43] Becker, S., De Bie, H. and Sweeney, J., 1999. Dynamic flow behaviour in bubble columns. *Chem. Eng. Sci.*, 54, pp. 4929–4935.

[44] Mudde, R.F., Groen, J.S. and van Den Akker, H.E.A., 1997. Liquid velocity field in a bubble column: LDA experiments. *Chem. Eng. Sci.*, 52, pp. 4217–4224.

[45] Mudde, R.F., 2005. Gravity-driven bubbly flows. *Annu. Rev. Fluid Mech.*, 37, pp. 393–423.

# Chapter 6

# Single bubble dynamics

A common approach to the lumped parameter analysis of multiphase systems is to make predictions about the behaviour of a system on the basis of the dynamics of a single bubble, droplet or particle. One example of this is drift-flux analysis, which uses the single bubble rise velocity as a basis for characterising the overall system hydrodynamics. For this reason, the accurate estimation of single bubble rise velocity is of the utmost importance in the design of gas-liquid unit operations, and has been the focus of much research. Models for the rise of small spherical bubbles ($< 0.5$ mm diameter) and large spherical caps ($> 15$ mm diameter) are well known. The former rise at a rate well described by Hadamard and Rybczynski [1, 2] in a pure (or non-polar) fluid, and by Stokes [3] in the presence of surfactants. At the other extreme, the rise velocity of large spherical cap bubbles is well predicted by the potential flow solution of Davies and Taylor [4]. The intermediate ellipsoidal bubbles, however, behave in a more complicated manner, and rise at a rate which has proven difficult to accurately predict.

The difficulty associated with understanding the dynamics of ellipsoidal bubbles stems from the emergence of a number of complex fluid phenomena as bubble size increases. Firstly, bubbles in the size range 1 mm $< d <$ 1.5 mm deform into ellipsoids as inertial forces begin to dominate over surface tension [5]. These bubbles undergo path deviations as they rise, and the flow field around a bubble begins to have a strong influence as the boundary layer in the rear of the bubble departs from potential flow and rotational

vortices form in the bubble's wake. For bubbles of size $d > 1.5$ mm, the bubble wake periodically detaches in a process known as vortex shedding, which is a phenomenon known to be coupled with the sinuous path followed by these bubbles as they rise [6]. Bubble shape oscillations also begin in this size range, and are also commonly attributed to vortex shedding [5]. These complications exist in addition to the influence held by any surface active molecules present. Surfactants act to inhibit surface mobility and decrease surface tension. Further, they tend to be swept to the rear of a bubble, forming a 'rigid cap', which acts to impart a positional dependence upon the interfacial shear state [7].

The rise velocity of ellipsoidal bubbles is influenced by the complicated mix of all of the effects described above. This is reflected in the well-known graph showing single bubble rise velocity as a function of bubble size, given in Figure 6.1 (reproduced from Clift *et al.* [5]), where a region of uncertainty exists for bubbles in the range 0.5 mm $< r_b <$ 5 mm. The classical models for determining the rise velocity of bubbles in this region are those of Mendelson [8], who predicted the upper-bound of the uncertain region, and Clift *et al.* [5] who gave a generalised correlation for surfactant contaminated drops and bubbles.

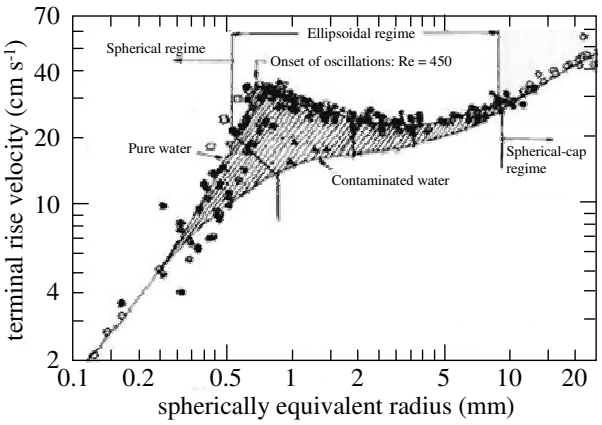


Figure 6.1: Single bubble rise velocity as a function of bubble size. Reproduced from Clift *et al.* [5].

The uncertainty associated with the rise velocity of ellipsoidal bubbles has conventionally been viewed as being principally dominated by the influence of surfactants. In an interesting recent study, however, Tomiyama *et al.* [9] demonstrated that for bubbles in a pure fluid, the initial bubble deformation strongly influenced the rise path and velocity. They noted that bubbles with a small initial deformation (i.e. that were formed in a capillary of comparable size to the bubble diameter) rose along a zig-zag path, and closely adhered to the curve describing the rise velocity of bubbles in heavily contaminated water, whereas

bubbles with a large initial deformity transitioned from a zig-zag to a helical path after rising 50 cm from the sparger, and rose at velocities scattered between the upper and lower bounds of the uncertain region. This trend is demonstrated in Figure 6.2, which is reproduced from Tomiyama *et al.* [9].

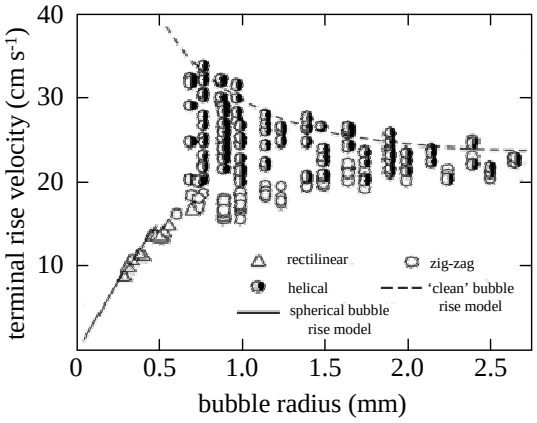


Figure 6.2: Influence of initial bubble deformation on single bubble rise velocity. Bubbles which rose along a zig-zag path had low initial deformation, while bubbles rising helically were initially highly deformed. This figure is reproduced from Tomiyama *et al.* [9].

It is clear from Figure 6.2 that the shape of the bubbles is a significant factor in determining the bubble rise velocity. It is likely that the presence of surfactants in a system has the dual influence on rise velocity of damping shape oscillations while also altering the interfacial slip condition. Tomiyama *et al.* [9] proposed a model for the rise velocity of bubbles in the ellipsoidal regime which accounts for the effect of bubble shape. Similar to the approach of Davies and Taylor, they coupled potential flow about the nose of the bubble, with the Young-Laplace equation and a model for the bubble curvature. The model of Tomiyama *et al.*, however, needs to be closed using a separate model for bubble aspect ratio. Unfortunately, it has proved difficult to produce such a model for bubble shape, and the rise model of Tomiyama *et al.* needs therefore to be closed using experimental data.

Experimentally characterising the shape of single bubbles is itself difficult owing to problems associated with characterising the 3-D shape of a bubble at any given instant. This problem arises because a 2-D projection (such as a photograph) of an asymmetrical bubble does not portray an accurate representation of the true bubble shape or orientation. In fact, as soon as the bubble loses radial symmetry the bubble orientation becomes ambiguous, and the projected length scales may not be representative of the true shape. This fact is demonstrated in Figure 6.3, where an arbitrary ellipsoid is shown with three

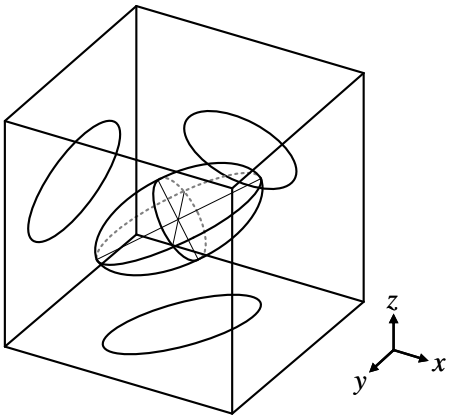


Figure 6.3: Demonstration of the problem associated with determining a 3D shape from 2D projections. In the absence of the $x$-$y$ projection, a poor estimate of the shape is obtained.

orthogonal projections. From this figure it is clear that the true shape of the ellipsoid cannot be accurately determined from only $x$-$z$ and $y$-$z$ plane projections (which typify the data commonly collected in the study of single bubbles). This dilemma has lead several previous authors to conclude that it is impossible to determine the three dimensional shape of a bubble [9, 10, 11]. Different approaches have been applied to avoid this problem: Ellingsen and Risso [12], who acquired two simultaneous orthogonal projections, assumed their bubbles to remain oblate ellipsoids symmetrical about the direction of the bubble motion, while Lunde and Perkins [10] suggested that the data may be filtered to only those occasions where two simultaneous projections are in agreement regarding the bubble orientation. Uncertainty about bubble shape has also prevented the direct observation of different modes of shape oscillations. Most studies of bubble shape oscillation resort to Fourier analysis to extract representative oscillation frequencies, which are then compared with models that predict the frequency of differing modes of shape oscillation [10, 11]. Note that some models for bubble shape oscillation need to be closed using information regarding bubble shape (for example, that of Lunde and Perkins [10], which requires ellipticity), which returns to the original problem of obtaining a representative description of bubble shape.

While it is well known that the presence of electrolytes has a significant effect upon the structure of a bubbly flow system (as discussed in Section 1.2), it is not clear whether the behaviour of a single bubble will be affected. It is contested in the literature whether the presence of a salt alters the bubble terminal velocity: Sato *et al.* [13] state that electrolytes have no effect, while Jamialahmadi and Müller-Steinhagen [14] claim that salt

decreases the bubble rise velocity. Further, it has been speculated that the presence of salt can change the boundary condition at a gas-liquid interface from slip to no-slip [15], however Henry *et al.* [16] have shown that the rise of very small bubbles in salt solutions is still governed by the Hadamard-Rybczynski law. The influence of electrolytes on bubble rise velocity is particularly important for the present study, as the continuous phase used was doped with paramagnetic salts in order to render the system suitable the for application of ultra-fast MRI.

In the present chapter the dynamics of single bubbles rising through an electrolyte solution are examined, with the goal validating a single bubble rise model for use with drift-flux analysis. Firstly bubble rise models from the literature are reviewed and tested in comparison to experimental data. As discussed above, some models require closure using information regarding bubble shape. In order to provide this information, a new experimental methodology is described for the determination of 3-D bubble shapes. The reconstructed bubbles allow the direct observation of bubble shape instability, and are employed to test the validity of different models of bubble shape oscillation. The bubble shape information is then coupled with the bubble rise model to provide an accurate description of single bubble rise velocity. To the best of the author's knowledge, this is the first time a three dimensional description of bubble shape has been produced.

## 6.1 Theoretical

### 6.1.1 Bubble rise models

Many models and correlations have been proposed for the prediction of single bubble rise velocity, which are reviewed in full by Kulkarni and Joshi [17]. In this section, a representative selection of these models is examined.

#### Stokes (1880), Hadamard and Rybczynski (1911)

The earliest attempt to model single bubble terminal rise velocity was provided by Stokes [3], who balanced drag and bouyancy forces to give:

$$V_{\mathrm{T}} = \frac{2}{9}\frac{\Delta\rho g r_{\mathrm{b}}^2}{\mu_{\mathrm{l}}} \tag{6.1}$$

where $\Delta\rho$ is the density difference between the two phases, $g$ is acceleration due to gravity, $r_{\mathrm{b}}$ is spherically equivalent bubble diameter and $\mu_{\mathrm{l}}$ is the viscosity of the liquid phase.

Note that equation (6.1) is only valid for spherical bubbles in laminar flow conditions ($r_\mathrm{b} < 0.25$ mm). Within this range, equation (6.1) provides accurate predictions for settling particles and bubbles in heavily contaminated systems (which exhibit a no-slip boundary condition). For small bubbles rising through pure solution, momentum can be transferred across the gas-liquid interface, and recirculating vortices will exist inside the bubble. This has the effect of decreasing drag, and hence increases the rise velocity. Hadamard [1] and Rybczynski [2] independently proposed a modification to Stokes law:

$$V_\mathrm{T} = \frac{2}{3}\frac{\Delta\rho g r_\mathrm{b}^2}{\mu_\mathrm{l}}\frac{\mu_\mathrm{l}+\mu_\mathrm{b}}{2\mu_\mathrm{l}+3\mu_\mathrm{b}} \tag{6.2}$$

where $\mu_\mathrm{b}$ is the viscosity of the dispersed phase. Note that in the limit $\mu_\mathrm{b}/\mu_\mathrm{l} \to \infty$ equation (6.2) approaches equation (6.1), while if $\mu_\mathrm{b} \approx 0$ (as is the case for a gas) equation (6.2) predicts a bubble velocity 1.5 times greater than that of equation (6.1). As both equations are only valid for bubbles of size $r_\mathrm{b} < 0.25$ mm, which is less than the smallest bubbles considered in the present study, the equations of Stokes, Hadamard and Rybczynski will not be further considered.

**Mendelson (1967)**

An innovative model was provided by Mendelson [8], who suggested that bubbles may be modelled as surface waves propagating through a fluid, for which the theory was established by Lamb [18]. By setting a characteristic length of the bubble (an equivalent circumference) to act as a wavelength, Mendelson gave the equation:

$$V_\mathrm{T} = \sqrt{\frac{\sigma}{\rho_\mathrm{l} r_\mathrm{b}} + g r_\mathrm{b}} \tag{6.3}$$

where $\sigma$ is surface tension and $\rho_\mathrm{l}$ is the liquid density. Equation (6.3) closely corresponds to the upper bound of the region of uncertainty for ellipsoidal bubbles, and gives good results for bubbles in the size range $r_\mathrm{b} > 2$ mm rising through a pure fluid. Tomiyama *et al.* [9] showed that the model of Mendelson provides a poor fit to bubbles with low initial deformity, which tend to behave like surfactant contaminated bubbles even in a pure fluid. Slight modifications to the model of Mendelson have been given for systems in which the dispersed phase density is not negligible by Lehrer [19] and Jamialahmadi *et al.* [20].

### Clift *et al.* (1978)

Clift *et al.* [5] gave a generalised correlation for ellipsoidal bubbles rising through surfactant contaminated solution. Those workers defined two dimensionless groups as:

$$\mathrm{H} = \frac{4}{3}\mathrm{Eo}\ \mathrm{M}^{-0.149}\left(\frac{\mu}{0.0009}\right)^{-0.14} \tag{6.4}$$

$$\mathrm{J} = \mathrm{Re}\ \mathrm{M}^{0.149} + 0.857 \tag{6.5}$$

where the Eötvös, Morton and Reynolds numbers are defined as:

$$\mathrm{Eo} = \frac{4\Delta\rho g r_e^2}{\sigma} \tag{6.6}$$

$$\mathrm{Re} = \frac{2\rho_\mathrm{l} V_\mathrm{T} r_\mathrm{b}}{\mu} \tag{6.7}$$

$$\mathrm{M} = \frac{g\mu^4\Delta\rho}{\rho_\mathrm{l}^2\sigma^3}. \tag{6.8}$$

Two correlations were found to be valid over the range $\mathrm{M} < 10^{-3}$, $\mathrm{Eo} < 40$ and $\mathrm{Re} > 0.1$:

$$\mathrm{J} = 0.94\mathrm{H}^{0.757} \qquad 2 < \mathrm{H} \leq 59.3 \tag{6.9}$$

$$\mathrm{J} = 3.42\mathrm{H}^{0.441} \qquad \mathrm{H} > 59.3. \tag{6.10}$$

The first correlation corresponds to bubbles not undergoing shape oscillations, and the second to oscillating bubbles. Equation (6.5) may be rewritten as:

$$V_\mathrm{T} = \frac{\mu}{2\rho_\mathrm{l} r_\mathrm{b}}\mathrm{M}^{-0.149}(\mathrm{J} - 0.857). \tag{6.11}$$

Thus by calculating dimensionless group H using equation (6.4), J may be inferred from either equation (6.9) or (6.10), which permits the bubble rise velocity to be calculated using equation (6.11). These correlations were noted to be accurate within 15% for surfactant solutions.

### Abou-el-hassan (1983)

Abou-el-hassan [21] found that bubbles rising at low and intermediate Reynolds numbers could be correlated on a single curve by two dimensionless numbers know as the flow

number, F, and the velocity number, V. These dimensionless numbers are defined as:

$$\mathrm{V} = V_{\mathrm{T}} \left( \frac{4\rho_{\mathrm{l}}^2 r_{\mathrm{b}}^2}{\sigma\mu} \right)^{1/3} \tag{6.12}$$

$$\mathrm{F} = g \left( \frac{256\rho_{\mathrm{l}}^5 r_{\mathrm{b}}^8}{\sigma\mu^4} \right)^{1/3} \tag{6.13}$$

and were found to be well correlated according to:

$$\mathrm{V} = (\log \mathrm{F})^2 \tag{6.14}$$

This correlation achieved good agreement over a wide range of conditions in comparison to a collection of data from the literature. The concept of using flow and velocity numbers to propose bubble rise correlations has since been extended to a broader range of Reynolds numbers by Rodrigue [22].

### Tomiyama *et al.* (2002)

The influence of bubble shape on rise velocity has been examined in detail by Tomiyama *et al.* [9], who found that bubbles with a large initial deformation tend to rise along spiral trajectories and at velocities up to that given by the model of Mendelson [8], while those bubbles with a small initial deformation tend to rise in zig-zag trajectories, and at velocities closer to that expected for bubbles in a surfactant contaminated system. To incorporate the effect of bubble shape into a terminal velocity model, Tomiyama *et al.* [9] used the Young-Laplace equation with potential flow theory applied in the region of the stagnation point at the nose of a bubble. For oblate spheroidal bubbles this model reduced to:

$$V_{\mathrm{T}} = \frac{\sin^{-1}\sqrt{1-E^2} - E\sqrt{1-E^2}}{1-E^2} \sqrt{\frac{4\sigma}{\rho_{\mathrm{l}} r_{\mathrm{b}}} E^{4/3} + \frac{\Delta\rho g r_{\mathrm{b}}}{\rho_{\mathrm{l}}} \frac{E^{2/3}}{1-E^2}}. \tag{6.15}$$

This model requires closure for the bubble aspect ratio, $E$, which must be provided from experimental data. For surfactant contaminated systems, Wellek *et al.* [23] state that the aspect ratio of single bubbles is well correlated by:

$$E = \frac{1}{1 + 0.163\mathrm{Eo}^{0.757}}. \tag{6.16}$$

No holistic correlation exists for the aspect ratio of bubbles in a pure solution, with bubbles above Eo = 0.5 exhibiting very low aspect ratios (less than 0.6), and there

being considerable scatter in the data [5]. Tomiyama *et al.* used the closure of Wellek *et al.*, and while they conceded that their model produced only modest agreement with experimental results, they noted that the performance of their model may be improved with the use of more accurate information for $E$. The accurate experimental measurement of bubble aspect ratios is limited by the problems associated with the determination of the true bubble shape, as previously discussed. The development of a bubble shape reconstruction procedure for use in supplying a more accurate closure correlation to the model of Tomiyama *et al.* is explored in Section 6.1.2.

### 6.1.2 Development of a bubble shape reconstruction procedure

An ellipsoid of constant density, centred at the origin, with three dissimilar principle axes each at some orientation to the laboratory reference frame, is described by the equation:

$$Ax^2 + By^2 + Cz^2 + Dxy + Exz + Fyz = 1 \tag{6.17}$$

where $A \leq 0$, $B \leq 0$, $C \leq 0$, $D^2 - 4AB \leq 0$, $E^2 - 4AC \leq 0$, $F^2 - 4BC \leq 0$. The reconstruction of such a shape from projections was first considered by Karl *et al.* [24]. They demonstrate that a linear relationship exists between an ellipsoid and orthogonal projections of that shape. This theory was applied by Noumeir [25] to quantify the rotation of an ellipsoid about a single axis from projections, and by Kayicioglu *et al.* [26], who reconstructed a static ellipsoid from two dimensional projections by estimating the line integral projection. The present reconstruction differs from this latter work in that, rather more simply, a projection matrix is used to link the equation of an ellipsoid to its projections. Additionally, it is sought to reconstruct a number of time sequential ellipsoids, and the labelling of principles axes of these must be consistent from one reconstruction to the next. The rotation conventions and notation for a projected ellipse with regard to the original ellipsoid are illustrated in Figure 6.4 a). The coordinate system employed for describing the orientation, position and shape of the reconstructed ellipsoid with respect to the laboratory frame is shown in Figure 6.4 b).

After Karl et al. [24], equation (6.17) may be expressed as:

$$u^T X u = 1 \tag{6.18}$$

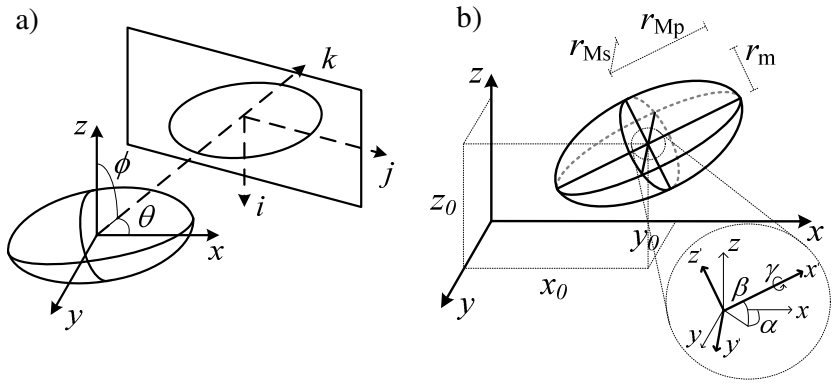


Figure 6.4: a) Coordinate system for describing the relationship between an ellipsoid and an elliptical projection. b) Notation for describing the size, orientation and position of a reconstructed ellipsoid.

where $u = [x\ y\ z]^T$ and

$$X = \begin{bmatrix} A & D/2 & E/2 \\ D/2 & B & F/2 \\ E/2 & F/2 & C \end{bmatrix}. \tag{6.19}$$

This ellipsoid may be rotated into the reference frame of a given projection $\tilde{u} = [i\ j\ k]^T$ by the transform:

$$\tilde{u} = Lu \tag{6.20}$$

where $L$ is the rotation matrix:

$$L = \begin{bmatrix} \cos\theta\cos\phi & -\sin\theta\cos\phi & \sin\phi \\ \sin\theta & \cos\theta & 0 \\ -\cos\theta\sin\phi & \sin\theta\sin\phi & \cos\phi \end{bmatrix}. \tag{6.21}$$

The ellipsoid in its new coordinates may be projected onto the $i$-$j$ plane by the transform:

$$\bar{u} = P^T\tilde{u} \tag{6.22}$$

where $P$ is the projection matrix:

$$P = \begin{bmatrix} 1 & 0 \\ 0 & 1 \\ 0 & 0 \end{bmatrix}. \tag{6.23}$$

Substituting (6.20), and subsequently (6.22), into (6.18) yields:

$$\bar{u}^T S \bar{u} = 1 \tag{6.24}$$

where $\bar{u} = [i\ j]^T$ and $S = P^T L X L^T P$. The coefficients of this matrix may be evaluated as:

$$S = \begin{bmatrix} s_1 & s_2 \\ s_2 & s_3 \end{bmatrix}. \tag{6.25}$$

where:

$$\begin{aligned} s_1 &= (A\cos^2\theta - D\cos\theta\sin\theta + B\sin^2\theta)\cos^2\phi + C\sin^2\phi \\ &\quad + (E\cos\theta - F\sin\theta)\cos\phi\sin\phi \qquad (6.26) \\ s_2 &= 0.5\left[((A-B)\sin 2\theta + D\cos 2\theta)\cos\phi + (E\sin\theta + F\cos\theta)\sin\phi\right] \qquad (6.27) \\ s_3 &= A\sin^2\theta + B\cos^2\theta + D\cos\theta\sin\theta. \qquad (6.28) \end{aligned}$$

Equation (6.24) may be rewritten as a projected ellipse:

$$s_1 i^2 + 2 s_2 ij + s_3 j^2 = 1. \tag{6.29}$$

It is this equation that we seek to fit to measured ellipses (measured using high-speed photography) for the determination of the parameters of an ellipsoid in the laboratory frame. If all projections are obtained orthogonal to the $x$-$y$ plane, and we assume that the ellipsoid remains oblate at all times, the projected ellipses will be of the form:

$$a_n j^2 + b_n ij + c_n i^2 = 1 \tag{6.30}$$

where $a$ and $c$ are the major and minor semi-axes, respectively, and $b$ is the coefficient containing rotational information of the ellipse. The subscript $n$ represents the projection number. In order to extract the coefficients of the equation (6.30) from images the technique of Fitzgibbon *et al.* [27] may be applied. According to Kayikcioglu *et al.* [26] a minimum of three projected ellipses are required for a unique reconstruction of an

ellipsoid. Equating (6.29) and (6.30) yields:

$$a_n - s_{3n} = 0 \tag{6.31}$$

$$b_n - 2s_{2n} = 0 \tag{6.32}$$

$$c_n - s_{1n} = 0. \tag{6.33}$$

Similarly to Kayikcioglu *et al.* [26], we define an error function as the unweighted sum of squares in equations (6.31) to (6.33):

$$h(A, B, C, D, E, F) = \sum_{n=1}^{N} \left( (a_n - s_{3n})^2 + (b_n - 2s_{2n})^2 + (c_n - s_{1n})^2 \right). \tag{6.34}$$

By seeking to minimise this error, subject to the constraints imposed upon equation (6.17), the coefficients of the ellipsoid may be determined. In implementing this technique we used the nonlinear least squares subroutine of the MATLAB optimisation toolbox. The reconstruction proved fairly robust to the choice of initial guess for the six coefficients, however to prevent convergence towards zero, it is helpful to ensure that the initial guesses are always larger than the expected values of the ellipsoid coefficients.

With the ellipsoid parameters quantified in this way, the orientations of the principle axes are given by the eigenvectors of matrix (6.19) whilst the semiaxis lengths are given by $1/\sqrt{\lambda_i}$, where $\lambda_i$ are the corresponding eigenvalues [24]. The eigenvectors may be converted to three angles to provide greater lucidity regarding the orientation of the bubble. In the present work, the $z$-$x$-$z$ Euler angle convention will always be used. The present reconstruction is given for ellipsoids centred at the origin, however the location of the ellipsoid centre with reference to some laboratory origin may be readily determined by triangulation (via back projection) of the centres of each projected ellipse. For the repeated application of this procedure towards obtaining a time-resolved shape of a dynamic ellipsoid, a complication arises in identifying which of the eigenvalues and eigenvectors match with those from the previous iteration, as these lengths and directions effectively result from the roots of a multivariate quadratic equation and hence have no particular order associated with them. This problem is simplified for the present system as it is known that the minor axis of the bubble is always orientated towards the positive axial direction, and that this length will always be the shortest of the three semi-axes. Thus, the problem reduces to differentiating between the two major axes. This is possible as the cross-product of the eigenvectors associated with these axes (which is equivalent to the minor axis) must always have a positive $z$-component. Using this sorting constraint,

all three axes may be separated, and the changing length and orientation of the bubble may be observed as the bubble rises. A more general solution for this problem may also be reached by examining the dot product of each of the current set of eigenvectors with those preceding, and using this information to order the eigenvalues and eigenvectors such that they are most consistent with the previous iteration.

### 6.1.3 Shape oscillation models

In addition to supplying closure to bubble rise models, the reconstruction of a 3D bubble shape allows bubble shape oscillations to be directly observed for the first time. This presents a unique opportunity to validate or challenge models for different modes of bubble shape oscillation. In this section the two most commonly applied models for bubble shape oscillation are reviewed.

#### Rayleigh-Lamb (1895)

The most commonly applied model for bubble shape oscillation is that of Lord Rayleigh (popularised by Lamb [18]), who derived an analytical expression for the frequency of bubble shape oscillations which correspond to modes of spherical harmonics:

$$f_{\mathrm{n}} = \frac{1}{2\pi}\sqrt{\frac{(n+1)(n-1)(n+2)\sigma}{\rho_{\mathrm{l}} r_{\mathrm{b}}^3}} \tag{6.35}$$

where $n$ is the mode number. Note that equation (6.35) is not valid for $n = 0$, which would correspond to the volume non-conserving radial expansion and contraction of the bubble. Most often, this model is used to consider mode 2 oscillations, which correspond to the oscillation of a bubble between prolate and oblate forms (as demonstrated in Figure 6.5 a). Setting $n = 2$ in equation (6.35):

$$f_2 = \frac{1}{2\pi}\sqrt{\frac{12\sigma}{\rho_l r_{\mathrm{b}}^3}} \tag{6.36}$$

#### Lunde and Perkins (1998)

More recently, Lunde and Perkins [10] offered a model that assumes the shape oscillation to behave as a capillary wave travelling over the surface of the bubble. This approach uses the same theory (given by Lamb [18]) as the bubble rise model of Mendelson [8].

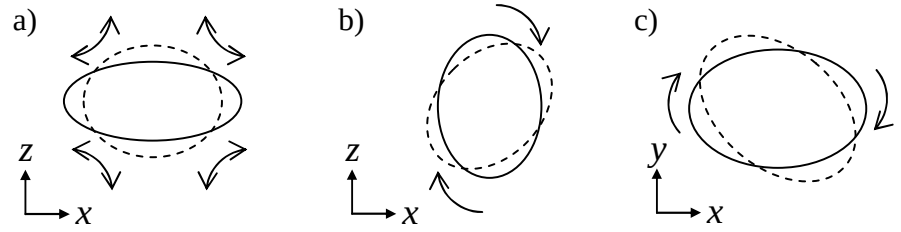


Figure 6.5: Demonstration of different modes of bubble shape oscillation: a) mode 2 b) mode 2,0 c) mode 2,2.

Using wavelengths equivalent to the circumference of the bubble (again, like Mendelson) they proposed expressions for the frequency of waves travelling between the poles of the bubble (so-called mode 2,0 oscillations; Figure 6.5 b), and for waves travelling around the equator of the bubble (mode 2,2; Figure 6.5 c):

$$f_{2,0} = \frac{1}{2\pi}\sqrt{\frac{16\sqrt{2}\varepsilon^2\sigma}{\rho_l(\varepsilon^2+1)^{3/2}r_\mathrm{b}^3}} \tag{6.37}$$

$$f_{2,2} = \frac{1}{2\pi}\sqrt{\frac{8\sigma}{\rho_l\varepsilon r_\mathrm{b}^3}}. \tag{6.38}$$

In this model $\varepsilon$ is bubble ellipticity, defined as being the inverse aspect ratio:

$$\varepsilon = \frac{1}{E} = \frac{r_\mathrm{b}}{r_\mathrm{m}} \tag{6.39}$$

where $r_\mathrm{m}$ is the bubble minor axis, and $r_\mathrm{b}$ is the equivalent major axis:

$$r_\mathrm{b} = \sqrt{r_\mathrm{Mp} r_\mathrm{Ms}}. \tag{6.40}$$

## 6.2 Experimental

All information required to measure the bubble rise velocity and reconstruct bubble shape was measured for two hundred bubbles in the size range 0.5 mm $< r_\mathrm{b} <$ 2.3 mm. Kayikcioglu *et al.* [26] demonstrate that three simultaneous projection contours are required for the reconstruction of an ellipsoid. Three such projections were attained of each bubble using a high-speed video camera and an arrangement of mirrors, as shown in Figure 6.6 a). For maximum projectivity it is desirable to have each projection evenly spaced around the bubble. To this end, the mirrors were arranged such that the camera recorded three simultaneous projections at 120° to each other. In orientating the mirrors, six equidistant marks were placed on the outside of the column, and the camera and mirrors were then

adjusted such that the opposite marks for each projection were aligned. This alignment is demonstrated in Figure 6.6 b). A Photron Fastcam SA-1 model 120K-M2 high-speed imaging system was used to record data at a rate of 500 fps, which was ten times greater than the highest frequency of bubble shape oscillation expected. The field of view of the recorded images was 25 cm $\times$ 25 cm, which was sufficient to capture several complete cycles of the secondary motion of the bubbles at a spatial resolution of 244 $\mu$m $\times$ 244 $\mu$m. A flood light reflected off a piece of foamed card was used to provide a diffuse light source for the photography.

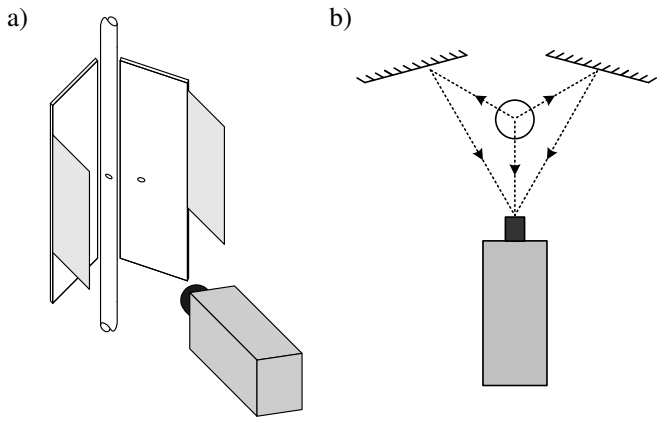


Figure 6.6: a) Schematic of experimental set up. b) Demonstration of the mirror alignment used in the present experiments.

The bubble column used was of inside diameter 50 mm, 1.5 m long and made of Perspex. The column was washed with ethanol and sealed quickly after drying to minimise surfactant contamination. A solution of 16.86 mM dysprosium chloride was used for the liquid phase in all experiments for consistency with earlier MRI measurements. The experimental setup used for the generation of bubbles of controllable size is shown in Figure 6.7. A modified version of the device described by Ohl [28] was employed, which is shown in Figure 6.7 a). This apparatus consists of a solenoid valve that permits discrete slugs of gas to form in a channel of diameter 5 mm prior to being conveyed to the base of the bubble column, where they detach to form stable bubbles. Steady flow along this channel was provided at a rate of 12.5 cm$^3$ min$^{-1}$ by a syringe pump (Harvard instruments 22). This corresponds to a superficial liquid velocity in the main column of 0.1 mm s$^{-1}$, which may be considered to be negligible. A 3 s delay was permitted before the generation of each bubble to ensure that the wake from the preceding bubble was fully dissipated. Note that the device of Ohl has been previously employed by Velhuis *et al.* [11], who used it to generate highly deformed bubbles. This is desirable for the present study, as it seems

likely that the bubbles generated in a full scale bubble column will be subject to a high degree of initial deformation. While the imaging system is not shown in Figure 6.7, it was arranged such that the centre of the imaging region lay at a position 1 m from the bubble generator.

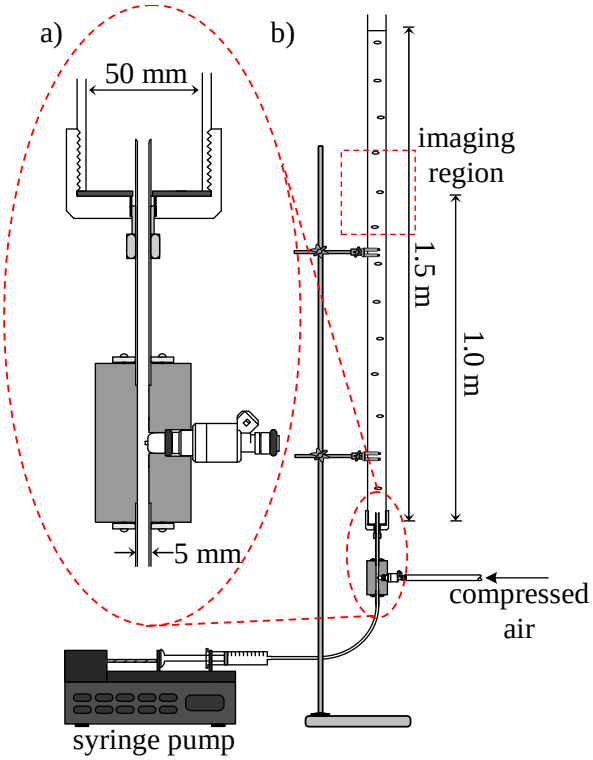


Figure 6.7: a) Detail of the bubble generator of Ohl [28], which was used in the present study for the generation of bubbles of controllable size. b) The overall experimental setup used for the study of single bubbles. The high-speed imaging equipment shown in Figure 6.6 is not shown here for greater clarity.

To aid in the analysis of the data, a 'blank' image consisting of the liquid filled column (with no bubbles present) was subtracted from all datasets. The bubble images were then segmented into the three column projections, which were scaled to correct for the effect of varying focal length and, in the case of the two mirror projections, flipped horizontally. The images were thresholded at a level sufficient to isolate the bubble from the background, and ellipses were fitted to these 'clean' data using the procedure described by Fitzgibbon *et al.* [27]. With the lengths and orientation of the principle axes of the projections thus quantified, the three dimensional shape of the bubble was determined by the procedure described in Section 6.1.2. The rise velocity of each bubble was measured using a central difference approximation of the gradient of vertical bubble position.

## 6.3 Results

### 6.3.1 Comparison of bubble rise models

The terminal velocity of 200 bubbles in the size range 0.5 mm $< r_b <$ 2.3 mm rising through 16.86 mM dysprosium chloride solution has been measured using high-speed photography. Rise velocity as a function of bubble size is shown in Figure 6.8 in comparison with several bubble rise models from the literature. Figure 6.8 a) shows the experimental data compared to the predictions of the model of Mendelson [8], which is well recognised to give accurate predictions for bubbles rising in a clean solution. Figure 6.8 b) shows a comparison with the correlation of Clift *et al.* [5], which is reported to give results within 15% error (calculated from the root mean square of velocity) for bubbles rising in surfactant contaminated solutions. The experimental data are contrasted with the correlation of Abou-el-hassen [21] in Figure 6.8 c), whose correlation was proposed using data from the literature across a broad range of conditions. Lastly, a comparison with the model of Tomiyama *et al.* [9], closed using the correlation of Wellek *et al.* [23], is shown in Figure 6.8 d).

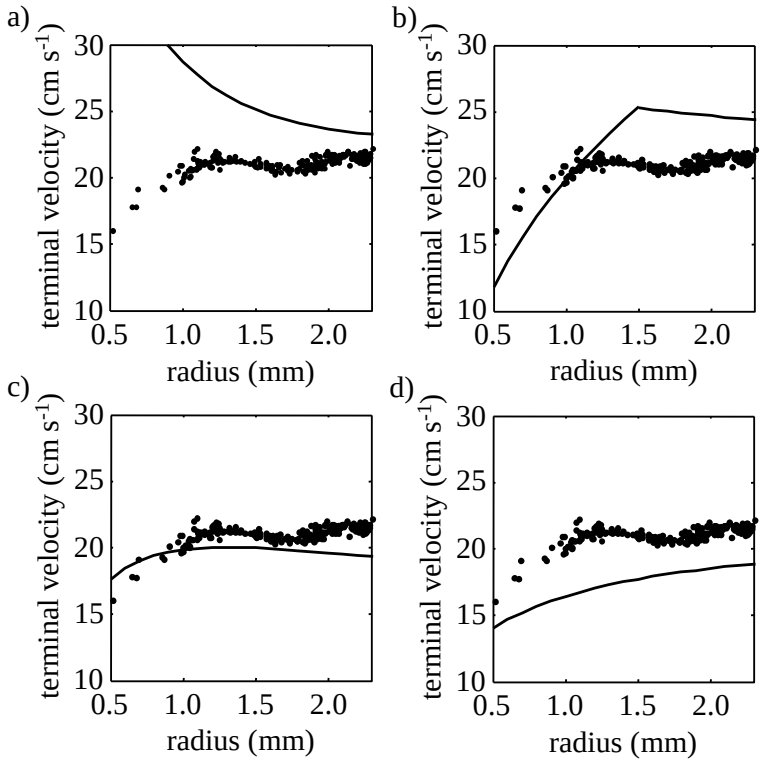


Figure 6.8: Comparison of measured rise velocities with the models of a) Mendelson [8], b) Clift *et al.* [5], c) Abou-el-hassen [21] and d) Tomiyama *et al.* [9] closed using the correlation of Wellek *et al.* [23].

Interestingly, the bubbles are seen to rise more slowly than predicted by both the model of Mendelson and the correlation of Clift *et al.*. It is anticipated that the present bubbles were generated with high initial deformity as the present method of bubble generation has been previously employed by Velhuis *et al.* [11], whose bubbles rose through a pure solution in spiral trajectories and close to the velocities predicted by Mendelson. This disparity suggests that it is the presence of the paramagnetic salt that has affected the bubble rise velocity. The correlation of Abou-el-hassen gives modest agreement, with an under-prediction of 10% seen for bubbles in the range 1 mm $< r_b <$ 2 mm. This correlation was developed from a great variety of different fluids, and may somewhat account for the influence of the dopant. Poor agreement is also seen with the predictions of the model of Tomiyama *et al.*. This seems unsurprising given that this model was closed using shape information obtained for bubbles in surfactant contaminated systems. The accuracy of this model may be improved by quantifying the aspect ratio for bubbles in the present system, which is examined in the following section.

### 6.3.2 Bubble shape reconstruction

Information about bubble shape is important both for the characterisation of single bubble dynamics, and to supply accurate closure correlations for use with bubble rise models such as that of Tomiyama *et al.* [9]. The 3D shape of 200 bubbles in the size range 0.5 mm $< r_b <$ 2.3 mm has been reconstructed, however in order to demonstrate the type of information produced by the shape reconstruction procedure, data for a single bubble of size $r_b = 2.3$ mm will first be focused upon. An example image showing the three simultaneous projections and fitted contours to this example bubble are shown in Figure 6.9

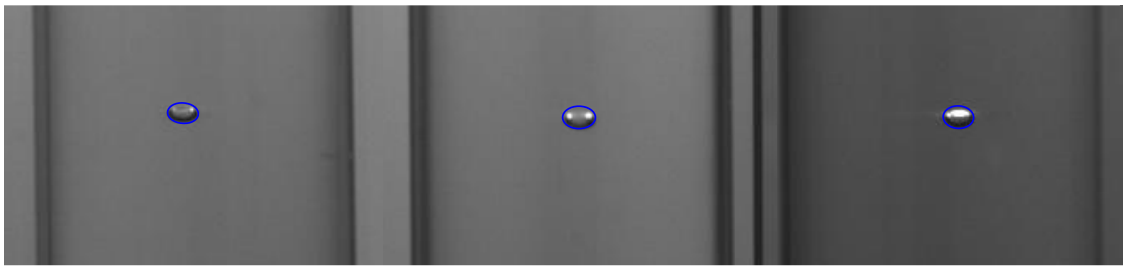

Figure 6.9: Example image obtained showing three simultaneous projections of a rising single bubble of size $r_b = 2.3$ mm.

All data quantifying the size, position and orientation of this bubble are given in Figure 6.10. The lengths of the primary and secondary major axes for this bubble are shown together with the minor axis in Figure 6.10 a), while the orientation of these axes with

regard to the laboratory frame is given in b). The position of the bubble's centroid with respect to the centre of the column is given in c), from which it is clear that the bubble rose along a zig-zag trajectory (reflected by the in-phase oscillation of the $x$ and $y$ position of the bubble). This is consistent with the behaviour of low-initial deformation bubbles observed by Tomiyama [9], however is more likely the influence of the salt in the present system as our method of bubble generation is identical to that used by Velhuis *et al.* [11], who generated bubbles that rose in a spiral trajectory in a pure fluid.

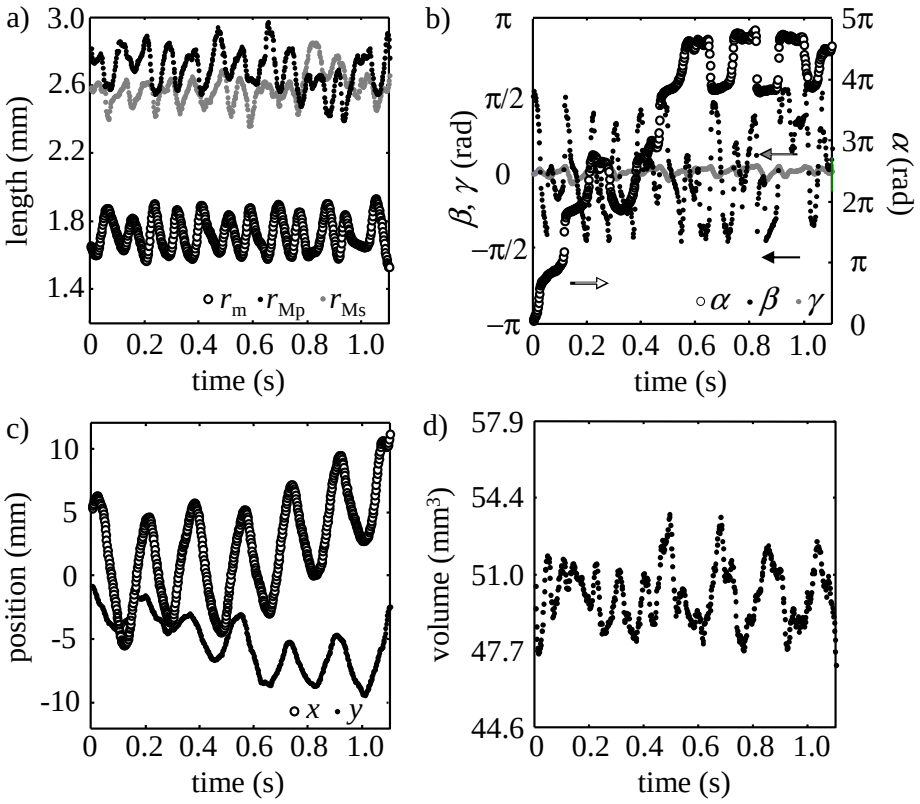


Figure 6.10: Example data from the three dimensional reconstruction of a bubble of size $r_e = 2.3$ mm: a) principle axes lengths; b) orientation of the primary major axis - note the differing ordinate for $\alpha$ as opposed to $\beta$ and $\gamma$; c) position of bubble centroid; d) bubble volume.

Interestingly, the reconstruction reveals that the two major axes have different means, reflecting that the bubble lacks fore-aft symmetry. This seems intuitive, given that it is known that bubbles almost, but not quite, align their minor axis with the direction of their motion [11], and that this slight misalignment will lead some component of the drag force to act along one of the bubble major axes, and flatten the bubble in its transverse plane, just as the majority of the drag acting along the minor axis distinctly flattens the bubble into an ellipsoid. The major axes also oscillate in phase with each other, contrary to the behaviour apparent in projection based measurements in the literature, where it

has been suggested that the major axes oscillate in antiphase about a common mean [10]. The reason for this disparity is due to the changing orientation of the bubble confusing the identification of each major axis. The elevation of the bubble, given by the angle $\beta$, oscillates between $-\pi/2$ and $\pi/2$ at twice the frequency of the bubble trajectory, as the bubble somewhat orientates itself with the direction of its motion. The bubble also undergoes occasional $\pi$ rotations about the central pole (characterised by the change in angle $\alpha$). These rotations correspond to turning points on the bubble trajectory, reflecting the reorientation of the bubble as it turns a corner. The volume of the reconstructed bubble is shown in Figure 6.10 d), which exhibits an oscillation at a frequency of 12 Hz. As it is known that bubbles in water shed their wakes at this frequency irrespective of bubble size [10], this volume oscillation can be speculatively attributed to the changing pressure field around the bubble associated with vortex shedding.

Figure 6.11 shows a comparison of the axis lengths from the reconstructed bubble with those measured directly from the projections. This comparison demonstrates that the primary and secondary major axes of the reconstructed bubble tend to adhere to the largest and smallest of the major axes measured from the projections. Similarly, the reconstructed minor axis is bound to the smallest of the three projected minor axes. This suggests that three simultaneous projections without a three-dimensional reconstruction are sufficient for an estimation of the bubble axis lengths at any given time, with the primary major axis able to be estimated by considering the largest major axis length at any given instant, and the secondary major and minor axes by taking the smallest apparent major and minor projected axes. The frequency of oscillation in the projections is also representative of that in the reconstruction; thus Fourier analysis of projected axis lengths remains a valid avenue for the testing of shape oscillation models. The comparison shown in Figure 6.11 also demonstrates that the reconstruction procedure produces length measurements in good accord with the projections, and thus the error in the bubble size measurements given in the present chapter can be considered equivalent to the spatial resolution of the projections ($\pm 244$ μm).

The three dimensional reconstruction has the advantage that the changing orientation of the bubble major axes can be observed directly, which permits different modes of shape oscillation to be viewed in isolation of each other. Consider, for example, the equivalent major axis of the bubble (as defined in equation (6.40)). The oscillation of this length scale is shown together with that of the minor axis in Figure 6.12. The oscillation of these two axes is anti-phase and almost exactly complementary; reflecting that these

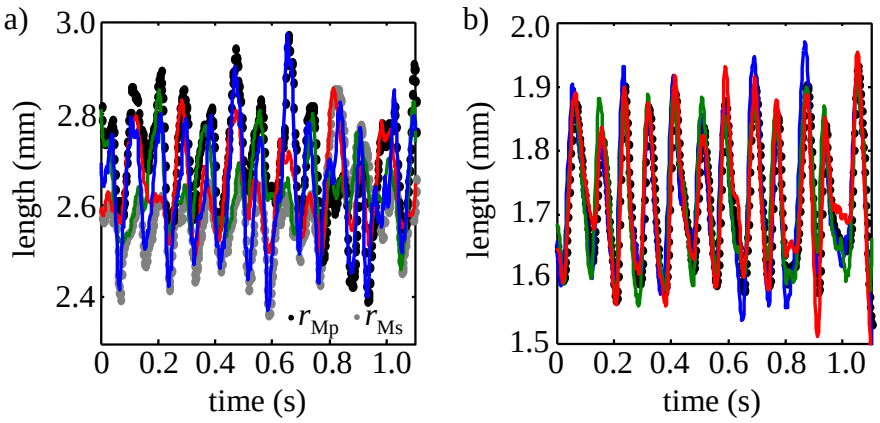


Figure 6.11: a) Comparison of the major and semi-major axis lengths from reconstructed bubble (black and grey points) with those measured in original three projections (blue, red and green lines). c) Comparison of the minor axis length from the reconstructed bubble (black points) with those measured in original three projections (blue, red and green lines).

data contain only information about mode 2 shape oscillations. If mode 2,0 oscillations were present they would be represented in the angles $\beta$ and $\gamma$ as shown in Figure 6.10 b). That these angles do not demonstrate a continuous rotation implies that the bubble was not experiencing this mode of shape oscillation. Similarly, the existence of mode 2,2 oscillations would be represented by a constant evolution of the angle $\alpha$. That $\alpha$ is relatively constant except for when the bubble is turning a corner, implies that mode 2,2 oscillations were not present either. Thus it appears that the present bubble was only undergoing mode 2 shape oscillations. Whether this is some influence of the salt present in the system, or whether mode 2,0 and 2,2 shape oscillations do not in-fact exist (and it is the changing orientation of the bubble which has been confused with a mode of shape oscillation in earlier studies) is not clear from these data. A clear avenue for future research is to apply the new bubble shape reconstruction procedure to bubbles in a pure solution.

The rise velocity of the bubble has been extracted from its vertical position in the column for each point in time. Using the instantaneous bubble size and aspect ratio quantified from the reconstructed bubble shape, the model of Tomiyama *et al.* [9] was used to calculate a theoretical rise velocity. A comparison of the experimental rise velocity with theory is given in Figure 6.13. From this comparison it is evident that the model approximately captures the mean and the frequency of the transient rise velocity, however consistently underestimates the extrema of the oscillation. In their original work, Tomiyama *et al.* found their model to accurately predict the minima of the oscillation, while underpredicting the mean. It seems likely, therefore, that the more accurate measurement of bubble

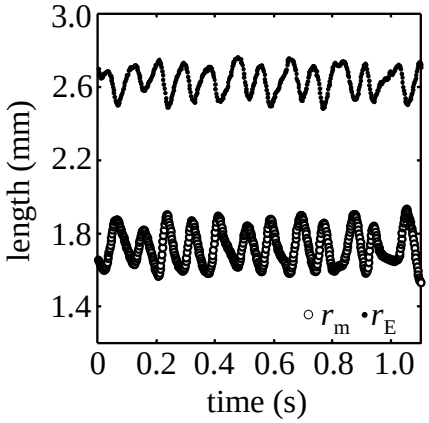


Figure 6.12: Comparison of the minor and equivalent major axes of the bubble. Note that the oscillation of the two axes is antiphase and also perfectly complimentary. These data represent mode 2 shape oscillations.

volume and aspect ratio enabled by the 3D reconstruction has improved the prediction of mean rise velocity, while highlighting that the model underpredicts the extrema of the oscillation. As noted by Tomiyama *et al.*, their model accounts for neither the added mass force associated with the bubble wake, nor the lift force associated with vortex shedding. These transient forces are possibly responsible for the larger oscillation in rise velocity observed experimentally.

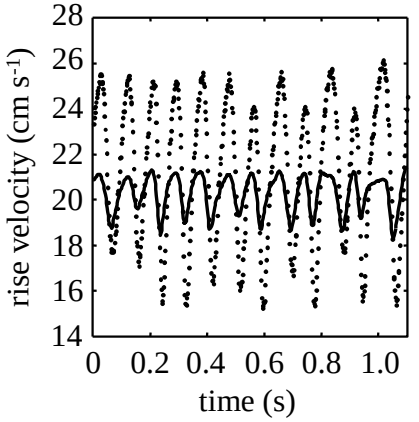


Figure 6.13: Comparison of experimentally measured rise velocity (points) with that predicted by the model of Tomiyama *et al.* [9] (line). The temporally resolved bubble radius and aspect ratio measured experimentally were used in the calculation. The mean rise velocity is approximately predicted but the magnitude of the oscillation is not.

### 6.3.3 Bubble shape oscillations

The three dimensional shape oscillations of two hundred bubbles have been quantified. The trends shown by these bubbles are congruent with those discussed in Section 6.3.2: mode 2 shape oscillations were present, however mode 2,0 and 2,1 were not. Figure 6.14 shows the frequency of mode 2 oscillations as a function of bubble size. The Rayleigh-Lamb model for mode 2 shape oscillations is also shown. The measured frequencies are seen to be substantially less than those predicted by the model, and are lower than the mode 2 oscillations for highly deformed bubbles in both pure and surfactant contaminated solutions previously reported in the literature [10, 11]. These data imply that the presence of salt in the solution has a significant effect upon dampening the shape oscillations of rising single bubbles. It is well known that some salts inhibit bubble coalescence by rendering thin liquid films more cohesive, and it has been speculated that the presence of a salt can decrease interfacial mobility [15], however the mechanisms of this effect are still not clear. Further research is required into the molecular level interactions between electrolyte and water molecules to determine the underlying physical phenomena that are responsible for the changes observed in the behaviour of gas-liquid flows on a macroscopic level.

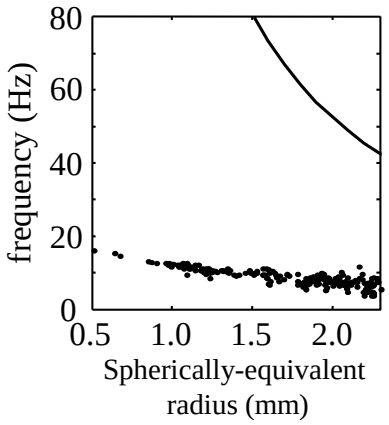


Figure 6.14: Comparison of the mode 2 oscillations frequencies for all bubbles measured in the present study with the predictions of the Rayleigh-Lamb bubble shape oscillation model.

### 6.3.4 Closure of bubble rise model using bubble shape

In Section 6.3.1 the bubble rise model of Tomiyama *et al.* was found to under predict the rise velocities of bubbles in the present system when closed for aspect ratio using the correlation of Wellek *et al.* [23]. Using the reconstructed bubble shapes, it is possible

to propose a new correlation specifically for the present system, which may improve the accuracy of the Tomiyama *et al.* rise model. The mean aspect ratio for all bubbles reconstructed in the present study is given as a function of the Eötvös number (similiarly to the correlation of Wellek *et al.*) in Figure 6.15 a). These data were well fitted by the correlation:

$$E = \frac{1}{1 + 0.29\mathrm{Eo}^{0.85}}. \tag{6.41}$$

The model of Tomiyama *et al.* has been closed using equation (6.41), and is shown in comparison with the experimental data in Figure 6.15 b).

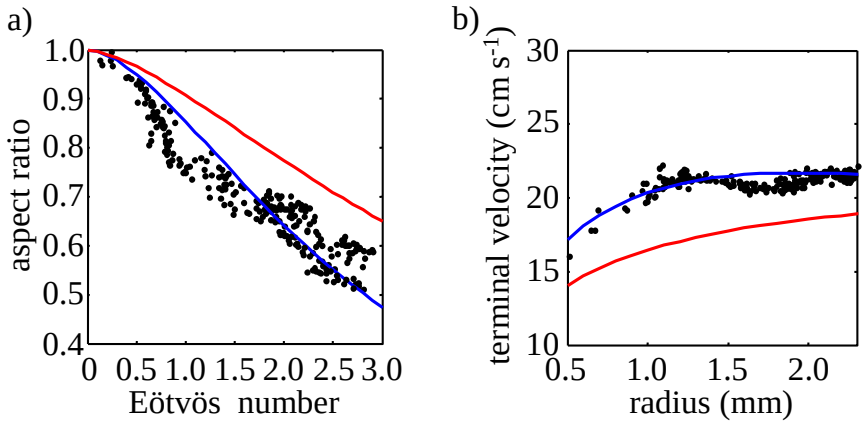


Figure 6.15: a) Bubble aspect ratio as a function of Eötvös number. A fit to these data given by equation (6.41) is shown by the blue line. The correlation of Wellek *et al.* is shown by the red line. b) Rise velocities calculated using the model of Tomiyama *et al.* closed using equation (6.41) (blue line) and the correlation of Wellek *et al.* (red line). It is clear that the improved closure model has greatly increased the accuracy of the bubble rise model.

From inspection of Figure 6.15, it is immediately apparent that the use of an aspect ratio closure model specifically formulated for the present system has greatly increased the accuracy of the terminal velocity model of Tomiyama *et al.*, with predictions of rise velocity now demonstrating a maximum of 9% error across all examined bubble sizes. The correlation of Wellek *et al.* is also shown for comparison. It is evident that the bubbles in the present system uniformly held aspect ratios lower than those expected from a surfactant contaminated system, but not as low as those expected in a pure solution [5]. It seems then, that the inorganic dopant holds its own unique influence over bubble shape. It is interesting that the local maximum in bubble velocity which occurs at a size of $r_\mathrm{b} = 1.1$ mm is accompanied by a sharp drop in aspect ratio. This demonstrates an intimate coupling between bubble aspect ratio and rise velocity, and suggests

that electrolytes primarily alter the bubble rise velocity by their influence over bubble shape. The model of Tomiyama *et al.* is thus validated for use with the present system. It is unfortunate that the effect of electrolytes on bubble shape, as with that on bubble coalescence and shape oscillation, remains poorly understood on a theoretical level.

Clearly the ellipsoidal shape assumed in the present reconstruction of bubble shape is only an approximation, and as bubble size increases modes of shape oscillation emerge that cannot be described using this simple shape. The fundamental modes of shape oscillation for smaller bubbles are, however, all represented by simple transformations of an ellipsoidal shape, and the present reconstruction and analysis should provide useful tools for investigating shape oscillations in more complex situations than the simplest case examined herein. In particular, it would be interesting to apply the bubble reconstruction procedure to bubbles in pure and surfactant contaminated solutions, and to high and low initial deformation bubbles for the validation of the results found in earlier works [10, 11]. Alternatively, the new experimental technique may find application in the study of bubbles which are subject to external pressure fields, and such as in sonochemistry or the study of cavitation [29].

## 6.4 Conclusions

In this chapter the terminal velocity of single bubbles rising though a 16.86 mM dysprosium chloride solution was examined, with the goal of validating a model for use in the drift flux analysis of the model bubble column. Firstly, bubble rise models from the literature were reviewed, and tested in comparison to data obtained by high-speed photography. Poor agreement was noted with the models of Mendelson [8] and Clift *et al.* [5], which suggested that the bubble rise velocity resembles neither that of pure nor surfactant contaminated systems. Modest agreement was found for the correlation of Abou-el-hassan [21], which was proposed using data for a wide variety of fluids. The most sophisticated first principles model in the literature for bubble terminal velocity is that of Tomiyama *et al.* [9], which requires an experimental closure for bubble aspect ratio. This model was, however, found to provide a poor fit when closed using the correlation of Welleck *et al.* [23], which was proposed for surfactant contaminated systems.

To improve the accuracy of the Tomiyama *et al.* model, it was sought to propose a closure correlation for aspect ratio specific to the present system. In providing this closure, it was desirable to address the standing problem in the literature relating to the determination of

true bubble shape. This problem stems from the information lost when two-dimensional projections (i.e. photographs) are obtained of a three-dimensional shape. To allow three-dimensional information to be obtained, the relationship between an ellipsoid and its 2D projections was derived, and applied to determine 3D bubble shapes from projections of bubbles acquired using high-speed photography. This technique was applied to characterise the shape oscillations of bubbles in the size range 0.5 mm $< r_b <$ 2.3 mm. It was noted that only mode 2 shape oscillations are present, with no evidence of the other modes commonly observed in the literature (such as mode 2,2). The frequency of the mode 2 oscillations was seen to be less than both the predictions of well known model of Rayleigh-Lamb [18], and previously observations from the literature [10, 11].

With the reconstructed bubble shapes used to provide closure for the model of Tomiyama *et al.*, good agreement was evident with the measured bubble rise velocities. Terminal velocities were predicted for all examined sizes to within 9% error (root mean square of velocity). An intimate coupling was evident between the bubble aspect ratio data, and that of the rise velocity, with a local maximum in bubble velocity occurring at a size of $r_b = 1.1$ mm being accompanied by a sharp drop in aspect ratio. This suggests that electrolytes primarily affect bubble rise velocity by exerting some influence over bubble shape. The model of Tomiyama *et al.*, when closed with the proposed correlation, is thus validated for use with the present system. The new bubble reconstruction technique permits fresh insights into the modes of bubble shape oscillation, and should prove useful for characterising bubble shape oscillations in more complex systems, such as bubbles with high initial deformation or those subject to a transient pressure field.

# Bibliography


[1] Hadamard, J.S., 1911. Mouvement permanent lent d'une sphere liquide et visqueuse dans un liquide visqueux. *CR Acad. Sci.*, 152, p. 1735.

[2] Rybszynski, W., 1911. On the translatory motion of a fluid sphere in a viscous medium. *Bulletin International de l'Académie Polonaise des Sciences et des Lettres, Classe des Sciences Mathematiques et Naturelles*, A, pp. 40–46.

[3] Stokes, G.G., 1880. *Mathematical and Physical Papers, 1.* Cambridge University Press, Cambridge.

[4] Davies, R.M. and Taylor, G., 1950. The mechanics of large bubbles rising through extended liquids and through liquids in tubes. *Proc. Roy. Soc.*, A200, pp. 375–390.

[5] Clift, R., Grace, J.R. and Weber, M.E., 1978. *Bubbles, drops, and particles.* Acadamic Press, New York.

[6] Fan, L.S. and Tsuchiya, K., 1990. *Bubble wake dynamics in liquids and liquid-solid suspensions.* Butterworth-Heinemann.

[7] Takagi, S. and Matsumoto, Y., 2011. Surfactant effects on bubble motion and bubbly flows. *Annu. Rev. Fluid. Mech.*, 43, pp. 615–636.

[8] Mendelson, H.D., 1967. The prediction of bubble terminal velocities from wave theory. *AIChE. J.*, 13, pp. 250–253.

[9] Tomiyama, A., Celata, G.P., Hosokawa, S. and Yoshida, S., 2002. Terminal velocity of single bubbles in surface tension force dominant regime. *Int. J. Multiphase Flow*, 28, pp. 1497–1519.

[10] Lunde, K. and Perkins, R.J., 1998. Shape oscillations of rising bubbles. *Appl. Sci. Res.*, 58, pp. 387–408.

[11] Veldhuis, C., Biesheuvel, A. and van Wijngaarden, L., 2008. Shape oscillations on bubbles rising in clean and in tap water. *Phys. Fluids*, 20, p. 040,705.

[12] Ellingsen, K. and Risso, F., 2001. On the rise of an ellipsoidal bubble in water: oscillatory paths and liquid-induced velocity. *J. Fluid Mech.*, 440, pp. 235–268.

[13] Sato, A., Aoki, M. and Wananabe, M., 2010. Single bubble rising motion in aqueous solution of electrolyte. *J. Fluid Sci. Tech.*, 5, pp. 14–25.

[14] Jamialahmadi, M. and Müller-Steinhagen, 1992. Effect of alcohol, organic acid and potassium chloride concentration on bubble size, buble rise velocity and gas hold-up in bubble columns. *Chem. Eng. J.*, 50, pp. 47–56.

[15] Henry, C.L., Dalton, C.N., Scruton, L. and Craig, W.S.J., 2007. Ion-specific coalescence of bubbles in mixed electrolyte solutions. *J. Phys. Chem. C*, 111, pp. 1015–1023.

[16] Henry, C.L., Parkinson, L., Ralston, J.R. and Craig, V.S.J., 2008. A mobile gas-water interface in electrolyte solutions. *J. Phys. Chem. C*, 39, pp. 15,094–15,097.

[17] Kulkarni, A.A. and Joshi, J.B., 2005. Bubble formation and bubble rise velocity in gas-liquid systems: a review. *Ind. Eng. Chem. Res.*, 44, pp. 5873–5931.

[18] Lamb, H., 1895. *Hydrodynamics*. Cambridge University Press, Cambridge.

[19] Lehrer, H.G., 1976. A rational terminal velocity equation for bubbles and drops at intermediate and high reynolds. *J. Chem. Eng. Jpn.*, 9, pp. 237–240.

[20] Jamialahmadi, M., Branch, C. and Müller-Steinhagen, H., 1994. Terminal bubble rise velocity in liquids. *Chem. Eng. Res. Des.*, 72(A), pp. 119–122.

[21] Abou-el hassan, M.E., 1983. A generalized bubble rise velocity correlation. *Chem. Eng. Comm.*, 22, pp. 243–250.

[22] Rodrigue, D., 2004. A general correlation for the rise velocity of single gas bubbles. *Can. J. Chem. Eng.*, 82, pp. 382–386.

[23] Wellek, R.M., Agrawal, A.K. and Skelland, A.H.P., 1966. Shape of liquid drops moving in liquid media. *AIChE J.*, 12, pp. 854–862.

[24] Karl, W.C., Verghese, G.C. and Willsky, A.S., 1994. Reconstructing ellipsoids from projections. *Graph. Model. Im. Proc.*, 56, pp. 124–139.

[25] Noumeir, R., 1999. Detecting three-dimensional rotation of an ellipsoid from its orthographic projections. *Pattern Recogn. Lett.*, 20, pp. 585–590.

[26] Kayikcioglu, T., Gangal, A. and Ozer, M., 2000. Reconstructing ellipsoids from three projection contours. *Pattern Recogn. Lett.*, 21, pp. 959–968.

[27] Fitzgibbon, A., Pilu, M. and Fisher, B., 1999. Direct least squares fitting of ellipses. *IEEE T. Pattern. Anal.*, 21, pp. 476–480.

[28] Ohl, C.D., 2001. Generator for single bubbles of controllable size. *Rev. Sci. Instr.*, 72(1), pp. 252–254.

[29] Brennen, C.E., 1995. *Cavitation and bubble dynamics.* Oxford University Press, Oxford.

# Chapter 7

# Drift-flux analysis

One of the primary goals of this thesis is to provide a hydrodynamic characterisation of the model bubble column under examination using drift-flux analysis. Drift-flux analysis is a tool commonly used in the design and operation of gas-liquid unit operations for the prediction of gas hold-up; it describes the holistic hydrodynamic behaviour of a bubble column on the basis of the dynamics of a single bubble. In doing this, it is common to assume a representative bubble size, and choose an appropriate model for single bubble rise velocity [1]. The bubble terminal velocity is then correlated with a bubble slip velocity, most commonly using a Richardson-Zaki type model [2]. In Chapter 5 ultra-fast MRI was applied to measure bubble size distributions, and experimental closures were given for mean bubble size as a function of voidage and position in the bubble column. In Chapter 6 the terminal rise velocity of single bubbles in the present system was examined in detail, and it was found that the model of Tomiyama *et al.* [3], when closed using a proposed correlation for bubble aspect ratio, gave predictions of terminal rise velocity in good agreement with experiments. These measurements are applied in drift-flux analysis in the present chapter.

While drift-flux analysis has previously been applied to the characterisation of systems as diverse as foam fractionation columns [4] to two-phase flow in a well-bore [5], it has not been widely applied in the literature to systems containing electrolytes. In fact, while several previous works have examined the impact of electrolytes on gas holdup,

with the general consensus being that some inorganic ions increase both hydrodynamic stability and gas-holdup [6, 7, 8], only the study of Ribeiro and Mewes [9] attempts to qualify these observations using drift-flux analysis. Those authors, however, deviate from the conventional, first-principles approach of drift-flux analysis, and directly fit an expression for slip velocity to their low voidage data. While this approach yielded good agreement between experiment and theory, it does not, however, test the applicability of the drift-flux model to electrolytic systems in general. The present study, conversely, seeks to provide an independently measured model for bubble slip velocity, and therefore provides an excellent basis for an assessment of the applicability of drift-flux analysis to electrolyte stabilised systems.

In this chapter, the drift-flux theory is firstly reviewed, with a particular focus on the assumptions that underpin the calculation of bubble slip velocity. These assumptions are then tested for the present system by experimentally measuring the slip velocity of bubbles of an NMR active gas as a function of voidage. Finally, drift-flux analysis is applied to produce a hydrodynamic characterisation of the model bubble column, and the applicability of the analysis technique for electrolytic systems is assessed.

## 7.1 Drift-flux theory

Drift-flux analysis is a procedure commonly applied to the design and operation of gas-liquid unit operations. It was originally developed by Wallis and Zuber [10, 11], and has since been applied towards the characterisation of bubbly flow in many contexts [4, 5, 12, 13]. As discussed in Section 1.1, drift-flux analysis defines a 'slip velocity' as the difference between the superficial gas and liquid velocities normalised by phase fraction:

$$U_{\mathrm{R}} = \frac{U_{\mathrm{g}}}{\varepsilon} - \frac{U_{\mathrm{l}}}{1-\varepsilon} \tag{7.1}$$

where $U_{\mathrm{g}}$ and $U_{\mathrm{l}}$ are the superficial gas and liquid velocities, and $\varepsilon$ is the gas fraction. The slip velocity is commonly predicted using a Richardson-Zaki correlation of the form:

$$U_{\mathrm{R}} = U_{\mathrm{T}\infty}(1-\varepsilon)^{N-1} \tag{7.2}$$

where $U_{\mathrm{T}\infty}$ is the single rise velocity of a bubble in an infinite medium and the Richardson-Zaki index, $N$, is a function of the Reynolds number and, for low Re, the ratio of the bubble to pipe diameter [2]. Many values have been proposed for $N$, which are discussed

in Section 7.2. Combining equations (7.1) and (7.2):

$$(1-\varepsilon)U_g - \varepsilon U_l = U_{T\infty}\varepsilon(1-\varepsilon)^N. \tag{7.3}$$

In the operation of gas-liquid unit operations this equation may be solved for $\varepsilon$ for a known set of operating conditions. Note that the left hand side of equation (7.3) is a function only of the gas and liquid superficial velocities, and is commonly known as the operating line. Conversely, the right hand side is a function only of the physical properties of the system, and is known as the hydrodynamic curve. The drift-flux of gas is defined as being the gas flux relative to a volume average velocity, and is therefore equivalent to either side of equation (7.3):

$$j_{\mathrm{g}} = -j_{\mathrm{l}} = (1-\varepsilon)U_g - \varepsilon U_l = U_{T\infty}\varepsilon(1-\varepsilon)^N \tag{7.4}$$

where $j_{\mathrm{g}}$ is the drift flux per unit area of gas, and $j_{\mathrm{l}}$ is the drift flux per unit area of liquid. Equation (7.3) may be solved analytically, or using a graphical Wallis construction, as shown in Figure 7.1. The production of a set of curves similar to this figure, describing the hydrodynamics as a function of position in the model bubble column, is one objective of the present chapter. Note that flow settings for which the hydrodynamic line lies tangent to the operating curve represents the transition to slug flow, and in this way drift-flux analysis can provide a description of hydrodynamic stability. With the hydrodynamic curve for a given bubble column is established, drift-flux analysis may be used in reverse to provide an estimate of bubble size in a column. This is achieved by measuring local voidage (most commonly using a local phase probe), from which a bubble rise velocity, and hence a bubble size can be inferred. Several approaches to this inverse problem are discussed by Banisi and Finch [14].

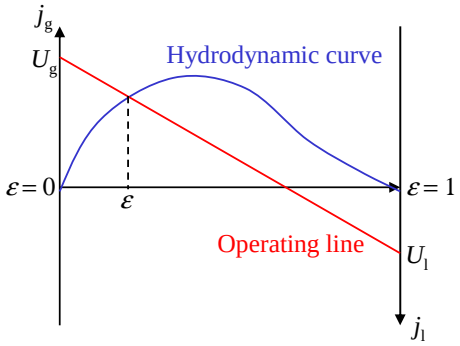


Figure 7.1: A Wallis graphical construction for determining the gas-holdup in bubbly flow for a given set of operating conditions. The voidage, $\varepsilon$, is determined by the intercept between the operating line and the hydrodynamic curve.

For the successful application of drift-flux analysis, an accurate estimation of the single bubble terminal rise velocity must be made. In Section 6.3.4 the terminal rise velocity was measured as a function of bubble size for the present system. It was found that a good fit to the data was provided by the model of Tomiyama *et al.* [3]:

$$U_{\mathrm{T}\infty} = \frac{\sin^{-1}\sqrt{1-E^2} - E\sqrt{1-E^2}}{1-E^2}\sqrt{\frac{4\sigma}{\rho_{\mathrm{l}} r_{\mathrm{b}}}E^{4/3} + \frac{\Delta\rho g r_{\mathrm{b}}}{\rho_{\mathrm{l}}}\frac{E^{2/3}}{1-E^2}}. \tag{7.5}$$

when closed for aspect ratio, $E$, by the correlation:

$$E = \frac{1}{1+0.29\mathrm{Eo}^{0.85}} \tag{7.6}$$

where $\rho_{\mathrm{l}}$ is liquid density, $r_{\mathrm{b}}$ is the spherically equivalent bubble radius, $\sigma$ is surface tension and Eo is the Eötvös number. In Section 5.3.5, the mean bubble diameter was found to be given by:

$$r_{\mathrm{b}} = a\varepsilon^b \qquad r_{\mathrm{b}} \leq 1.6 \text{ mm} \tag{7.7}$$

$$r_{\mathrm{b}} = a\varepsilon + b \qquad r_{\mathrm{b}} > 1.6 \text{ mm} \tag{7.8}$$

where the coefficients $a$ and $b$ are given in Table 7.1.

Table 7.1: Coefficients describing mean bubble size as a function of voidage and position in column.

| Distance from | $r_{\mathrm{b}} \leq 1.6$ mm | | $r_{\mathrm{b}} > 1.6$ mm | |
|---|---|---|---|---|
| distributor (cm) | $a$ | $b$ | $a$ | $b$ |
| 2.5 | 1.90 | 0.24 | - | - |
| 12.5 | 2.11 | 0.27 | - | - |
| 22.5 | 2.46 | 0.31 | - | - |
| 32.5 | 2.63 | 0.32 | - | - |
| 42.5 | 2.75 | 0.33 | 1.59 | 1.28 |
| 52.5 | 3.04 | 0.36 | 1.59 | 1.33 |
| 62.5 | 2.96 | 0.35 | 1.59 | 1.35 |
| 72.5 | 3.08 | 0.35 | 1.59 | 1.34 |
| 82.5 | 3.33 | 0.38 | 1.59 | 1.36 |
| 92.5 | 3.30 | 0.36 | 1.59 | 1.38 |
| 102.5 | 3.93 | 0.41 | 1.59 | 1.40 |

Thus, equations (7.6) through (7.8) can be used in equation (7.5) to provide an estimate of the single bubble rise velocity as a function of voidage and position in the column. For calculation of a slip-velocity using equation (7.2), the Richardson-Zaki index, $N$, is also required. The selection of an appropriate value of this index is examined in Section 7.2.

## 7.2 Richardson-Zaki index

Much variation exists in the literature regarding the selection of the Richardson-Zaki index for application to bubbly flow. The original theory, which was proposed for settling particles, states that the slip velocity is independent of particle size for $\mathrm{Re} > 500$, and is not affected by the column walls for columns of radius $r_{\mathrm{col}} < 10r_{\mathrm{b}}$ [2]. In studies focusing on bubbly flow $N$ has been found to be constant in the range $\mathrm{Re} > 500$, however the value this constant has varied substantially. Richardson-Zaki indices proposed for bubbles in this range in several previous studies are given in Table 7.2.

Table 7.2: Richardson-Zaki indices applied to bubbly flow

| $N$ | References |
|---|---|
| 1.75 | [13] |
| 2 | [15, 16] |
| 3 | [14] |

In this section, $N$ is measured experimentally for comparison with these earlier works. For a semi-batch system (i.e. with zero superficial liquid velocity) equation (7.1) may be written as:

$$U_{\mathrm{R}} = \frac{U_{\mathrm{g}}}{\varepsilon}. \tag{7.9}$$

This equation is valid for use in systems where the gas slip velocity is represented by a single mean (i.e. the slip velocity distribution is unimodal). Substituting equation (7.2) into equation (7.9) and rearranging:

$$N = \frac{\ln\left(\frac{U_{\mathrm{g}}}{\varepsilon U_{\mathrm{T}\infty}}\right)}{\ln(1-\varepsilon)} + 1. \tag{7.10}$$

Thus, for a semi-batch system, only measurements of the gas-fraction and bubble terminal velocity are required to quantify the Richardson-Zaki index. As noted above, this analysis does assume that the slip velocity distribution is unimodal. This assumption is validated experimentally prior to the calculation of Richardson-Zaki indices in the present section.

### 7.2.1 Experimental

To verify that equation (7.9) is valid for the present measurements it is necessary to measure the bubble slip velocity and voidage as a function of the superficial gas velocity. This is possible by performing velocimetric MRI measurements directly on bubbles of an

MRI active gas as they rise through the bubble column. The main complication that afflicts MRI measurements of gases is the very low atomic density (relative to a liquid) which results in a poor signal-to-noise ratio. This is generally overcome by increasing signal averaging (with proportionately increased acquisition times), which limits velocity imaging to systems where the geometry of the phase interfaces is at steady state (for example, in a trickle bed reactor: see the work of Sankey [17]). Due to the dynamic nature of the gaseous phase in the present study, however, imaging the gaseous phase is not possible, and spatially averaged measurements must be made. As discussed in Section 2.3.1, it is possible to acquire spatially averaged velocity distributions known as propagators, which fully characterise the range of velocities present in an examined system. The shape of these propagators will reveal whether the assumption of unimodality in slip velocity is valid, and will permit the mean slip velocity of the system to be quantified.

Several factors must be considered in the selection of the gaseous phase. Firstly, some method of isolating the gas signal from that of the liquid is necessary. This is a problem for gas phase MRI based on the $^{1}$H nuclei, as sufficient chemical shift must be present to separate the signal from the $^{1}$H in the water to that of the gas. Secondly, as the relaxation times and signal attenuation due to molecular diffusion tend to be much faster for a gas than a liquid, the velocity measurement technique must be optimised for these constraints. The former problem can be avoided by exciting signal from a nuclei not present in the liquid phase (for example by performing measurements on $^{19}$F). The latter can be addressed by pressurising the system, which increases relaxation times, until the relaxation time is long enough to permit a measurement. In the present study bubbles of sulphur hexafluoride $SF_6$ rising through a magnetic susceptibility matched solution will be examined. While $SF_6$ is much more dense than air (6.3 kg m$^{-3}$ [18]), the density difference between gas and liquid phase remains effectively negligible. The relative signal-to-noise and relaxation times for $SF_6$ as a function of gas pressure are given in Figure 7.2.

A spin-echo propagator pulse sequence was employed for measurement of a velocity distribution of the gaseous phase. The system was pressurised to 3 bara in a PEEK reactor of diameter 28 mm using the $SF_6$ compressor apparatus described by Sankey [17]. According to Figure 7.2, under these conditions $SF_6$ has a $T_1$ of 4.2 ms and a $T_2^*$ of 2.4 ms. While it is likely that pressurising the system will have an effect upon the structure of the bubbly flow [16], this is not considered problematical as the goal of the present experiments is simply to demonstrate that equation (7.9) can be applied for the accurate estimation of bubble slip velocity. Bubbles were generated by sparging $SF_6$ through the distributor

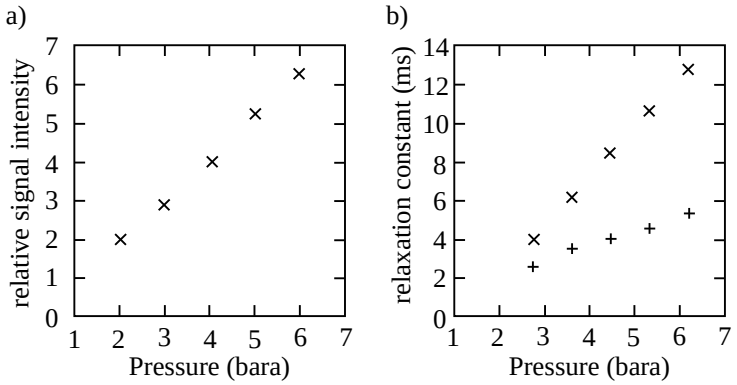


Figure 7.2: a) Relative signal intensity of $SF_6$ as a function of pressure. b) $T_1$ ($\times$) and $T_2^*$ ($+$) relaxation time constants as a function of pressure. Reproduced from Sankey [17].

described in Section 5.2. Measurements were performed on bubbly flow systems with 5 equal increments in superficial gas velocity up to a maximum of 1 L min$^{-1}$. The flow rate controlled using a needle valve and rotameter, the limit of reading of which was $\pm$10 ml min$^{-1}$. To demonstrate that the present measurements are largely independent of observation time ($\Delta$), propagators were obtained at observation times of 2.5 ms, 5 ms, 10 ms and 25 ms. At the longest observation time displacements of no more than 1.5 cm are expected, which corresponds to less than half of the 5 cm long imaging coil used for these experiments.

All experiments were performed on a Bruker DMX-200 super wide-bore spectrometer operating at a $^1$H frequency of 199.7 MHz, and using a 13.9 G cm$^{-1}$ 3-axis shielded gradient system and 64 mm diameter birdcage coil. For each propagator, the echo time was equivalent to $\Delta$ and 512 complex data points were acquired at a spectral width of 100 kHz, for a total acquisition time of $(2\Delta + 10.24)$ ms. Using a constant flow encoding time, $\delta$, of 1 ms, **q**-space was discretised into 32 increments between -6 G cm$^{-1}$ and 6 G cm$^{-1}$ for a field-of-flow of 1 m s$^{-1}$. Each experiment was averaged 64 times. Pulse-acquire experiments on the $^1$H nuclei were also acquired, which allowed the voidage for each flow rate to be quantified according to equation (5.1).

### 7.2.2 Results

#### Measurement of bubble slip velocity

Propagators of $SF_6$ bubbles rising through a 16.86 mM dysprosium chloride solution are shown for several voidages in Figure 7.3. The solid curves are log-normal distributions (as defined in Section 5.3) fitted to the measured data points. It is clear that the distributions

are unimodal, and well fitted by a log-normal distributions, which was as expected given that the underlying bubble size distributions were log-normal in form.

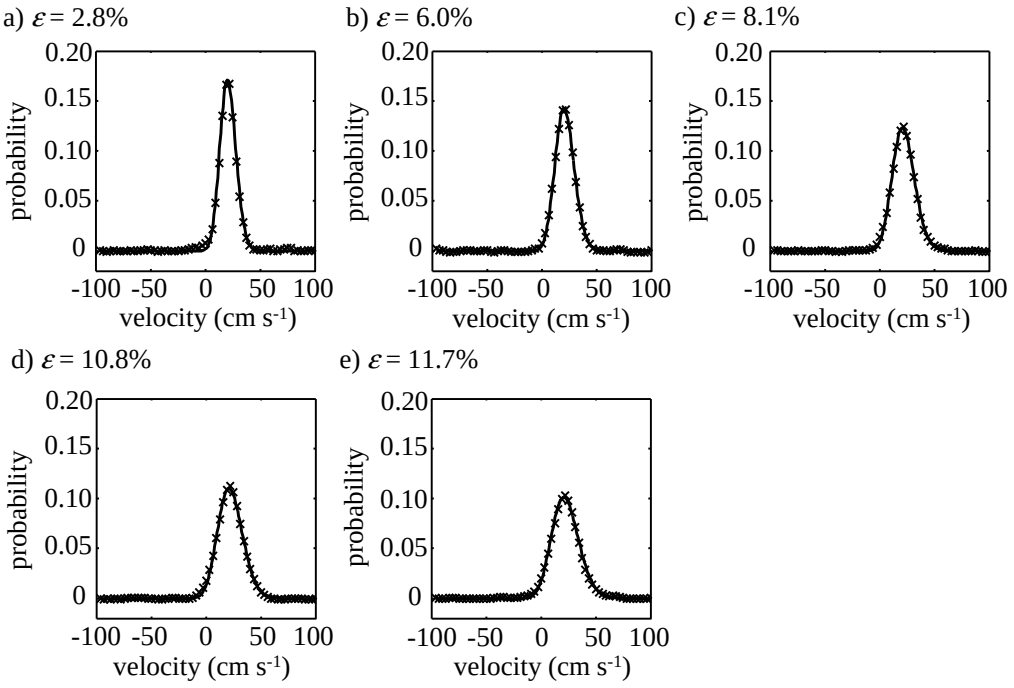


Figure 7.3: Velocity distributions measured of $SF_6$ bubbles rising through a magnetic susceptibility matched solution (×). Also shown are fitted log-normal distributions.

These propagators may be juxtaposed with those measured for the liquid phase in Section 5.3.7. Whereas the liquid velocity measurements each demonstrated symmetry about a mean velocity of zero, reflecting that mass of that phase is being conserved, the gaseous propagators have a non-zero mean, which shows that gas is being continuously passed through the system, and is representative of the bubble slip velocity. For the higher voidages examined here, a small proportion of the gaseous phase (approximately 2%) is seen to have a downward velocity, which likely corresponds to smaller bubbles which are entrained in the downwards flowing recirculating liquid. As it is the passage of bubbles which is solely responsible for the motion of fluid in the present system, it would be expected that the liquid phase propagators must always be broad enough to encompass the full range of gas velocities. By inspection of Figure 5.17 it is clear that this is the case, with the tail of the distributions stretching to include liquid flowing in excess of 50 cm $s^{-1}$.

The unimodality of the propagators shown in Figure 7.3 reflects that the slip velocity of all bubbles in the system can be represented by a single mean, and hence that equation (7.9) is valid for use with the present system. To demonstrate this, slip velocities calculated using equation (7.9) are shown in comparison with the means of the velocity distributions

in Figure 7.4. From these data, it is clear that good agreement exists between the measured bubble slip velocities and those calculated from the superficial gas velocity and voidage. This suggests that equation (7.9) can be applied with confidence to the data presented in Chapter 5.

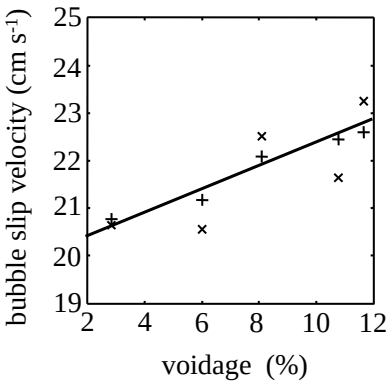


Figure 7.4: Comparison of mean slip-velocities of $SF_6$ bubbles rising extracted from propagator measurements (+) and slip-velocities calculated from superficial gas-velocity and measured voidage using equation (7.9) (×). A linear trend fitted to the latter is shown to guide the eye. An observation time of 5 ms was used for these measurements.

When performing propagator measurements it is important to ensure that a sufficiently long observation time is used such that a representative average of the system is obtained, with shorter observation times potentially revealing temporally local flow features. A possible source for this confusion in the present system is the recirculation of gas within the rising bubbles. It is anticipated that the 5 ms observation time used for the above measurements is sufficient to average-out this motion, and hence ensure that the produced velocity distributions represent only the net motion of bubbles, however to check this assumption propagators were also measured as a function of observation time. Figure 7.5 shows the mean velocity extracted from these propagators, which were all obtained for a system of voidage 8.1%. From this figure it is clear that the propagator measurements are largely independent of observation time; suggesting that the velocity distributions represent only the motion of the gas due to bubble rise, and are therefore an accurate depiction of the slip velocity.

### Calculation of the Richardson-Zaki index

Having validated equation (7.9) for use with the present system, the bubble slip velocity can be calculated as a function of voidage for data presented in Chapter 5. For example, using the data shown in Figure 5.12, the slip velocity has been calculated as a function of voidage and is shown in comparison to the single bubble rise velocity (calculated using

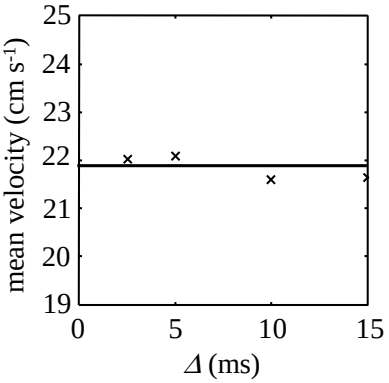


Figure 7.5: Variation of the measured mean slip velocity as a function of observation time. That the measurements appear independent of observation time reflects that it is the motion of the bubble being represented in the propagator.

equations (7.5) and (7.6)) in Figure 7.6. It is clear from this figure that the slip velocity in the column was equivalent to the single bubble rise velocity until a voidage of 9.3% was reached, after which the rise velocity of the bubbles began to drop. This drop away from the single bubble terminal velocity is due to increasing bubble interactions as the bubbles begin to hinder each other as they rise.

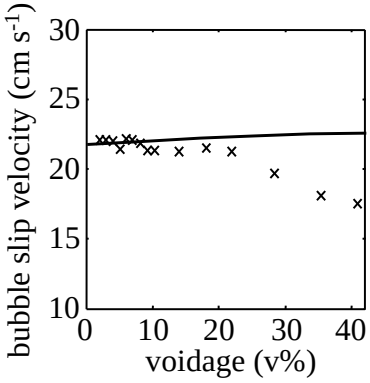


Figure 7.6: Bubble slip velocity as a function of voidage for a column position 52.5 cm from the sparger. The single bubble terminal velocity calculated using the model of Tomiyama *et al.* [3] is shown for comparison.

Richardson-Zaki indices have been calculated for the above data using equation (7.10). These indices are shown as a function of Reynolds number in Figure 7.7. It is apparent that the Richardson-Zaki index is constant for Re $\geq$ 450 (which is as expected), with a value of 1.3. This is substantially less than those values given by the literature (see Table 7.2), which is most likely the influence of the salt in solution. This conjecture will be explored in detail in Section 7.3. For Re $<$ 450, which corresponds to systems of voidage 8.9% and below, the Richardson-Zaki index is approximately unity. This occurs

because the bubble slip velocity is approximately equivalent to the single bubble rise velocity for low gas-fraction systems. A Richardson-Zaki index of 1.3 will be assumed for the hydrodynamic characterisation of the examined column in Section 7.3, where the influence of electrolytes on the drift-flux model should be more clear.

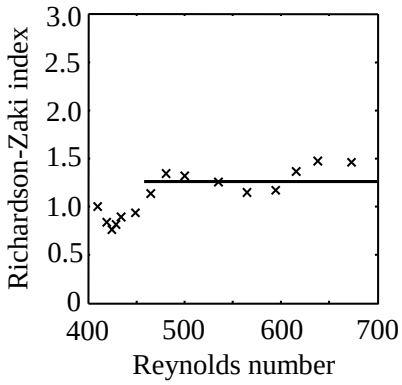


Figure 7.7: Richardson-Zaki indices measured as a function of bubble Reynolds number. The index is seen to be constant with a value of 1.3 for Re $\geq$ 450. A line representing this index is shown to guide the eye.

## 7.3 Application of drift-flux analysis

Equations (7.5) to (7.8) can be substituted into equation (7.2), with a Richardson-Zaki index of 1.3, which is in turn substituted into equation (7.3) to yield the hydrodynamic curve characterising the model bubble column. For a semi-batch bubble column ($U_\mathrm{l} = 0$), the hydrodynamic and operating lines can be combined to give:

$$U_\mathrm{g} = U_{\mathrm{T}\infty}\varepsilon(1-\varepsilon)^{N-1}. \tag{7.11}$$

The accuracy of the developed drift-flux model can be readily tested by comparing the experimentally observed gas-hold up response (shown in Figure 5.3.2) to equation (7.11). This comparison is shown for data acquired at a position 52.5 cm from the sparger in Figure 7.8. It is clear from this figure that the drift-flux model has successfully characterised the gas holdup behaviour of the bubble column, with the model predicting the experimentally measured voidages within 5% error for all voidages. The effect of the selected Richardson-Zaki index on the drift-flux model is also demonstrated in Figure 7.8, where curves are shown which have been calculated using the commonly assumed Richardson-Zaki indices given in Table 7.2. This comparison clearly demonstrates that it is the stabilising influence of the electrolytes which is responsible for the lowered Richardson-

Zaki index measured in Section 7.2, with the convex behaviour of the gas hold-up response curve known to be associated with the presence of electrolytes (as discussed in Section 5.3.2).

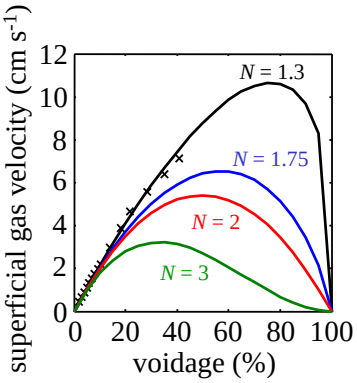


Figure 7.8: Experimental data for superficial velocity as a function of voidage shown in comparison to equation (7.11) calculated using a range of Richardson-Zaki coefficients. It is clear that the model calculated using the measured coefficient of 1.3 is in good agreement with the experimental data.

The hydrodynamic curves characterising the system are shown as a function of position in column in Figure 7.9. It is clear from this figure that the voidage is relatively independent of column height, with the changing bubble size distribution only giving rise to a change in the maximum of the hydrodynamic curves of 2.2% between the top and bottom of the column. This is in good agreement with what was observed experimentally in Section 5.3.5, where no change in voidage was evident as a function of position in the column within the signal-to-noise ratio of the images (within an error of 4.7%). The independence of the gas-holdup behaviour of the column to bubble size stems from the single bubble terminal velocity, which was observed in Section 6.3.4 to be fairly independent of bubble size over the range 1 mm $< r_e <$ 3 mm. This size range covers the majority of bubbles examined in the present study. Having a wide distribution of rise velocities present in a system can instigate bubble coalescence, as faster bubbles will tend to collide with those more slowly rising [19], and it is known that possessing a uniform size distribution (and hence uniform velocity distribution) greatly aids hydrodynamic stability [20]. Thus, it seems plausible that the electrolyte may have the dual influence on hydrodynamic stability of rendering gas-liquid films more cohesive while also moderating the bubble rise velocity.

A Wallis graphical construction for the present system at a position 52.5 cm from the sparger is given in Figure 7.10. The point at which the operating line lies tangential to

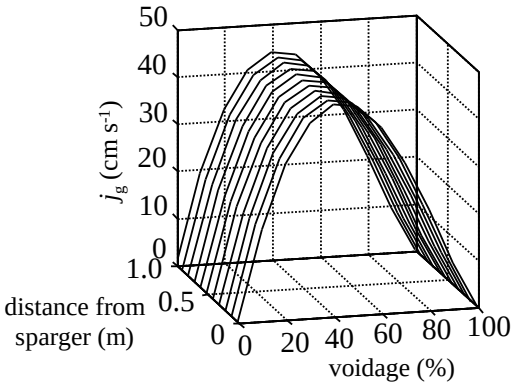


Figure 7.9: Hydrodynamic curves for the present system as a function of position in the column. Note that the evolving bubble size distribution has a limited effect upon the column hydrodynamics as the bubble rise velocity is largely independent of bubble size for the range of bubble sizes examined.

the hydrodynamic curve (as shown in this figure; $U_g = 10.5$ cm s$^{-1}$) typically corresponds the transition from bubbly flow to slug flow, and in this case occurs at a voidage of 75%. This prediction is greatly in excess of the flow regime transition observed experimentally, which occurred at a voidage of approximately 41%. As discussed in Section 1.2, the influence of electrolytes on bubbly flow is complex indeed; no effect is had by some salts, and by others only after a critical concentration is reached, at which point a step-change in the behaviour of the system occurs [21, 9]. Given that the present system transitions from stable bubbly flow to slug flow without any apparent change in the behaviour of the gas hold-up response, it seems likely that some other step-change in the behaviour of the electrolytic dopants has occurred. This highlights a significant problem for the application of drift-flux analysis to electrolyte stabilised bubbly flow, which cannot account for the behaviour of the electrolytic dopants effect other than via the influence asserted over the single bubble rise velocity and Richardson-Zaki index. Thus, while drift-flux analysis can be applied for the prediction of gas-holdup during stable bubbly flow, further research is required into the fundamental nature of the interaction between gas bubbles and inorganic ions before the hydrodynamic stability of the system can be accurately predicted.

## 7.4 Conclusions

In this chapter, measurements of bubble size and voidage previously obtained were applied to the hydrodynamic characterisation of the model bubble column using drift-flux analysis. In doing this, it was first necessary to quantify the Richard-Zaki index for the

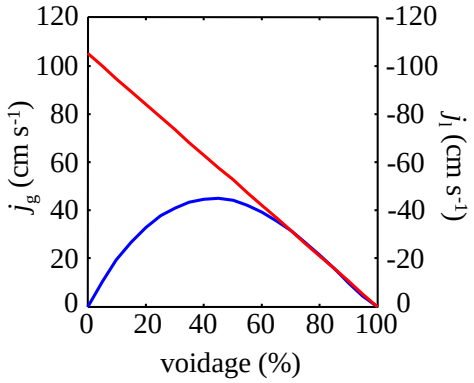


Figure 7.10: A Wallis graphical construction characterising the hydrodynamics of the present system. The operating line is constructed to represent the flooding condition.

system, which relates the rise velocity of a single bubble in an infinite medium to the slip velocity of a bubble in a swarm. While it is possible to determine the mean bubble slip velocity as the quotient of gas superficial velocity and voidage, this calculation requires the assumption that the slip velocity can be represented by a single mean. This assumption was verified experimentally by obtaining propagators of $SF_6$ bubbles rising through magnetic susceptibility matched solution. From these measurements it was clear that the velocity distribution of the bubbles was log-normal in form, and thus the assumption of a unimodal velocity distribution was accurate. The Richardson-Zaki index for the system was thereby determined to be 1.3, which is significantly less than that used in most previous studies.

By comparing the drift-flux model of the system to the experimental data, it was clear that the stabilising influence of the electrolytic dopants used for magnetic susceptibility matching is well represented in the model, with the voidage being predicted as a function of superficial gas velocity within 5% error. Little change ($< 2\%$) was apparent in the voidage as a function of column position in both the drift-flux model and experiments. This is due to the near independence of the bubble rise velocity as a function of bubble size for the range of bubble sizes examined in the present study. Drift-flux analysis could not accurately predict the regime transition of the system, with the curve generated for electrolyte stabilised bubbly flow predicting a transition to slug flow at a voidage of approximately 75%. This occurs because the simple drift-flux model cannot account for the more complex effects of the electrolytes, whose stabilising influence becomes ineffectual at a voidage of 41%. Further research is required into the fundamental nature of the interaction of inorganic dopants with the gas-liquid interfaces before these complex phenomena can be modelled.

# Bibliography


[1] Brennen, C.E., 2005. *Fundamental of multiphase flows.* Cambridge University Press, Cambridge.

[2] Coulson, J.M., Richardson, J.F., Harker, J.H. and Backhurst, J.R., 1991. *Chemical engineering volume 2, 4th Edition.* Butterworth-Heinemann, Oxford.

[3] Tomiyama, A., Celata, G.P., Hosokawa, S. and Yoshida, S., 2002. Terminal velocity of single bubbles in surface tension force dominant regime. *Int. J. Multiphase Flow*, 28, pp. 1497–1519.

[4] Stevenson, P., Fennell, P.S. and Galvin, K.P., 2008. On the drift-flux analysis of flotation and foam fractionation processes. *Can. J. Chem. Eng.*, 86, pp. 635–642.

[5] Shi, H., Holmes, J.A., Durlofsky, L.J., Aziz, K., Diaz, L., Alkaya, B. and Oddie, G., 2005. Drift-flux modelling of two-phase flow in wellbores. *SPE Journal*, 10, pp. 24–33.

[6] Ruthiya, K.C., van der Schaaf, J., Kuster, B.F.M. and Schouten, J.C., 2006. Influence of particles and electrolyte on gas hold-up and mass transfer in a slurry bubble column. *Int. J. Chem. React. Eng.*, 4, p. A13.

[7] Růžička, M.C., Vecer, M.M. and Drahoš, O.J., 2008. Effect of surfactant on homogeneous regime stability in bubble column. *Chem. Eng. Sci.*, 63, pp. 951–967.

[8] Orvalho, S., Růžička, M. and Drahoš, J., 2009. Bubble columns with electrolytes: gas holdup and flow regimes. *Ind. Eng. Chem. Res.*, 48, pp. 8237–8243.

[9] Ribeiro, C.P. and Mewes, D., 2007. The influence of electrolytes on gas hold-up and regime transition in bubble columns. *Chem. Eng. Sci.*, 62, pp. 4501–4509.

[10] Wallis, G.B., 1969. *One-dimensional two-phase flow.* McGraw-Hill, New York.

[11] Zuber, N. and Findlay, J., 1965. Average volumetric concentration in 2-phase flow systems. *ASME J.*, 87, p. 453.

[12] Clark, N.N. and Flemmer, R.L., 1985. Predicting the holdup in two-phase bubble upflow and downflow using the zuber and findlay drift-flux model. *AIChE J.*, 31, pp. 500–503.

[13] Hibiki, T. and Ishii, M., 2002. Distribution parameter and drift velocity of drift-flux model in bubbly flow. *Int. J. Heat Mass Trans.*, 45, pp. 707–721.

[14] Banisi, S. and Finch, J.A., 1994. Technical note reconciliation of bubble size estimation methods using drift flux analysis. *Miner. Eng.*, 7, pp. 1555–1559.

[15] Xu, M., 1991. *Radial gas holdup profile and mixing in the collection zone of flotation columns*. Ph.D. thesis, McGill Univesity.

[16] Krishna, R., Urseanu, M.I. and Dreher, A.J., 2000. Gas hold-up in bubble columns: influence of alcohol addition versus operation at elevated pressures. *Chem. Eng. Process.*, 39, pp. 371–378.

[17] Sankey, M.H.S., 2008. *Velocity mapping in Trickle-bed reactors and multiphase systems using MRI*. Ph.D. thesis, University of Cambridge.

[18] Lide, D.R., 1998. *CRC handbook of chemistry and physics*. CRC press, Boca Raton.

[19] Hibiki, T. and Ishii, M., 2009. Interfacial area transport equations for gas-liquid flow. *J. Comp. Multiphase Flow*, 1, pp. 1–22.

[20] Harteveld, W., 2005. *Bubble columns: structures or stability?* Ph.D. thesis, Delft University of Technology.

[21] Zahradník, J., Fialová, M., Růžička, M., Drahoš, J., Kaštánek, F. and Thomas, N.H., 1997. Duality of the gas-liquid flow regimes in bubble column reactors. *Chem. Eng. Sci.*, 1997, pp. 3811–3826.

# Chapter 8

# Bubble wake dynamics

It is well recognised that the behaviour of a bubble wake has a strong influence on both the shape oscillations and path deviations of a rising bubble. The tools developed in this thesis are potentially very useful for characterising fluid phenomena in multiphase flow systems, and in this chapter are applied to investigate the dynamics of bubble wakes. The behaviour of bubble wakes is very complicated, with several simultaneous fluid phenomena coexisting, and each exerting an influence on the behaviour of the bubble. By direct numerical simulation of the Navier-Stokies equations for fluid flow over a constant spheroidal shape, Mougin and Magnaudet [1] showed that the path deviation of rising ellipsoidal bubbles is associated with the formation of a non-axisymmetric double threaded wake. This asymmetry was evident in the experimental study of Brücker [2], who also noted the existence of two horizontal plane vortices, which were observed to be coupled with bubble path deviations. It is also apparent in the experimental results of several authors [3, 4, 5] that vortex shedding events are coupled with both changes in direction of the bubble and with some modes of shape oscillation.

To better understand the fluid phenomena that drive these bubble dynamics, it is highly desirable to obtain quantitative experimental data describing the flow field around a bubble and in its wake. Most early attempts to obtain this type of information were limited to examination of small spherical bubbles at low Reynolds numbers, where the wakes are at steady state (as reviewed by Fan and Tsuchiya [6]). Beginning with Brücker [2], several

studies have employed particle imaging velocimetry (PIV) or laser Doppler anemometry (LDA) to characterise bubble wake dynamics [7, 8, 9, 10]. Inherent both to PIV and LDA, however, is the use of small particles as tracers, which can behave in a surfactant like manner [11]. Further, using optical imaging techniques it is difficult (although possible, see Brücker [2]) to obtain horizontal plane information in the presence of a bubble due to optical distortion. MRI overcomes both of these problems, with its sole disadvantage being that MRI acquisitions are slow to acquire relative to the highly transient flow phenomena in the wake of bubbles. In Section 4.2.4 high-temporal resolution, one-component velocity fields were acquired demonstrating the potential for spiral imaging to characterise highly transient turbulent flow features. In Section 4.3 these measurements were further accelerated by undersampling, with a compressed sensing reconstruction employed to remove under sampling artefacts, which permitted the measurement of three component velocity vectors with no penalty to acquisition time. In the present chapter these measurement techniques are applied to elucidate the complex wake behaviours exhibited by rising single bubbles.

To permit the observation of bubble wakes over an extended period, it is desirable to detain the bubbles in some manner. The literature is firstly reviewed for different approaches to this problem, before applying the spiral velocity imaging technique, developed in Section 4.2, to quantify the velocity fields in the wakes of both freely rising and static single bubbles. The insights into bubble wake dynamics enabled by these new experimental measurements are then discussed.

## 8.1 Static bubble apparatus

Bubbles which are allowed to rise freely have a residence time of less than 200 ms in the imaging region of our MRI spectrometer, which is sufficient for the observation of only a single full period of the bubble secondary motion. In order to observe bubble wake behaviours for longer than this it is necessary to detain the bubble in some fashion. A bubble can be held vertically stationary, or 'levitating', in several ways. Firstly, using the technique of Bjerknes *et al.* [12], bubbles can be held static in a fluid subject to vibrations at a certain resonant frequency, which generates a downward force on the bubble that can be rendered equal to the buoyancy force [13]. Alternatively, it is possible to hold a bubble stationary against a downward flow such that the buoyancy and drag forces acting on the bubble are balanced. Brücker [2] achieved this by allowing bubbles to rise a short way into a vessel before opening a valve controlling the downward flow. Alternatively, if the

bubble rises through a contraction against a downward flow, the superficial liquid velocity becomes a function of height in the column, and the bubble will be held static at some constant position. In this chapter this latter device is used as it does not introduce an invasive pressure field to the system, and it allows the bubble to be accurately positioned in the MRI spectrometer. This technique has featured in several previous works (see, for example, the work of Davidson and Kirk [14]), and was recently applied by Amar *et al.* [15, 16], who held an oil droplet static and used MRI to obtain quantitative, though time-averaged, velocity fields of the internal flow within the droplet.

The principle problem associated with holding a bubble static against a downward flow is the influence of the velocity profile of the affronting fluid. Assuming laminar flow in the contraction, the parabolic velocity profile will assert a lift force on the bubble which will push it to the wall region of the tube, as shown in Figure 8.1 a). It is desirable to impose a uniform flow profile (except at the walls were a no-slip boundary must exist), such that the dynamics of the bubble are governed by its wake behaviours alone as shown in Figure 8.1 b).

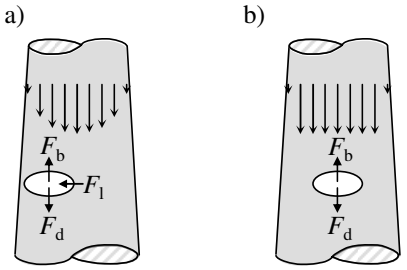


Figure 8.1: Schematics of a) the interaction of a bubble held static in a contraction and the parabolic velocity field of the downward flow and b) an ideal uniform flow profile in which the bubble wake dynamics could be observed without influence from the affronting velocity profile.

Davidson and Kirk [14] suggested an innovative device for the manipulation of the flow profile. They inserted a tube bank upstream of a contraction, with the longest tubes in the middle, and the shortest at the edge, as shown in Figure 8.2. The pressure drop is therefore greatest through the central tubes, and the velocity profile exiting the tube bank has a local minimum. Davidson and Kirk used their device to stabilise the nose of a Taylor bubble, the internal circulations of which could then be studied in the absence of shape oscillations. There will be some entry length associated with the manipulated velocity profile as the natural parabolic flow profile begins to reassert itself. At some intermediate position, therefore, the flow profile will go through a transitional state in which it is approximately uniform. By suspending a bubble in this region, it is therefore

possible to observe the bubble behaviours without the influence of the downward flow profile.

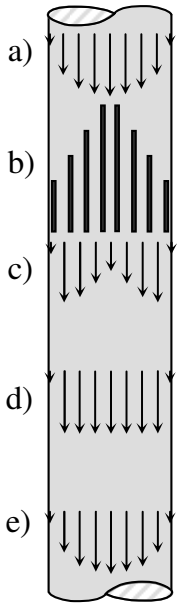


Figure 8.2: Schematic demonstrating the concept of manipulating a velocity profile using a tube-bank. a) The velocity profile is initially assumed to be laminar. b) The fluid enters a tube bank with the longest tube in the centre and shortest tubes at the wall. c) the larger pressure drop along the longer tubes leads to a decreased velocity in the centre of the column. d) As the fluid flows down the column the natural parabolic profile begins to reassert itself (as shown in e), however at some transitionary region the fluid demonstrates a radially uniform velocity profile.

## 8.2 Experimental

Using a magnetic susceptibility matched solution, vertical-plane velocity encoded spiral images were acquired of single bubbles of spherically equivalent radius 1.4 mm rising in a 16 mm diameter pipe. Bubbles were generated by sparging air through a glass capillary of radius 1 mm using a syringe pump (Harvard Apparatus 22). Bubbles of this size were also investigated held static in a contraction against a downward flow. A schematic showing the dimensions of the static bubble apparatus is given in Figure 8.3 a). The column was constructed from a rotameter tube bonded to glass pipes with epoxy resin. The flow profile manipulation device described in Section 8.1 was manufactured from a piece of monolith reactor, as shown in Figure 8.3 b). This monolith contained 1 mm square channels, and tapered in diameter from 20 mm to 4 mm over the course of 30 cm. The liquid flow rate was gravity fed under a constant pressure head (which ensured smooth

flow), and was controlled using a needle valve at the column outlet. Fluid was recycled from a reservoir at the base of the column to one at its head using a Watson-Marlow 330s peristaltic pump.

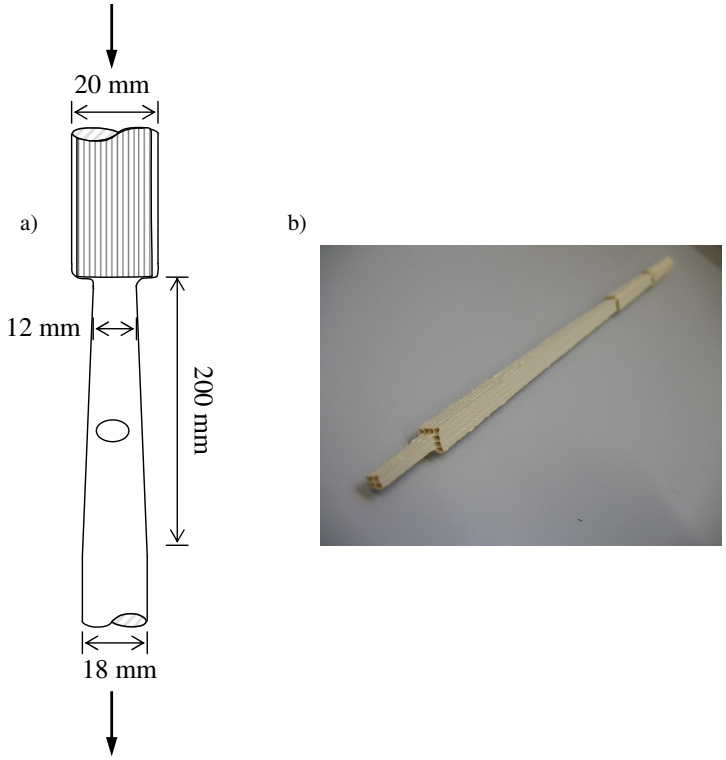


Figure 8.3: a) schematic of static droplet apparatus with dimension. b) Photograph of the flow profile manipulation device.

Prior to the examination of static bubbles, the single phase flow field through the contraction was quantified by taking velocity encoded spiral images at 2 cm increments in height (by shifting the position of the column with respect to the magnet). Using these measurements, the region in the column corresponding to a relatively uniform flow profile was identified. A bubble of spherically equivalent radius 1.4 mm was then introduced to the column, and the liquid flow rate was set to maintain the bubble at the desired position. Highspeed photography footage was obtained of this static bubble using a Photron Fastcam SA-1 model 120K-M2 high-speed imaging system operating an acquisition rate of 500 fps. The column was then raised such that the bubble was in the imaging region of the magnet and MRI data were acquired. Vertical plane velocity encoded images of the static bubble and the bubble wake were acquired, as were horizontal plane images immediately under the bubble. Images were also obtained of the bubble with increasing liquid flow rate, as the drag force began to overcome buoyancy, and for falling bubbles, which are dominated by drag. All images were sampled to a 64 pixel $\times$ 64 pixel raster,

with fully sampled, single velocity-component images acquired at a rate of 83 fps, and 28.7% undersampled images acquired at a rate of 188 fps. Using the latter, 3-component velocity images could be generated at a rate of 63 fps. The velocity encoding gradient used in these experiments was of magnitude 29.2 G cm$^{-1}$ in the vertical ($z$) direction, and 73 G cm$^{-1}$ for the transverse plane components ($x$ and $y$). The flow contrast and observation times used were 368 μs and 388 μs, respectively. Horizontal plane images were acquired at a field of view of 20 mm × 20 mm, for a spatial resolution of 313 μm × 313 μm, while vertical plane images were acquired at a field of view of 20 mm × 30 mm, for a spatial resolution of 313 μm × 469 μm. For all experiments phase reference images were acquired of uniform, stationary liquid for the isolation of phase imparted during velocity encoding. Note that this procedure can only be applied to a magnetic susceptibility matched two-phase system, as otherwise phase shifts due to $B_0$ inhomogeneity will occur at the phase interface.

All measurements were performed on a Bruker AV-400 spectrometer, operating at a $^1$H resonance frequency of 400.25 MHz. A three-axis, shielded micro-imaging gradient system with a maximum strength of 146 G cm$^{-1}$ was used for zeroth and first gradient moment encoding, and a 25 mm diameter birdcage r.f. coil was used for excitation and signal reception. Unless stated above, all MRI parameters employed were identical to that used for the quantification of velocity fields for turbulent flow, described in Section 4.2.

## 8.3 Results

### 8.3.1 Rising single bubbles

Velocity encoded spiral images were acquired of single bubbles rising through stagnant solution in a 16 mm diameter pipe. Eight sequential frames acquired at a rate of 83 Hz of a bubble of radius 1.4 mm rising through the imaging region are shown in Figure 8.4. The approximate position and shape of the bubble (identified from the modulus images) is represented by the filled ellipses. An air bubble of spherically equivalent diameter 1.4 mm can be expected to rise at a rate of approximately 20 cm s$^{-1}$ in surfactant free water (see Figure 6.1) and have velocities exceeding this in the bubble's wake. From the modulus images, the rise rate of the bubble was measured to be $18.3 \pm 0.5$ cm s$^{-1}$, with velocities in the range -29.2 cm s$^{-1}$ to 29.2 cm s$^{-1}$ in the bubble wake, which is consistent with the theory [17].

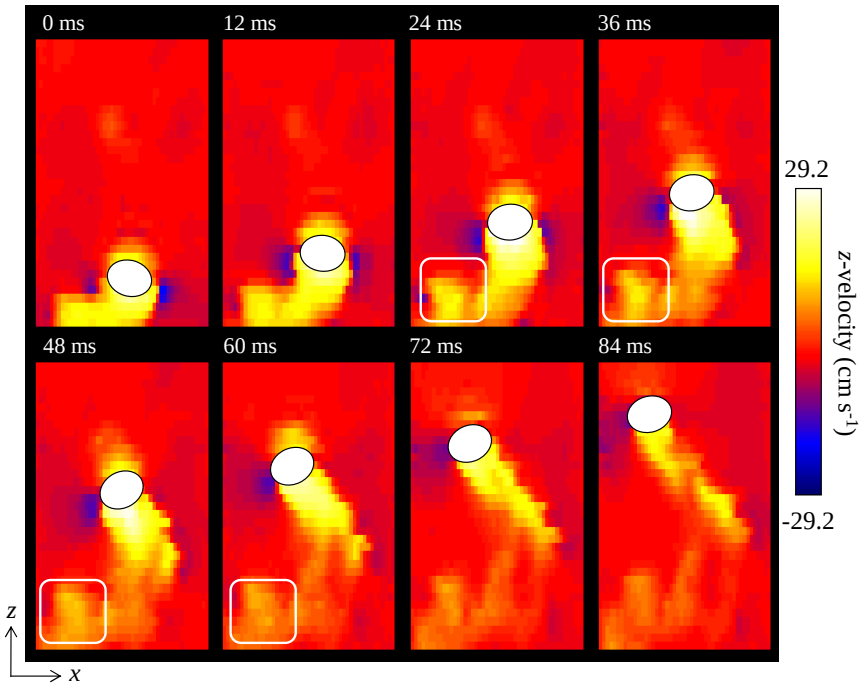


Figure 8.4: Vertical maps of the $z$-velocity for a single bubble freely rising through a magnetic susceptibility matched dysprosium chloride solution. The approximate location of the bubble is highlighted by the filled white ellipses. A vortex shedding event is highlighted by the rounded white box. The acquisition rate of these data was 83 fps. The times shown on the images refer to the start of the acquisition. The spatial resolution is 390 µm × 586 µm for field of view of 20 mm × 30 mm.

The structure of the wake is clear in these images, as is the liquid displaced downward at the sides of the bubble (indicated by the negative velocities). Also visible are periodic vortex shedding events, wherein the wake of the bubble detaches and a region of liquid flows upward independently until its momentum has been dispersed throughout the fluid. It is known that these wake shedding events occur at a frequency of 12 Hz independent of bubble size [4]. Each bubble was present in the imaging region for 150 ms, which is long enough for one complete cycle of wake shedding to occur. The frequency of wake shedding was observed to be constant within the temporal resolution of the technique (± 1.1 Hz) for ten consecutive bubbles, and occurs at a rate of 12.8 Hz, which is consistent with the expected frequency.

Liquid is displaced upward at the nose of the bubble is evident in Figure 8.4, as is downflowing liquid recirculating at the slides of the bubble. This behaviour is as expected for potential flow in a moving frame of reference [18]. Interestingly, however, it is clear that as the bubble adopts an angle of attack as it rises, the velocity of the recirculating liquid

is greater at the lower extremity of the bubble, with the fluid readily slipping across the angled face of the bubble. This may give rise to an interesting fluid phenomenon, as the faster moving fluid over one side of the bubble will exert a lift force not unlike that experienced during flow over an aerofoil, which will pull the bubble in that direction. Thus, it seems possible that potential flow over the nose of the bubble may be in part responsible for the path deviations of rising bubbles.

Three component velocity images of a freely rising single bubble are shown in Figure 8.5. The structure of the bubble wake is more clear in these images, as is the potential flow condition about the bubble nose. The double threaded nature of the wake is evident, and it can be seen that the entire wake undergoes a transverse plane rotation (seen here as a steady rolling of the wake into and out-of the imaging plane). A wake shedding event may be observed, and is accompanied by a 'kink' in the bubble wake which is apparent in both the in-plane and through-plane velocity components. Here, as in Figure 8.4, the recirculating vortex on the downward side of an angled bubble is seen to be faster flowing than its counter-part.

### 8.3.2 Static bubbles

Prior to imaging the velocity field around a static bubble, it was necessary to determine the position in the contraction which corresponds to a uniform velocity profile, as described in Section 8.1. In doing this, the velocity field was quantified at all positions in a contraction downstream of the flow profile manipulation device. These velocity images have been appended to form a single image, which is shown in Figure 8.6. Also shown are flow profiles extracted from this image at key points. It is clear that the velocity profile entering the contraction approximated that expected, with a local minimum present at the centre of the column. The flow profile is then seen to invert over a distance of 6 cm before approaching fully developed laminar flow. The desirable flow condition occurs between approximately 1.5 cm and 3.5 cm from the inlet of the contraction.

Single bubbles were then introduced to the system and suspended in the uniform flow region. Bubbles of radius 1.4 mm were examined. These bubbles were undergoing shape oscillations and path deviations, as demonstrated by highspeed photography shown in Figure 8.7. The bubbles were noted to oscillate slightly off-centre, and are perhaps still somewhat affected by the velocity profile of the down-flowing liquid. While the path deviation of these bubbles is clearly inhibited by the walls of the column, the manner in which the bubbles orientate themselves with the direction of their motion is reminiscent

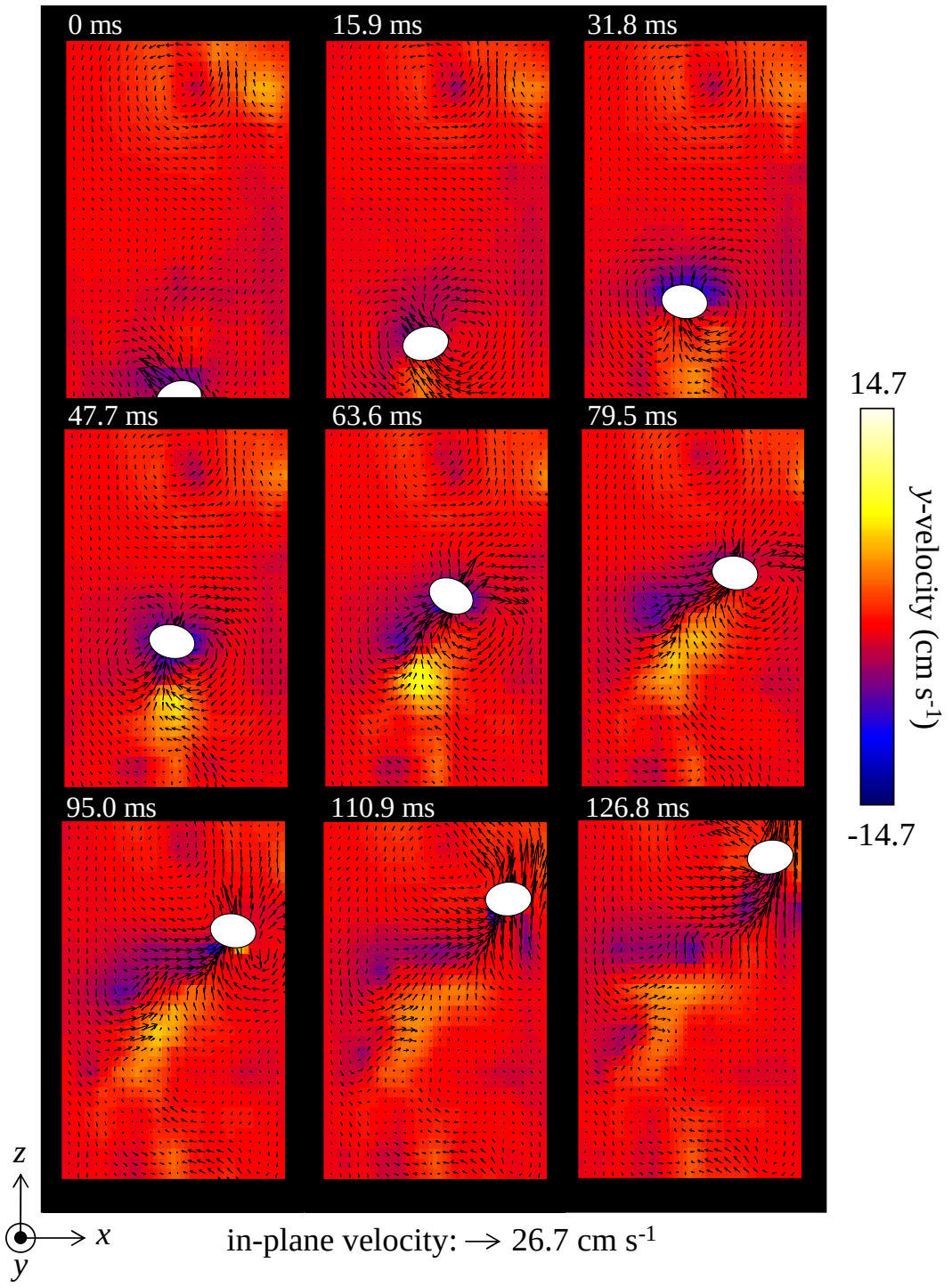


Figure 8.5: Three component velocity map for a single bubble freely rising through a magnetic susceptibility matched solution of dysprosium chloride. The approximate location of the bubble is highlighted by the filled white ellipses. The acquisition rate of these data was 63 fps. The times shown on the images refer to the start of the acquisition. The spatial resolution is 390 μm × 586 μm for field of view of 20 mm × 30 mm.

of the unrestricted secondary motion of a rising bubble, as seen in Section 8.3.1, which suggests that the underlying fluid phenomena driving this instability is still present.

The column was then raised such that the suspended bubble was positioned in the imaging region of the magnet, and velocity images were obtained of the flow field around the bubble using spiral imaging. Three-component velocity images showing the dynamics of the bubble wake over a 143 ms period are shown in Figure 8.8. Note that the mean $z$-velocity has been subtracted from this flow field, and the magnitude of the $z$-component of the velocity vectors has been scaled back to 5% of its original value in these images to render the in-plane rotations of the wake visible. The potential flow condition (for a stationary frame of reference) is clear about the bubble nose, and two counter-rotating vortices are apparent in the bubble wake. Vortex shedding events are evident at a frequency of 12.6 Hz $\pm$ 1.1 Hz, which is in agreement with that observed for freely rising bubbles, and the expected frequency of vortex shedding. The shed wake is observed to continue rotating as it is washed away down the column.

Interestingly, in some images in Figure 8.8 there exists the suggestion of two counter rotating vortices in the transverse plane (particularly in the data acquired between times 79.5 ms and 95.0 ms), in addition to those evident in the longitudinal plane. These secondary rotations of the bubble wake have been previously observed by Brücker [2], who suggested that they might be linked to the zig-zag motion exhibited by bubbles as they rise. The horizontal plane vortices, apparent in the through-plane velocity component, are seen to reverse direction following the observed wake shedding event, in a manner reminiscent of a von Kármán street. To explore this phenomenon, velocity maps were acquired of the horizontal plane immediately under the static bubble, at the position shown by the dotted grey box in Figure 8.8. Three-component velocity maps are shown in Figure 8.9 a), while the $x$-velocity component (extracted from the same data) is shown in b). Note that the $x$-velocity maps correspond to the through-plane velocity shown in Figure 8.8.

The formation of two counter rotating vortices is apparent between 0 ms and 47.7 ms in Figure 8.9 a), which clearly circle about local minima in the $z$-velocity. This suggests an intimate coupling between the transverse plane vortices, and the longitudinal rotations of the bubble wake. The instability of the transverse plane rotations is evident between 63.6 ms and 110.9 ms, where the vortices seem to merge before two fresh vortices form, this time rotating in the opposite direction. Between 126.8 ms and 174.5 ms the vortices

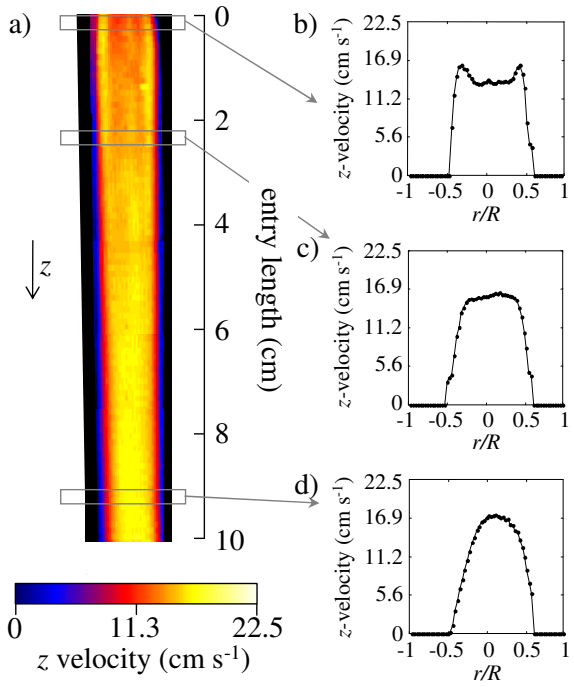


Figure 8.6: a) $z$-encoded velocity image of central slice in a contraction following the outlet of the flow profile manipulation device. Flow profiles are shown extracted at positions b) 3 mm c) 2.2 mm and d) 9.2 mm from entry to contraction.

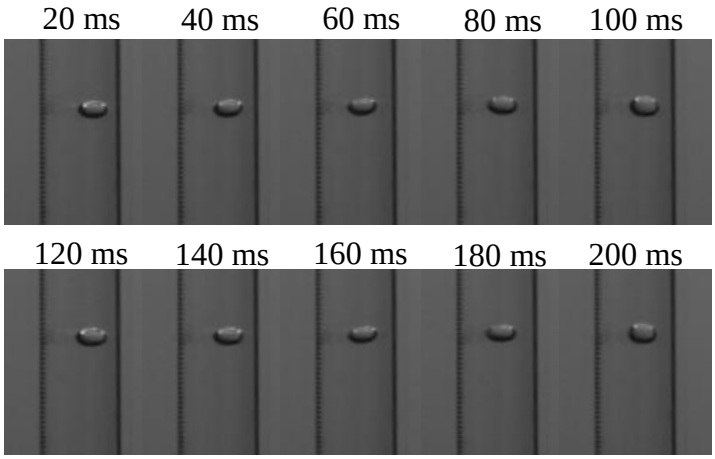


Figure 8.7: Highspeed photography footage of a bubble suspended in a contraction against a downflowing liquid.

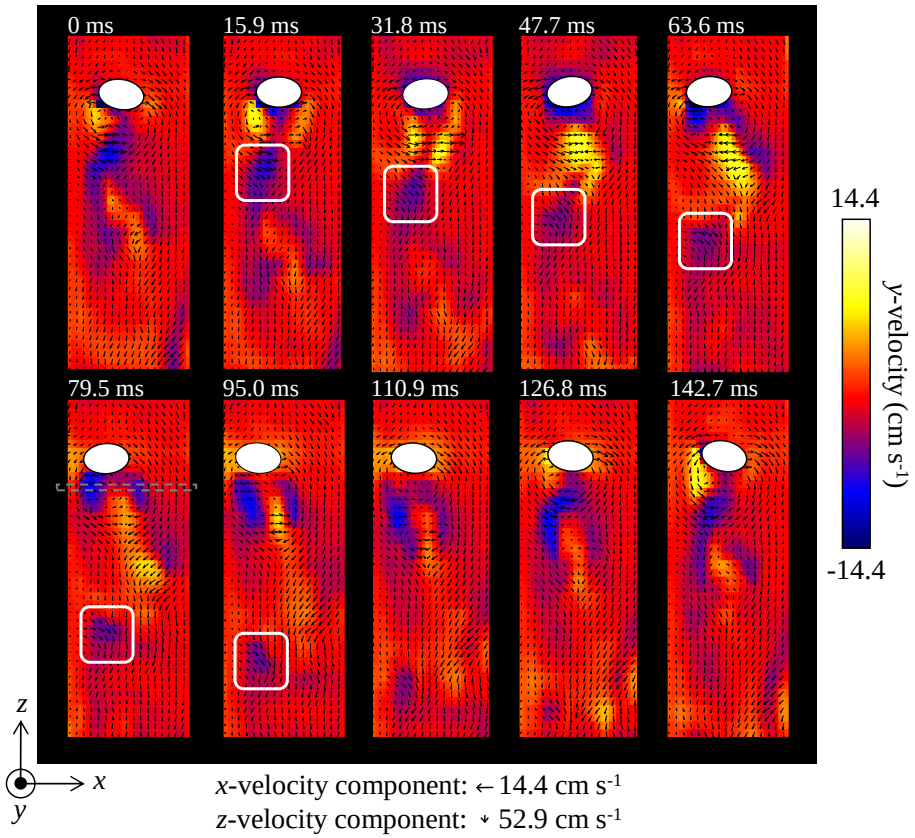


Figure 8.8: Vertical maps of the z-velocity for static bubbles of spherically equivalent radius 1.4 mm. The location of the bubble is highlighted by the filled white ellipses. A vortex shedding event is highlighted by the rounded white box. The location of the horizontal plane imaged is shown with respect to the bubble by the dotted grey box. The acquisition rate of these data is 63 fps. Note that the $z$ component of the velocity vectors has been scaled back to 5% of its original value in order to render the in-plane rotations of the wake more visible. The times shown on the images refer to the start of the acquisition. The spatial resolution is 313 μm × 469 μm for field of view of 20 mm × 30 mm.

are seen to merge and reverse again, returning to their original direction. The period of stability for the two vortices is 79.5 ms ± 15.9 ms, which corresponds to a frequency of 12.6 Hz ± 1.1 Hz: the frequency observed for vortex shedding in the present system. The coupling of the reversal of the transverse plane vortices with wake shedding can be observed directly in the vertical plane data given in Figure 8.8, where the newly formed wake at 15.9 ms is seen to be of opposite direction to that just shed. The bubble also is seen to shift during the formation of the transverse plane vortices, which suggests that this rotation either influences or is influenced by the path deviations, concurrent with the observations of Brücker [2]. While it is clear that the transverse plane rotations of the bubble wake are closely related to both vortex shedding and the bubble secondary motions, the causal relationship between these phenomena remains uncertain.

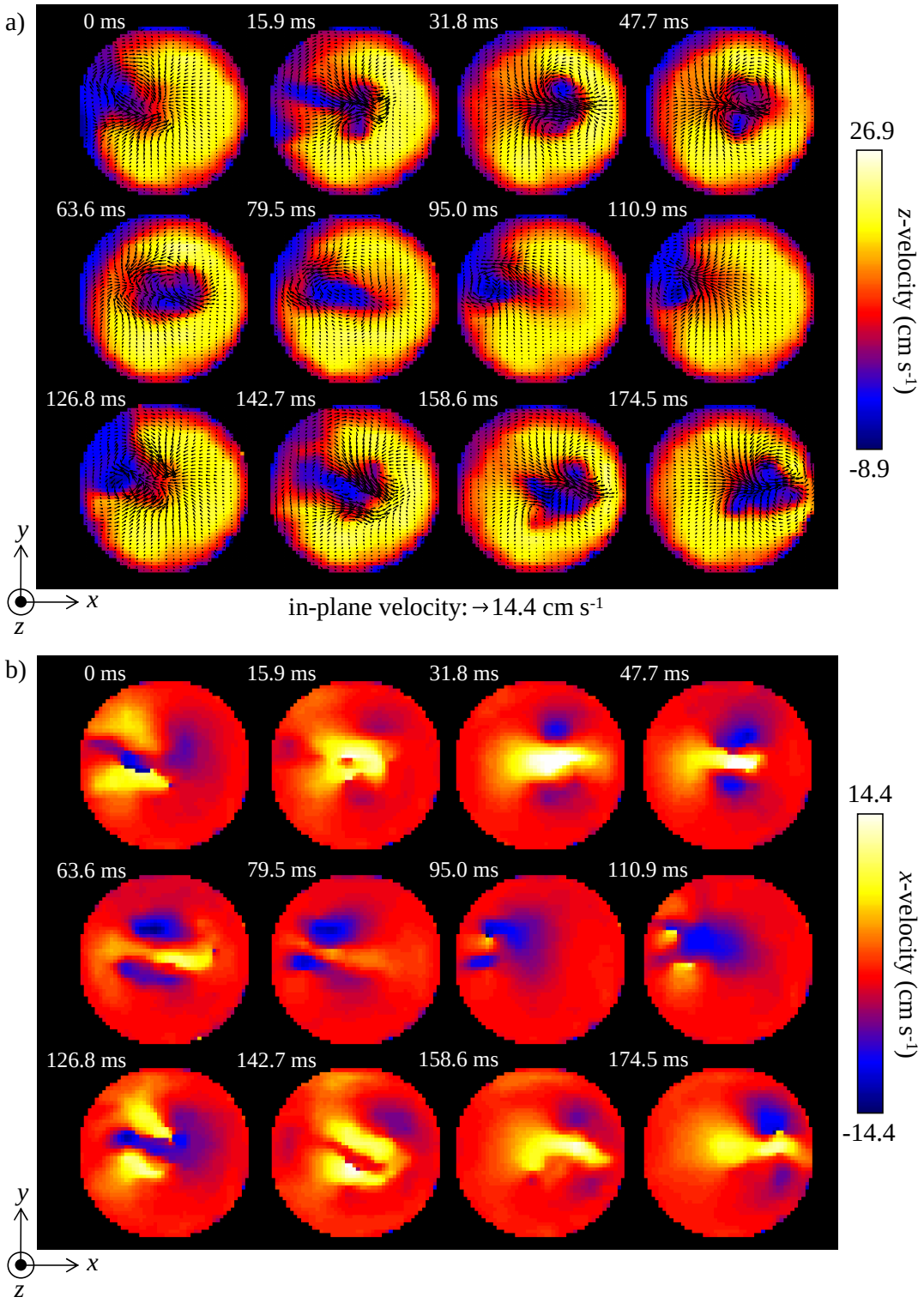


Figure 8.9: a) Horizontal plane, three-component velocity maps acquired immediately under a static bubble, at the position shown by the dotted grey box in Figure 8.8. The formation and periodic reversal of two counter-rotating transverse plane vortices is evident. b) $x$-component velocity maps extracted from the data which more clearly demonstrate the periodic nature of the inversion of the two vortices. The spatial resolution is 313 µm × 313 µm for field of view of 20 mm × 20 mm.

Note that the wake exhibited by the freely rising bubble shown in Figure 8.5 differs somewhat to that of the static bubble examined above, with an overall rolling motion being apparent rather than two counter rotating vortices. It is possible that the static bubble, which can only be viewed in a constrained geometry is not able to display the full range of wake behaviours seen by an unhindered bubble. The rolling motion of the freely rising bubble wake does suggest some rotational transverse plane behaviour; it is possible that the two counter-rotating transverse-plane vortices do exist behind this bubble, however are rendered heavily asymmetrical by the large angle of attack adopted by the freely rising bubble; similar to the asymmetry demonstrated by the potential flow about the bubble nose. Two such asymmetrical vortices would experience a significant lift force between them, which would drive an over-all rotation of the wake as observed. Further experimentation of both freely rising and static single bubbles is required for validation of this hypothesis.

### 8.3.3 Falling bubbles

An interesting phenomenon was observed while performing the static bubble experiments. When the downward flow around a static bubble was increased to the point that drag just began to overcome buoyancy, the bubble drifted downward while still undergoing shape oscillations and path deviations. When the downward flow was further increased, however, both forms of bubble secondary motion were seen to cease entirely, and the bubble fell along a straight line without shape oscillations. Velocity maps for both cases are shown in Figure 8.10 a) and b), respectively. Note that single component $z$-velocity maps are shown to highlight the difference in the wakes of the two bubbles. It is clear that the recirculating wake evident by the upward flowing fluid in Figure 8.10 a) (represented by the yellow pixels) is not present in Figure 8.10 b), where it is apparently 'washed-away' from the underside of the bubble by the increased flow rate. This concisely demonstrates that it is the recirculating wake that is responsible for bubble secondary motions, as opposed to potential flow about the nose of the bubble. Bubble secondary oscillations have long been attributed to the asymmetry of the bubble wake and vortex shedding [1, 6], and the present observation supports that conclusion. As noted in Section 8.3.2, while the causality between the transverse plane rotations of a bubble wake and bubble secondary motions is not certain, given that the falling bubbles clearly indicate that no secondary motion occurs without the presence of the wake, it may thus be hypothesised that it is the horizontal plane rotations of the bubble wake which instigates the path deviations exhibited by rising single bubbles.

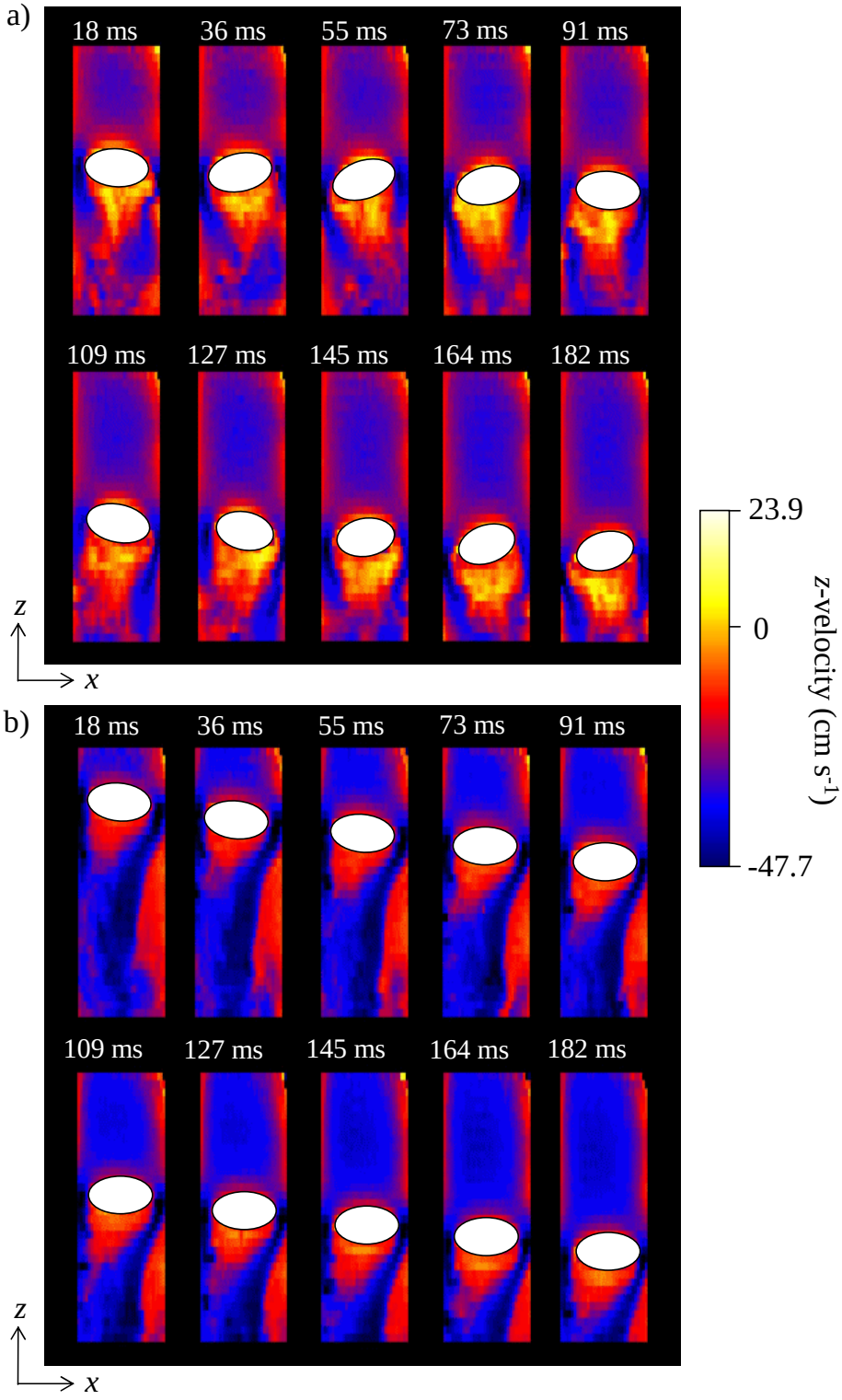


Figure 8.10: Vertical maps of the z-velocity for falling bubbles. a) Downward flow rate just sufficient to shift bubble downwards: bubble wake still apparent as are bubble shape oscillations and path deviations. b) Downward flow rate sufficient to wash bubble wake away. Note that both forms of bubble secondary motion have ceased. The spatial resolution is 313 μm × 469 μm for field of view of 20 mm × 30 mm.

Velocity encoded spiral imaging has proved to be a potent tool for experimentally quantifying bubble wake behaviours. The true nature of bubble wakes remains elusive, however, and further experimentation and analysis of numerical results is required to conclusively characterise the full range fluid phenomena influencing the system. By applying the developed methodology to a range of bubble sizes and under different flow conditions, it may be possible to construct a clearer picture of this most complex system. Spiral imaging may also prove useful in application to systems beyond the investigation of bubble wake dynamics. In particular, the behaviour of single oil droplets is of interest, and while these have been studied using MRI before [15, 16], time resolved measurements such as those enabled by the present technique have not yet been produced. Further points of interest may be to modify spiral imaging to exploit the chemically selective nature of MRI, and examine mass-transfer within a two-phase system, or surfactant spread across a droplet interface.

## 8.4 Conclusions

Spiral imaging has been applied to quantify the dynamics of single bubble wakes. Temporally resolved, three-component velocity maps were acquired of freely rising single bubbles, bubbles held static and falling bubbles. For the freely rising bubbles, vortex shedding events were evident, and were noted to coincide with changes in the bubble orientation. The bubble wake was seen to undergo a continuous rolling motion as the bubble rose. To enable the extended observation of bubble wakes, bubbles were held static in a contraction against a downward flow, such that the buoyancy and drag forces experienced by the bubble were equivalent. To minimise the influence of the flow profile of the counter-current flow, a bank of channels of radially decreasing length was inserted upstream of the contraction, which had the effect of flattening the parabolic flow profile. In studying the static bubble, images of both the vertical plane and the horizontal plane immediately behind the bubble were used. In these data, two counter rotating transverse plane vortices were visible, which appear linked with the two well-known longitudinal vortices. These horizontal vortices were seen to form and become unstable in sync with wake shedding in the system, and inverted their direction of rotation following each shedding event. In this way, the change in transverse plane velocity components appeared reminiscent of a von Kármán street. The transverse plane rotations also showed evidence of being related to the direction of path deviations of the bubble. In performing these experiments it was noted that both bubble shape oscillations and path deviations cease

when the downward liquid flow rate is sufficiently increased to convey the bubble down the column. MRI velocimetry measurements on such a 'smooth falling' bubble revealed that the wake for these bubbles is entirely washed away, which, indicates that the bubble secondary motions are entirely instigated by flow in the recirculating wake. Thus while the exact causal relationship between the transverse plane vortices and bubble secondary motions remains unclear, it is hypothesised that the rotations of a bubble wake in the horizontal plane govern the sinuous path exhibited by bubbles as they rise.

# Bibliography


[1] Mougin, G. and Magnaudet, J., 2002. Path instability of a rising bubble. *Phys. Rev. Lett.*, 88, p. 014,502.

[2] Brücker, C., 1999. Structure and dynamics of the wake of bubbles and its relevance for bubble interaction. *Phys. Fluids*, 11, pp. 1781–1796.

[3] Ellingsen, K. and Risso, F., 2001. On the rise of an ellipsoidal bubble in water: oscillatory paths and liquid-induced velocity. *J. Fluid Mech.*, 440, pp. 235–268.

[4] Lunde, K. and Perkins, R.J., 1998. Shape oscillations of rising bubbles. *Appl. Sci. Res.*, 58, pp. 387–408.

[5] Veldhuis, C., Biesheuvel, A. and van Wijngaarden, L., 2008. Shape oscillations on bubbles rising in clean and in tap water. *Phys. Fluids*, 20, p. 040,705.

[6] Fan, L.S. and Tsuchiya, K., 1990. *Bubble wake dynamics in liquids and liquid-solid suspensions*. Butterworth-Heinemann.

[7] Schouveiler, L. and Provansal, M., 2002. Self-sustained oscillations in the wake of a sphere. *Phys. Fluids*, 14, pp. 3846–2854.

[8] Fujiwara, A., Danmoto, Y., Hishida, K. and Maeda, M., 2004. Bubble deformation and flow structure measured by double shadow images and PIV/LIF. *Exp. Fluids*, 36, pp. 157–165.

[9] Liu, Z. and Zheng, Y., 2006. PIV study of bubble rising behaviour. *Powder Tech.*, 168, pp. 10–20.

[10] Sakakibara, K., Yamada, M., Miyamoto, Y. and Saito, T., 2007. Measurement of the surrounding liquid motion of a single rising bubble using a dual-camera PIV system. *Flow Meas. Instr.*, 18, pp. 211–215.

[11] Binks, B.P., 2002. Particles as surfactants-similarities and differences. *Curr. Opin. Colloid In.*, 7, pp. 21–41.

[12] Bjerknes, V., 1909. *Die Kraftfelder*. Vieweg, Braunschweig.

[13] Jameson, G.J. and Davidson, J.F., 1966. The motion of a bubble in a vertically oscillating liquid: theory for an inviscid liquid, and experimental results. *Chem. Eng. Sci.*, 21, pp. 29–34.

[14] Davidson, J.F. and Kirk, F.A., 1969. Holding a bubble fixed by downward flow. *Chem. Eng. Sci.*, 24, pp. 1529–1530.

[15] Amar, A., Gross-Hardt, E., Khrapitchev, A.A., Stapf, S., Pfennig, A. and Blümich, B., 2005. Visualizing flow vortices inside a single levitated drop. *J. Mag. Res.*, 177, pp. 74–85.

[16] Amar, A., Blümich, B. and Casanova, F., 2010. Rapid multiphase flow dynamics mapped by single-shot MRI velocimetry. *ChemPhysChem.*, 11, pp. 2630–2638.

[17] Clift, R., Grace, J.R. and Weber, M.E., 1978. *Bubbles, drops, and particles.* Acadamic Press, New York.

[18] Batchelor, G.K., 1967. *An introduction of fluid mechanics.* Cambridge University Press, Cambridge.

# Chapter 9

# Conclusions

This thesis describes the first applications of ultra-fast magnetic resonance imaging (MRI) towards the characterisation of bubbly flow systems. The primary goal of this study was to provide a hydrodynamic characterisation of a model bubble column using drift-flux analysis [1, 2] by closing the model using experimental data obtained using MRI. To achieve this, it was sought to: measure bubble size distributions, interfacial area and liquid phase hydrodynamics; validate a model for single bubble terminal rise; and apply the developed techniques towards the study of single bubble dynamics.

The first challenge in applying MRI to bubbly flow lay in determining a workable balance between the highly transient nature of the system and the relatively slow data acquisition associated with MRI. To enable the fastest acquisition techniques it was necessary to render the magnetic susceptibility of the dispersed and continuous phases equivalent by doping the liquid with a paramagnetic salt. Using the technique of Sains *et al.* [3], it was determined that a 16.86 mM dysprosium chloride solution was required for this purpose. In addition to altering the magnetic response of the fluid, this salt was found to have a strong stabilising influence on the structure of bubbly flow, which was desirable in order to enable the present measurements across as wide range of conditions, and all further measurements were performed on a magnetic susceptibility matched solution.

In the first instance, the MRI protocols FLASH, RARE and EPI were applied to low

voidage bubbly flow. It was found that FLASH and RARE acquisitions were simply too slow to capture the highly transient structure of bubbly flow, with the slice of excited fluid changing greatly over the course of the acquisition period. Conversely, EPI, the fastest conventional imaging technique, proved capable of producing non-temporally averaged images. EPI, however was found to suffer from heavy signal attenuation for all voidages greater than 3.5%. The cause of this was identified as the accrual of a velocity proportionate ('first moment') phase shift generated by the imaging gradients used in EPI. The combination of a heavily mixed, high-shear system and velocity proportionate phase accrual leads to strongly dissimilar phase shifts being generated in close spatial proximity, which when then dispersed, leads to net signal attenuation in the high-shear region. The accrual of first moment phase also undermines quantitative nature of phase contrast MRI velocimetry; preventing accurate velocity information from being obtained. An EPI based velocity imaging technique which overcame the problems associated with the accrual of first moment phase during imaging was proposed. This technique acquires both reference and velocity encoded phase maps following a single excitation, which are therefore exposed to similar velocity fields, allowing first moment imaging phase to be removed. While the technique cannot be applied to bubbly flow due to the shear attenuation artefact, it may still be applied to less heavily mixed, unsteady flow systems. In particular, the technique was demonstrated on the flow around an impeller, and on rising droplets of oil.

For measurements on high voidage bubbly flow systems it was necessary to consider alternate EPI-style acqusitions that minimise the accrual of first moment phase during imaging. A technique known as spiral imaging was selected on this basis, as it samples the high-power centre of reciprocal space at the start of the sequence, before spurious phase shifts have the chance to accrue, and as it uses oscillatory read gradients in both directions, which equips spiral imaging with a significant amount of first moment refocusing. Accurate knowledge of the sampled **k**-space points is a necessity for the success of spiral imaging, and two techniques for the measurement of gradient waveforms were examined. The first, based on the use of a specialised magnetic field monitor [4], was found to be inappropriate for use with imaging hardware. The second, an imaging based approach [5], produced good results, and was adopted for all further applications of spiral imaging in the study. Velocity measurements on unsteady systems using spiral imaging were examined in detail. Using simulated acquisitions, it was shown that the accrual of first moment phase shifts during imaging are minimal for spiral imaging. While it is well acknowledged in the literature that in-plane flow has an adverse effect upon the

point-spread function for images obtained using spiral imaging [6, 7], it was found that in application to physical systems these artefacts are minimised by the presence of boundary affected flows. Single-velocity component spiral images were then obtained of single phase unsteady flow in a pipe (Re = 4,500), with 32 pixel × 32 pixel images acquired at a rate of 91 frames per second (fps). The high temporal resolution of these measurements allowed highly transient wall instabilities to be captured. By under-sampling and employing a compressed sensing reconstruction the technique was accelerated to permit the acquisition of 64 pixel × 64 pixel images at a rate of 188 fps, which allowed the production of three-component velocity vector maps at a rate of 63 fps.

Using spiral imaging, images of bubbly flow in a vertical pipe of diameter 31 mm were successfully produced up to a voidage of 40.8%, which corresponds to the whole range for which dispersed bubbly flow was possible. Spiral imaging proved to be so robust to fluid shear (error in signal intensity less than 3.5% for Reynolds numbers of upto 12,000) that bubbles could be volumetrically sized using signal intensity, in addition to the projected measurement of bubble size obtained directly from the images. These two measurements of bubble size were combined to yield a measurement of bubble shape, which in turn permitted the quantification of interfacial area. Thus, both the evolution of the bubble size distribution and interfacial area were quantified as a function of position in the column. A set of experimental closures for bubble size as a function of voidage and position in the column were produced for use with drift-flux analysis. The spiral imaging velocity measurement technique was applied to bubbly flow across the full range of voidages, with one-component velocity fields successfully produced. Unfortunately 3-component velocity maps could not be produced of this system due to hardware limitations. The produced velocity maps compared well with propagators also measured for the system. Measurements such as these should prove useful for validation of increasingly prevalent gas-liquid computational fluid dynamics codes.

For the hydrodynamic characterisation of bubbly flow using drift-flux analysis it is of critical importance that the single bubble rise velocity be accurately calculated. A number of models for bubble terminal velocity from the literature were compared with experimental rise velocities measured for the present system using highspeed photography. Adequate agreement was reached for the model of Abou-el-hassan [8], however it was hypothesised that more accurate predictions could be made using the model of Tomiyama *et al.* [9], which must be closed using information about bubble aspect ratio. Obtaining an accurate description of bubble shape is a standing problem in the literature [10, 11, 9], as 2D

projections (i.e. photographs) of a 3D bubble are not representative of the true bubble shape or orientation. To overcome this problem, the relationship was derived between an ellipsoid and the ellipses obtained by projecting this shape onto a given plane. Using this model, an experimental methodology for measuring bubble projections, and fitting the 3D shape equation to these contours was proposed. In this way, the first true 3D description of bubble shape was produced. Bubble shapes were reconstructed for bubbles in the size range 0.5 mm $< r_e <$ 2.3 mm. Using these measurements, an empirical closure for bubble aspect ratio as a function of bubble size was proposed for the present system. When closed using the developed correlation, the model of Tomiyama *et al.* produced predictions within 9% of those measured experimentally. The reconstructed 3D bubbles also permitted different modes of shape oscillation to be viewed in isolation of each other. While the well known prolate-oblate ('mode 2') oscillations were evident (although at a frequency less than that predicted by literature models [12], which was likely the influence of the paramagnetic dopant in the system), other modes of shape oscillation commonly observed in the literature (such as capillary waves travelling over the bubble [10]) were not present. The bubble shape reconstruction should provide a useful tool for the future study of single bubble dynamics.

Using the measurements of bubble size, the proposed aspect ratio closure correlation, and the validated bubble rise model of Tomiyama *et al.* [9], a hydrodynamical model of the system was proposed using drift-flux analysis. In doing this it was necessary to determine the Richardson-Zaki index for the system, which is a parameter that relates the single bubble rise velocity to the hindered bubble rise velocity in high voidage systems [13]. For a semi-batch system, this parameter can be calculated from the superficial velocity of the gas, and a measurement of the voidage. This calculation, however, assumes that the bubble slip velocity can be represented by a single mean. In verifying this assumption, propagators were obtained of bubbles of sulfphur hexafluoride rising through magnetic susceptibility matched solution. The mean of these velocity distributions was found in acceptable agreement with the slip velocity calculated from the superficial gas velocity and voidage, which indicates that for the present system the slip velocity can be determined for a given set of operating conditions directly from a measurement of the gas-fraction. On the basis of the calculation, it was determined that the Richardson-Zaki index of the present system was 1.3 for all bubbles examined in the present study. A drift-flux model of the system was then proposed. This model was found to accurately predict liquid hold-up as a function of gas superficial velocity (within 5% error for all measurements), however failed to predict the transition from bubbly flow to slug flow. This was attributed

to the inability of the drift-flux model to account for the more complex behaviour of the present electrolyte stabilised system, in which the voidage increased monotonically with superficial velocity until unpredictably making the transition to slug flow at a voidage of 41%.

Finally, the effect of bubble wake behaviours upon single bubble dynamics was investigated using the newly developed spiral imaging velocimetry technique. Three-component velocity vector fields around single rising bubbles were measured, with all expected wake behaviours (i.e. vortex shedding) evident. The bubble wake dynamics were investigated in more detail by obtaining velocity measurements around a bubble held static in a contraction (such that the buoyancy and drag forces on the bubble were balanced), with the velocity profile of the counter-current flow rendered uniform by means of a tube bank of varying radial length upstream of the contraction. Both vertical and horizontal plane velocity images were acquired of the wakes of static bubbles, where it was noticed that periodic and unstable, counter-rotating vortices exist in the transverse plane. The vortices were noted to be coupled with the well-known longitudinal plane vortices, which were also apparent. The transverse plane vortices became unstable and were lost during each vortex shedding event, only to subsequently reform rotating in the opposite direction. These changes in the direction of rotation of the were noted accompany the changing direction of the bubble's motion. The transverse plane vortices were thus seen to be coupled with both vortex shedding, and the secondary motions of the bubble, though it remains unclear which phenomena instigates which. It was noted that when the downward flow around the bubble was sufficiently increased to 'wash' the wake away from the underside of the bubble, all secondary motions of the bubble rapidly ceased. This concisely demonstrates that the bubble wake dynamics are responsible for the shape oscillations and path deviations exhibited by bubbles as they rise (as opposed to potential flow about the nose of the bubble). These observations provide a new avenue by which the mechanisms of vortex shedding may be modelled, and demonstrate the great potential of spiral imaging for the phenomenological characterisation of single bubble dynamics.

## 9.1 Future work

Over the course of these experiments many interesting avenues for future research have emerged. Clearly, the principle objective of the present measurements is to provide a basis for which multiphase computational fluid dynamics (CFD) codes can be validated. A comparison of the measurements presented in this thesis, and the results of CFD sim-

ulations is therefore a clear direction for future research. In particular, the nature of multiphase induced turbulence remains poorly understood, as is the coupling of momentum between gas and liquid phases. By performing simulations using common closures for these terms, and comparing the results to the present measurements, some insight may be gained to the accuracy of each approach.

Further, the present measurements provide a firm basis for the testing of individual closure models. In particular, as noted in Section 5.3.5, periodic bubble breakup and coalescence events are visible in the high temporal, vertical plane images of bubbly flow. To be able to quantify rates of bubble break-up and coalescence in high gas-fraction systems is valuable, as a common approach to the numerical modelling of multiphase flows involves coupling a population balance equation with CFD [14]. This approach needs to be closed using models for break-up and coalescence rates (as reviewed by Hibiki and Ishii [15]); the veracity of which has proven difficult to test due to a lack of experimental information. Validating these models in the past has been limited to either low voidage systems (where the amounts of break-up and coalescence are likely very different to high gas-fraction systems) or using invasive local-phase probes [16]. The invasive effect of the probe aside, local phase probes cannot isolate rates of bubble break-up and coalescence from each other. This makes the individual validation of the closure models difficult, unlike in the MRI data, where-in either event can be visually identified. As the experimental procedures are already in place, the challenge here lies in developing image processing procedures which can accurately identify bubble break-up and coalescence in data of the form shown in Figure 5.15. This would require some form of bubble tracking procedure that can account for the bubbles entering and leaving the slice of excited fluid. A good approach to developing this technique would be to acquire both optical and MRI data of a low voidage, high Reynolds number system (i.e. with a high superficial liquid velocity), and demonstrate that in this case the image processing procedure produces break-up rates in agreement with the optical data. It is also interesting to note that the same break-up/coalescence closures are applied to both gas-liquid and liquid-liquid systems [17]. By applying the developed methodology to both oil-water and gas-liquid systems, it may be possible to suggest alterations to the closure models that account for the differences between the two.

Much opportunity also exists to study single bubble dynamics. The bubble shape reconstruction procedure should be very useful for studying bubble shape oscillations in a wider range of conditions that those examined in the present thesis. In particular, char-

acterising the shape oscillations of both low and high initial deformity bubbles in both pure and surfactant contaminated fluids would be of interest. Additionally, the study of shape oscillations of bubbles exposed to an external pressure field may be beneficial. Much potential also exists for the study of single bubbles using the developed MRI techniques. This was demonstrated in Chapter 8, where new insights about the behaviour of bubble wakes were are enabled using spiral imaging. More experimentation is required to apply the developed techniques to a wider range of bubble sizes and flow conditions before the full range of fluid phenomena occurring in bubble wakes can be characterised. Further, it would be interesting to compare the present measurements with simulations of the same systems obtained using a volume-of-fluid CFD [18].

The presence of the electrolytic dopants used in the present study for magnetic susceptibility matching had a strong influence on every area of the system; from stabilising bubbly flow to permit higher voidages to be reached, to slowing bubble rise velocities and dampening shape oscillations. It is well known in the literature that electrolytes have a strong influence on gas-liquid flows [19, 20], however the underlying physical mechanisms for many of these effects remain poorly understood. While it is generally agreed that the effects are ion specific [21] and that electrolytes inhibit bubble coalescence by slowing the drainage of gas-liquid films, there are conflicting results regarding the impact of salts on bubble terminal velocity [22, 23], and little work exists on the effect had on bubble shape. Thus to build up a large enough dataset for a clear picture to emerge, more experimental work is needed to quantify the effect of different ions on the gas-liquid interface. Further, the proposed hypotheses for the origin of these effects range from the formation of ionic bonds between salt ions and water molecules [24], to some form of hydrophobic attraction [25]. These hypotheses require testing and validation, which may involve such experiments as the quantification of local ionic concentrations, or the modelling of molecular dynamics.

In an interesting recent study, workers in Aachen [26] presented MRI measurements of the time-averaged flow-field within a droplet of oil, which was held steady in a contraction as described in Section 8.1. These measurements could be advanced by using an MRI technique capable of producing temporally resolved information. While spiral imaging may not be appropriate for this task due to its poor response to off-resonance effects, radial EPI [27] is noted to be strongly robust in this regard, and may be an appropriate basis for these measurements. The examination of static droplets of oil using ultrafast MRI would allow the dynamics of the drop-side flow field to be quantitatively captured

for the first time. Further, other transient transport phenomena in the system may be studied using the proposed technique. In particular, it may be possible to image droplet side mass transfer by introducing an oil-water soluble compound to the system. The chosen species would need to have some form of chemical resolution associated with it, and would probably need to be fluorinated. These measurements would be of great value for the validation of mass transfer models, as it is known that the droplet-side mass transport can have a great influence on the overall rate of mass transfer [28].

Another transient phenomena which may now be studied for the first time is the adsorption and spread of surfactant over a fluid interface. Due to the very small localised concentrations of surfactant associated with this process, it would be necessary to introduced some strong MRI contrast mechanism to the system. In particular, it may be possible to use a surfactant molecule chelated with a paramagnetic nuclei, which would affect the relaxation rates of nearby water molecules aswell as the surfactant itself. The distribution of surfactant over a drop is phenomenologically interesting, as it is generally hypothesised that the surfactant is swept to be rear of the drop, forming a 'rigid cap', which imparts a positional dependence to the interfacial shear state [29]. Alternatively, if high-enough spatial resolution velocity fields could be measured it may be possible to extract shear rates, which would directly reveal the surface shear condition. The amount of surface shear is one of the great unknowns in the modelling of multiphase systems, and the proposed measurements could be used suggest realistic boundary conditions.

# Bibliography


[1] Wallis, G.B., 1969. *One-dimensional two-phase flow*. McGraw-Hill, New York.

[2] Zuber, N. and Findlay, J., 1965. Average volumetric concentration in 2-phase flow systems. *ASME J.*, 87, p. 453.

[3] Sains, M., 2006. *Ultra-fast visualisation of unsteady flow using magnetic resonance imaging*. Ph.D. thesis, University of Cambridge.

[4] Han, H., MacGregor, R.P. and Balcolm, B.J., 2009. Pure phase encode magnetic field gradient monitor. *J. Magn. Reson.*, 201, pp. 212–217.

[5] Duyn, J.H., Yang, Y., Frank, J.A. and van der Veen, J.W., 1998. Simple correction method for k-space trajectory deviations in MRI. *J. Magn. Reson.*, 132, pp. 150–153.

[6] Butts, K. and Riederer, S.J., 1992. Analysis of flow effects in echo-planar imaging. *J. Magn Reson. Im.*, 2, pp. 285–293.

[7] Gatehouse, P.D. and Firmin, D.N., 1999. Flow distortion and signal loss in spiral imaging. *Magn. Reson. Med.*, 41, pp. 1023–1031.

[8] Abou-el hassan, M.E., 1983. A generalized bubble rise velocity correlation. *Chem. Eng. Comm.*, 22, pp. 243–250.

[9] Tomiyama, A., Celata, G.P., Hosokawa, S. and Yoshida, S., 2002. Terminal velocity of single bubbles in surface tension force dominant regime. *Int. J. Multiphase Flow*, 28, pp. 1497–1519.

[10] Lunde, K. and Perkins, R.J., 1998. Shape oscillations of rising bubbles. *Appl. Sci. Res.*, 58, pp. 387–408.

[11] Veldhuis, C., Biesheuvel, A. and van Wijngaarden, L., 2008. Shape oscillations on bubbles rising in clean and in tap water. *Phys. Fluids*, 20, p. 040,705.

[12] Lamb, H., 1895. *Hydrodynamics*. Cambridge University Press, Cambridge.

[13] Coulson, J.M., Richardson, J.F., Harker, J.H. and Backhurst, J.R., 1991. *Chemical engineering volume 2, 4th Edition*. Butterworth-Heinemann, Oxford.

[14] Wang, T. and Wang, J., 2007. Numerical simulation of gas-liquid mass transfer in bubble column with a CFD-PBM coupled model. *Chem. Eng. Sci.*, 62, pp. 7107–7118.

[15] Hibiki, T. and Ishii, M., 2009. Interfacial area transport equations for gas-liquid flow. *J. Comp. Multiphase Flow*, 1, pp. 1–22.

[16] Hibiki, T., Goda, H., Kim, S., Ishii, M. and Uhle, J., 2003. Experimental study on interfacial area transport of a vertical downward bubbly flow. *Exp. Fluids*, 35, pp. 100–111.

[17] Andersson, R. and Andersson, B., 2006. On the breakup of fluid particles in turbulent flows. *AICHe J.*, 52, pp. 2020–2030.

[18] Krishna, R. and van Baten, J.M., 1998. Simulating the motion of gas bubbles in a liquid. *Nature*, 398, p. 208.

[19] Ribeiro, C.P. and Mewes, D., 2007. The influence of electrolytes on gas hold-up and regime transition in bubble columns. *Chem. Eng. Sci.*, 62, pp. 4501–4509.

[20] Orvalho, S., Růžička, M. and Drahoš, J., 2009. Bubble columns with electrolytes: gas holdup and flow regimes. *Ind. Eng. Chem. Res.*, 48, pp. 8237–8243.

[21] Henry, C.L., Dalton, C.N., Scruton, L. and Craig, W.S.J., 2007. Ion-specific coalescence of bubbles in mixed electrolyte solutions. *J. Phys. Chem. C*, 111, pp. 1015–1023.

[22] Jamialahmadi, M. and Müller-Steinhagen, 1992. Effect of alcohol, organic acid and potassium chloride concentration on bubble size, buble rise velocity and gas hold-up in bubble columns. *Chem. Eng. J.*, 50, pp. 47–56.

[23] Henry, C.L., Parkinson, L., Ralston, J.R. and Craig, V.S.J., 2008. A mobile gas-water interface in electrolyte solutions. *J. Phys. Chem. C*, 39, pp. 15,094–15,097.

[24] Zieminski, S.A. and Whittemore, R.C., 1971. Behavior of gas bubbles in aqueous electrolyte solutions. *Chem. Eng. Sci.*, 26, pp. 509–520.

[25] Craig, V.S.J., Ninham, B.W. and Pashley, R.M., 1993. The effect of electrolytes on bubble coalescence in water. *J. Phys. Chem.*, 97, pp. 10,192–10,197.

[26] Amar, A., Gross-Hardt, E., Khrapitchev, A.A., Stapf, S., Pfennig, A. and Blümich, B., 2005. Visualizing flow vortices inside a single levitated drop. *J. Mag. Res.*, 177, pp. 74–85.

[27] Silva, A.C., Barbier, E.L., J., L.I. and Koretsky, A., 1998. Radial echo-planar imaging. *J. Magn. Reson.*, 135, pp. 242–247.

[28] Kronig, R. and Brink, J.C., 1951. On the theory of extraction from falling droplets. *Appl. Sci. Res.*, A2, pp. 142–154.

[29] Takagi, S. and Matsumoto, Y., 2011. Surfactant effects on bubble motion and bubbly flows. *Annu. Rev. Fluid. Mech.*, 43, pp. 615–636.